



HELMUT SCHMIDT
UNIVERSITÄT

Universität der Bundeswehr Hamburg

Modeling and Simulation of the Breakage of Cohesive Particle Agglomerates in Turbulent Wall-Bounded Flows

Doctoral Thesis

approved by the

Department of Mechanical Engineering

of the

Helmut-Schmidt-University

University of the German Federal Armed Forces

for obtaining the academic degree of

Doktor Ingenieur (Dr.-Ing.)

presented by

Ali Ahmad A. Khalifa

from Amman/Jordan

Hamburg, 2022

Referees

Univ.-Prof. Dr.-Ing. habil. Michael Breuer

Professur für Strömungsmechanik (PfS)
Institut für Mechanik
Fakultät für Maschinenbau und Bauingenieurwesen
Helmut-Schmidt-Universität Hamburg
Holstenhofweg 85 / Postfach 70 08 22
22043 Hamburg / Germany

Univ.-Prof. Dr. Berend van Wachem

Lehrstuhl Mechanische Verfahrenstechnik
Institut für Verfahrenstechnik
Fakultät für Verfahrens- und Systemtechnik
Otto-von-Guericke-Universität Magdeburg
Universitätsplatz 2
39106 Magdeburg / Germany

The day of submission: March 18, 2022

The day of completion of the oral examination: September 19, 2022

Kurzfassung

Diese Dissertation befasst sich mit der Entwicklung von Vorhersagemodellen für den Aufbruch von kohäsiven Partikelagglomeraten in turbulenten wandgebundenen Strömungen. Die Modelle werden für eine vorhandene effiziente Euler-Lagrange Simulationsmethode formuliert, bei der die Agglomerate durch einzelne Kugeln mit effektiven Durchmessern dargestellt werden. In diesem Kontext werden deutliche Fortschritte in den folgenden Schwerpunkten erreicht: **(i)** Der Beschreibung der Eigenschaften der Agglomerat-Struktur, **(ii)** dem Bruch von Agglomeraten durch fluidinduzierte Spannungen und **(iii)** dem Bruch von Agglomeraten durch Wandkollisionen.

Das Strukturmodell weist den Agglomeraten Eigenschaften zu, die eine Festlegung des effektiven Durchmessers erlauben, welcher zur Lagrangeschen Verfolgung und zur Bestimmung der Stärke des Agglomerats genutzt wird, um ein mögliches Auseinanderbrechen zu evaluieren. In dem Modell für den Zerfall durch Fluidkräfte werden Ideen aus der Literatur aufgegriffen und erweitert, um Aufbruchkriterien herzuleiten. Die Vorgehensweise beruht auf einem Vergleich zwischen den Fluidspannungen, denen ein Agglomerat entlang seiner Lagrange-Trajektorie ausgesetzt ist, und einer kritischen Belastungsschwelle, die durch die Stärke des Agglomerats definiert wird. Es werden drei Spannungsarten berücksichtigt, die Turbulenz, der Luftwiderstand und die Rotationsspannung. Darüber hinaus wird ein besonderer Schwerpunkt auf die Geschwindigkeiten der Fragmente nach dem Auseinanderbrechen der Agglomerate gelegt. Für die Ableitung des Bruchmodells durch Wandkollisionen wird eine große Anzahl detaillierter diskreter Elemente-Simulationen einzelner Agglomerate durchgeführt. Weite Bereiche unterschiedlicher Aufprallbedingungen wie die Aufprallgeschwindigkeit, der Aufprallwinkel, die Anzahl der Primärpartikel und deren Größe werden berücksichtigt. Die Ergebnisse werden auf der Grundlage repräsentativer Parameter analysiert, die es ermöglichen, die Anzahl der entstehenden Fragmente sowie deren Größen- und Geschwindigkeitsverteilung zu quantifizieren. Um Beziehungen zwischen Aufprallbedingungen und den Parametern des Zerfalls aufzustellen, werden zwei Ansätze genutzt. Der erste beruht auf herkömmlicher Dimensionsanalyse und Regressions-techniken, während der zweite künstliche neuronale Netze verwendet.

Schließlich wird die beschriebene LES-basierte Euler-Lagrange-Methodik angewendet, um die Leistungsfähigkeit der neuen Modelle anhand von drei Anwendungen zu beurteilen: 1- Trichter-Kanal-Strömung angelehnt an ein Experiment zur Untersuchung des Aufbrechens von Agglomeraten in einem Dispergierer im Labormaßstab, 2- Kanal-Strömung und 3- Strömung in Rohrbögen inspiriert durch experimentelle und numerische Studien über die Wirkung des Biegungsdesigns auf die Desagglomerationsleistung von Trockenpulver-Inhalatoren. Die erzielten Ergebnisse zeigen, dass aussagekräftige Vorhersagen zu erschwinglichen Rechenkosten mit der gewählten Simulationsstrategie erreicht werden können. Außerdem werden wichtige Einblicke in das Aufbruch-Verhalten gewonnen. Dazu gehört das Verständnis der relativen Wichtigkeit der unterschiedlichen Bruchmechanismen und die Bestimmung der kritischen Fluid- und Partikeleigenschaften für das Auseinanderbrechen. Darüber hinaus werden die Wechselwirkungen zwischen Agglomerat-Bruch und anderen konkurrierenden Phänomenen wie der Agglomeration erforscht.

Abstract

The present thesis is concerned with the development of predictive models for the deagglomeration of cohesive particle entrained in turbulent wall-bounded flows. The models are derived for an existing efficient Euler–Lagrange simulation strategy, in which agglomerates are represented by single spheres possessing effective diameters. In this context, serious meaningful advancements to the state of the art are achieved concerning the following issues: **(i)** the description of the structural features of agglomerates, **(ii)** the breakup by fluid-induced stresses, and **(iii)** the wall-impact breakage.

The model of the structural features endows the spheres used for representing agglomerates with properties allowing to reasonably determine the effective diameter used in the Lagrangian tracking and the strength of the agglomerate needed for evaluating the possibility of breakage.

In the model for the fluid-induced breakup ideas from the literature are revisited and extended to derive breakup criteria. The approach relies on a comparison between the fluid stresses exerted on an agglomerate along its Lagrangian trajectory with a critical stress threshold defined by the strength of the agglomerate. Three types of stresses are considered, which are the turbulent, the drag, and the rotary stress. Furthermore, a special emphasis is put on the post-breakup treatment, i.e., the arising velocities of the disintegrated fragments.

For the derivation of the wall-impact breakage model, an extensive number of detailed discrete element simulations of single agglomerates is carried out. Wide ranges of different impact conditions such as the impact velocity, the impact angle, the number of primary particles and the size of the particles are taken into account. The results are analyzed based on useful parameters allowing to quantify the number of arising fragments, their size distribution, and the distribution of their post-breakage velocities. To establish relationships between the impact conditions and the breakage parameters two approaches are explored. The first relies on conventional dimensionality reduction and regression techniques, whereas the second employs feed-forward artificial neural networks.

Lastly, the described LES-based Euler–Lagrange methodology is applied to assess the performance of the new models based on three investigations: 1- funnel-duct flows inspired by an experimental investigation to study the breakup of agglomerates in a lab-scale disperser, 2- duct flows, and 3- the flow in pipe bends inspired by experimental and numerical studies on the effect of the bend design on the deagglomeration performance of dry powder inhalers. The results obtained demonstrate the clear advantage of the simulation strategy in offering reasonable predictions at affordable computational costs. Furthermore, important insight into the breakage behavior are gained. These include the understanding of the relative importance of the different breakage mechanisms and the identification of the critical fluid and particle properties for breakup. In addition, the interaction between breakage and other competing phenomena such as agglomeration is explored.

Acknowledgments

First of all, I would like to express my deepest appreciation to my supervisor Prof. Michael Breuer for offering me the chance to be part of his group and for his extraordinary guidance, patience, and support throughout this journey. Working closely with Prof. Breuer and learning from him inspired me in many ways and helped me to sharpen my character and to establish my academic career. I would also like to extend my sincere thanks to my second examiner Prof. Berend van Wachem for his efforts in evaluating my work and for his valuable comments and remarks.

I also wish to thank my past and present colleagues at the "Professur für Strömungsmechanik" (PFS), including Guillaume, Nick, Naser, Felix, Waldemar, Khaled, Arul, Torben, Surya, and Martin for maintaining a friendly atmosphere over the years and for their helpful remarks and suggestions. A special thanks goes to my Master students Constance and Jasper for the enjoyable experience and for their important contributions to my research.

Of course, I am extremely grateful to my loving parents, my parents in law, and my friends whose help and support can't be overestimated. Without their encouragement, the completion of my dissertation would not have been possible.

Last but by no means least, no words can tell my wife Sondos Jaber how much thankful I am for her patience, understanding, and unwavering support. For your sacrifices I remain indebted forever. To you and to our children Ahmad and Salma I dedicate this work... and the rest of my life.

The initial part of this work was financially supported by the Deutsche Forschungsgemeinschaft (DFG). All kind of supports are acknowledged.

Contents

Kurzfassung	i
Abstract	iii
Acknowledgments	v
Contents	vii
List of Figures	xi
List of Tables	xix
1 Introduction	1
1.1 Motivation for Considering Particle-Laden Flows	1
1.2 Modeling Approaches	4
1.3 Objectives of the Thesis	8
1.4 Outline of the Thesis	9
2 Literature Review on the Modeling of Breakage	11
2.1 Structure of Agglomerates	11
2.1.1 Detailed Structure	12
2.1.2 Idealized Structure	14
2.2 Breakup by Fluid Stresses	16
2.2.1 Fluid-Induced Breakup Predicted by Condition-Free Techniques . .	16
2.2.2 Fluid-Induced Breakup Predicted by Condition-Based Techniques .	19
2.2.2.1 Breakup of Rigid Agglomerates with Detailed Structures .	19
2.2.2.2 Breakup of Agglomerates Idealized as Spheres	21
2.3 Wall-Impact Breakage	25
2.3.1 Wall-Impact Breakage Predicted by Condition-Free Techniques . . .	25
2.3.2 Wall-Impact Breakage Predicted by Condition-Based Techniques . .	26
3 Description of the Continuous Phase	29
3.1 Governing Equations of Large-Eddy Simulation	29
3.2 Subgrid-Scale Modeling	30
3.2.1 Smagorinsky Model	31
3.2.2 Dynamic Model by Germano	32
3.3 Boundary Conditions	33

4	Description of the Disperse Phase	37
4.1	Classification of Point Particles and Interphase Coupling	37
4.2	Fluid-Induced Motion of Particles	40
4.2.1	Forces and Torque Acting on the Particle	41
4.2.2	Subgrid-Scale Model for the Particles	44
4.2.3	Feedback Effect on the Continuous Phase	45
4.2.4	On the Suitability of the Point-Particle Approach for the Present Work	45
4.3	Hard-Sphere Particle-Particle Collisions and Agglomerations	47
4.4	Interaction with Domain Boundaries	52
5	Model for the Structural Features of Agglomerates	55
5.1	Definitions and Overview on the Modeling Strategy	55
5.2	Generation of Agglomerates	58
5.3	Scaling of the Structural Features of Agglomerates	59
5.4	Application of the Model in Euler–Lagrange Simulations	62
6	Models for Breakup by Fluid Stresses	63
6.1	Overview on the Modeling Strategy	63
6.2	Strength of Agglomerates	64
6.3	Stress Mechanisms and Conditions for Breakup	65
6.3.1	Turbulent Stress	66
6.3.2	Drag Stress	68
6.3.3	Rotary Stress	71
6.4	Post-Breakup Kinetics	74
6.4.1	Kinetics for Breakup by Turbulent Stress	74
6.4.2	Kinetics for Breakup by Drag Stress	76
6.4.3	Kinetics for Breakup by Rotary Stress	78
6.5	Breakup Time Lag	80
7	Models for Breakage due to Wall Impact	83
7.1	Overview on the Data-Driven Modeling Strategy	83
7.2	DEM Wall-Impact Simulations	85
7.2.1	Discrete Element Method (Soft-Sphere)	85
7.2.2	Properties of the Particles and the Agglomerates	89
7.2.3	Wall-Impact Simulation Setup and Procedure	92
7.3	Breakage Parameters	94
7.3.1	Number of Fragments and Fragment Size Distribution	94
7.3.2	Post-Breakage Kinetics	96
7.4	Model Based on Traditional Regression Techniques	98
7.4.1	Fragmentation Ratio and Fragment Size Parameters	98
7.4.1.1	Wall-Impact Database	98
7.4.1.2	Trend Analysis	99
7.4.1.3	Derived Model	102

7.4.2	Spreading and Reflection Angles and Fragment Velocity Ratio . . .	109
7.4.2.1	Considered Impact Cases	110
7.4.2.2	Probability Distribution Analysis	110
7.4.2.3	Derived Model	114
7.5	Model Based on Artificial Neural Networks	119
7.5.1	Theoretical Background of Artificial Neural Networks	119
7.5.2	Fragmentation Ratio and Fragment Size Parameters	121
7.5.2.1	Extended Database	122
7.5.2.2	Derived ANN	124
7.5.3	Spreading and Reflection Angles and Fragment Velocity Ratio . . .	127
7.5.3.1	Considered Impact Cases	128
7.5.3.2	Derived ANN	129
7.5.4	Realization of the Model in the Euler–Lagrange Approach	133
8	Numerical Methodology	135
8.1	Numerical Methods for the Continuous Phase	135
8.2	Numerical Methods for the Dispersed Phase	138
8.2.1	Interpolation of Fluid Quantities to Particle Positions	138
8.2.2	Solution of the Particle Equations of Motion	139
8.2.2.1	Translatory Motion	139
8.2.2.2	Rotational Motion	142
8.2.3	Detection of Particle Collisions and Wall Impacts	143
8.2.4	Treatment of Agglomerate Breakage	144
9	Test Cases and Results	145
9.1	Powder Disperser	145
9.1.1	Flow Configuration	146
9.1.2	Computational Setup	149
9.1.2.1	Boundary Conditions	149
9.1.2.2	Computational Grids	150
9.1.2.3	Time-Step Size	153
9.1.3	Simulation Procedure	154
9.1.4	Continuous Flow in the Auxiliary Duct	155
9.1.5	Continuous Flow in the Disperser	156
9.1.6	Breakup Positions for Powder A	159
9.1.7	Breakup Statistics	162
9.1.8	Influence of the Breakup Time Lag	166
9.1.9	Summary and Conclusions	167
9.2	Duct Flows	168
9.2.1	Computational Setup	168
9.2.2	Simulation Procedure	170
9.2.3	Continuous Flow in the Duct	171
9.2.4	Part I: Traditional Regression Wall-Impact Breakage Model	174
9.2.4.1	First Set of Simulations: Pure Wall-Impact Breakage	174

9.2.4.2	Second Set of Simulations: Interaction with Other Phenomena	180
9.2.5	Part II: Comparison with the ANN-Based Wall-Impact Breakage Model	182
9.2.5.1	First Set of Simulations: Pure Wall-Impact Breakage	184
9.2.5.2	Second Set of Simulations: Interaction with Other Phenomena	190
9.2.6	Summary and Conclusions	192
9.3	Pipe Bend Flows	195
9.3.1	Flow Configurations	195
9.3.2	Computational Setup	197
9.3.3	Simulation Procedure	198
9.3.4	Validation of the Inflow Data	200
9.3.5	Continuous Flow in the Pipe Bends	202
9.3.5.1	Flow in the 90° Pipe Bend	203
9.3.5.2	Flow in the 45° Pipe Bend	206
9.3.6	Breakage of Agglomerates	207
9.3.7	Summary and Conclusions	212
10	Conclusions and Outlook	215
10.1	Conclusions	215
10.2	Future Work	218
A	Quantities Used in the Contact Models	221
B	Verification of the Reflection and Spreading Model	223
	Bibliography	225
	Curriculum Vitae	245
	Publications	247

List of Figures

1.1	Examples on particle-laden flows: (a) A dust storm traveling from north Africa to Italy spanning about 10^3 km, (b) The Zambezi river in Africa with a total length of 2574 km pouring water and sediment into the Indian Ocean (Images: NASA, Visible Earth), (c) A dry powder inhaler <i>Easyhaler</i> [®] (after Lavorini, 2019), (d) Exhaust fumes from smoking chimneys (Image: University of Freiburg).	2
1.2	Inhalation of particulates in the human respiratory tract (after Mao, 2011).	3
1.3	Schematic representation of the common modeling approaches for particle-laden flows (after Capecelatro, 2021).	4
2.1	Agglomerates represented by detailed structures (a)-(c) and an idealized one based on an effective sphere (d).	12
2.2	Convex hull wrapping an agglomerate consisting of 100 primary particles. .	15
2.3	Carrier-based powder formulation. This type of agglomerates is not considered in the present thesis.	17
4.1	Interphase and intraphase coupling regimes based on the volume fraction of the disperse phase Φ_p (Crowe, 2005; Elghobashi, 1991, 1994).	38
4.2	Schematic representation of the response of particles to a change of the flow motion based on the Stokes number St (Crowe et al., 1988).	39
4.3	Schematic representation of the response of a collision event. Note that the tangential vector \mathbf{t} depicted in the figure points towards one of many possible directions. The exact tangential direction is decided based on Eq. (4.39).	48
5.1	Random loose packing of $2 \cdot 10^5$ particles within a box generated by a Monte Carlo simulation.	59
5.2	Samples of the agglomerates artificially generated by a gradual accumulation of particles from the initial packing of $2 \cdot 10^5$ particles. The envelope containing the agglomerate is the corresponding convex hull used to represent the volume of the agglomerate V_{ag}	60
5.3	Scaling the Monte Carlo results by Eq. (5.8) for (a) the packing fraction f_{pack} and (b) the average coordination number k_c . Here the properties of the powders defined in Table 9.2 are assumed.	60
6.1	Fluid-induced breakup mechanisms considered in the present work. Here, $\mathbf{u}_{ag,slip}$ is the relative velocity vector between the fluid and the agglomerate and $\boldsymbol{\omega}_{ag}$ is the angular velocity vector of the agglomerate.	66

6.2	Schematic sketch of an agglomerate in uniform flow. Erosion by drag stress (after Breuer and Khalifa, 2019a,b).	69
6.3	Separation of two asymmetric fragments after breakage by the drag stress.	77
6.4	Sketch of the spherical agglomerate and the two-fragment structure. Note that a_1 and a_2 are the radii of the first and second fragments, i.e., $d_{fr1}/2$, $d_{fr2}/2$, respectively.	79
6.5	Time lag Δt_{lag} defines the minimum period separating two successive breakup events of the same agglomerate in time.	81
7.1	Spring-dashpot analogy for the normal and the tangential forces in DEM.	86
7.2	Comparison between the agglomerates obtained in the present study and those reported in Yang et al. (2008) concerning the packing fraction f_{pack} and the coordination number k_c . The data refer to seven agglomerates consisting of 10^4 equally-sized primary particles possessing the size d_{pp} given by the abscissa. As previously pointed out, in the present work a contact is detected if two particles are within the force cut-off distance l_{max} (i.e., $\delta_n/d_{pp} \leq -5 \cdot 10^{-2}$). However, the values of k_c here are computed restricting the criterion for counting a contact to $\delta_n/d_{pp} \leq -5 \cdot 10^{-3}$ in order to match the condition in Yang et al. (2008). The packing fraction $f_{pack} = N_{pp}^{tot} V_{pp}/V_{ag}$ of the agglomerates generated in the present work are computed assuming that the total volume of the agglomerate V_{ag} is equal to the volume of the convex hull closely wrapped around the primary particles (Dadkhah et al., 2012; Dietzel and Sommerfeld, 2013). The volume of the convex hull is computed using the built-in function <code>convhull</code> available in MATLAB®.	92
7.3	General setup of the DEM wall-impact simulations (Khalifa and Breuer, 2021).	94
7.4	Characterization of the results of wall-impact events using the number of fragments and the size of the three largest fragments (Khalifa and Breuer, 2021).	95
7.5	Schematic representation of the reflection angle α , the spreading angle β , and the velocity of the center of mass of a fragment \mathbf{v}_{cm}^{fr} , respectively. Note that \mathbf{n}_t , $\mathbf{v}_{imp,\parallel}$, and $\mathbf{v}_{cm,\parallel}^{fr}$ are spanning the wall plane (Khalifa and Breuer, 2021; Khalifa et al., 2022).	97
7.6	Fragmentation ratio FR as a function of the impact velocity $v_{imp,n}$ for a normal impact of agglomerates of powder A , B and C consisting of 50 to 10^4 primary particles. No error bars appear for the 10^4 particle agglomerates since solely a single impact was considered (see Section 7.2.3).	100
7.7	Number of detached fragments (the numerator in Eq. (7.18)) as a function of the impact velocity $v_{imp,n}$ for agglomerates of powder C consisting of 25 to 10^3 primary particles undergoing a normal impact.	101

7.8	Fragmentation ratio FR as a function of the normal component of the impact velocity $v_{\text{imp},n}$ (a, c) and as a function of the total impact velocity v_{imp} (b, d) for two exemplary agglomerates of powder C consisting of 50 or 10^3 primary particles impacting with varying impact angles Θ_{imp}	102
7.9	Number of detached fragments (the numerator in Eq. (7.18)) as a function of the dimensionless number π^* for normally impacting agglomerates of powder C consisting of 50 to 10^3 primary particles. The dashed line refers to the slope of the number of detached fragments ($N_{\text{fr}}^{\text{max}} - 1$) at low values of π^*	104
7.10	Fragmentation ratio FR as a function of the proposed dimensionless number π^{***} (Eq. (7.30)) for selected agglomerates related to powders A , B and C comprising 50 to 10^4 primary particles for a fixed impact angle of $\Theta_{\text{imp}} = 90^\circ$ (Note that in this case $\pi^{***} = \pi_{\text{imp}}$).	105
7.11	Fragmentation ratio FR as a function of the proposed dimensionless number π_{imp} (Eq. (7.31)) for selected agglomerates related to powders A and C comprising 50 to 10^4 primary particles for two different impact angles Θ_{imp} (90° vs. 15°).	106
7.12	History of the number of bonds generated during an impact normalized by the number of bonds in the original agglomerate at $\pi_{\text{imp}} = 2.12 \cdot 10^{-3}$ for agglomerates of powders A and C consisting of 50 to 10^4 primary particles.	107
7.13	Simulation results and fitting curves by Eqs. (7.32) for (a) the fragmentation ratio FR and the particle size parameters (b) ζ_1 , (c) ζ_2 and (d) ζ_3 as functions of the proposed dimensionless number π_{imp} . The included simulation data refer to all impact events carried out based on agglomerates of powders A , B and C comprising 10 to 10^3 primary particles with an impact angle Θ_{imp} varying between 7° and 90° . The most appropriate fitting parameters are given in Table 7.3.	108
7.14	Results based on 16 different impact events with $\Theta_{\text{imp}} = 7^\circ$ and $N_{\text{pp}}^{\text{tot}} = 100$ and full fragmentation (i.e., 1600 fragments): (a) reflection angle $\alpha/\Theta_{\text{imp}}$; (b) spreading angle $\beta/\Theta_{\text{imp}}$; (c) velocity ratio v_{ratio} . The solid line is fitted to the data by the Weibull distribution given by Eq. (7.33).	111
7.15	Comparison between the Weibull PDFs obtained for the full set of investigated cases. Again the reflection angle $\alpha/\Theta_{\text{imp}}$, the spreading angle $\beta/\Theta_{\text{imp}}$ and the velocity ratio v_{ratio} are depicted. The key legend provided in the first subfigure of a column applies to all subfigures of the same column. The (discrete) color bar refers to the impact angle Θ_{imp}	113
7.16	Scale and shape parameters λ and k of the Weibull PDFs (Fig. 7.15) as functions of the impact angle Θ_{imp}	115
7.17	Fitting curves for the parameters λ and k used in the Weibull PDFs as functions of the impact angle Θ_{imp} . The values of the coefficients of the fourth-order relationships are given in Table 7.5.	116
7.18	Ratios of energies ER_{trans} and ER_{rot} as functions of the impact angle Θ_{imp} . The blue solid line is a logarithmic fitting function, which is added here for guidance only.	118

7.19	Schematic representation of a multilayer feed-forward artificial neural network. The symbols x_I , a_M and y_J stand for the network input, the activation of a hidden node, and the network output, respectively. The indices I , M , and J stand for the number of nodes in the respective layers and m is an arbitrary node in the hidden layer. w and b refer to the weight of a connection (artificial synapse) and the bias in a particular node, respectively. $f_{\text{act}}^{\text{h}}$ denotes the activation function of the hidden layer.	120
7.20	Results for (a) the fragmentation ratio FR and the fragment size parameters (b) ζ_1 , (c) ζ_2 and (d) ζ_3 as functions of the dimensionless number π_{imp} for varying impact angles Θ_{imp} . The black curves refer to the regression relationships proposed in Section 7.4.1.3 before extending the DEM database and are solely added here as a reference. Note that for the two-particle agglomerates solely the fragmentation ratio is provided.	124
7.21	Results for (a) the fragmentation ratio FR and the fragment size parameters (b) ζ_1 , (c) ζ_2 and (d) ζ_3 as functions of the dimensionless number π_{imp} for varying numbers of primary particles $N_{\text{pp}}^{\text{tot}}$ in the agglomerate. The black curves refer to the regression relationships proposed in Section 7.4.1.3 before extending the DEM database and are solely added here as a reference. Note that for the two-particle agglomerates solely the fragmentation ratio is provided.	125
7.22	ANN predictions of the fragmentation ratio FR and the fragment size parameters ζ_i for (a) the training dataset and (b) the testing dataset. The reference line is dashed and has a slope of unity.	127
7.23	Results based on 64 different impact events with $\Theta_{\text{imp}} = 0.2^\circ$ and $N_{\text{pp}}^{\text{tot}} = 100$ achieving a mean fragmentation ratio of FR = 0.47: (a) reflection angle α ; (b) spreading angle β ; (c) velocity ratio v_{ratio} . The solid line is fitted to the data by the Weibull distribution given by Eq. (7.33).	129
7.24	Scale and shape parameters λ and k of the Weibull PDFs as functions of the impact angle Θ_{imp}	130
7.25	Ratio of translational kinetic energy of the fragments ER_{trans} as a function of the impact angle Θ_{imp}	131
7.26	ANN predictions of the six Weibull distribution parameters (scale λ and shape k parameter for the reflection angle α , the spreading angle β and the fragment velocity ratio v_{ratio}) and the kinetic energy ratio ER_{trans} for (a) the training dataset and (b) the testing dataset. The reference line is dashed and has a slope of unity.	132
8.1	Transformation of the coordinate system between the physical and the computational space.	136
9.1	Schematic sketch of the dry powder disperser (deagglomerator) (Breuer and Khalifa, 2019b).	147

9.2	Cross-sections of the (a) main pipe in the original configuration (Weiler, 2008) and (b) the square duct in the simplified configuration (Breuer and Khalifa, 2019a,b).	147
9.3	Variation of the strength S with the size of the agglomerate (number of primary particles $N_{\text{pp}}^{\text{tot}}$ included).	149
9.4	Computational grid for the duct-funnel case. (a) 3-D view of the multi-block structure; (b) Zoom of the cross-section in the y - z plane; (c) Zoom of the cross-section in the x - y plane.	152
9.5	Contours of the mean streamwise velocity u/U_b in the cross-section of the duct with superimposed streamlines of the mean secondary flow for the (a) low-Re and the (b) high-Re case.	155
9.6	Contour plots of the instantaneous streamwise velocity u/U_b for the (a) low-Re case and the (b) high-Re case; time-averaged streamwise velocity $\langle u \rangle / U_b$ for the (c) low-Re case and the (d) high-Re case; time-averaged resolved Reynolds stress in streamwise direction $\langle u'u' \rangle / U_b^2$ for the (e) low-Re case and the (f) high-Re case; time-averaged resolved Reynolds stress in y -direction $\langle v'v' \rangle / U_b^2$ for the (g) low-Re case and the (h) high-Re case; and time-averaged resolved Reynolds shear stress $\langle u'v' \rangle / U_b^2$ for the (i) low-Re case and the (j) high-Re case. All results are depicted in the x - y symmetry plane ($z/d_h = 0$).	157
9.7	Contour plots of (a) the turbulent kinetic energy $\langle k \rangle / U_b^2$, (b) the magnitude of the strain rate tensor computed based on the mean velocities, and (c) the magnitude of the vorticity vector based on the mean velocities. All results are depicted in the x - y symmetry plane ($z/d_h = 0$) in the high-Re case.	158
9.8	Positions of the breakup events of powder A in the low-Re and high-Re number cases by the drag stresses ((a) & (b)) and the rotary stresses ((c) & (d)), respectively. The locations are depicted for the central region $-0.1 \leq z/d_h \leq 0.1$ over a dimensionless time period of about $\Delta T^* = 15$. The color levels describe the number of primary particles included in the agglomerate at the time of its breakage.	161
9.9	(a) Characteristic diameters at the outlet of the disperser and (b) dispersion rates (numerical and experimental data by Weiler (2008) for all six cases.	164
9.10	Cumulative number size distribution of powder A at the outlet of the disperser for both Reynolds numbers.	165
9.11	Contour plots of the averaged streamwise velocity $\langle u \rangle / U_b$ and the resolved turbulent kinetic energy $\langle k \rangle / U_b^2$ for the cases Re_1 , Re_3 and Re_5 . The lines in subfigures (a)–(c) represent the projected streamlines of the secondary flow in the duct cross-section.	173
9.12	Impact-breakage events in the first set of simulations accumulated over a time interval of $\Delta T^* = 100$: Distribution functions for (a) the dimensionless impact velocity and (b) the impact angle. The data are collected for wall-impact events leading to breakage.	177

9.13	Impact-breakage events in the first set of simulations accumulated over a time interval of $\Delta T^* = 100$: (a) Cumulative distribution functions of the fragmentation ratio, (b) Distribution functions of the breakage positions as a function of the distance from the corner, averaged over all four (cross-sectional) edges and all cross-sections.	178
9.14	Impact-breakage events in the second set of simulations accumulated over a time interval of $\Delta T^* = 100$: (a) Distribution functions for the dimensionless impact velocity, (b) Cumulative distribution functions of the number of particles included in the agglomerates undergoing wall-impact breakage, (c) Cumulative distribution functions of the fragmentation ratio, (d) Temporal evolution of the reduction rate of the Sauter mean diameter. The inset in subfigure (a) shows the peak of the distribution of the dimensionless impact velocity for powder A at Re_1	183
9.15	Temporal evolution of the reduction rate of the Sauter mean diameter for powder (a) A and (b) C , respectively. Cumulative distribution functions of the fragmentation ratio in the first set of simulations (without collisions, agglomerations, and breakage by fluid stress) accumulated over a time interval of $\Delta T^* = 100$ for powder (c) A and (d) C , respectively.	186
9.16	Predictions of the ANN-based model (colored points) and the regression model (black curves) for the fragmentation ratio FR (a) and the fragment size parameters ζ_1 (b) as a function of the dimensionless number π_{imp} . The results refer to the breakage events obtained in the simulation of powder A at Re_1 accumulated over a time interval of $\Delta T^* = 100$. The points corresponding to impact angles below 10° are depicted in a reduced size in order to improve the visibility of the less frequent points representing larger impact angles.	187
9.17	Predictions of the ANN-based model of the Weibull PDF parameters λ and k of the reflection angle α , the spreading angle β , and the fragment velocity ratio v_{ratio} . The results refer to the breakage events obtained in the simulation of powder A at Re_1 accumulated over a time interval of $\Delta T^* = 100$	188
9.18	Probability density functions of the predicted reflection angle α , spreading angle β , and fragment velocity ratio v_{ratio} based on the ANN model and the regression model. The results refer to the breakage events obtained in the simulation of powder A at Re_1 accumulated over a time interval of $\Delta T^* = 100$	189
9.19	Percentage contributions of different breakup mechanisms for (a) Re_1 , (b) Re_2 and (c) Re_3 accumulated over a time interval of $\Delta T^* = 100$. The contribution of the turbulent stress mechanism is omitted since it is negligibly small in all cases. The exact numbers are listed in Table 9.14.	191
9.20	Geometries of the investigated pipe bend configurations.	196
9.21	Cross-section views of the computational grids of both bend configurations at Re_L . The grids for the high Reynolds number Re_H differ only in the number of grid points.	199

9.22	Distribution of the (a) equiangle skewness and the (b) non-orthogonality index. Higher is worse applies for both measures.	199
9.23	Validation of the inflow data at both Re numbers. The experimental measurements are provided by Durst et al. (1995).	201
9.24	Time-averaged dimensionless velocity magnitude and streamlines of the 90° case in the x - y plane at $z/D = 0$	203
9.25	Time-averaged dimensionless streamwise velocity $\langle v \rangle / U_b$ and streamlines of the 90° cases in the x - z plane at $y/D = -1.5$	204
9.26	Time-averaged dimensionless turbulent kinetic energy $\langle k \rangle / U_b^2$ ((a) and (b)) and Reynolds shear stress $\langle u'v' \rangle / U_b^2$ ((c) and (d)) of the 90° case in the x - y plane at $z/D = 0$	205
9.27	Time-averaged dimensionless velocity magnitudes and streamlines of the 45° case in the x - y plane at $z/D = 0$	206
9.28	Time-averaged dimensionless streamwise velocity $\langle v \rangle / U_b$ and streamlines of the 90° cases in the x - z plane at $y/D = -1.5$	207
9.29	Time-averaged dimensionless turbulent kinetic energy $\langle k \rangle / U_b^2$ ((a) and (b)) and Reynolds shear stress $\langle u'v' \rangle / U_b^2$ ((c) and (d)) of the 45° case in the x - y plane at $z/D = 0$	208
9.30	PDF of the impact angles Θ_{imp} associated with the breakage events of the initial agglomerates comprising $N_{\text{pp}}^{\text{tot}} = 1200$ particles.	210
9.31	Positions of the wall-impact breakage event along the axis of the pipe bend. The axial distance is normalized by the total length of the pipe.	210
9.32	Cumulative mass-weighted agglomerate size distribution Q_3 at the outlet of the pipe.	212
B.1	Verification of the model. The number of analyzed fragments in the Euler-Lagrange simulations is $5 \cdot 10^4 \times 100 = 5 \cdot 10^6$	223

List of Tables

6.1	Eddy subranges with corresponding expressions for the root-mean-square velocity difference (Δu) and the resulting fluid dynamic stresses acting on agglomerates of comparable size (Lu et al., 1998; Neeße et al., 1987).	67
7.1	Properties and other characteristic parameters of the considered silica particles (SiO_2) used in the DEM wall-impact simulations.	91
7.2	Overview of the impact conditions used for analyzing the breakage behavior concerning the fragmentation ratio FR and the fragment size parameter ζ_i	99
7.3	Values of the fitting parameters γ_1 and γ_2 introduced in Eqs. (7.32), and the root-mean-square of the residuals. Note that the first value was corrected in comparison to the original value in Khalifa and Breuer (2020).	109
7.4	Description of the cases considered in the analysis of the post-breakage kinetics of the fragments predicted by DEM. All provided cases refer to powder C	110
7.5	Values of the fitting coefficients obtained by a nonlinear least-squares regression for the relationship between Θ_{imp} and the parameters k and λ of the Weibull PDFs (Fig. 7.17), and the root-mean-square errors.	114
7.6	Values of the fitting coefficients for ER_{trans} depicted in Fig. 7.18.	118
7.7	Impact conditions of the newly investigated cases. Note that the results of the two-particle agglomerates ($N_{\text{pp}}^{\text{tot}} = 2$) are not considered in the training of the ANN.	122
7.8	MSE and R^2 values of the outputs of the ANN predicting the fragmentation ratio FR and the fragment size parameters ζ_i	127
7.9	MSE and R^2 values of the outputs of the ANN predicting the kinetics of the fragments.	133
9.1	Flow properties for the powder disperser.	146
9.2	Properties and other characteristic parameters of the considered silica particles (SiO_2).	148
9.3	Summary of the grid details for the duct-funnel low-Re case. The first and last cells are defined with respect to the coordinate system. The edges E_1 to E_{10} are depicted in Fig. 9.4. The grid spacing is normalized by d_h	153
9.4	Summary of the grid details for the duct-funnel high-Re case. The first and last cells are defined with respect to the coordinate system. The edges E_1 to E_{10} are depicted in Fig. 9.4. The grid spacing is normalized by d_h	154
9.5	Summary of the statistical results obtained in the disperser.	163

9.6	Comparison of the numerical and experimental values (Weiler, 2008) of the dispersion rate at the outlet of the disperser. The values in the last row are the median volumetric diameters $d_{50,3}^{CD}$ achieved in a high-end commercial disperser provided by Weiler (2008).	165
9.7	Influence of the breakup time delay on the statistics of powder A .	166
9.8	Flow properties and domain (spatial and temporal) discretization settings for all duct flow cases.	169
9.9	Summary of the particle-related models considered in the different set of simulations.	172
9.10	Breakage results due to wall impact only (first set of simulations). The results are accumulated over a time interval of $\Delta T^* = 100$. The number of released agglomerates N_{ag}^{rel} is 10^5 for all powders. Note that the value of $R_{d_{32}}$ for powder A at Re_3 and for powder C at Re_1 are slightly corrected in comparison to the corresponding value given in Khalifa and Breuer (2021).	175
9.11	Summary of the most important results of the second set of simulations. The results are accumulated over a time interval of $\Delta T^* = 100$. The number of released agglomerates N_{ag}^{rel} is 10^5 , 6400 and 730 agglomerates for powders A , B and C , respectively.	181
9.12	Results obtained by the ANN-based model and the regression model in the first set of simulations. The number of released agglomerates N_{ag}^{rel} is 10^5 for both powders. N_{break}^{tot} is accumulated over a time interval of $\Delta T^* = 100$ and $R_{d_{32}}$ is given at the end of this time interval.	185
9.13	Results obtained by the ANN-based model and the regression model in the second set of simulations. To ensure the same volume fraction, the number of released agglomerates N_{ag}^{rel} is 10^5 and 730 agglomerates for powders A and C , respectively. N_{ag}^{event} and N_{break}^{all} are accumulated over a time interval of $\Delta T^* = 100$ and $R_{d_{32}}$ is given at the end of this time interval.	190
9.14	Comparison between the percentage contributions of the different breakage mechanisms obtained by the ANN-based model and the regression model in the second set of simulations (including collisions, agglomerations, and breakage by fluid stresses and wall impacts).	192
9.15	Number of grid points of the block-structured grids used for LES of the bend flows.	198
9.16	Summary of the main breakage results obtained in the pipe bends. The evaluation time interval is $\Delta T^* = 350$ starting at the release of the first agglomerate.	209

1 Introduction

The simultaneous flow of materials with different components or different states of matter such as gas, liquid, solid, and plasma is generally called multiphase flow. The simplest case of a multiphase flow is the two-phase flow consisting of: (1) two states of the same component (e.g., water and steam), (2) two components of the same state (e.g., oil and water), or (3) two components of two different states (e.g., solid particles in gas). Computational methods have become a key tool for investigating the fundamentals of such flows allowing to explore the underlying physics in great detail and on different scales. Consequently, numerical simulations of multiphase flows are nowadays extensively employed to tackle engineering problems in several industrial branches.

The scope of the present thesis is the numerical modeling and simulation of turbulent fluid flows involving cohesive solid particles. In particular, the focus is directed towards the breakage of agglomerates, which plays an important role in dictating the particle size distribution in many particle-laden flows. The effective decrease of the particle size by the disintegration of agglomerates is in favor of obtaining desirable material properties and operational conditions, e.g., delivering medical aerosols with uniform dosing. On the contrary, breakage can be problematic as the reduction of the particle size decreases the settling velocity of particles in cyclone separators hindering the separation process.

In this chapter some examples pointing out the significance of particle-laden flows in general will be discussed first, followed by an overview on the most important modeling approaches available in the literature (Section 1.2). In Section 1.3 the objectives of this thesis are elaborated and clearly defined. Lastly, the organization of the thesis is outlined in Section 1.4.

1.1 Motivation for Considering Particle-Laden Flows

Particle-laden flows are abundant in nature. Typical examples of environmental processes include the formation of dust and sand storms, the transportation of sediment in rivers and streams, and the formation of ash clouds by volcanic eruption plumes. The satellite image shown in Fig. 1.1(a) depicts clouds of sand and dust originated from the Sahara (north Africa) and transported to the European continent across the Mediterranean Sea with a span of about 10^3 km. Such dust storms deteriorate the air quality, worsen the public health, and affect the frequency of North Atlantic hurricanes (Clifford et al., 2019). Considering that the size of sand particles varies between microns and millimeters, the image portrays a special characteristic of particle-laden flows, which is the potential vast range of spatial and temporal scales involved in the physics of a single problem. Another related example from nature is the Zambezi river delta depicted in Fig. 1.1(b), which flows about 230 km across six African countries to eventually pour its water and transported

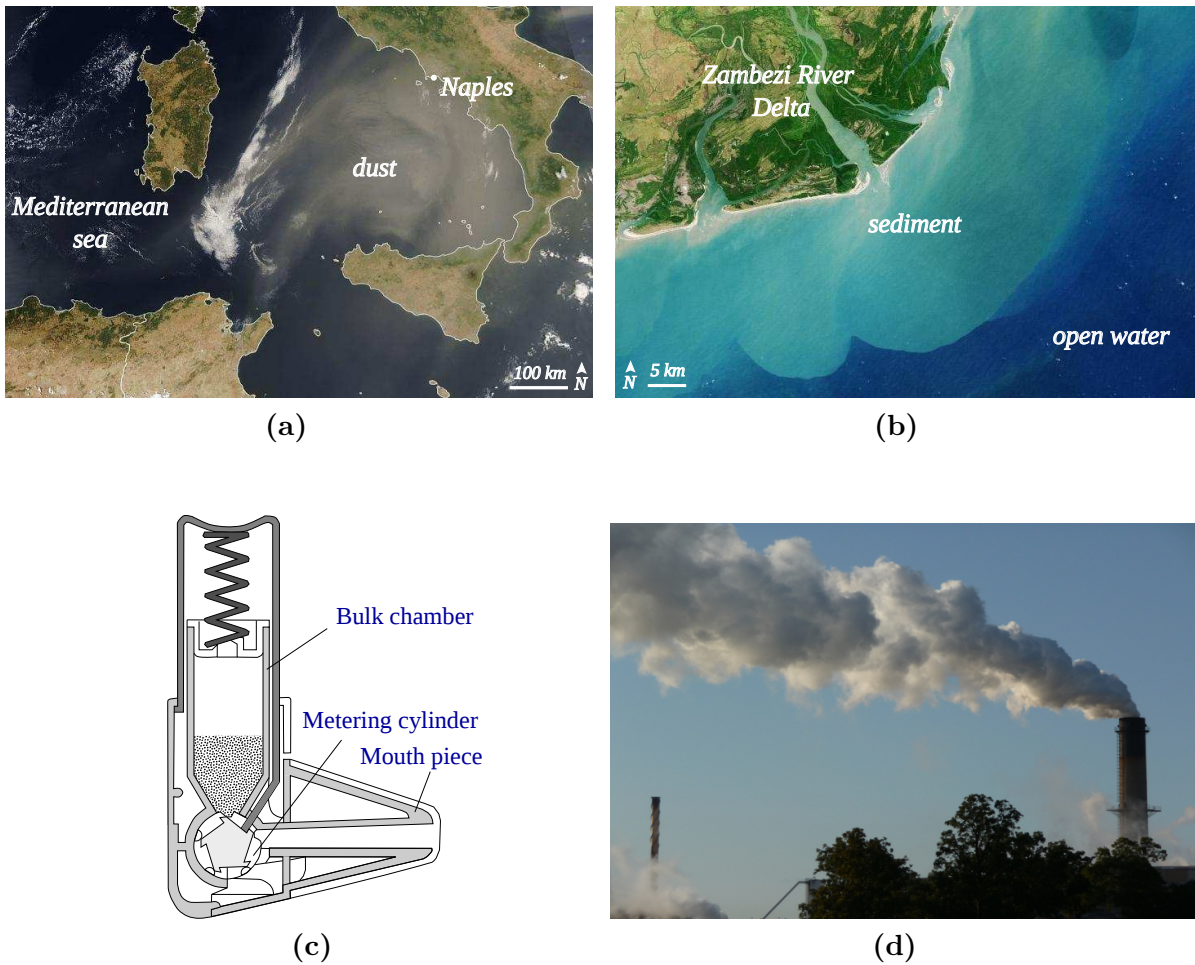


Fig. 1.1. Examples on particle-laden flows: (a) A dust storm traveling from north Africa to Italy spanning about 10^3 km, (b) The Zambezi river in Africa with a total length of 2574 km pouring water and sediment into the Indian Ocean (Images: NASA, Visible Earth), (c) A dry powder inhaler *Easyhaler*[®] (after Lavorini, 2019), (d) Exhaust fumes from smoking chimneys (Image: University of Freiburg).

sediment into the Indian Ocean. This discharge of sediments preserves the quality and softness of the water inside the Delta, leading to fertile soil and suitable water for farming and fishing, respectively. Unfortunately, the Zambeszi river nowadays is not capable of transporting the sediment out of the continent like it used to do due to the presence of hydropower dams upstream, which in turn reduce the flow of the river causing the sediment to accumulate (Kunz, 2011).

Besides nature, particle-laden flows are present in various technical applications ranging from cyclone separators, particle-based solar receivers, pharmaceutical inhalers (see Fig. 1.1(c)) to the emission of pollutants in different industrial branches (see Fig. 1.1(d)). In many of these applications, particles are found to be naturally cohesive and the particle size is normally measured in microns. In this specific size range, the effect of cohesion

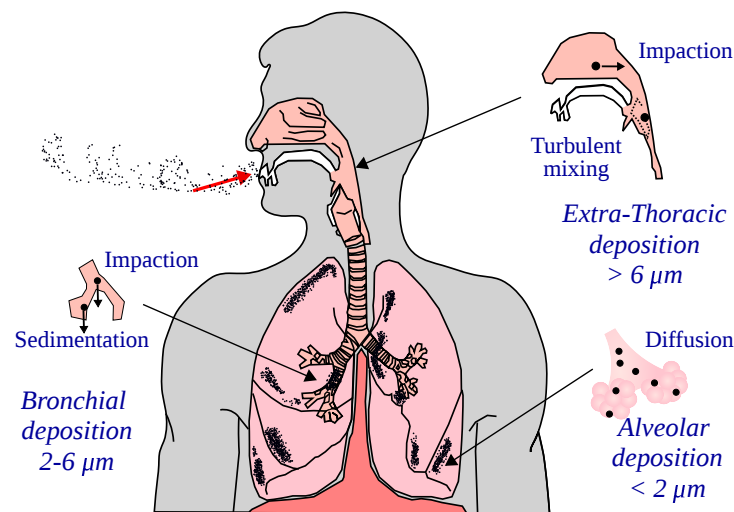


Fig. 1.2. Inhalation of particulates in the human respiratory tract (after Mao, 2011).

is found to be significant and thus the presence of particles in the form of clusters (i.e., agglomerates) is very likely. However, agglomerates in turn are prone to breakage (i.e., fragmentation) due to intense interactions with the turbulent flow or strong collisions with the surrounding objects. These circumstances are fulfilled in many applications since turbulent, wall-bounded flows (e.g., chimney, mouth piece of an inhaler) are dominant in practice. Hence, the size evolution of the particle phase in such systems is governed by a competition between counteracting physical phenomena.

In fact, the particle size is a crucial feature for the aforementioned applications and others. For instance, the particle size plays a major role for optimizing the efficacy of inhaled medications or describing the harmfulness of particulate pollutants. Fig. 1.2 schematically depicts particles deposited in the human respiratory system. As illustrated, particles are able to reach different regions of the respiratory tract depending on their size among other factors (Darquenne, 2012). In general, large particles ($> 6 \mu\text{m}$) are unable to exactly follow the paths of the inhaled air when a bend is met due to their high inertia. Consequently, large particles impact and deposit in the upper airways, e.g., in the nose or throat and thus drugs cannot be delivered to the lung tissues. In order to effectively treat the central and narrow airways, particles must be in the size range of 2 to $6 \mu\text{m}$. Even smaller particles tend to penetrate deep into the alveolar region where the exchange of oxygen and carbon dioxide takes place or even into the bloodstream posing great health problems in case of pollutants.

In summary, particle-laden flows are of paramount importance to diverse fields of science and engineering. The examples discussed above indicate that the profound knowledge of such flows can improve the human well-being through the optimization of medical and other consumable products and contribute to the alleviation of serious environmental problems. In many cases, the design and the dynamics of particle-laden flows strongly depends on the particle size and its evolution within the system. Therefore, it is inevitable to take phenomena such as agglomeration and breakup in predictions into account to obtain useful and physically meaningful forecasts.

The first approach is the Euler–Euler (two-fluid model) formulation treating the continuous and the disperse phases as interpenetrating continua. Consequently, conservation equations need to be solved for both phases. These are most frequently expressed based on the Reynolds-Averaged Navier-Stokes equations (RANS) delivering statistical descriptions of both phases (e.g., Elghobashi and Abou-Arab, 1983; Zhou, 2010). Nevertheless, different studies have been recently devoted to develop instantaneous Euler–Euler methods in the context of large-eddy simulations (LES) (e.g., Ma et al., 2015; Moreau et al., 2010) and direct numerical simulations (DNS) (e.g., Masi et al., 2014). In the Euler–Euler approach the interactions between particles are not realized in terms of discrete collision events. Instead, the momentum transfer within the solid phase is modeled through the stress tensor appearing in the momentum conservation equation relying on an analogy with the fluid phase (van Wachem et al., 2001). In addition, the two phases are coupled by an exchange of momentum and energy. For this purpose, source terms described by constitutive models are introduced into the corresponding conservation equations (Balachandar, 2009).

The Euler–Euler approach has been widely applied in simulations involving a huge number of particles since the computational load is related to the solution of the governing equations and does not scale with the number of particles (Sommerfeld et al., 2008). However, if particles possessing different sizes are present (i.e., a polydisperse system), each size class is ideally treated as a different continuum (multi-fluid model). For this purpose, a set of conservation equations needs to be solved for each size class requiring considerably higher computational efforts (Kuerten, 2016). In addition, predicting the development of the particle size due to agglomeration and breakage requires coupling the Euler–Euler approach with CPU-time intensive population balance models (Marchisio et al., 2003; Ramkrishna, 2000). The solution of the population balance equations depends on collision, agglomeration, and breakage rate functions, which are often termed as kernels. These kernels are mostly derived from experiments relying on certain assumptions regarding the flow and particle properties. That renders the Euler–Euler solution in real applications heavily dependent on modeling issues since the discrete nature of the particles is ignored.

The other extreme is the fully resolved approach where the flow scales introduced by the particle beside all the scales of the ambient turbulence are completely resolved. Various methods can be used to capture the unsteady boundary layer around the particles and the resulting wakes. In the context of Navier-Stokes solvers, direct numerical simulations based on body-fitted spherical grids or on the immersed boundary method are common techniques (Burton and Eaton, 2005; Uhlmann, 2005, 2008; Vowinckel et al., 2019a; Vowinckel et al., 2019b; Vreman, 2016). As an alternative, fully resolved simulations can be conducted applying the lattice-Boltzmann method (Cui and Sommerfeld, 2018; Dietzel et al., 2016; Jebakumar et al., 2019). Obviously, the fully resolved approach offers the most detailed description of the physics behind the fluid-particle interactions. Consequently, the motion of particles follows directly from Newton’s second law using the resolved forces and torques imposed by the ambient fluid. However, despite the ever-growing available computational power, such methods are still restricted to dilute systems involving up to $\mathcal{O}(10^4)$ particles (e.g., de Motta et al., 2019; Jain et al., 2021; Kempe and Fröhlich, 2012;

Kempe et al., 2014; Picano et al., 2015; Uhlmann and Chouippe, 2017; Vowinckel et al., 2014). Even for such relatively small systems the problem becomes quickly intractable if agglomerates are present and the inter-particle interactions should be resolved in space and time. Hence, at the present time fully resolved simulations are not an affordable option to comprehensively investigate real applications. Nevertheless, the insightful knowledge offered by the high resolution is frequently exploited to derive and improve closure models for the less detailed approaches. This is typically achieved by conducting resolved simulations in controlled configurations while focusing on a specific phenomenon, e.g., the drag force and the lift force (e.g., Akiki and Balachandar, 2020; Bagchi and Balachandar, 2002; Beetstra et al., 2007; Bogner et al., 2015; Dietzel et al., 2016; Hölzer and Sommerfeld, 2009; Kurose and Komori, 1999; Yali Tang et al., 2015). Recently, the utilization of detailed results in improving efficient but less conclusive models has been greatly empowered by data-driven approaches relying on modern machine learning techniques (Balachandar et al., 2020; Beck et al., 2019; Duraisamy et al., 2019; Montáns et al., 2019). In particular, artificial neural networks have shown great potential to efficiently reproduce knowledge obtained under realistic operating conditions. That is a clear advantage over traditional models, which mostly refer to simplified scenarios.

The third approach is the Euler–Lagrange point-particle method, which finds a middle ground between the two extremes (Euler–Euler and fully resolved particle). In this framework the carrier fluid is treated as usual in the Eulerian frame of references. In addition, a Lagrangian tracking based on Newton’s second law is applied to describe the motion of particles. However, in contrast to the fully resolved approach the particles are approximated as point-masses. Thus, the fluid-particle interface vanishes and the motion of particles is assumed to be governed by the local properties of the undisturbed flow at the particle center (Maxey and Riley, 1983). For this purpose, a variety of closure models has been proposed in the literature to describe the forces and torques exerted by the fluid in the equation of motion of the particle. If the volume fraction of the disperse phase is sufficiently large, it becomes necessary to account for the feedback effect of the particles on the fluid (i.e., two-way coupling). This is typically done by adding a source term to the momentum conservation equation of the fluid.

Due to the circumstance that the small flow scales induced by the presence of particles are ignored, the ambient turbulence does not necessarily need to be fully resolved by time-consuming DNS. Depending on the required accuracy and the available computational resources alternatively, LES or RANS can be employed to predict the turbulent flow field (Balachandar, 2009; Kuerten, 2016). The latter can offer a drastic reduction of the computational costs especially for statistically steady turbulent flow problems. This is attributed to the fact that the RANS solution solely provides an averaged description of turbulence allowing to "freeze" the mean flow field once the solution is developed. As a result, the tracking of particles follows as a post-processing step (Kuerten, 2016). However, the challenge here is that particles in reality interact with the instantaneous flow field and not the averaged one. Therefore, the velocity fluctuations need to be mimicked by additional models of stochastic nature (Sommerfeld et al., 2008). For these reasons, LES is gaining a considerable attention since it offers reasonably accurate instantaneous solutions

by resolving the most important flow structures at moderate costs. However, often the effects of the unresolved subgrid-scale structures on the flow field and the particles are not negligible and thus need to be adequately accounted for.

Furthermore, the Euler–Lagrange method offers the possibility to describe the inter-particle interactions (i.e., four-way coupling) at different levels of detail. Owing to the persistence of the discrete nature of particles in this method, the collision events can be individually detected either by stochastic (Sommerfeld, 2001) or deterministic (Bird, 1976; Breuer and Alletto, 2012) algorithms. For particle-wall collisions the detection is even more straightforward.

Collisions lay the groundwork for important phenomena such as particle agglomeration, particle-wall adhesion, and agglomerate breakage. This implies that the prediction of these phenomena substantially depends on the method by which the collisions are treated. For this purpose, two methods are commonly applied. The first is the soft-sphere approach, which is also known as the discrete element method (DEM) (Cundall and Strack, 1979). This method describes collisions as gradually evolving processes which are resolved in space and time. The interactions between a certain particle and multiple others can be simultaneously taken into account. Consequently, particles form agglomerates and deposit at walls according to the balance of forces between the interacting objects. Hence, agglomeration and wall-adhesion are implicitly taken into account without additional modeling. Following the same concept, the breakup of agglomerates and the re-suspension of deposited particles naturally occurs. However, this direct prediction is associated with high computational burdens since apart from the costly full resolution of the collisions, the tracking of contacts is not trivial. A cost-efficient alternative for the soft-sphere treatment is the hard-sphere model which treats collisions as instant events instead of resolving them in time (Crowe et al., 1998). In the original formulation of this model solely the post-collision dynamics are predicted by a momentum balance employing the pre-collision conditions of the colliding objects. Agglomeration and wall adhesion can also be predicted either by extending the underlying momentum balance (Almohammed and Breuer, 2016b; Breuer and Almohammed, 2015; Kosinski and Hoffmann, 2009, 2010) or by applying energy-based models (Almohammed and Breuer, 2016a; Hiller, 1981; Jürgens, 2012). A drawback of the hard-sphere model is that it solely handles binary collisions.

Agglomerates may be geometrically represented by their real, fracture-like structures. In this case, a physically meaningful description of the dynamics of the agglomerates requires a continuous determination of the fluid-particle and particle-particle interactions for each primary particle. In another approach, the structure of agglomerates is replaced by a single particle possessing an effective diameter, which allows to track agglomerates as single entities. The discussion on both concepts including the possible methods to treat the fluid-particle and particle-particle interactions and their implications for the prediction of the agglomerate breakage is extended in Chapter 2.

In summary, a variety of computational methods exist to describe particle-laden flows. The Euler–Lagrange approach combined with the point-particle approximations offers important advantages over the other methods. On the one hand, compared to Euler–Euler models, it allows a greater flexibility in the level of captured details for both phases and

their coupling. On the other hand, it offers a significant reduction of the computational costs (multiple orders of magnitude) over fully-resolved models. Consequently, simulating flows comprising millions of particles while accounting for diverse flow and particle phenomena is possible. However, efforts are still required in order to further narrow the accuracy gap between the point-particle models and the fully resolved solutions.

1.3 Objectives of the Thesis

The main goal of this thesis is to advance the current state of the art in computational modeling of particle-laden flows in an important yet less-established area. More specifically, the scope is to develop physical models for numerical simulations describing the breakage of particle agglomerates in turbulent flows. The models are intended for (but not restricted to) the in-house CFD code *LES OCC* (Large-Eddy Simulation On Curvilinear Coordinates) (Breuer, 1998a,b, 2000, 2002), which provides an efficient multiphase flow simulation methodology relying on large-eddy simulation for the continuous phase and a Lagrangian point-particle tracking for the disperse phase. The aim is to propose an advanced simulation strategy capable of delivering reliable predictions of particle-laden flows in practically relevant setups. This can only be achieved by reasonably taking various important phenomena at manageable computational costs into account.

In more practical terms, the objectives of the present thesis are to:

- (1) Enhance the modeling of the structural features of agglomerates, namely, the porosity and the coordination number (i.e., average number of contacts per particle).
- (2) Develop a model for the breakage of agglomerates by fluid-induced stresses.
- (3) Develop a model for the breakage of agglomerates by wall impacts.
- (4) Apply the entire simulation methodology including the newly developed models to investigate the breakage of agglomerates in wall-bounded turbulent flows under various operating conditions.

For the first objective, an adequate representation of the porosity and the coordination number is sought. Since agglomerates are porous by nature, the porosity is an essential characteristic for determining the corresponding density and diameter of the spherical particles used to replace the structure of agglomerates in the present methodology. In addition, both the porosity and the coordination number are important parameters for determining the resistance of agglomerates against breakage, i.e., its strength.

Simplifying the complex structure of agglomerates by single spheres poses certain challenges on the prediction of breakage, which need to be tackled. More specifically, the full characterization of a breakage event in the second and third objectives requires addressing three issues, hereafter called the breakage modeling tasks:

- (i) A criterion for the onset of breakage.
- (ii) The number of resulting fragments and their size distribution.

(iii) The velocity vectors of the fragments arising due to breakage.

The attention in this thesis is restricted to spherical, monodisperse (i.e., equally-sized) primary particles in the micrometer size range. In addition, the particles are assumed to be dry and electrostatically neutral, and the cohesion between particles can solely be attributed to the van-der-Waals force. All other specific assumptions will be mentioned in the corresponding discussion.

To realize the fourth objective, test cases inspired by experimental investigations reported in the literature are taken into account. The aim is to assess the influence of a wide range of operating conditions on the breakage of agglomerates and to analyze the interplay between breakage and other phenomena.

1.4 Outline of the Thesis

This thesis is organized in ten chapters. The next chapter provides a literature review to identify and analyze modeling strategies for the structure of agglomerates, the breakage due to fluid stresses, and the breakage by wall impacts.

Chapters 3 and 4 present a theoretical background on the description of the continuous and the disperse phase in the adopted Euler–Lagrange framework, respectively. The proposed models for the structural features of agglomerates, the breakage by fluid-induced stresses, and the wall-impact breakage are introduced in Chapters 5, 6, and 7, respectively. Subsequently, the numerical methods used for computing the continuous and the particle phase are explained in Chapter 8. In Chapter 9, LES predictions of particle-laden flows in a generic powder disperser, a square duct, and pipe bends relevant for dry powder inhalers are carried out and the results are discussed in detail mainly focusing on issues relevant for the breakage phenomenon. Finally, Chapter 10 summarizes the major findings and conclusions from this work, and gives an outlook on related future research possibilities.

2 Literature Review on the Modeling of Breakage

The deagglomeration of particles in fluid flows has been the subject of research for a long time. Various modeling approaches with varying degrees of complexity are found in the literature. Provided that the presence of agglomerates is a prerequisite for breakage, the first section of this chapter looks at the available methods for handling the complex structure of agglomerates. Afterwards, studies focusing on the breakup of agglomerates due to fluid stresses and wall impact are explored. The aim is to assess the state of existing models and to identify areas for potential improvements. Note that major parts of this review were published in the papers related to this thesis (Breuer and Khalifa, 2019a,b; Khalifa and Breuer, 2020, 2021; Khalifa et al., 2022; Khalifa et al., 2021).

It must be mentioned that breakage might additionally arise due to collisions between agglomerates and other agglomerates or particles. However, this mechanism is not addressed in the present thesis. Therefore, the collisions-induced breakage is not covered in this literature review.

2.1 Structure of Agglomerates

Agglomerates, also commonly denoted aggregates or flocs, describe clusters of particles interconnected by different types of binding mechanisms (Fayed and Otten, 2013). In some cases the geometry of agglomerates can be highly irregular, whereas in other cases agglomerates are referred to as fractal-like objects, since they show a high degree of self-similarity, but are not infinitely scale-invariant (Friedlander, 1977). Hence, the morphology of agglomerates is typically characterized by a parameter denoted the fractal dimension, which varies between unity for chain-like arrangements and three for spherical ones. Exemplary sphere-like and open agglomerates are depicted in Figs. 2.1(a) and 2.1(b), respectively.

A special case is the isostatic structure (Fig. 2.1(c)), which exhibits a number of inter-particle contacts less than or equal to the number of primary particles minus one. Such a morphology evolves when chains of particles are cross-linked to form a larger agglomerate. The assumption of isostatic agglomerates is frequently encountered in the literature, since it simplifies the modeling of breakage as will be discussed in Section 2.2.2.1.

Particle-laden flow simulation methodologies which deal with cohesive particles can be distinguished into structure resolving and structure idealizing methods. In the former, the detailed morphology of agglomerates is fully taken into account (e.g., Figs. 2.1(a) –

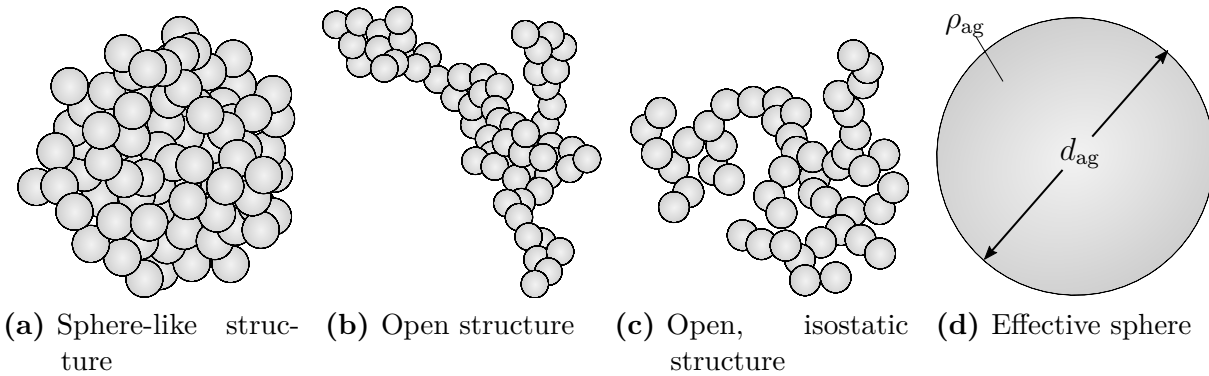


Fig. 2.1. Agglomerates represented by detailed structures (a)-(c) and an idealized one based on an effective sphere (d).

2.1(c)), whereas the latter methods replace the structure by a single effective particle (e.g., Fig. 2.1(d)). Both techniques are discussed in the following.

2.1.1 Detailed Structure

In the first category the structure of the agglomerate is fully taken into account, i.e., agglomerates are realized as assemblies of primary particles. In addition, the dynamics of the agglomerates are determined by the fluid-particle and inter-particle interactions occurring at the scale of the constituting primary particles. Hence, both types of interactions need to be adequately addressed.

Obviously, the most accurate way to determine the fluid-particle interaction in the context of agglomerates is to fully resolve the fluid around each particle (e.g., Cui and Sommerfeld, 2018; Derksen and Eskin, 2010; van Wachem et al., 2017). However, this technique is computationally demanding. Less burdensome are methods, which conserve the structure of agglomerates relying on a Lagrangian (i.e., unresolved) point-particle tracking of the constituting particles. However, the proper estimation of the fluid forces on the primary particles shielded by the surrounding particles of the same agglomerate poses an onerous challenge. To deal with this issue various approaches have been put forward: (1) the free-draining, (2) the crowding factor, (3) the hydrodynamic screening, (4) the Stokesian dynamics, and (5) the pairwise-interaction extended point-particle model (PIEPP).

The *free-draining* approximation is the simplest approach suggesting to entirely ignore the fluid shielding effects (e.g., Becker et al., 2009). In a more reasonable technique, the effect of the neighboring particles is accounted for by incorporating a *crowding factor* into the point-particle force and torque models. For this purpose, a large number of experimental (e.g., Di Felice, 1994) and particle-resolved numerical (e.g., Beetstra et al., 2007) studies proposed correlations describing the crowding factor as a function of the particle Reynolds number and the mean local volume fraction of the particles. However, most correlations are mainly focused on the drag force and independent of the effect of

the spatial arrangement (i.e., relative locations) of the particles, which can strongly vary despite an equal local volume fraction.

To overcome these drawbacks, different possibilities are available. One of them is the *hydrodynamic screening* method, which computes the fluid-induced forces and torques exerted on a particle by considering solely the portion of the surface area of the particle exposed to the flow field (Higashitani et al., 2001). Another alternative is the *Stokesian dynamics* (Durlofsky et al., 1987), which allows to calculate the fluid forces and torques exerted on the primary particles taking the relative positions of particles into account. In this method the fluid forces and moments are related to the velocities of the particles by the so-called mobility matrix, assuming that particles are surrounded by a flow field with a uniform velocity gradient, i.e., a creeping flow. A more generally applicable technique is the *pairwise-interaction extended point-particle (PIEPP)* model, which was recently proposed by Akiki et al. (2017a), Akiki et al. (2017b) and Balachandar et al. (2020). The model allows to compute the drag and lateral forces on individual particles within a random array while systematically accounting for realistic surrounding flow conditions and for the relative positions of the neighboring particles.

In principle, all above mentioned approaches can be considered for describing the fluid forces acting on aggregated particles while dealing with the inter-particle interactions based on one of two typical options: (1) the discrete element method (DEM), (2) the rigid-body dynamics.

In the present terminology, *DEM* refers to the method, in which the inter-particle forces and torques are computed based on a soft-sphere (i.e., viscoelastic) model. In addition, the velocity and displacement of each individual particle are obtained by integrating its equation of motion taking the external (i.e., fluid and gravity) and the internal (i.e., contact) forces into account (Cundall and Strack, 1979). Hence, in DEM the attachment and detachment of particles are directly dictated by the resolved motion of particles. However, a stable and accurate DEM solution requires very small time increments, which can be much smaller than the flow time-step size especially for stiff particles (i.e., high modulus of elasticity). Therefore, it is a very common practice to artificially scale down the modulus of elasticity to allow larger DEM time-step sizes. Note that DEM studies adopting the direct prediction for the breakup by fluid stresses and by wall impacts are discussed in Sections 2.2.1 and 2.3.1, respectively.

The second possibility is more efficient since it treats agglomerates as *rigid structures* (e.g., De Bona et al., 2014; Fellay and Vanni, 2012; Schutte et al., 2015; Seto et al., 2011; Vanni and Gastaldi, 2011). In practice, rigid agglomerates indicate stable inter-particle bonds which remain fixed or spontaneously break when the exerted forces or torques exceed certain thresholds. Computationally, the motion of a rigid agglomerate is described by the translational and rotational velocities of the center of mass of the agglomerate. These velocities are obtained by solving the corresponding equations of motion of the whole agglomerate taking the external forces and torques acting on the constituting primary particles into account. The main advantage of this approach over typical DEM is that it does not necessitate the prediction of the internal interactions or solving the equations of motion for each primary particle. However, the assumed rigidity

of agglomerates implies that the primary particles are always intact and thus additional criteria are required to determine breakage. Further discussion on the modeling of the fluid-induced breakage for rigid agglomerates is given in Section 2.2.2.1. Note that to the best of the author's knowledge, studies dealing with the wall-impact breakage of rigid agglomerates with detailed structures do not exist in the literature.

2.1.2 Idealized Structure

In the second category of studies, the detailed agglomerate morphology is replaced by a single particle conserving the mass of the original agglomerate. Very often the model particle is assumed to be a sphere characterized by an effective diameter (see Fig. 2.1(d)).

Due to its practicality, the *replacement technique* has been extensively utilized in the literature. For instance, the effective agglomerate diameter is an essential parameter which frequently appears in the closures, e.g., the agglomeration and breakage kernels used in the population balance equation. The replacement approach is also popular in the Euler–Lagrange formalism (e.g., Breuer and Almohammed, 2015; Chun and Koch, 2005; Ho and Sommerfeld, 2002; Kosinski and Hoffmann, 2011; van Wachem et al., 2020) since it offers a considerable reduction of the computational load by giving up the continuous tracking and updating of the inter-particle contacts. In addition, modeling agglomerates as single spherical entities allows to apply the same closure relationships for the fluid forces (e.g., drag and lift and their corresponding drag and lift coefficients) developed for spherical primary particles to predict the motion of agglomerates. The effective sphere model is especially beneficial for simulations parallelized by domain decomposition techniques since the inter-processor communication and exchange of aggregated particles is not a simple task.

Certainly, an effective sphere provides solely an approximation of the dynamics of the original agglomerate. The achieved accuracy was found to be affected by the considered definition of the effective diameter (Dietzel et al., 2016). In most studies, a volume-equivalent diameter is taken into account, which conserves the total volume as well as the total mass of the primary particles. That requires the density of the agglomerate to be equal to that of the primary particles ignoring the interstitial spaces between the particles.

Breuer and Almohammed (2015) followed an extended approach denoted closely-packed sphere model. It accounts for the porous nature of agglomerates by defining the density of an agglomerate as the product of the density of the primary particle and a prescribed porosity value. Consequently, the volume of the sphere representing the agglomerate structure is larger than the total volume of the constituting particles. Since agglomerates of different number of primary particles might arise in the simulations, the packing fraction (i.e., the complement of the porosity) of agglomerates was provided in a look-table depending on the number of particles. The tabulated values of the packing fraction stem from an optimization study on the smallest volume of a cube enclosing a certain number of equal spheres without overlapping (Packomania, 2013). Due to the assumption of closely packed particles in a cube, the resulting values of the packing fraction are found to be very high in comparison to the typical range of values for randomly packed, spherical particles

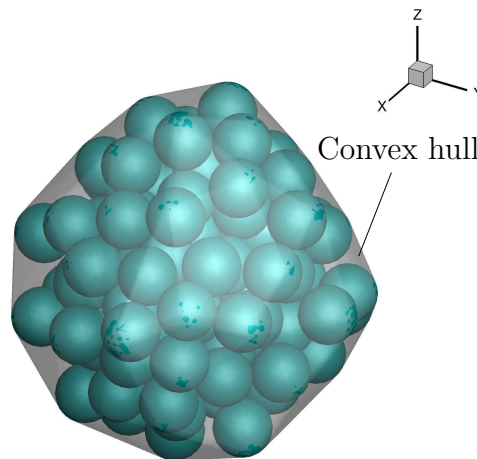


Fig. 2.2. Convex hull wrapping an agglomerate consisting of 100 primary particles.

(e.g., Finney, 1970; Scott, 1962; Yang et al., 2008).

To assess the suitability of the effective sphere assumption, Harshe et al. (2010) simulated the motion of rigid agglomerates in a uniform shear flow by means of Stokesian dynamics. Agglomerates of sizes varying between 10 and 1000 primary particles, possessing different open and sphere-like structures were investigated. It was shown that the simplifying effective sphere approach is useful to reproduce the behavior of realistic agglomerates. Specifically, sphere-like agglomerates can be well represented by equivalent spheres, whereas ellipsoids are more suited for open structures.

Another important contribution in this area was presented by Dietzel and Sommerfeld (2013) who performed particle-resolved lattice-Boltzmann simulations at low Reynolds numbers (i.e., Stokes regime) to investigate drag and lift force coefficients of agglomerates possessing different open and sphere-like structures. It was concluded that a drag force coefficient computed based on the diameter of a volume-equivalent sphere is not adequate since it remarkably deviates from the standard drag coefficient correlation by Schiller and Naumann (1933). A considerably better agreement was achieved based on a sphere with an area equal to the projected surface area of the convex hull wrapping the agglomerate (see Fig. 2.2). Namely, the diameter of a circle possessing an area equal to the projected cross-section area of the convex hull resulted in drag coefficients which are nearly independent of the morphology and the orientation of the agglomerates (Dietzel et al., 2016; Dietzel and Sommerfeld, 2013). However, unlike the drag coefficient, the lift force coefficient was not well predicted by any of the two structural assumptions (sphere and convex hull).

In a subsequent study, Sommerfeld and Stübing (2017) proposed a strategy for predicting the effective diameters of agglomerates based on a volume-equivalent convex hull. The model was developed for Euler-Lagrange point-particle simulations and can be summarized as follows: When an agglomerate appears, the volume of the convex hull enclosing the aggregated particles is computed. Subsequently, the relative positions of the agglomerated particles are stored and the agglomerate is replaced by a sphere with a volume equal to that of the convex hull. Upon further agglomeration or breakup, the positions of the

added or removed particles are used together with the stored relative positions of the current particles to compute the volume of a new convex hull, and so forth.

The breakup of agglomerates idealized as spheres due to the interactions with a fluid flow field and as a result of wall impacts are discussed next in Sections 2.2.2.2 and 2.3.2, respectively.

2.2 Breakup by Fluid Stresses

The role of fluid forces in splitting agglomerates has been computationally studied in a growing body of literature. Loosely speaking, independent from the level of resolution of the fluid-particle coupling (particle-resolved or point-particle) the breakup of agglomerates can be reproduced based on *condition-free* methods or by imposing external breakup conditions. Note that "condition-free" and "imposed conditions" in this context strictly refer to the forecasting of breakup.

2.2.1 Fluid-Induced Breakup Predicted by Condition-Free Techniques

As aforementioned, to enable a condition-free forecast of fragmentation of agglomerates the detailed structure must be taken into account. In addition, the equations of motion of each primary particle need to be solved. Consequently, breakage follows directly from the equations of motion of the individual particles without additional modeling. Hence, in all studies discussed in this section the structures of agglomerates are fully taken into account and the inter-particle interactions are treated according to DEM.

Studies utilizing the most accurate approach, which combines **resolved fluid-particle interactions** with DEM have been concerned with the development of dry powder inhalers (e.g., Cui and Sommerfeld, 2018; van Wachem et al., 2017). Within the context of inhalers, different powder formulations are usually discussed: The carrier-based formulation referring to drug particles attached to a larger carrier as depicted in Fig. 2.3, and the drug-based (carrier-free) formulation representing agglomerates of small drug particles analogous to those shown in Figs. 2.1(a) to 2.1(c) (Longest et al., 2013). Bearing in mind that the present thesis deals with agglomerates resembling the carrier-free powder type, the remainder of this review will focus on studies describing the breakage of such agglomerates. Publications addressing the disintegration of carrier-based agglomerates are of little value for the scope of the present thesis and thus the interested reader is referred to the relevant reviews, e.g., by Sommerfeld et al. (2019), Yang et al. (2015) and Zheng et al. (2021).

Other studies considered **unresolved particle** methods. These studies are grouped in the following based on the approach used for dealing with the fluid shielding within the agglomerate.

The first group adopted the *hydrodynamic screening method*. In one of the earliest contributions, Higashitani et al. (2001) studied the breakup of agglomerates in simple

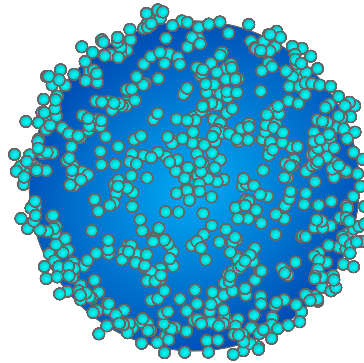


Fig. 2.3. Carrier-based powder formulation. This type of agglomerates is not considered in the present thesis.

shear and elongational flows. Agglomerates possessing open, loose structures as well as spherical, rather compact structures were investigated. The size of the agglomerates varied between 256 and 1024 identical particles. The effect of shielding on the fluid forces experienced by a particle was accounted for based on a geometrical analysis taking solely the exposed part of the surface area of the particle into account. In addition, the undisturbed local flow velocity was adjusted by a factor accounting for the presence of neighboring particles. It was shown that elongational flows induce higher breakup than shear flows. In addition, power-law relations describing the average number of particles in the broken fragments were proposed. Adopting the same methodology, Fanelli et al. (2006a,b) investigated the breakage of single agglomerates in steady and unsteady shear flows, respectively.

The second group employed the *Stokesian dynamics*. Harada et al. (2006) studied the fragmentation of agglomerates in a simple shear flow. The scope was to compare the breakage behavior of two 100-particle agglomerates distinguished solely by the fractal dimension (open vs. sphere-like). It was pointed out that open-structured agglomerates are more fragile than spherical ones and that the breakup behavior in general depends on the strain and rotation effects in shear flows. In an effort to reduce the computational costs associated with DEM, Frungieri and Vanni (2021) presented a method, which combines a Stokesian dynamics and a stochastic Monte-Carlo algorithm to track single particles and detect the occurrence of binary collisions. A DEM approach was incorporated in the framework of Stokesian dynamics to solely describe the collisions of primary particles and the dynamics of the formed agglomerates. The method was applied to study the agglomeration and breakup under a uniform shear flow condition for a suspension of monodisperse particles possessing a volume fraction of 10^{-4} .

In the third group of studies, the *free-draining approximation* was applied. Becker et al. (2009) investigated the restructuring of single monodisperse agglomerates in a simple shear flow applying the free-draining approximation. To assess the appropriateness of the free-draining assumption, additional finite element simulations were carried out, in which the fluid flow around a small agglomerate comprising eight particles was fully resolved. The obtained fluid forces on each particle were compared with results of standard constitutive

force models assuming an undisturbed flow field around the particle. The analysis revealed that the free-draining assumption leads to an overestimation of the fluid forces experienced by the particles exposed to the flow field. Furthermore, the perpendicular forces induced by neighboring particles in the inner part of the agglomerates are underestimated.

Eggersdorfer et al. (2010) examined the restructuring of single agglomerates of identical particles in a simple shear flow. Agglomerate comprising up to 2048 particles were generated by a hierarchical stochastic algorithm leading to widely open agglomerate structures. It was highlighted that after agglomerates split, the arising fragments undergo a relaxation phase leading to more compact structures than the original agglomerates.

Another study using the free-draining assumption was published by Calvert et al. (2011) who evaluated the effect of cohesion, the diameter of the agglomerate, and the fluid-agglomerate relative velocity (commonly referred to as the slip velocity) on the disintegration of agglomerates in uniform flow. For this purpose, sphere-like agglomerates comprising a number of primary particles varying between 250 and 8000 particles were taken into account. In addition, five different slip velocities were considered and a range of one order of magnitude of surface energy values was considered. To characterize the breakup behavior, a parameter called the dispersion ratio was introduced, which related the number of broken contacts to the initial number of contacts. It was found that a higher relative velocity is needed to break an agglomerate if the surface energy of the particle increases. In contrary, the onset of breakage for larger agglomerates takes place at lower slip velocities than in the case of small agglomerates. A correlation incorporating a dimensionless number analogous to the Weber number was found to characterize the dependence of the dispersion ratio and the operating (flow and agglomerate) conditions.

In a recent study, Zhao et al. (2021) investigated the dynamics of 10^4 single cohesive particles in homogeneous isotropic turbulence employing one-way coupled DNS. A rapid aggregation phase was initially observed before a steady equilibrium phase prevailed due to the balance between agglomeration and breakup. The flow-shielding effects on the agglomerated particles were neglected. It was found that agglomerates are elongated along the strongest Lagrangian stretching direction before breakage. Based on the obtained results, a model describing the transient development of the aggregate size and shape was proposed.

DEM-based methodologies accounting for the flow-shielding effect in the calculation of the drag force by a *crowding factor* have been reported in different recent studies (the fourth group). Dizaji et al. (2019) investigated the breakup of agglomerates in a linear shear flow focusing on the effect of the fluid forces and the collisions of two agglomerates. For this purpose, two sets of simulations involving one or two agglomerates were carried out. The considered agglomerates were generated in a preceding DNS of homogeneous turbulence and had open (loose) structures consisting of 328 to 577 evenly-sized particles. It was demonstrated that the breakage behavior, especially for open agglomerate structures, is more complex than can be reproduced by effective spheres. Furthermore, Chen and Li (2020) applied a coupled DNS–DEM to investigate the collision-induced breakage of agglomerates in homogeneous isotropic turbulence. After randomly seeding $4 \cdot 10^4$ single primary particles of the same size, the breakage of the small (mostly two-particle) agglomerates formed during the simulations was analyzed. In addition, a model for the

rate of the collision-induced breakage in such flow scenarios was proposed. Moreover, Yao and Capecelatro (2021) performed two-way coupled DNS–DEM to investigate the disintegration of single agglomerates in homogeneous isotropic turbulence. The closely-packed sphere-like agglomerates comprising 682 and 5500 equally-sized particles were composed by a centripetal packing procedure prior to the breakup investigations. As an outcome, a model describing the condition of breakup and the breakup rate was derived based on arguments motivated by the Taylor analogy breakup (TAB) model (O’Rourke and Amsden, 1987), which is readily used for droplet breakup.

Obviously, DEM-based methods are insightful and provide detailed knowledge on the primary particle scale. However, to keep the required computational efforts tractable, simplifications need to be made. Even in the most recent studies, the scope was restricted to single or few agglomerates under simple flow conditions. For these reasons, such detailed methods are still limited to fundamental investigations and not feasible for practical applications.

2.2.2 Fluid-Induced Breakup Predicted by Condition-Based Techniques

In the conditions-based approaches, the equations of motion of the primary particles constituting an agglomerate are not individually solved. Instead, the agglomerates are tracked either as rigid bodies consisting of a number of particles, or as effective spheres. In either case, additional criteria are required to decide upon the occurrence of breakup. In the case of an effective sphere, additional models are needed to describe the arising fragment size distribution and the velocity of the fragments.

2.2.2.1 Breakup of Rigid Agglomerates with Detailed Structures

The first type of the conditions-based methods suggests to track agglomerates as single rigid entities while accounting for their detailed structures. This allows to determine the motion of the whole agglomerate without resolving the inter-particle interactions. However, in order to formulate a breakup criterion that makes use of the available morphology, knowledge on the inter-particle forces and torques becomes necessary. For general agglomerates possessing arbitrary structures, applying a force or a torque balance (external forces versus contact forces and likewise for torque) per particle leads to an ill-defined problem (Derksen and Eskin, 2010). This situation arises when the number of unique inter-particle contacts (i.e., unknowns) is larger than the number of particles (i.e., equations). For this purpose, isostatic agglomerates (e.g., Fig. 2.1(c)) are frequently considered in the studies dealing with the restructuring (i.e., agglomeration and breakup) of rigid agglomerates. An isostatic structure means that the number of inter-particle contacts is less than or equal to the number of particles minus one (Schutte et al., 2018). As a consequence, the structure is statically determined, i.e., imposing a force and a torque balance on each particle yields two closed systems, which can be solved to obtain the inter-particle forces and torques.

Derksen and Eskin (2010) performed **particle-resolved** lattice-Boltzmann simulations to study the breakage of agglomerates in micro-channels under laminar flow conditions. Agglomerates comprising solely 2 to 4 particles were tracked as rigid bodies, i.e., the interactions between the particles of the same agglomerate are not resolved. However, the collisions between agglomerates were considered by resolving the interactions between the colliding particles of different agglomerates based on a soft-sphere interaction model. Since the agglomerated particles were assumed to maintain their integrity, the scope of the problem was restricted to analyzing the development of the normal contact force between the particles.

Considering an **unresolved particle** approach on the basis of *Stokesian dynamics*, Vanni and Gastaldi (2011) examined the behavior of single agglomerates of different fractal dimensions immersed in simple shear flow. The inter-particle interactions within the agglomerates were computed by applying a force and a torque balance on each particle. Since the forecast of breakup requires to define critical thresholds for the forces and torques in three directions (i.e., six degrees of freedom), the focus was limited to examining the evolution of the inter-particle interactions within the agglomerate.

Using the same method, Seto et al. (2011) studied the relation between the size of the agglomerates and the forces acting on the particle contacts in simple shear flows.

Furthermore, De Bona et al. (2014) followed a similar approach to investigate the breakup of agglomerates in homogeneous isotropic turbulence. The failure of contacts was solely attributed to the normal (tensile) stresses. Other possible breakup modes such as shearing, bending and twisting of contacts were not considered. Consequently, a critical tensile stress model suggested by the contact mechanics was employed to set a criterion for breakup. A simple case of two-particle agglomerates and a more complicated one involving agglomerates possessing open structures were considered. As an outcome, a model describing the breakup rate in homogeneous isotropic turbulence was suggested. In addition, it was found that the orientation of the agglomerate with respect to the flow, especially for the two-particle agglomerate, has considerable effects on breakup.

In a recent work, Frungieri et al. (2020) studied the breakup of rigid aggregates in an internal mixer. Two-dimensional, unsteady simulations of the flow in the cross-section of the mixer were conducted at two different rotor speed ratios taking 100 tracer particles representing agglomerates in a one-way coupled simulation into account. In parallel, the interactions between the flow field and the detailed isostatic structure of each agglomerate were computed applying the Stokesian dynamics method. In addition, the inter-particle forces and torques were obtained based on balances imposed at each contact as typical in the rigid-body method. A bond was assumed to instantaneously rupture when it experiences a tensile force exceeding a prescribed critical threshold. However, no further elaboration on the relation between the critical tensile force and the particle properties was given.

Schutte et al. (2015) used the rigid, isostatic structure assumption to study the dynamics of asphaltene agglomerates including breakup in channel flows. The flow was simulated one-way coupled by means of DNS and LES considering four turbulent flow conditions and $2.5 \cdot 10^5$ primary particles. Solely the drag and added-mass forces were considered

for the flow-particle interactions and the flow-shielding effect was neglected (*free-draining approximation*). Four modes of breakage, i.e., straining (tensile), shearing, bending, and twisting were considered. However, the values of the critical forces and torques leading to breakup were varied to explore the breakup behavior for different levels of bond strength. Hence, no rigorous derivations of these quantities were proposed. In a subsequent investigation, Schutte et al. (2018) extended their methodology to take the effect of two-way coupling into account. The method was applied to study the breakage of agglomerates in channel flows. It was concluded that agglomerates tend to break into fragments of asymmetric sizes rather than identical ones.

Moreover, a simplified version of the rigid-body model exists (Kousaka et al., 1992; Kousaka et al., 1979, 1980; Niedballa and Husemann, 2000). Therein, agglomerates are idealized by two-particle (doublet) structures and the contact forces are estimated to evaluate the possibility of breakup. The main drawback of this model is that the condition of breakage strongly depends on the relative orientation of the two-particle structure to the flow direction and on the size ratio of the two particles. Hence, the prediction of a breakup is strongly affected by modeling issues.

Overall, the assumption of rigid, isostatic agglomerates facilitates less CPU-intensive computations since the motion of each constituting particle does not need to be directly resolved. However, as pointed out before, tracking the structure especially in multi-block grids on parallel computers is rather complicated. Furthermore, isostatic agglomerates split as soon as a single contact within the agglomerate breaks up. This is a specific case which does not necessarily represent the breakage behavior in the more general case of arbitrary (hyperstatic) agglomerates. Finally, the main drawback of this modeling approach is the lack of rigorous models to describe the critical forces and torques leading to breakage.

2.2.2.2 Breakup of Agglomerates Idealized as Spheres

The second type of conditions-based methods describes the structure of agglomerates based on the *effective sphere* approximation. Numerous studies have adopted this approach to study the fluid-induced breakup of agglomerates in the context of the Euler-Euler as well as the Euler-Lagrange framework. In the former, breakage rate models are required, whereas in the latter beside a breakage condition the size and the motion of the resulting fragments must be addressed. Such rate functions and breakage models are typically formulated based on simplified analytical derivations, experimental observations, or results of detailed numerical simulations.

Characterizing the breakage of agglomerates and deriving predictive models has been the goal of several theoretical studies (e.g., Rumpf and Raasch, 1962; Sonntag and Russel, 1987; Thomas, 1964; Tomi and Bagster, 1978; Zaccone et al., 2009). Therein, a general hypothesis was accepted, which states that breakage occurs when the fluid dynamic stress exceeds a critical threshold that strongly depends on the type of the inter-particle cohesive forces, i.e., the yield stress or the strength. Consequently, the focus therein has been put on elucidating both sides of the problem considering agglomerates of idealized structures,

e.g., porous spheres or cylinders, surrounded by various flow patterns ranging from simple uniform or shear flows to more complicated and irregular turbulent flows.

Considering *simple flow cases*, Rumpf and Raasch (1962) described different disruptive mechanisms such as (1) the stresses acting on agglomerates accelerating or decelerating in a uniform flow field and the (2) shear and (3) centrifugal stresses imposed on agglomerates rotating in simple shear flows. The available analytical solutions for the considered simple flow cases allowed to determine the key flow quantities responsible for each mechanism. Based on that, expressions for computing these fluid-induced stresses were derived considering various assumptions. For example, the stress experienced by an agglomerate accelerating or decelerating in a flow field (often denoted *inertia stress* or *drag stress*) was attributed to the relative velocity between the agglomerate and the fluid flow. Hence, it has been approximated by the ratio of the drag force acting on a spherical agglomerate to its surface area. In addition, an expression for the shear stress acting on the surface of spherical or cylindrical agglomerates in a shear flow was derived on the basis of the elasticity theory, assuming agglomerates as elastic objects. Moreover, the angular velocity of agglomerates in shear flows has been approximated based on the shear rate of the fluid, so that the application of the elasticity theory has led to the prediction of the stress developing in spherical or cylindrical agglomerates due to rotation, denoted *rotary stress*. Furthermore, the stress threshold needed for a successful breakup has been introduced based on the famous model by Rumpf (1962), who has postulated that the size of the primary particles, their structural properties, and the type of the binding mechanism are the main factors determining the strength of agglomerates.

In the seminal work by Tomi and Bagster (1978) the stresses developing within a sphere in simple shear or uniform flow fields have been elaborated in detail aiming to define planes of maximum stress, which resemble the likely surfaces of failure. The critical stress needed for breakup was related to the properties of the agglomerates as suggested by the yield stress model by Thomas (1963) which is similar to the model by Rumpf (1962), albeit a slightly different relationship is used. As an alternative to the model by Thomas (1963), the Bingham plastic yield model was suggested to estimate the critical yield stress beyond which agglomerates are assumed to become flowable and therefore split.

The breakup of agglomerates under *turbulent flow conditions* has also been studied theoretically and experimentally by several authors. Thomas (1964) has suggested a breakup model, in which the mechanism of disruption is mainly referred to the pressure difference on opposite sides of the agglomerates caused by random velocity fluctuations. Assuming locally isotropic turbulence, Kolmogorov's theory of local isotropy has been applied to estimate the root-mean-square velocity fluctuations over distances comparable to the diameters of the agglomerates by integrating the energy spectrum over the range of wave numbers (eddy sizes) related to the size of the agglomerate. Two main subranges have been considered: The viscous subrange characterized by eddy sizes smaller than the Kolmogorov's length scale, and the inertial subrange, in which the eddies are much larger than the Kolmogorov's length scale but smaller than the integral length scale of turbulence. The root-mean-square velocity in each subrange was used to calculate the

turbulent stress imposed on agglomerates with sizes comparable to the corresponding eddy size. Consequently, breakage rate functions were derived taking the critical yield stress model (Thomas, 1963) into account. The rate functions were used to determine an average agglomerate size denoted steady-state diameter.

Following similar arguments, Neeße et al. (1987) collected formulas for estimating the root-mean-square velocity fluctuations in the viscous, inertial, and two intermediate subranges of turbulence from the literature. Subsequently, the proposed expressions are applied to compute the turbulent shear or normal stresses based on the nature of the flow in the corresponding subrange. It has been argued that the interactions between agglomerates and viscous eddies lead to surface shearing, and hence the expected breakup mode is erosion, whereas the interaction with inertial eddies results in bulk deformations or rupture. Note that these considerations are in line with the postulations and suggestions of Gregory (1989), Mühle (1993) and Yeung et al. (1997). Accordingly, the strength of the agglomerates has been included in the model taking the breakup mode (i.e., erosion or bulk rupture) into account. For rupture, the strength model by Rumpf (1962) was found adequate. However, a pseudo-surface tension model was proposed to describe strength against erosion (Neeße et al., 1987). The background of this approach combines ideas from Rumpf's tensile strength model and from the Bingham plastic yield model.

Motivated by observations of agglomerates breaking down due to unstable propagation of internal cracks, Zaccone et al. (2009) provided a model, which aims at predicting the largest stable diameter of agglomerates in laminar and turbulent regimes. Applying an energy balance, the occurrence of breakup was attributed to the circumstance that the supplied energy by the fluid dynamic stresses exceeds the energy required for extending the fracture surface. Employing several empiric scaling laws and assumptions, a relationship correlating the applied stress σ and the steady-state diameter of the agglomerate d_{ag} was suggested in the form $\sigma = m d_{ag}^n$. This power-law relationship is generally in agreement with several experimental findings (e.g., Adler and Mills, 1979; Ammar et al., 2012; Saha et al., 2015; Serra et al., 1997; Sonntag and Russel, 1986; Soos et al., 2008; Wengeler and Nirschl, 2007). However, it is noted that the correlation parameters depend on the flow configuration, the material, and the structure of the agglomerates, which explains the deviations in the values provided for the parameters m and n in the aforementioned studies.

The models discussed so far have been used in several subsequent *computational studies*. For example, Kusters (1991) studied the agglomeration and breakage of agglomerates comprising small polystyrene particles ($1 \mu\text{m}$) in isotropic and homogeneous turbulence. The breakup condition was derived by equating the turbulent stresses as introduced to the strength of the agglomerate based on an extended version of the model by Rumpf (1962) which accounts for the fractal dimension of the agglomerate. Based on these considerations a breakup rate function was derived.

Ammar et al. (2012) performed an Euler–Euler study on the breakup of Titanium dioxide agglomerates ($0.1\text{--}10 \mu\text{m}$) in a highly turbulent pipe flow ($\text{Re} = 10^5\text{--}10^7$). The breakup rate was derived taking the turbulent stresses and the strength of the agglomerates proposed by Rumpf into account. Despite neglecting its influence, the authors have pointed out the relative importance of the drag stress mechanism in their case, since the

formed agglomerates are expected to possess considerable inertial characteristics. Bähler et al. (2008) investigated the breakage of small and light agglomerates in homogeneous turbulence using the Euler–Euler approach. Breakup was assumed to be invoked by sufficiently strong turbulent stresses. The rate of breakup was determined using a power-law function describing the maximum stable size of agglomerates under a given stress.

Within the Euler–Lagrange framework, a frequently reported practice is to record the stresses acting on the point agglomerate to evaluate the possibility of breakup, without actually modeling the fragmentation event. According to a very recent review by Zheng et al. (2021) on the modeling of the flow in dry powder inhalers, this approach has been widely applied in the context of inhalers and is generally referred to as *particle trajectory modeling*. For example, Weiler (2008) and Weiler et al. (2010) computed the turbulent, drag and rotary stresses acting on agglomerates while they are transported through an accelerated turbulent flow to identify the dominating stress in different regions of the configuration. Longest et al. (2013) performed RANS predictions of airflow passages with varying flow conditions while tracking point particles representing agglomerates. The scope was to evaluate the potential effect of several flow quantities on the deagglomeration of powders in pharmaceutical inhalers. The evaluated quantities include the turbulent kinetic energy and the dissipation rate, the shear stress, and the number of wall hits among others. The possibility of breakage was evaluated based on a comparison with experiments conducted in parallel.

Apart from powder inhalers, the particle trajectory modeling approach has been applied in more general Euler–Lagrange investigations. Bähler et al. (2012) conducted a DNS of a diluted particle-laden homogeneous and isotropic turbulent flow to compute the so-called exit-time, which describes the time interval needed for agglomerates to reach flow regions where they become for the first time exposed to turbulent stresses greater than a critical threshold. The exit-time has been used to develop breakup rates for each case, which can be further used in population balances. In a subsequent study by Bähler et al. (2015), the critical stress was characterized by the size and fractal dimension of the agglomerate in a power-law relationship, and the same method was applied to derive breakup rates for various bounded and unbounded flows. Marchioli and Soldati (2015) followed a similar approach to compute the exit-time, arguing that agglomerates tend to break in a ductile mode due to the accumulation of the stresses over time rather than the brittle (instantaneous) mechanism usually assumed. It was postulated that the process of breakage starts when the acting stress reaches a certain value and ends when the accumulated amount exceeds another prescribed threshold.

It can be concluded that Euler–Lagrange methods dealing with the idealized sphere concept have mainly focused on describing the onset of breakage. Models for the resulting fragment size distribution and the velocity of the fragments are not well established. For example, Njobuenwu and Fairweather (2018) published an investigation on the agglomeration and breakup of agglomerates in a turbulent channel flow adopting the breakup model suggested by Bähler et al. (2015). The breakup event was realized by replacing the broken agglomerate by two equally-sized fragments (symmetrical breakup). However,

elaborations on the post-breakup kinetics of the fragments are missing.

In summary, different stress mechanisms (i.e., turbulent, drag and rotation) were identified in the literature to take part in the breakup of agglomerates in fluid flows. In addition, models describing the strength of agglomerates are also available. That enabled the specification of breakup conditions in various studies. However, refined methodologies which deliver a complete description especially for the behavior of the arising fragments due to breakage in the context of the effective sphere approach are still missing.

2.3 Wall-Impact Breakage

In practical applications of particle-laden flow, the interactions between particles and the surrounding walls are often inevitable, which renders the mechanism of breakage by wall impact of particular interest.

In an analogy to the case of the breakup by fluid stresses, particle-laden flow simulation methodologies which offer forecasting for the wall-impact breakage phenomena can be distinguished into two categories based on the level of captured details. The first conserves the structure and applies DEM to describe the dynamics of the primary particles within the agglomerate. If an agglomerate hits a wall, the contact forces and torques exerted by the wall onto the wall-touching particles are computed according to the soft-sphere treatment. Consequently, these particles start to bounce against the wall leading to a propagation of the impact force into the next layer of neighboring particles and so forth. As typical for DEM, the disintegration of particles is directly governed by the force and torque balances applied on the level of the single particles. Exemplary studies adopting this approach, which combines computational fluid dynamics and DEM will be discussed in Section 2.3.1.

In the second method agglomerates are represented by effective spheres. In the absence of inter-particle contacts, the progress of the impact energy within the agglomerate causing the breakup of certain particle contacts cannot be determined. For this purpose, various efforts have been undertaken in the literature towards developing models describing the outcome of an impact event based on the conditions of the impact incident. The contributions relying on this concept are addressed in Section 2.3.2.

2.3.1 Wall-Impact Breakage Predicted by Condition-Free Techniques

Investigations employing a direct wall-impact breakage forecasting have been mostly concerned with dry powder inhalers. Tong et al. (2011) carried out Euler–Lagrange simulations based on DEM to assess the deagglomeration performance of different inhaler designs taking mannitol (drug-only) agglomerates into account. The simulations employed single agglomerates consisting of 3000 polydisperse particles. Various configurations including five pipe bend designs and three volumetric flow rates were investigated. The pipe bends are distinguished by the number of bends (single or double) and the bend angle. It was demonstrated that a pipe bend design that deflects the flow by a 90° using two 45° bends

delivers the best performance, i.e., the finest particle distribution at the outlet and the smallest amount of particle deposition on the wall. The results of the simulations are found to be in qualitative agreement with earlier experimental measurements (Adi et al., 2010). Tong et al. (2013) applied the same Euler–Lagrange DEM simulation technique to investigate the performance of a commercial dry powder inhaler (Aerolizer®). Eight agglomerates each comprising 3000 mannitol particles were simultaneously taken into account. It was found that the wall-impact breakage is the most effective deagglomeration mechanism in the device.

Again, the condition-free prediction of breakage based on DEM is CPU-time intensive and is currently limited to elementary investigation and a low number of considered agglomerates.

2.3.2 Wall-Impact Breakage Predicted by Condition-Based Techniques

Efforts towards understanding the wall-impact breakage phenomenon and developing predictive models have been reported in numerous experimental works (e.g., Davies et al., 1951; Froeschke et al., 2003; John and Sethi, 1993; Samimi et al., 2004). In addition, fundamental DEM studies have been extensively carried out to study the breakage phenomenon focusing on impact events of single agglomerates in isolated environments. By precisely controlling the impact conditions, these simulations allowed to systematically evaluate the effect of the operating conditions on the fragmentation providing important insights which are not accessible by experiments (e.g., Mishra and Thornton, 2001; Moreno et al., 2003; Ning et al., 1997; Thornton et al., 1996; Tong et al., 2009). In general, it can be concluded that the breakage behavior of agglomerates is influenced by several parameters: The properties of the primary particles and the impacted wall, the nature of the inter-particle binding mechanism, the structure of the agglomerate, and the dynamics of the agglomerate, i.e., the impact velocity and angle (Ghadiri et al., 2007).

In an early attempt to formulate a criterion for the wall-impact breakage, Kousaka et al. (1979) suggested a simple model based on theoretical arguments. They compared the compressive stress at the center plane of a perfect sphere impacting a wall with the tensile strength of the agglomerate as suggested by Rumpf (1962). However, this approach suffers from a number of pitfalls. First, the stress is linearly related to the so-called collision time, which was not properly defined. In addition, the formula of the compressive stress is only valid for normal wall impacts and an extension towards oblique and shear impact events is not discussed. Lastly, the model does not offer any information on the resulting fragment size distribution or the kinetics of the arising fragments.

More recent research has followed a different strategy, which uses the data obtained from experiments and DEM simulations to develop and tune (semi-)empirical breakage models. A common practice in these studies is to characterize the outcomes of impact events by means of dimensionless numbers describing the functional relationship between various process parameters in a physically meaningful manner. Subsequently, phenomenological

models are proposed in the form of correlations between the dimensionless numbers and the investigated breakage measures.

For example, Kafui and Thornton (1993) found that the damage ratio defined as the number of broken contacts over the number of initial contacts within an agglomerate can be expressed as a function of the Weber number defined by the impact velocity v_{imp} and the diameter d_{pp} and the surface energy γ_s of the primary particle, i.e., $We = \rho_f d_{\text{pp}} v_{\text{imp}} / (2\gamma_s)$. This means that the damage ratio curves obtained under different conditions tend to collapse into a single curve when plotted as a function of We . However, this conclusion was found considering solely normal impact events carried out with different impact velocities and varying particle surface energies while keeping all other conditions fixed. In subsequent studies, Thornton et al. (1996) and Subero et al. (1999) followed the same approach and suggested that a better representation of the results can be obtained based on a modified Weber number, in which the minimum velocity needed for starting breakage is subtracted from the impact velocity.

Moreno-Atanasio and Ghadiri (2006) derived a new dimensionless number based on an energy balance assuming that the work needed for breaking all contacts within an agglomerate is proportional to the incident kinetic energy. The new dimensionless number can be seen as a product of the Weber number and a second dimensionless number including the particle diameter, the modulus of elasticity and the surface energy. The proposed dimensionless number allowed an improved unification of the results, which was achieved over a wider range of surface energies.

Le Bouteiller and Naaim (2011) carried out 2D simulations for agglomerate breakage under normal and shear (wall-parallel) impact scenarios. For normal impact, a dimensionless number analogous to the Weber number was considered. However, in the shear impact case a different dimensionless number was proposed, which describes the ratio between the frictional work and the work of cohesion. Based on these considerations, the values of the damage ratio obtained in each case were well unified by the corresponding dimensionless numbers.

Although these studies are very insightful contributions, it is important to point out the limitations that prevent a direct application of the models presented in these studies in particle-laden flow simulations. First, the investigations strictly focused on evaluating the effect of cohesion on the breakage of contacts. In other words, the relationship between a certain dimensionless number and the damage ratio was investigated while varying the inter-particle bond strength (i.e., surface energy or Hamaker constant). However, the influence of other impact conditions such as the impact angle and the diameters and number of the primary particles was not appropriately taken into account since these parameters were fixed in the simulations. Another shortcoming is that the measure used for quantifying the results, i.e., the damage ratio, does not allow a unique description of the post-breakage particle size distribution since different breakage patterns can be observed for the same damage ratio (Tong et al., 2009). Moreover, the models also lack a description for the post-breakage motion of the disintegrated fragments.

In a recent contribution, van Wachem et al. (2020) have been probably the first to present a fragmentation model applicable for particle-laden flow simulations avoiding

some of the main drawbacks mentioned above. The model relies on the data obtained by DEM simulations of normal wall-impact events accounting for agglomerates consisting of monodisperse particles. The reference simulations took into account a range of impact velocities, particle surface energy magnitudes, primary particle diameters, and agglomerate sizes. The analysis of the results focused on characterizing the fraction of the detached primary particles based on an extended version of the dimensionless number proposed by Moreno-Atanasio and Ghadiri (2006). In addition, the size distribution of the arising fragments was estimated by dividing the remaining volume of the original agglomerates into the largest possible number of discrete size classes after subtracting the volume of the detached primary particles. The study suggests to describe the post-breakage velocities of the fragments by means of a momentum factor. This factor expresses the fraction of the kinetic energy of the original agglomerate which is devoted to move the fragments after breakage. Although the introduction of a model that allows to determine the momentum factor based on the conditions of the impact event was part of the objectives of the study, a further elaboration on this issue is not available. Furthermore, it is not described in which directions the fragments are supposed to spread after breakage. The main drawback of the model is that it only provides forecasts for normal impact events since the effect of the impact angle was not investigated.

It is worth mentioning that the concept of using detailed methods to develop practical wall-impact breakage models for Euler–Lagrange point-particle computations has been also applied in the context of carrier-based agglomerates (e.g., Ariane et al., 2018; van Wachem et al., 2017). However, the suggested breakage models for carrier-based agglomerates mainly incorporate arguments specific for particles connected to a larger carrier. Thus, they are generally not applicable for traditional agglomerates. Since the carrier-based formulation of agglomerates is not of interest for the present thesis as mentioned earlier, such studies are not further discussed here. The interested reader is referred to the relevant reviews, e.g., Sommerfeld et al. (2019), Yang et al. (2015) and Zheng et al. (2021).

To conclude, models describing the wall-impact breakage in the context of the description of agglomerates as effective spheres are scarce. The advantages of the recent data-driven model by van Wachem et al. (2020) over the simple theoretical model by Kousaka et al. (1979) are clear since the former mimics both important features of the breakage scenario, i.e., the breakage onset and the fragment size distribution as predicted in detailed DEM simulations. However, since solely normal impact events were considered in the model by van Wachem et al. (2020), the applicability of the model in flow cases dominated by very small wall-impact angles must be explored.

3 Description of the Continuous Phase

In this chapter, the first part of the Euler–Lagrange simulation methodology adopted in this thesis is presented. Namely, a brief theoretical background is given on the Eulerian treatment of the carrier phase in the context of the large-eddy simulation (LES). In addition, the different types of boundary conditions relevant for the present work are discussed.

3.1 Governing Equations of Large-Eddy Simulation

As the name implies, in large-eddy simulations solely the large-scale, problem-dependent turbulent structures are predicted, whereas the small, mostly universal structures are modeled (Pope, 2000). To achieve that a filtering operation is applied to the Navier-Stokes equations yielding the equations governing the motion of the large, energy-containing eddies. In the applications of interest for the present thesis, the carrier fluid can be assumed to be incompressible and isothermal. Hence, the fluid density is constant and solely the mass and the momentum conservation equations need to be considered. In dimensionless form the filtered mass and momentum conservation equations for an incompressible fluid read (Breuer, 2002):

$$\frac{\partial \bar{u}_j}{\partial x_j} = 0, \quad (3.1)$$

$$\frac{\partial \bar{u}_i}{\partial t} + \frac{\partial (\bar{u}_i \bar{u}_j)}{\partial x_j} = -\frac{\partial \bar{p}}{\partial x_i} - \frac{1}{\text{Re}} \frac{\partial \bar{\tau}_{ij}^{\text{mol}}}{\partial x_j} + f_j^{\text{PSIC}}. \quad (3.2)$$

Here, x_i stand for the three spatial directions and t for the time. Keeping in mind that the overline refers to a filtered (i.e., resolved) quantity, the variables \bar{u}_i , \bar{p} , and $\bar{\tau}_{ij}^{\text{mol}}$ denote the filtered velocity vector, the filtered pressure field, and the viscous stress tensor, respectively. The latter is given under the assumption of a Newtonian behavior of the fluid by the dynamic viscosity of the fluid μ_f and the strain-rate tensor \bar{S}_{ij} based on the filtered velocities:

$$\bar{\tau}_{ij}^{\text{mol}} = -2\mu_f \bar{S}_{ij} \quad \text{with} \quad \bar{S}_{ij} = \frac{1}{2} \left(\frac{\partial \bar{u}_i}{\partial x_j} + \frac{\partial \bar{u}_j}{\partial x_i} \right). \quad (3.3)$$

Note that in this non-dimensional formulation, the density ρ_f and the viscosity μ_f of the fluid are equal to unity. In addition, Re appearing in Eq. (3.2) is the Reynolds number. Lastly, the source term f_j^{PSIC} included in Eq. (3.2) facilitates the coupling of momentum between the carrier and the particle phase (i.e., two-way coupling) as will be elaborated in Section 4.2.3.

The non-linear convective term in the filtered momentum Eq. (3.2) differs from the corresponding term in the original Navier-Stokes equation, since the filtered product $\overline{u_i u_j}$ differs from the product of the filtered velocities $\bar{u}_i \bar{u}_j$ (Pope, 2000). The difference can be expressed by the so-called subgrid-scale stress tensor:

$$\tau_{ij}^{\text{SGS}} = \overline{u_i u_j} - \bar{u}_i \bar{u}_j, \quad (3.4)$$

which describes the influence of the unresolved, small turbulent structures on the large resolved ones. The subgrid-scale stress tensor can be decomposed into a deviatoric (i.e., anisotropic) part $\tau_{ij}^{\text{SGS,a}}$ and an isotropic part $\tau_{ij}^{\text{SGS,i}}$:

$$\tau_{ij}^{\text{SGS}} = \tau_{ij}^{\text{SGS,a}} + \tau_{ij}^{\text{SGS,i}} = \tau_{ij}^{\text{SGS,a}} + \frac{1}{3} \tau_{kk}^{\text{SGS}}. \quad (3.5)$$

That allows to combine the isotropic part with the filtered pressure \bar{p} , which leads to the modified filtered pressure \bar{P} (Breuer, 2002; Pope, 2000):

$$\bar{P} = \bar{p} + \tau_{ij}^{\text{SGS,i}} = \bar{p} + \frac{1}{3} \tau_{kk}^{\text{SGS}}. \quad (3.6)$$

Applying the definitions (3.4), (3.5), and (3.6) into Eq. (3.2) yields the final form of the filtered momentum equation:

$$\frac{\partial \bar{u}_i}{\partial t} + \frac{\partial (\bar{u}_i \bar{u}_j)}{\partial x_j} = - \frac{\partial \bar{P}}{\partial x_i} - \frac{1}{\text{Re}} \frac{\partial \bar{\tau}_{ij}^{\text{mol}}}{\partial x_j} - \frac{\partial \tau_{ij}^{\text{SGS,a}}}{\partial x_j} + f_j^{\text{PSIC}}. \quad (3.7)$$

Consequently, in order to close the system of the governing equations, the anisotropic part of the subgrid-scale stress tensor $\tau_{ij}^{\text{SGS,a}}$ needs to be addressed by a model. The respective models used in the present thesis are discussed next in Section 3.2.

It is worth mentioning that the adopted LES methodology relies on an implicit filtering. This means that no explicit filtering function is applied to the governing equations (see Chapter 8). Instead, the filtering is performed by the numerical discretization scheme (finite-volume method), which offers a considerable simplicity in comparison to explicit filtering. From a practical viewpoint, the implicit filtering is equivalent to the application of an explicit top-hat filter with a filter width Δ_i matching the grid spacing h_i (Breuer, 2002).

3.2 Subgrid-Scale Modeling

The anisotropic part of the subgrid-scale stress tensor $\tau_{ij}^{\text{SGS,a}}$ can be described based on a variety of models (Breuer, 2002; Pope, 2000). In the simulations reported in this thesis two models are used: The Smagorinsky model (Smagorinsky, 1963) and the dynamic model by Germano et al. (1991). These are briefly discussed in the following.

3.2.1 Smagorinsky Model

The model by Smagorinsky (1963) is the simplest and the most employed LES subgrid-scale model (Breuer, 2002; Pope, 2000). By analogy to the viscous shear stress $\bar{\tau}_{ij}^{\text{mol}}$ (Eq. (3.2)), the Smagorinsky model assumes a linear relationship between the anisotropic part of the subgrid-scale stress tensor $\tau_{ij}^{\text{SGS,a}}$ and the filtered strain-rate tensor \bar{S}_{ij} :

$$\tau_{ij}^{\text{SGS,a}} = -2 \mu_{\text{T}} \bar{S}_{ij}. \quad (3.8)$$

The arising coefficient of proportionality μ_{T} represents the local eddy viscosity and thus varies in space and time (Pope, 2000). Considering that in the present dimensionless formulation the density of the fluid is equal to unity (i.e., $\rho_{\text{f}} = 1$), the eddy viscosity can be expressed in terms of the Smagorinsky length scale l_{S} and a characteristic velocity scale determined by the product of the length scale l_{S} and the magnitude of the characteristic filtered strain rate $|\bar{S}_{ij}|$ (Breuer, 2002; Pope, 2000):

$$\mu_{\text{T}} = l_{\text{S}}^2 |\bar{S}_{ij}| \quad \text{with} \quad |\bar{S}_{ij}| = \sqrt{2 \bar{S}_{ij} \bar{S}_{ij}}. \quad (3.9)$$

The length scale l_{S} is considered to be proportional to the filter width Δ :

$$l_{\text{S}} = C_{\text{S}} \Delta, \quad (3.10)$$

with the Smagorinsky constant C_{S} as the proportionality constant, which has a value of 0.165 according to a theoretical analysis by Lilly (1967) based on homogeneous isotropic turbulence (Breuer, 2002). However, in wall-bounded flows such as channel flows, a value in the range $0.065 \leq C_{\text{S}} \leq 0.1$ is typically assigned to C_{S} to achieve reasonable results (Breuer, 2002; Pope, 2000). By inserting Eqs. (3.9) and (3.10) in Eq. (3.8), the anisotropic part of the resolved subgrid-scale tensor reads:

$$\tau_{ij}^{\text{SGS,a}} = -2 (C_{\text{S}} \Delta)^2 |\bar{S}_{ij}| \bar{S}_{ij}. \quad (3.11)$$

Note that in the present methodology, the filter width Δ used for the determination of the Smagorinsky length scale l_{S} is related to the volume of the computational cell:

$$\Delta = (\Delta x \Delta y \Delta z)^{\frac{1}{3}}. \quad (3.12)$$

The simplicity of the Smagorinsky model encouraged its wide application in the literature. However, the model suffers from well-known drawbacks. For instance, different Smagorinsky constants C_{S} might be needed for the same test case upon varying the Reynolds number. In addition, a single Smagorinsky constant might not be appropriate for different flow regions within a certain setup. Specifically, a non-zero C_{S} means that the eddy viscosity and thus the subgrid-scale stress does not vanish in situations where a subgrid-scale model is not required, e.g., in laminar flow regimes or at walls. Since wall-bounded simulations are of interest for the present work, the damping function proposed by van Driest (1956) is used to scale the Smagorinsky length l_{S} down to zero at the wall. By introducing

the van Driest damping function into Eq. (3.10), the Smagorinsky length l_S reads (Breuer, 2002; Pope, 2000):

$$l_S = C_S \Delta \underbrace{\left[1 - \exp\left(-\frac{y^+}{A^+}\right)^3 \right]^{\frac{1}{2}}}_{\text{van Driest damping function}} \quad \text{with} \quad y^+ = \frac{u_\tau y}{\nu_f} \quad \text{and} \quad A^+ = 25. \quad (3.13)$$

Here, y^+ is the dimensionless wall-normal distance from the wall, A^+ is the van Driest constant and u_τ is the friction velocity.

3.2.2 Dynamic Model by Germano

As an alternative to the Smagorinsky model, the dynamic model by Germano et al. (1991) is applied in some of the simulations reported in the present work. The dynamic model offers a method to effectively compute the required parameters of a basic subgrid-scale model instead of using pre-defined values. Building on the Smagorinsky model, the aim of the dynamic approach is to determine a local and time-dependent value for the Smagorinsky coefficient C_S (no longer a constant) taking the local flow structure into account.

The derivation of the model starts by introducing a second (test) filter $\tilde{\Delta}$ of a wider width than the original one. More specifically, the width of the test filter in the present methodology is two times larger than the original filter, i.e., $\tilde{\Delta}/\Delta = 2$ (Breuer, 2002). The test filter is applied to the formerly filtered Navier-Stokes equations (3.1) and (3.2). Subsequently, the non-linear convective term in the double-filtered momentum equation is treated in a manner analogous to Eq. (3.4) leading to the subgrid-scale stress tensor corresponding to the test filter:

$$T_{ij}^{\text{SGS}} = \widetilde{\widetilde{u_i u_j}} - \widetilde{u_i} \widetilde{u_j}. \quad (3.14)$$

The tensor T_{ij}^{SGS} is not to be confused with the tensor resulting from applying the test filter to the subgrid-scale tensor of the first filtering operation given by Eq. (3.4):

$$\tilde{\tau}_{ij}^{\text{SGS}} = \widetilde{\widetilde{u_i u_j}} - \widetilde{\widetilde{u_i} \widetilde{u_j}}. \quad (3.15)$$

The difference between both tensors defines an identity according to Germano et al. (1991):

$$L_{ij} = T_{ij}^{\text{SGS}} - \tilde{\tau}_{ij}^{\text{SGS}} = \widetilde{\widetilde{u_i u_j}} - \widetilde{u_i} \widetilde{u_j}, \quad (3.16)$$

which has the advantage over T_{ij}^{SGS} and $\tilde{\tau}_{ij}^{\text{SGS}}$ that it solely involves resolved quantities. Thus, the resolved turbulent stress tensor L_{ij} is used to determine local values of the Smagorinsky coefficient C_S . To accomplish that, L_{ij} is decomposed into isotropic and anisotropic parts. The latter can be readily computed in a LES using:

$$L_{ij}^a = L_{ij} - \frac{1}{3} \delta_{ij} L_{kk}. \quad (3.17)$$

However, to establish a relationship to the Smagorinsky coefficient C_S , L_{ij}^a is expressed based on Eq. (3.16):

$$L_{ij}^a = T_{ij}^{\text{SGS},a} - \widetilde{\tau}_{ij}^{\text{SGS},a}. \quad (3.18)$$

The anisotropic part of the subgrid-scale stress tensor $T_{ij}^{\text{SGS},a}$ corresponding to the test filter is expressed based on an analogy to the Smagorinsky model according to Eq. (3.11):

$$T_{ij}^{\text{SGS},a} = -2 (C_S \widetilde{\Delta})^2 |\widetilde{S}_{ij}| \widetilde{S}_{ij}. \quad (3.19)$$

In addition, applying the test filter $\widetilde{\Delta}$ to Eq. (3.11) yields:

$$\widetilde{\tau}_{ij}^{\text{SGS},a} = \overbrace{-2 (C_S \Delta)^2 |\widetilde{S}_{ij}| \widetilde{S}_{ij}}^{\widetilde{\phantom{-2 (C_S \Delta)^2 |\widetilde{S}_{ij}| \widetilde{S}_{ij}}}}. \quad (3.20)$$

Inserting Eqs. (3.19) and (3.20) in Eq. (3.18) and simplifying the relation by moving the term $(C_S \Delta)^2$ out of the test-filter operation results in:

$$L_{ij}^a = -2 (C_S \Delta)^2 \left[\frac{\widetilde{\Delta}^2}{\Delta^2} |\widetilde{S}_{ij}| \widetilde{S}_{ij} - \widetilde{|\widetilde{S}_{ij}| \widetilde{S}_{ij}} \right] = -2 (C_S \Delta)^2 M_{ij}. \quad (3.21)$$

Since L_{ij}^a and M_{ij} are readily available as local quantities in a LES, the Smagorinsky coefficient C_S can be dynamically obtained. However, since both L_{ij}^a and M_{ij} are symmetric and traceless tensors, a single C_S does not necessarily satisfy Eq. (3.21) for five unique components. To address this issue, the method proposed by Lilly (1992) is presently followed, which suggests a least-squares approach to minimize the mean squared error of Eq. (3.21) by:

$$(C_S \Delta)^2 = -\frac{1}{2} \frac{L_{ij}^a M_{ij}}{M_{mn} M_{mn}}. \quad (3.22)$$

One of the obvious advantages of the dynamic model is that the locally determined C_S , and hence the eddy viscosity μ_T , naturally drops to zero at walls without additional scaling. However, the strong local variations of μ_T for inhomogeneous turbulent flows might lead to instabilities in the numerical solution of the governing equations (Breuer, 2002). To circumvent this issues in the present work, the minimum value of μ_T is restricted to zero and a low-pass filter is applied to remove the high-frequency oscillations of $C_S \Delta$. More details on the latter procedure can be found in Breuer (2002) and Hoppe (2020).

3.3 Boundary Conditions

The governing Navier-Stokes equations (3.1) and (3.2) are first-order in time and second-order in space partial differential equations. Hence, obtaining a unique solution requires the system of equations to be equipped with proper initial and boundary conditions. In this section, the boundary conditions applied in the simulations presented in this work are discussed in general. More detailed and problem-dependent specifications on the initial and boundary conditions are given in the description of the corresponding test cases in

Chapter 9.

Since the breakage of agglomerates is investigated in practical wall-bounded setups, the *no-slip boundary condition* is applied at physical walls. Hence, the fluid in contact with the wall moves with the same velocity as the wall (i.e., no relative motion at the fluid-wall interface). Considering that in all investigated test cases the walls are stationary and impermeable, the Stokes no-slip boundary condition means that the tangential and normal fluid velocity components at the wall are equal to zero, which is mathematically expressed as:

$$\bar{u}_i(x_i^w) = 0, \quad (3.23)$$

where \bar{u}_i denotes the filtered fluid velocity and x_i^w is the position of the wall. The no-slip condition is justifiable for the present LES, since solely wall-resolved simulations are considered. This implies that no wall models are used. Instead, the resolution of the computational grids at the wall is sufficiently fine to directly resolve the viscous sublayer. In other words, the dimensionless spacing of the first cell center lays in the viscous sublayer given by $0 < y^+ \leq 5$, and the total number of grid points within the viscous sublayer is adequate, i.e., larger than 5 (Breuer, 2002).

The straightforward way to establish a fully developed turbulent flow in a certain setup is to consider an entry region following the inlet boundary. However, the entrance length adds considerable computational burden and is physically not interesting since its sole purpose is to assure the development of the turbulent flow field. To circumvent the issue of unnecessarily long and thus demanding computational domains, different alternatives are available depending on the nature of the problem. If the flow in the streamwise direction is homogeneous (i.e., statistically invariant) such as the duct flow case (Section 9.2), applying *periodic boundary conditions* in the streamwise direction is a viable option. For flows with an inhomogeneous streamwise direction, turbulent *inflow conditions* at the inlets and *outflow conditions* at the outlets are required. This circumstance is encountered in the disperser flow and the pipe bend flow described in Sections 9.1 and 9.3, respectively. Both scenarios (i.e., periodic and inflow/outflow conditions) are discussed in the following.

In general, periodic boundaries define corresponding boundaries at which the flow quantities are set equal to each other:

$$\bar{u}_i(x_i^{(1)}, t) = \bar{u}_i(x_i^{(2)}, t). \quad (3.24)$$

Here, $x_i^{(1)}$ describes the position vector of the first boundary and $x_i^{(2)} = x_i^{(1)} + L_i$ the position of the second boundary with L_i being a vector describing the extension of the domain in the homogeneous direction. However, to obtain a physically adequate solution while using periodic boundary conditions the dimensions of the domain in the homogeneous directions (L_i) must be sufficiently large. Typically, a criterion based on the two-point correlation is used to ensure that the largest turbulent structures are contained. The criterion suggests that the two-point correlations of the velocity fluctuations have to decay

to effectively zero at half of the length of the periodic direction (Piomelli and Chasnov, 1996).

The assumption of periodic conditions in the streamwise direction does not hold for the pressure, since a pressure drop occurs due to the friction at the walls and the presence of particles in case the two-way coupling is taken into account. To allow a pressure drop and to maintain a constant mass flow rate in the streamwise direction under periodic conditions, the instantaneous pressure gradient is decomposed into a mean part and a fluctuating one. The latter is assumed to be periodic, whereas the former (i.e., the mean pressure gradient) is estimated by a dynamically adjusted forcing term f^{n+1} (Benocci and Pinelli, 1990):

$$f^{n+1} = f_i^n + \frac{\alpha}{\Delta t} \rho_f \left(u_{\text{mean}}^0 + u_{\text{mean}}^n - 2 u_{\text{mean}}^{n+1} \right), \quad (3.25)$$

which is added as a source term to the conservation equation of the streamwise momentum equation. Here, $\alpha = 0.3$ stands for an under-relaxation factor and Δt is the size of the time step. The superscripts $n + 1$ and n refer to quantities computed in the present and the previous time step, respectively. Finally, u_{mean} denotes the mean velocity defining the flow rate and u_{mean}^0 is the desired mean velocity.

In the case of an inhomogeneous flow in streamwise direction, i.e., the disperser flow (Section 9.1) and the pipe bend flow (Section 9.3), periodic boundary conditions are not applicable. Thus, inflow boundary conditions are generated by auxiliary straight duct and straight pipe flow simulations employing periodic conditions at the same Reynolds number, respectively. The instantaneous flow quantities (i.e., filtered velocity) within an arbitrary cross-section are extracted from the auxiliary simulations in form of successive datasets. Subsequently, the inflow data are applied in the right order at the inlet boundary of the intrinsic cases. It is worth mentioning that in order to ensure a correct mapping of the data and to avoid numerical issues, the grid resolution and the time-step size in the auxiliary cases and the corresponding main cases have to be identical.

At the outlets of the intrinsic cases a classical convective boundary condition is applied:

$$\frac{\partial \bar{u}_i}{\partial t} + u_{\text{conv}} \frac{\partial \bar{u}_i}{\partial \chi} \Big|_{\text{outflow}} = 0. \quad (3.26)$$

Here, $\partial/\partial\chi$ refers to the gradient in the direction of the convective velocity, u_{conv} which depends on the nature of the problem. In the present work, u_{conv} is chosen to be equal to the mean velocity.

In general, the outlet boundary must be placed far downstream from the region of interest to avoid any possible disturbances and especially the occurrence of a backflow. The convective boundary condition chosen in the present work ensures that the turbulent eddies leave the computational domain almost without disturbance and without reflections (Breuer, 2002).

4 Description of the Disperse Phase

This chapter introduces the Lagrangian point-particle method, which is employed to describe the dynamics of the disperse phase. In Section 4.1 an overview on the modeling strategy is given. Afterwards, the mechanisms dictating the motion of particles are elaborated. These are: (I) the fluid-particle interactions (Section 4.2), (II) the particle-particle collisions including possible agglomeration processes (Section 4.3), and (III) the interactions between particles and domain boundaries (Section 4.4).

In order to realistically predict the particulate phase, knowledge on the evolution of important features are needed besides the velocities. These are the size distribution and the temperature of the particles. However, since solely isothermal flows are presently considered, the effect of heat transfer is neglected. The change of the size distribution of the disperse phase is attributed in the present work to two counteracting phenomena: The agglomeration of primary particles and the breakage of agglomerates. The model considered to describe the agglomeration of particles in the reported simulations is described in Section 4.3. Since the breakage of agglomerates is the main topic of this work, the respective models are explained separately in Chapters 6 and 7. These models account for the breakage due to the interactions with the fluid flow and due to the impact at walls. As already mentioned before, the breakage of agglomerates due to inter-particle collisions is not covered in this thesis. In addition, the fracture of single primary particles is a fundamentally different problem which is outside the present scope.

Note that in general, the derivations presented in this chapter are expressed in vector notation for better readability. However, the subgrid-scale model for the particles (Section 4.2.2) and the particle-fluid feedback term (Section 4.2.3) are expressed in index notation for convenience.

4.1 Classification of Point Particles and Interphase Coupling

The dynamics of the disperse phase is governed by a large number of interwoven phenomena. Thus, it is useful to classify a particle-laden flow based on characteristic parameters. Such parameters help to identify the most important physical effects that need to be taken into account in the numerical modeling of the flow system. Note that for brevity and convenience, the notation hereafter uses the phrase "particle" and the corresponding subscript "p" to denote a point-particle entity, i.e., a primary particle or an agglomerate. This is practical since an agglomerate is treated as a single spherical particle. However, in case a distinction is necessary, "pp" and "ag" are used to refer to primary particles and agglomerates, respectively.

The first characteristic parameter is the volume fraction of the disperse phase Φ_p , which indicates how dense or dilute the system is. For systems employing a number n_{pp} of monodisperse spherical primary particles, the volume fraction of the disperse phase is defined by:

$$\Phi_p = \frac{n_{pp} V_{pp}}{V_s} = \frac{n_{pp} \pi d_{pp}^3}{6 V_s}, \quad (4.1)$$

where V_s is the total volume of the flow system and V_{pp} and d_{pp} are the volume and the diameter of a primary particle, respectively. In the literature (e.g., Elghobashi, 1991,

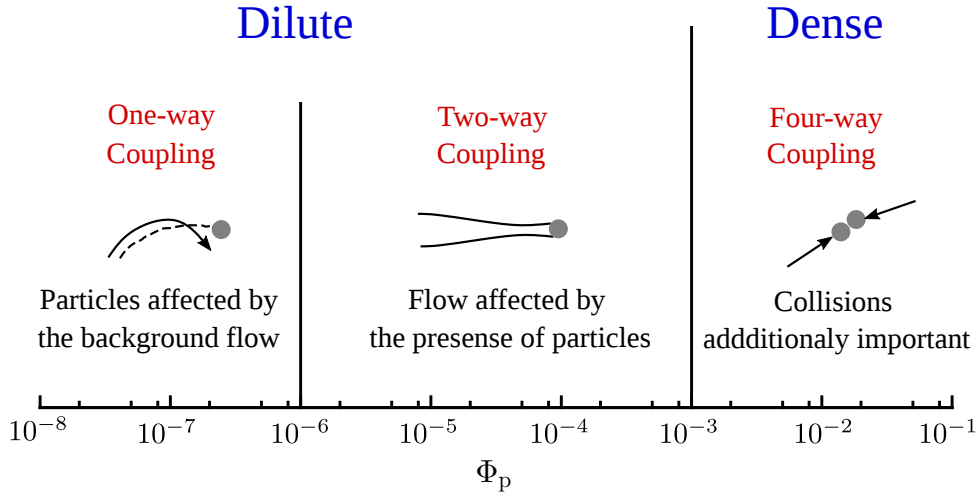


Fig. 4.1. Interphase and intraphase coupling regimes based on the volume fraction of the disperse phase Φ_p (Crowe, 2005; Elghobashi, 1991, 1994).

1994), Φ_p is primarily used to indicate the coupling mechanism that dominates the particle motion (see Fig. 4.1). For very dilute flows (i.e., $\Phi_p \lesssim 10^{-6}$), particles are mobilized in response to the motion of the carrier fluid, i.e., owing to the transfer of momentum from the continuous phase to the particulate phase. However, the counteracting effect of the particles on the fluid and the effects of the inter-particle collisions can be fairly neglected in this regime. Hence, the particle-laden flow in this case is described as one-way coupled. For higher values of Φ_p (i.e., $10^{-6} \lesssim \Phi_p \lesssim 10^{-3}$), the flow is moderately dilute and the transfer of momentum from the particulate phase to the continuous phase needs to be accounted for (two-way coupling). This coupling is accomplished by means of the source term f_j^{PSIC} included in the momentum equation (3.2) of the fluid flow. The definition of f_j^{PSIC} is attributed to the particle-source-in-cell (PSIC) method by Crowe et al. (1977), which will be discussed in Section 4.2.3. Furthermore, in dense systems (i.e., $\Phi_p \gtrsim 10^{-3}$) the inter-particle collisions start to dominate the motion of particles and thus must additionally be taken into account (four-way coupling).

Another important parameter is the Stokes number St , which measures the ability of particles to follow the changes in the motion of the carrier phase (Sommerfeld et al., 2008).

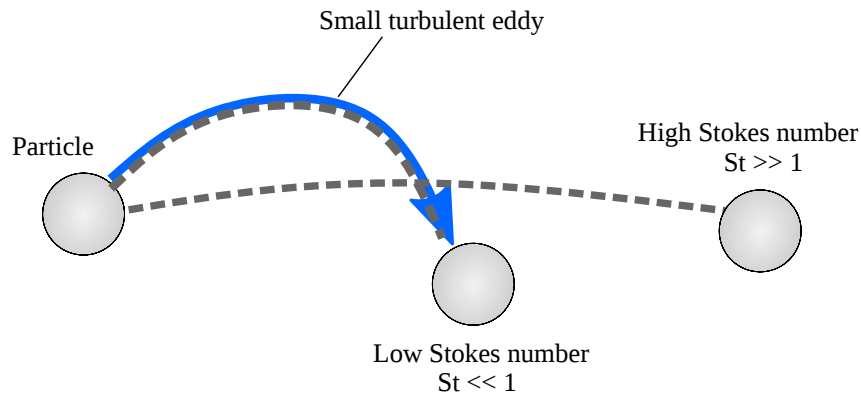


Fig. 4.2. Schematic representation of the response of particles to a change of the flow motion based on the Stokes number St (Crowe et al., 1988).

The Stokes number is expressed by the ratio of the response time of the particle τ_p to a characteristic time scale of the fluid motion:

$$\begin{aligned} St &= \frac{\tau_p}{\tau_f}, \text{ or alternatively} \\ St^+ &= \frac{\tau_p}{\tau_f^+}, \end{aligned} \quad (4.2)$$

The particle relaxation time τ_p is given in terms of the diameter d_p and density ρ_p of the particle and the viscosity of the fluid μ_f . The relationship can be derived by considering the motion of a sphere in a Stokes flow and reads $\tau_p = \rho_p d_p^2 / (18 \mu_f)$. Furthermore, different possibilities exist to express the characteristic time scale of the fluid flow. In the present work, two definitions are used: (1) the convective time scale $\tau_f = D / (2 U_b)$ defined using the diameter of the duct or the pipe D (see Chapter 9) and the bulk velocity U_b , (2) the viscous time scale $\tau_f^+ = \mu_f / (\rho_f u_\tau^2)$, where u_τ denotes the shear stress velocity.

As schematically depicted in Fig. 4.2, the Stokes number characterizes the patterns of the particle motion. For $St \ll 1$, particles are designated as small and light and they tend to act as tracers closely following the streamlines of the carrier flow. Hence, in this case the dynamic behavior of the particles is affected even by the smallest eddies. Thus, the trajectories of tracer-like particles can be determined by the local fluid velocity. That renders the calculation of the forces and torques imposed by the fluid on the particles unnecessary. In contrast, particles associated with larger Stokes numbers, i.e., $St \gg 1$ are called inertial since they move along their own trajectories and do not follow the flow exactly.

Similar to the Stokes number, the particle Reynolds number Re_p :

$$Re_p = \frac{\rho_f |\mathbf{u}_f - \mathbf{u}_p| d_p}{\mu_f}, \quad (4.3)$$

is commonly used to characterize the motion of particles. It accounts for the velocity of the particle relative to the velocity of the fluid $|\mathbf{u}_f - \mathbf{u}_p|$ (also called the slip velocity) for

describing the nature of the fluid-particle interaction.

In the present LES-based Lagrangian tracking, the movement of particles is predicted as follows: First, the fluid-induced motion of particles (i.e., velocity and position) is determined by solving the equations of motion of each particle. For this purpose, the forces and torques exerted by the fluid on the particles are computed taking the effects of the unresolved subgrid-scale eddies into account (see Sections 4.2.1 and 4.2.2). In a subsequent step, the inter-particle and particle-wall collisions are accounted for. This is achieved by adjusting the velocity of the particle determined in the first step (Bird, 1976). The additional contribution represents the change in the particle velocity due to the momentum exchange during the collision event and it is computed according to the hard-sphere framework (see Sections 4.3 and 4.4). Hence, unlike in the soft-sphere treatment¹ the collisions are not directly incorporated in the equations of motions of particles.

4.2 Fluid-Induced Motion of Particles

As aforementioned, the fluid-induced motion is determined by solving the equations of motion of individual particles. According to Newton's second law, the equations of the translatory and rotational motions are respectively given by:

$$m_p \frac{d\mathbf{u}_p}{dt} = \sum_i \mathbf{F}_{p,i}, \quad (4.4)$$

$$I_p \frac{d\boldsymbol{\omega}_p}{dt} = \mathbf{T}_p. \quad (4.5)$$

Here, \mathbf{u}_p and m_p denote the translational velocity vector and the mass of the particle and $\mathbf{F}_{p,i}$ stands for the forces acting on the particle. In addition, $\boldsymbol{\omega}_p$ and I_p represent the angular velocity and the moment of inertia of a spherical particle (i.e., $I_p = 0.1 m_p d_p^2$), whereas \mathbf{T}_p is the torque exerted on a particle due to the viscous interaction with the fluid. Hence, the displacement of a particle is obtained by solving the equation:

$$\frac{d\mathbf{x}_p}{dt} = \mathbf{u}_p. \quad (4.6)$$

Applying the point-particle approximation, the particles (i.e., primary particles and agglomerates) are treated as point masses and the flow around the particles is not resolved. Accordingly, the fluid forces $\mathbf{F}_{p,i}$ and the torque \mathbf{T}_p are provided by constitutive relations. In principle, exact solutions are available for the Stokes flow regime (i.e., small Re_p) (Basset, 1888; Boussinesq, 1885; Oseen, 1927). For non-uniform flows, Maxey and Riley (1983) derived the equation of motion of a small rigid particle. However, the extension to-

¹In the present thesis, the soft-sphere model is solely applied in the discrete element method simulations, which are conducted to obtain data for modeling the wall-impact breakage. The adopted soft-sphere approach is discussed in Section 7.2.1.

wards higher particle Reynolds numbers employs models based on empirically determined coefficients (see Section 4.2.1).

4.2.1 Forces and Torque Acting on the Particle

Following the approach suggested by Maxey and Riley (1983), the total force acting on a disperse particle is computed by a superposition of different contributions, which can be expressed based on the properties of the undisturbed flow field (i.e., the presence of the particle is not accounted for) at the position of the particle. The forces considered in the equation of the translatory motion (4.4) are:

$$\sum_i \mathbf{F}_{p,i} = \mathbf{F}_G + \mathbf{F}_B + \mathbf{F}_D + \mathbf{F}_L + \mathbf{F}_{AM} + \mathbf{F}_{PG} + \mathbf{F}_{BA}. \quad (4.7)$$

Here, \mathbf{F}_G denotes for the gravity force, \mathbf{F}_B is the buoyancy force, \mathbf{F}_D is the drag force, \mathbf{F}_L is the lift force, \mathbf{F}_{AM} is the added-mass force, \mathbf{F}_{PG} is the pressure gradient force, and \mathbf{F}_{BA} is the Basset history force. Note that for the present work solely solid heavy particles in gas flows are of interest, i.e., the particle-fluid density ratio is large ($\rho_p/\rho_f \gg 1$). In this case, the buoyancy force, the pressure-gradient force, the added-mass force, and the Basset history force are negligibly small in comparison to the drag force and hence can be ignored (Kuerten, 2016). However, the former three contributions are taken into account, since they are rather easy to evaluate. By contrast, the determination of the Basset history force is computationally challenging, which provides an additional reason for leaving the Basset history force out.

The gravity force \mathbf{F}_G is given by the weight of the particle, and the buoyancy force \mathbf{F}_B describes the weight of the displaced fluid by the presence of the particle. Both forces can be combined and calculated as:

$$\mathbf{F}_{G+B} = \mathbf{F}_G + \mathbf{F}_B = m_p \mathbf{g} \left(1 - \frac{\rho_f}{\rho_p} \right). \quad (4.8)$$

The drag force on the particle is calculated according to the well-known drag formula:

$$\mathbf{F}_D = C_D \frac{\rho_f}{2} A_p |\mathbf{u}_f - \mathbf{u}_p| (\mathbf{u}_f - \mathbf{u}_p) = \frac{C_D}{8} \pi \rho_f d_p^2 |\mathbf{u}_f - \mathbf{u}_p| (\mathbf{u}_f - \mathbf{u}_p). \quad (4.9)$$

Here, A_p denotes the projected area of the sphere. Assuming Stokes flow around a sphere, the drag coefficient is given by $C_D = 24 / \text{Re}_p$. In order to extend the range of applicability of this relation towards larger particle Reynolds numbers Re_p , an empirically determined

correction factor is applied leading to the following drag coefficient (Schiller and Naumann, 1933; Sommerfeld et al., 2008):

$$C_D = \begin{cases} \frac{24}{\text{Re}_p} (1 + 0.15 \text{Re}_p^{0.687}) & \text{for } \text{Re}_p \leq 1000 , \\ 0.44 & \text{for } \text{Re}_p > 1000 . \end{cases} \quad (4.10)$$

Note that the definition of the particle Reynolds number Re_p is given in Eq. (4.3).

The lift force \mathbf{F}_L is expressed as the sum of two contributions:

$$\mathbf{F}_L = \mathbf{F}_L^{\text{Saf}} + \mathbf{F}_L^{\text{Mag}}. \quad (4.11)$$

The first is the lift effect due to the velocity shear (Saffman force), which is calculated as follows:

$$\mathbf{F}_L^{\text{Saf}} = \frac{\rho_f}{2} \frac{\pi}{4} d_p^3 C_{\text{LS}} [(\mathbf{u}_f - \mathbf{u}_p) \times \boldsymbol{\omega}_f]. \quad (4.12)$$

Here, $\boldsymbol{\omega}_f$ stands for the rotation vector of the fluid flow (i.e., $\boldsymbol{\omega}_f = \nabla \times \mathbf{u}_f$) and C_{LS} is the Saffman lift coefficient expressed by the following correlation (Crowe et al., 1998; Mei, 1992):

$$C_{\text{LS}} = \frac{4.1126}{\sqrt{\text{Re}_s}} \cdot \begin{cases} (1 - 0.3314 \sqrt{\beta_{\text{LS}}}) \exp(-0.1 \text{Re}_p) + 0.3314 \sqrt{\beta_{\text{LS}}} & \text{for } \text{Re}_p \leq 40 , \\ 0.0524 \sqrt{\beta_{\text{LS}} \text{Re}_p} & \text{for } \text{Re}_p > 40 . \end{cases} \quad (4.13)$$

Here, the shear Reynolds number Re_s and the dimensionless shear rate β_{LS} are defined as:

$$\text{Re}_s = \frac{d_p^2 |\boldsymbol{\omega}_f|}{\nu_f} \quad \text{and} \quad \beta_{\text{LS}} = \frac{1}{2} \frac{\text{Re}_s}{\text{Re}_p} , \quad (4.14)$$

where ν_f is the kinematic viscosity of the fluid. It is noteworthy that correlation (4.13) is valid for $0.1 \leq \text{Re}_p \leq 100$ and $0.005 \leq \beta_{\text{LS}} \leq 0.4$ (Mei, 1992).

The second lift contribution is the Magnus lift force, which is attributed to the rotational motion of the particle (Crowe et al., 1998):

$$\mathbf{F}_L^{\text{Mag}} = \frac{\rho_f}{2} \frac{\pi}{4} d_p^2 C_{\text{LR}} |\mathbf{u}_f - \mathbf{u}_p| \frac{\boldsymbol{\Omega}_{\text{rel}} \times (\mathbf{u}_f - \mathbf{u}_p)}{|\boldsymbol{\Omega}_{\text{rel}}|}. \quad (4.15)$$

Here, the relative rotation of the particles $\boldsymbol{\Omega}_{\text{rel}}$ is given by:

$$\boldsymbol{\Omega}_{\text{rel}} = \frac{1}{2} \nabla \times \mathbf{u}_f - \boldsymbol{\omega}_p , \quad (4.16)$$

where $\boldsymbol{\omega}_p$ denotes the angular velocity of the particle. The lift coefficient C_{LR} is based on an experimentally determined correlation for $Re_p < 140$ (Oesterlé and Bui Dinh, 1998):

$$C_{LR} = 0.45 + \left(\frac{Re_r}{Re_p} - 0.45 \right) \exp(-0.05684 \cdot Re_r^{0.4} Re_p^{0.3}), \quad (4.17)$$

where the Reynolds number of the particle rotation Re_r is defined as:

$$Re_r = \frac{d_p^2 |\boldsymbol{\Omega}_{rel}|}{\nu_f}. \quad (4.18)$$

Furthermore, the added-mass force \mathbf{F}_{AM} arises due to the acceleration or deceleration of the fluid adjacent to the particle due to the unsteady motion of the particle (Brennen, 1982; Crowe et al., 1998). Consequently, the added-mass force is proportional to the changes of the particle velocity and to the total changes of the fluid velocity (local and convective) at the particle position:

$$\mathbf{F}_{AM} = C_{AM} \rho_f \frac{\pi}{6} d_p^3 \left(\frac{D\mathbf{u}_f}{Dt} - \frac{d\mathbf{u}_p}{dt} \right), \quad (4.19)$$

where the added-mass coefficient C_{AM} is set to 0.5 (Brennen, 1982; Kuerten, 2016).

The drag force incorporates pressure and viscosity effects originating from the flow around the particle. However, the presence of a pressure gradient in the fluid flow surrounding the particle leads to an additional pressure-gradient force \mathbf{F}_{PG} . Assuming that the pressure gradient is constant over the diameter of the particle, the pressure-gradient force can be described as (Maxey and Riley, 1983):

$$\mathbf{F}_{PG} = \rho_f \frac{\pi}{6} d_p^3 \frac{D\mathbf{u}_f}{Dt}. \quad (4.20)$$

Similar to the gravity and buoyancy force, the added-mass and pressure gradient force can be combined:

$$\mathbf{F}_{AM+PG} = \rho_f \frac{\pi}{6} d_p^3 \left[(1 + C_{AM}) \frac{D\mathbf{u}_f}{Dt} - C_{AM} \frac{d\mathbf{u}_p}{dt} \right]. \quad (4.21)$$

Regarding the rotational motion, the viscous torque exerted by the fluid on a rotating particle is computed as (Crowe et al., 1998; Sommerfeld, 2003):

$$\mathbf{T}_p = C_R \frac{\rho_f}{2} \left(\frac{d_p}{2} \right)^5 |\boldsymbol{\Omega}_{rel}| \boldsymbol{\Omega}_{rel}. \quad (4.22)$$

According to the analytical solution of the Stokes equations in a spherical coordinate system (Rubinow and Keller, 1961), the torque coefficient can be expressed as $C_R = 64 \pi / \text{Re}_r$, which is valid for $\text{Re}_r < 32$. Extensions towards higher Re_r were proposed based on experiments (Sawatzki, 1970) and numerical simulations (Dennis et al., 1980). However, in the present work the torque coefficient obtained by the analytical solution is adequate.

4.2.2 Subgrid-Scale Model for the Particles

The force models described in the preceding Section 4.2.1 are functions of the full instantaneous fluid velocity u_i at the position of the particle. Since in LES solely the large-scale (filtered) velocity field \bar{u}_i is directly resolved, the subgrid-scale motion "sensed" by the particles $u'_{s,i}$ need to be mimicked by a model to obtain the required full velocity:

$$u_i = \bar{u}_i + u'_{s,i}. \quad (4.23)$$

The consideration of these fine-scale velocity fluctuations is especially important for light particles, which are characterized by small Stokes numbers. This is attributed to the fact that the dynamic behavior of small particles is strongly affected by the interactions with the smallest eddies.

For this purpose, the present work utilizes a stochastic particle subgrid-scale model originally proposed by Pozorski and Apte (2009) and recently enhanced and extended by Breuer and Hoppe (2017) and Hoppe (2020). The model applies the Langevin equation to derive a description for the subgrid-scale velocity fluctuations (Breuer and Hoppe, 2017; Hoppe, 2020):

$$du'_{s,i} = -G_{ij} u'_{s,j} dt + \sqrt{2 \sigma_{\text{SGS}}^2} B_{ij} dW_j. \quad (4.24)$$

Here, G_{ij} and B_{ij} are the drift and diffusion matrices of the stochastic process and σ_{SGS} is the characteristic velocity of the subgrid scales sensed by the particle. In addition, dW_j are the increments of a Wiener process, which obey a Gaussian distribution with zero mean and a variance equal to the time step size. Pozorski and Apte (2009) suggested to estimate σ_{SGS} by the turbulent kinetic energy k_{SGS} of the subgrid scales:

$$\sigma_{\text{SGS}} = \sqrt{\frac{2}{3} k_{\text{SGS}}}. \quad (4.25)$$

The latter was determined by Breuer and Hoppe (2017) and Hoppe (2020) relying on the approach by Bardina et al. (1980):

$$k_{\text{SGS}} = \frac{1}{2} (\bar{u}_i - \bar{\bar{u}}_i)^2 \quad (4.26)$$

where the second filtering operation for the determination of $\bar{\bar{u}}_i$ uses a filter width of $\tilde{\Delta} = 2 \Delta$ and accounts for the 27 neighboring grid points with weighting factors based on a trilinear interpolation. To obtain the subgrid-velocity fluctuations sensed by the particles $u'_{s,i}$, the Langevin equation (4.24) is integrated between the time instants t_0 and

t . The complete solution is not presented here since it does not fall within the scope of the present work and the interested reader is referred to Breuer and Hoppe (2017) and Hoppe (2020) for more details. Nevertheless, the finally derived equation for determining the required particle subgrid-scale velocity at the current time step ($n + 1$) is given for the sake of completeness:

$$u'_{s,i}{}^{(n+1)} = E_{ij}(t, t_0) u'_{s,j}{}^{(n)} + W_{ij}(t, t_0) \xi_j. \quad (4.27)$$

Here, $E_{ij}(t, t_0)$ is the matrix exponential of the drift matrix, $W_{ij}(t, t_0)$ is the square-root of the covariance matrix of the stochastic process, and ξ_j denotes a normally distributed random vector. The exact definition of these matrices can also be found in the cited references.

4.2.3 Feedback Effect on the Continuous Phase

As discussed in Section 4.1, when the volume fraction of the disperse phase increases beyond a certain value, i.e., the threshold of $\Phi_p \gtrsim 10^{-6}$, the disturbances of the fluid flow caused by the presence of the particles become non negligible and need to be accounted for. For this purpose, the momentum transfer from the particles to the fluid is considered by means of the source term f_j^{PSIC} added to the momentum equation (3.7) of the fluid phase. The source term is formulated based on the particle-source-in-cell (PSI-CELL) method by Crowe et al. (1977). The method suggests to use the reaction force exerted on the fluid by all particles N_p located in a certain computational cell of the volume ΔV . Recalling that the present work focuses on solid particles transported in gas (i.e., $\rho_p/\rho_f \gg 1$), solely the dominant drag force is incorporated in the feedback source term f_i^{PSIC} :

$$f_j^{\text{PSIC}} = -\frac{1}{\Delta V} \sum_{k=1}^{N_p} F_{D,j}^k. \quad (4.28)$$

Here, the index j refers to the Cartesian coordinates and the superscript k is the index running over the particles in the cell. In the present methodology, the feedback drag is distributed to the centers of the eight computational cells surrounding the particle to ensure a smooth source-term distribution (Alletto, 2014). The weighting factors are determined following a trilinear interpolation scheme, where the coefficients depend on the distance between the particle position and the center of the corresponding cell, see Alletto (2014) for further details.

4.2.4 On the Suitability of the Point-Particle Approach for the Present Work

It is well known that the accuracy of the predictions obtained by the point-particle model can be readily affected by the ratio of the particle size to the underlying grid resolution. In the present work, large particles (e.g., agglomerates) are tracked in wall-resolved LES computations. Considering the complexity of some of the investigated geometries, ade-

quately fine grids are employed. Hence, in some specific flow cases (high Re) and some flow regions (e.g., near walls) it is possible to have a local grid spacing, which is smaller than the particles size.

In one-way coupled simulations the point-particle approximation is justified when the size of the particle is much smaller than the grid cell. This restriction is posed by the fact that the undisturbed fluid velocity used in the expressions of the fluid forces has to be interpolated from the neighboring Eulerian grid points to the center of the particle. Therefore, an accurate estimation of the flow velocity at the position of the particle necessitates the particles to be adequately smaller than the underlying grid cells. If the particles are larger than the cells, they encounter a local flow field which might include smaller scales than those driving the actual particles (Portela and Oliemans, 2003; Sommerfeld et al., 2008). However, the error introduced by particles larger than the grid cells is not critical in the case of heavy particles (i.e., high particle-to-fluid density ratios) relevant for the present application. This comes from the fact that the motion of the heavy (inertial) particles is influenced mostly by the large eddies rather the smaller ones (Portela and Oliemans, 2003; Sommerfeld et al., 2008).

For two-way coupled simulations the situation is more complicated. In this case, the fluid velocity is disturbed by the particles due to two effects: The feedback of the particles on the momentum of the fluid and the local volume occupied by the particles (Balachandar et al., 2019; van Wachem and Almstedt, 2003). While the impact of the former effect is generally more pronounced (Balachandar et al., 2019), the significance of both effects grows with the relative size of the particle to the cell (see, e.g., Balachandar et al., 2019; Evrard et al., 2020, and the references therein). In the limit of a high volume fraction Φ_p of the particle phase and particle sizes comparable to the local grid resolution, additional measures are usually considered to ensure an accurate representation of the disturbances.

First, the volume occupied by the particles can be accounted for by introducing the volume fraction of the disperse phase Φ_p into the governing equations of the fluid (Balachandar et al., 2019; van Wachem and Almstedt, 2003). This can be achieved relying on an ensemble averaging (Zhang and Prosperetti, 1997) or local volume filtering (Capecelatro and Desjardins, 2013) of the governing equations.

Second, the source term representing the feedback of momentum is projected to the Eulerian grid using weighting factors determined by means of regularized kernel functions, e.g., Gaussian and Wendland (see, e.g., Balachandar et al., 2019; Capecelatro and Desjardins, 2013; Evrard et al., 2020; Poustis et al., 2019). Such kernel functions allow a smooth projection of the source term for arbitrary particle-to-cell size ratios, i.e., the number of affected grid cells depends on the size of the particle and is not restricted to the surrounding eight cells as in the method described above relying on weighting factors according to a trilinear interpolation. However, even when the disturbances are well accounted for, a persistent challenge remains to be tackled: The undisturbed flow velocity at the position of the particle needs to be recovered. This is necessary since the fluid-particle interaction models described in Section 4.2.1 are functions of quantities corresponding to the undisturbed flow field. Recently, different methods were proposed

for evaluating and subtracting the self-induced velocity of the particle, which enables to recover the undisturbed flow velocity at the position of the particle (Balachandar et al., 2019; Evrard et al., 2020; Poustis et al., 2019).

In the present approach, the two-way coupling method ignores the volume fraction of the particle phase in the mass and momentum equations of the fluid. In addition, to determine the weighing factors for projecting the feedback force of the particles to the Eulerian grid, a method devised from a trilinear interpolation scheme is used instead of a regularization kernel function capable of arbitrary particle-to-cell size ratios. Moreover, no procedure is applied to recover the undisturbed flow velocity. This choice is justified by the fact that these issues are not critical to the present applications, since in most simulations reported in Chapter 9, the two-way coupling is insignificant or entirely neglected. In more detail, the volume fraction of the particles Φ_p does not reach the two-way coupling threshold of $\Phi_p \simeq 10^{-6}$ (Sections 9.1 and 9.3) or barely exceeds this limit (Section 9.2).

4.3 Hard-Sphere Particle-Particle Collisions and Agglomerations

The hard-sphere approach treats the colliding particles as rigid spheres and models the outcome of binary collision events relying on momentum-based arguments (Crowe et al., 1998). The model was first extended by Kosinski and Hoffmann (2010, 2011) to account for the cohesion of particles and to devise conditions for agglomeration. Breuer and Almohammed (2015) and Almohammed (2018) further extended the agglomeration model and introduced various improvements. The most important features of the extended hard-sphere model for cohesive particles are briefly discussed below. The detailed derivation and further information can be found in Breuer and Almohammed (2015) and Almohammed (2018).

Considering the binary collision event including friction depicted in Fig. 4.3, the momentum conservation can be formulated as follows:

$$m_{p,1} (\mathbf{u}_{p,1}^+ - \mathbf{u}_{p,1}^-) = -\hat{\mathbf{f}}^{\text{col}} \quad , \quad (4.29a)$$

$$m_{p,2} (\mathbf{u}_{p,2}^+ - \mathbf{u}_{p,2}^-) = \hat{\mathbf{f}}^{\text{col}} \quad , \quad (4.29b)$$

$$I_{p,1} (\boldsymbol{\omega}_{p,1}^+ - \boldsymbol{\omega}_{p,1}^-) = -\frac{d_{p,1}}{2} \mathbf{n} \times \hat{\mathbf{f}}^{\text{col}} \quad , \quad (4.29c)$$

$$I_{p,2} (\boldsymbol{\omega}_{p,2}^+ - \boldsymbol{\omega}_{p,2}^-) = \frac{d_{p,2}}{2} \mathbf{n} \times \hat{\mathbf{f}}^{\text{col}} \quad . \quad (4.29d)$$

Here, the superscripts + and – indicate the post-collision and the pre-collision quantities, respectively. In addition, the subscript 1 and 2 refer to the two collision partners, d_p is the diameter of the collision partner, and \mathbf{n} denotes the normal unit vector connecting

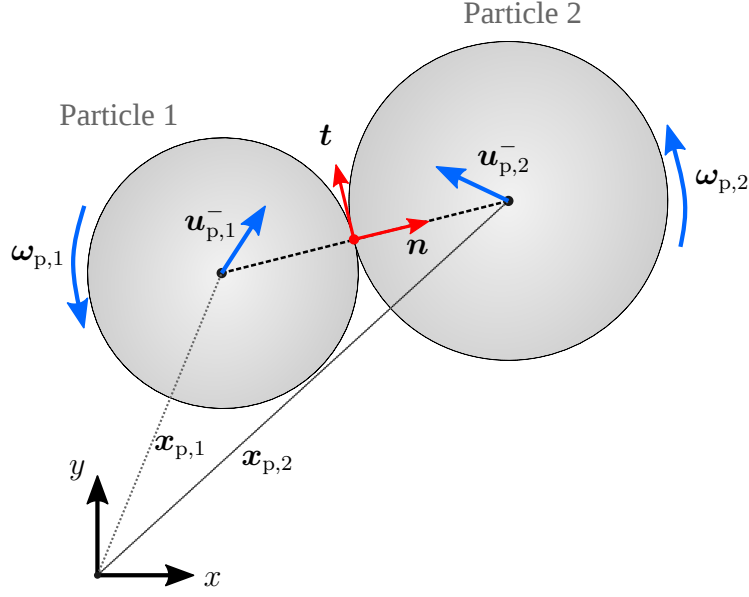


Fig. 4.3. Schematic representation of the response of a collision event. Note that the tangential vector \mathbf{t} depicted in the figure points towards one of many possible directions. The exact tangential direction is decided based on Eq. (4.39).

the centers of the collision partners and pointing towards particle 2. Mathematically, \mathbf{n} is expressed as:

$$\mathbf{n} = \frac{\mathbf{x}_{p,2} - \mathbf{x}_{p,1}}{|\mathbf{x}_{p,2} - \mathbf{x}_{p,1}|}, \quad (4.30)$$

where \mathbf{x}_p is the position vector of the particle in the given system of reference.

In Eq. (4.29) the vector $\hat{\mathbf{f}}^{\text{col}}$ denotes the total collision impulse, which can be decomposed into a normal component $\hat{\mathbf{f}}_n^{\text{col}}$ and a tangential component $\hat{\mathbf{f}}_t^{\text{col}}$ with respect to the contact plane:

$$\hat{\mathbf{f}}^{\text{col}} = \hat{\mathbf{f}}_n^{\text{col}} + \hat{\mathbf{f}}_t^{\text{col}}. \quad (4.31)$$

Note that the direction \mathbf{n} which is normal to the contact plane is uniquely defined by Eq. (4.30). However, the exact tangential direction \mathbf{t} depends on the tangential component of the relative collision velocity as will be given by Eq. (4.39).

The normal collision impulse $\hat{\mathbf{f}}_n^{\text{col}}$ can be expressed by the sum of a contribution which is attributed to the mechanical deformation $\hat{\mathbf{f}}_n^{\text{con}}$ and a second contribution representing the effect of the cohesive van-der-Waals force $\hat{\mathbf{f}}_n^{\text{vdW}}$:

$$\hat{\mathbf{f}}_n^{\text{col}} = \hat{\mathbf{f}}_n^{\text{con}} + \hat{\mathbf{f}}_n^{\text{vdW}}. \quad (4.32)$$

To derive an expression for the normal contact impulse $\hat{\mathbf{f}}_n^{\text{col}}$, the normal restitution coefficient is introduced $e_{n,p}$ and employed in a momentum balance leading to (Crowe et al., 1998):

$$\hat{\mathbf{f}}_n^{\text{con}} = -(1 + e_{n,p}) \left[(\mathbf{u}_{p,2}^- - \mathbf{u}_{p,1}^-) \cdot \mathbf{n} \right] \mathbf{n}. \quad (4.33)$$

Kosinski and Hoffmann (2010, 2011) proposed to express the cohesive impulse based on the van-der-Waals force model by Hamaker (1937):

$$F_n^{\text{vdW}} = \frac{H}{6 \delta_0^2} \hat{R}, \quad (4.34)$$

where H is the Hamaker constant and \hat{R} is the effective radius of the inter-particle contact (defined in Appendix A). The symbol δ_0 represents the minimum separation distance between the surfaces in contact and is attributed to the surface roughness. By integrating F_n^{vdW} over the entire collision time $\Delta \hat{t}_c$, the cohesive impulse can be expressed as follows (Kosinski and Hoffmann, 2010, 2011):

$$\hat{\mathbf{f}}_n^{\text{vdW}} = -\frac{1}{6} \left(\frac{9}{4}\right)^{1/5} \left\{ \frac{\hat{m}^{-3}}{\hat{E}_s^2 [(\mathbf{u}_{p,1}^- - \mathbf{u}_{p,2}^-) \cdot \mathbf{n}]} \right\}^{1/5} \frac{H}{\delta_0^2} \hat{R}^{4/5} \Delta \hat{t}_c \mathbf{n}, \quad (4.35)$$

where \hat{m} and \hat{E}_s are the effective mass and modulus of elasticity defined in Appendix A. Kosinski and Hoffmann (2010) determined the collision time $\Delta \hat{t}_c$ based on a relation for a fully elastic frictionless collision. In the work by Breuer and Almohammed (2015) the hard-sphere model was extended using knowledge acquired based on the soft-sphere interaction model. More specifically, the effect of the cohesive force on the dynamics of the collision was analyzed in detail. It was found that the cohesive force accelerates the relative motion of the particles in the direction normal to the collision during the compression phase (partners deforming each other). By contrast, the cohesion decelerates the bounce-off of the particles in the restitution phase (partners departing from each other). In addition, it was shown that in the realistic case of inelastic collisions (i.e., $e_{n,p} < 1$) the restitution phase takes a longer time than the compression phase. To correctly account for these observations in the hard-sphere model, Breuer and Almohammed (2015) argued that the cohesive impulse should not be evaluated over the entire collision time. Instead, a characteristic time scale $\Delta \hat{t}_c^*$ defining the difference between the time intervals of the two collision phases is introduced to model the cohesive impulse:

$$\hat{\mathbf{f}}_n^{\text{vdW}^*} = -\frac{1}{6} \left(\frac{9}{4}\right)^{1/5} \left\{ \frac{\hat{m}^{-3}}{\hat{E}_s^2 [(\mathbf{u}_{p,1}^- - \mathbf{u}_{p,2}^-) \cdot \mathbf{n}]} \right\}^{1/5} \frac{H}{\delta_0^2} \hat{R}^{4/5} \Delta \hat{t}_c^* \mathbf{n}. \quad (4.36)$$

To determine the time scales $\Delta \hat{t}_c$ and $\Delta \hat{t}_c^*$, Breuer and Almohammed (2015) numerically solved an ordinary differential equation, which relates the collision time to the deformation (overlap between particles) in a normalized form. Note that the original form of the equation was derived in the context of the soft-sphere collision model (Marshall, 2009). The solution of the equation provides the required collision time scales in a dimensionless form solely as functions of the particle properties, i.e., independent of specific collision circumstances such as the pre-collision velocities. Hence, these dimensionless time scales are computed only once by numerically solving the ordinary differential equation at the beginning of the simulation.

Furthermore, Breuer and Almohammed (2015) and Almohammed (2018) argued that the cohesive impulse enhances friction during the entire collision time. Hence, the standard tangential impulse model relying on Coulomb's law of friction was extended by taking the van-der-Waals impulse $\hat{\mathbf{f}}_n^{\text{vdW}}$ into account. This means that the normal collision impulse $\hat{\mathbf{f}}_n^{\text{col}}$ depends on the van-der-Waals impulse evaluated over the entire collision time $\Delta\hat{t}_c$, i.e., the compression and the restitution period. If the tangential impulse $\hat{\mathbf{f}}_t^{\text{col}}$ is smaller than the limit by Coulomb's law of static friction, a sticking collision is assumed. Otherwise, a sliding collision takes place. In the framework of the hard-sphere model, such conditions are expressed as follows (Breuer and Almohammed, 2015; Crowe et al., 1998):

$$\hat{\mathbf{f}}_t^{\text{col}} = \begin{cases} \hat{\mathbf{f}}_{\text{st,t}}^{\text{col}} = -\frac{2}{7} (1 + e_{t,p}) \mathbf{u}_{c,t,r}^- & \text{if } |\mathbf{u}_{c,t,r}^-| \leq \frac{7}{2} \frac{\mu_{\text{st,p}}}{(1 + e_{t,p})} \hat{f}_n^{\text{col}} \text{ (sticking),} \\ \hat{\mathbf{f}}_{\text{sl,t}}^{\text{col}} = -\mu_{\text{kin,p}} \hat{f}_n^{\text{col}} \frac{\mathbf{u}_{c,t,r}^-}{|\mathbf{u}_{c,t,r}^-|} & \text{otherwise (sliding).} \end{cases} \quad (4.37a)$$

Here, $\mu_{\text{st,p}}$ and $\mu_{\text{kin,p}}$ are the static and kinematic friction coefficients of the particles, respectively. In addition, $e_{t,p}$ denotes the tangential restitution coefficient and $\mathbf{u}_{c,t,r}^-$ is the tangential velocity of the pre-collision relative motion at the contact point given by:

$$\mathbf{u}_{c,t,r}^- = (\mathbf{u}_{p,2}^- - \mathbf{u}_{p,1}^-) - [(\mathbf{u}_{p,2}^- - \mathbf{u}_{p,1}^-) \cdot \mathbf{n}] \mathbf{n} - \left(\frac{d_{p,1}}{2} \boldsymbol{\omega}_{p,1}^- + \frac{d_{p,2}}{2} \boldsymbol{\omega}_{p,2}^- \right) \times \mathbf{n}. \quad (4.38)$$

Based on this tangential relative motion, the exact tangential vector of the collision event can be defined:

$$\mathbf{t} = \frac{\mathbf{u}_{c,t,r}^-}{|\mathbf{u}_{c,t,r}^-|}. \quad (4.39)$$

To evaluate the possibility of agglomeration, Kosinski and Hoffmann (2010) proposed two conditions. In general, agglomeration takes place if each of the impulses $\hat{\mathbf{f}}_n^{\text{vdW}^*}$ and $\hat{\mathbf{f}}_t^{\text{col}}$ exceed certain thresholds (Kosinski and Hoffmann, 2010):

$$\hat{\mathbf{f}}_n^{\text{vdW}^*} \cdot \mathbf{n} > -e_{n,p} [(\mathbf{u}_{p,2}^- - \mathbf{u}_{p,1}^-) \cdot \mathbf{n}], \quad (4.40)$$

$$|\hat{\mathbf{f}}_t^{\text{col}} \cdot \mathbf{t}| > |(\mathbf{u}_{p,2}^- - \mathbf{u}_{p,1}^-) \cdot \mathbf{t}|. \quad (4.41)$$

In the case of a sticking collision the second condition (4.41) is always satisfied owing to the vanishing relative velocity of the two particles. This means that the second condition is only relevant for sliding collisions. Hence, applying the sliding tangential impulse given by Eq. (4.37b) in the second agglomeration condition (4.41) leads to:

$$|\mu_{\text{kin,p}} (\hat{\mathbf{f}}_n^{\text{con}} + \hat{\mathbf{f}}_n^{\text{vdW}}) \cdot \mathbf{n}| > |(\mathbf{u}_{p,2}^- - \mathbf{u}_{p,1}^-) \cdot \mathbf{t}|. \quad (4.42)$$

If agglomeration occurs, the two collision partners are replaced by a single agglomerate, which is represented by an equivalent sphere according to the closely-packed sphere model (Almohammed, 2018; Breuer and Almohammed, 2015). The diameter of this new sphere is calculated by applying the mass conservation, which takes the packing fraction $f_{\text{pack}}(N_{\text{pp}}^{\text{tot}})$

into account. Note that the packing fraction is the complement of the porosity, i.e., $f_{\text{pack}} = 1 - \epsilon$ and is explained in detail in Chapter 5. The packing fraction of the new sphere is obtained from a look-up table based on the total number of particles in both agglomeration partners. Hence, the diameter of the equivalent sphere for the newly formed agglomerate reads (Almohammed, 2018; Breuer and Almohammed, 2015):

$$d_{\text{ag}} = \left(\frac{d_{\text{pp},1}^3 f_{\text{pack}}(N_{\text{pp},1}^{\text{tot}}) + d_{\text{pp},2}^3 f_{\text{pack}}(N_{\text{pp},2}^{\text{tot}})}{f_{\text{pack}}(N_{\text{pp},1}^{\text{tot}} + N_{\text{pp},2}^{\text{tot}})} \right)^{1/3}, \quad (4.43)$$

where N_{pp}^{tot} stands for the number of primary particles in the agglomeration partners, which can be primary particles or agglomerates. Note that the model (4.43) is only valid for collision partners comprising monodisperse primary particles. A broader discussion and more details on this model are given in Chapter 5.

Beside the diameter, a full description of the kinematics of the agglomerate is required. For this aim, the position of the center of mass of the resulting agglomerate is computed as follows:

$$\mathbf{x}_{\text{ag}}^+ = \frac{m_{\text{p},1} \mathbf{x}_{\text{p},1}^- + m_{\text{p},2} \mathbf{x}_{\text{p},2}^-}{m_{\text{p},1} + m_{\text{p},2}}. \quad (4.44)$$

In addition, the translational and angular velocities of the agglomerate are given by:

$$\mathbf{u}_{\text{ag}}^+ = \frac{m_{\text{p},1} \mathbf{u}_{\text{p},1}^- + m_{\text{p},2} \mathbf{u}_{\text{p},2}^-}{m_{\text{p},1} + m_{\text{p},2}}, \quad (4.45)$$

$$\boldsymbol{\omega}_{\text{ag}}^+ = \frac{\mathbf{L}_{\text{ag}}}{I_{\text{ag}}}. \quad (4.46)$$

Here, \mathbf{L}_{ag} and I_{ag} are the angular momentum and the moment of inertia of the agglomerate. The former is calculated based on the pre-collision velocity of the agglomeration partners:

$$\mathbf{L}_{\text{ag}} = I_{\text{p},1} \boldsymbol{\omega}_{\text{p},1}^- + I_{\text{p},2} \boldsymbol{\omega}_{\text{p},2}^- + \frac{\hat{m}}{2} (d_{\text{p},1} + d_{\text{p},2}) \mathbf{n} \times (\mathbf{u}_{\text{p},2}^- - \mathbf{u}_{\text{p},1}^-), \quad (4.47)$$

and the moment inertia of the agglomerate (i.e., sphere) is obtained by:

$$I_{\text{ag}} = \frac{1}{10} m_{\text{ag}} d_{\text{ag}}^2 = \frac{\pi}{60} \rho_{\text{ag}} d_{\text{ag}}^5. \quad (4.48)$$

For the derivation of these relations, refer to Breuer and Almohammed (2015) and Almohammed (2018). If the conditions for agglomeration are not fulfilled, then the collision

partners bounce off. In the case of a sticking collision, the post-collision velocities of the partners are given by:

$$\mathbf{u}_{p,1}^+ = \mathbf{u}_{p,1}^- - \frac{\hat{m}}{m_{p,1}} \left\{ \left(\hat{f}_n^{\text{con}} + \hat{f}_n^{\text{vdW}^*} \right) \mathbf{n} - \frac{2}{7} (1 + e_{t,p}) |\mathbf{u}_{c,t,r}^-| \mathbf{t} \right\}, \quad (4.49a)$$

$$\mathbf{u}_{p,2}^+ = \mathbf{u}_{p,2}^- + \frac{\hat{m}}{m_{p,2}} \left\{ \left(\hat{f}_n^{\text{con}} + \hat{f}_n^{\text{vdW}^*} \right) \mathbf{n} - \frac{2}{7} (1 + e_{t,p}) |\mathbf{u}_{c,t,r}^-| \mathbf{t} \right\}, \quad (4.49b)$$

$$\boldsymbol{\omega}_{p,1}^+ = \boldsymbol{\omega}_{p,1}^- + \frac{\hat{m}}{m_{p,1}} \left\{ \frac{10}{7d_{p,1}} (1 + e_{t,p}) |\mathbf{u}_{c,t,r}^-| (\mathbf{n} \times \mathbf{t}) \right\}, \quad (4.49c)$$

$$\boldsymbol{\omega}_{p,2}^+ = \boldsymbol{\omega}_{p,2}^- + \frac{\hat{m}}{m_{p,2}} \left\{ \frac{10}{7d_{p,2}} (1 + e_{t,p}) |\mathbf{u}_{c,t,r}^-| (\mathbf{n} \times \mathbf{t}) \right\}. \quad (4.49d)$$

For a sliding collision, the velocities read:

$$\mathbf{u}_{p,1}^+ = \mathbf{u}_{p,1}^- - \frac{\hat{m}}{m_{p,1}} \left\{ \left(\hat{f}_n^{\text{con}} + \hat{f}_n^{\text{vdW}^*} \right) \mathbf{n} - \mu_{\text{kin},p} \left(\hat{f}_n^{\text{con}} + \hat{f}_n^{\text{vdW}} \right) \mathbf{t} \right\}, \quad (4.50a)$$

$$\mathbf{u}_{p,2}^+ = \mathbf{u}_{p,2}^- + \frac{\hat{m}}{m_{p,2}} \left\{ \left(\hat{f}_n^{\text{con}} + \hat{f}_n^{\text{vdW}^*} \right) \mathbf{n} - \mu_{\text{kin},p} \left(\hat{f}_n^{\text{con}} + \hat{f}_n^{\text{vdW}} \right) \mathbf{t} \right\}, \quad (4.50b)$$

$$\boldsymbol{\omega}_{p,1}^+ = \boldsymbol{\omega}_{p,1}^- + \frac{\hat{m}}{m_{p,1}} \left\{ \frac{5}{d_{p,1}} \mu_{\text{kin},p} \left(\hat{f}_n^{\text{con}} + \hat{f}_n^{\text{vdW}} \right) (\mathbf{n} \times \mathbf{t}) \right\}, \quad (4.50c)$$

$$\boldsymbol{\omega}_{p,2}^+ = \boldsymbol{\omega}_{p,2}^- + \frac{\hat{m}}{m_{p,2}} \left\{ \frac{5}{d_{p,2}} \mu_{\text{kin},p} \left(\hat{f}_n^{\text{con}} + \hat{f}_n^{\text{vdW}} \right) (\mathbf{n} \times \mathbf{t}) \right\}. \quad (4.50d)$$

It is important to mention that agglomeration is disregarded in some of the simulations which are reported in the present work. The background and the motivation are given in the corresponding result sections in Chapter 9. To neglect agglomeration in the extended hard-sphere collision model, the cohesive van-der-Waals impulse is set to zero:

$$\hat{\mathbf{f}}_n^{\text{vdW}} = \hat{\mathbf{f}}_n^{\text{vdW}^*} = 0. \quad (4.51)$$

Subsequently, the expressions presented above are reduced leading to the standard (non-cohesive) hard-sphere model by Crowe et al. (1998).

4.4 Interaction with Domain Boundaries

When particles arrive at domain boundaries, certain actions need to be undertaken. In the present work, three types of boundary conditions are relevant for particles: (1) the outlet boundary, (2) the periodic boundary, and (3) the wall boundary.

In the case of a periodic boundary, particles are transferred to the corresponding boundary by adjusting their positions while keeping all other properties unchanged. If particles cross an outlet boundary, they are assumed to leave the domain and hence they are deleted.

When a particle hits a wall, the hard-sphere procedure is applied. The formulation in case of a particle-wall collision is similar to that of inter-particle collisions described in Section 4.3. The main differences relate to the following matters. First, the collisions parameters, i.e., the static $\mu_{\text{st,w}}$ and kinematic $\mu_{\text{kin,w}}$ friction coefficients and the normal $e_{\text{n,w}}$ and tangential $e_{\text{t,w}}$ restitution coefficients of the particle-wall collision are set according to the pairing of the materials. Second, the effective radius \hat{R} , mass \hat{m} , and modulus of elasticity E_s of the particle-wall collision are determined differently as explained in Appendix A. In fact, the wall-deposition phenomenon is not considered in any of the present simulations (justifications are provided in Chapter 9). Hence, the post wall-collision kinetics of the particles are given by the standard hard-sphere model (Breuer and Almohammed, 2015; Crowe et al., 1998). Furthermore, if breakage is detected according to the wall-impact breakage model proposed in the present thesis, the post-breakage velocities of the fragments are defined by the breakage model as explained in Chapter 7. For these reasons, a detailed discussion on the hard-sphere model for wall impact is omitted here.

5 Model for the Structural Features of Agglomerates

As mentioned earlier, in the present Euler–Lagrange simulation methodology the multi-particle morphology of agglomerates is idealized by a single spherical particle. Recalling the discussion in the literature review in Section 2.1, the accuracy of the Lagrangian tracking of such agglomerates depends on the approach used for determining the corresponding diameter of the effective sphere representing the agglomerate. Besides the tracking issue, some parameters characterizing the arrangement of the constituting particles must be provided to allow a reasonable forecasting of the breakage of agglomerates. This chapter explains what are the required structural features (also commonly denoted morphological descriptors) of agglomerates in the present modeling strategy. In addition, the approach used for describing these features is presented in detail. Note that the model presented in this chapter was first introduced in Breuer and Khalifa (2019a) and later used in other publications related to the present thesis (Breuer and Khalifa, 2019b; Khalifa and Breuer, 2021; Khalifa et al., 2022; Khalifa et al., 2021).

5.1 Definitions and Overview on the Modeling Strategy

Agglomerates can arise in the Euler–Lagrange simulations in three different ways: The direct injection into the domain, the agglomeration of particles, and the disintegration of larger agglomerates. In any case, the diameter of the effective particle representing the agglomerate is determined applying a mass balance:

$$\rho_{\text{ag}} V_{\text{ag}} = \sum_{i=1}^{N_{\text{pp}}^{\text{tot}}} \rho_{\text{pp}} V_{\text{pp}}, \quad (5.1)$$

where ρ_{ag} and V_{ag} are the density and the volume of the agglomerate. Assuming the effective particle replacing the structure of an agglomerate to be spherical, the volume of the agglomerate relates to the volume of a sphere, i.e., $V_{\text{ag}} = \pi/6 d_{\text{ag}}^3$. In addition, restricting the scope of the modeling to monodisperse primary particles, the summation over the number of primary particles comprising the agglomerate $N_{\text{pp}}^{\text{tot}}$ in Eq. (5.1) can be replaced by a multiplication with $N_{\text{pp}}^{\text{tot}}$. Introducing these definitions in Eq. (5.1) leads to:

$$\rho_{\text{ag}} \frac{\pi}{6} d_{\text{ag}}^3 = N_{\text{pp}}^{\text{tot}} \rho_{\text{pp}} \frac{\pi}{6} d_{\text{pp}}^3, \quad (5.2)$$

where ρ_{pp} and d_{pp} are the density and the diameter of the primary particle. Hence, the mass-equivalent diameter of the agglomerate reads:

$$d_{\text{ag}} = \left(N_{\text{pp}}^{\text{tot}} \frac{\rho_{\text{pp}}}{\rho_{\text{ag}}} \right)^{1/3} d_{\text{pp}}. \quad (5.3)$$

Applying the conservation of mass again, the ratio of the densities $\rho_{\text{pp}}/\rho_{\text{ag}}$ can be substituted by the inverse ratio of the volume of the primary particles $N_{\text{pp}}^{\text{tot}} V_{\text{pp}}$ within the agglomerate to the total volume occupied by the agglomerate V_{ag} :

$$d_{\text{ag}} = \left(N_{\text{pp}}^{\text{tot}} \frac{V_{\text{ag}}}{N_{\text{pp}}^{\text{tot}} V_{\text{pp}}} \right)^{1/3} d_{\text{pp}}. \quad (5.4)$$

A traditionally applied approach in the literature (e.g., Ho and Sommerfeld, 2002) suggests to set the ratio of volumes to unity, i.e., $V_{\text{ag}}/(N_{\text{pp}}^{\text{tot}} V_{\text{pp}}) = 1$. The obtained diameter of the agglomerate under this assumption is denoted the volume-equivalent diameter, which ignores the porous nature of agglomerates. To circumvent this limitation, the closely-packed sphere model proposed by Breuer and Almohammed (2015) is followed. The model builds on the fact that the ratio of the volumes in Eq. (5.4) is the reciprocal of a well-known quantity denoted the packing fraction f_{pack} :

$$f_{\text{pack}} = \frac{N_{\text{pp}}^{\text{tot}} V_{\text{pp}}}{V_{\text{ag}}}, \quad (5.5)$$

which is often referred to as the packing density and describes the fraction of the volume of the agglomerate occupied by its primary particles. In other words, as mentioned earlier the packing fraction is the complement of the porosity, i.e., $f_{\text{pack}} = 1 - \epsilon$. Introducing the definitions of the packing fraction into Eq. (5.4) yields:

$$d_{\text{ag}} = \left(\frac{N_{\text{pp}}^{\text{tot}}}{f_{\text{pack}}} \right)^{1/3} d_{\text{pp}}. \quad (5.6)$$

Hence, the packing fraction accounts for the realistic structure by means of the effective diameter of agglomerates. In comparison to the traditional volume-equivalent diameter, this approach allows a more accurate Lagrangian tracking of agglomerates by a proper description of the packing fraction (Dietzel et al., 2016; Dietzel and Sommerfeld, 2013). The method applied to determine the packing fraction is given in the next section.

Aside from the Lagrangian tracking issue, certain structural features are important for characterizing the stability of agglomerates against breakage. Different well-known theories (e.g., Kendall, 1988; Rumpf, 1962) relate the strength of agglomerates to the packing fraction and the average coordination number k_c besides some of the properties of the primary particles. Thus, the average coordination number is the second structural

feature of interest for the present work. It is defined as the average number of inter-particle contacts per primary particle within the agglomerate:

$$k_c = \frac{1}{N_{pp}^{\text{tot}}} \sum_{i=1}^{N_{pp}^{\text{tot}}} N_{c,i} , \quad (5.7)$$

where $N_{c,i}$ is the number of connections involving the particle i . Note that in the present thesis, an inter-particle contact is identified if the separation between the surfaces of two particles does not exceed the threshold of $l_{\text{max}} = 5 \cdot 10^{-2} d_{pp}$. A unique criterion for identifying a contact does not exist in the literature. This is partly due to the fact that a certain surface gap might persist depending on the roughness of the contacting surfaces. In addition, particles may interact through the van-der-Waals force even while being physically separated. According to the particle size range and the material properties (see Table 9.2) the van-der-Waals force can be readily shown to drop several orders of magnitudes over an inter-particle gap of $5 \cdot 10^{-2} d_{pp}$ justifying the chosen value.

In the absence of the detailed structure of agglomerates during the Euler–Lagrange simulations, models have to be employed in order to obtain values for the packing fraction f_{pack} and the coordination number k_c . Several experimental and numerical studies (see, e.g., Deng et al., 2016; German, 1989; Gray, 1968; Suzuki and Oshima, 1989; Yang et al., 2008, and the references therein) have proposed models describing the dependence of the two aforementioned features on the parameters controlling the agglomeration process. These parameters include among others, the primary particle size and shape, the binding mechanism between particles and the kind of the external forces applied to generate the packing. Furthermore, correlations between the packing fraction and the coordination number were proposed considering a variety of packing conditions. However, the available models are limited to the case of agglomerates comprising a very large number of primary particles ranging from several hundred to several thousand particles. Hence, they mostly do not provide useful information about the development of the packing features as a function of the size of the agglomerate.

Since agglomerates of arbitrary sizes ranging from two to a couple of hundred primary particles are important for the present simulations, a different strategy is followed here to determine the required structural features. Assuming that all agglomerates arising in the simulations are compact and possess a (nearly) spherical shape, the packing fraction and coordination number are provided by look-up tables based on the number of primary particles comprising the agglomerate N_{pp}^{tot} . The look-up tables are generated prior to the simulations by a multi-step procedure, which involves analyzing the structure of almost spherical agglomerates. These model agglomerates are extracted from a large packing of particles produced by a Monte-Carlo simulation. Since physical forces are not taken into account in the stochastic packing process, the packing fraction and coordination number of the resulting agglomerates are rescaled in a subsequent step to address the effect of the inter-particle cohesion on the structure. The details of the procedure are explained in the following sections.

5.2 Generation of Agglomerates

In the first step, a Monte-Carlo simulation is carried out for filling $2 \cdot 10^5$ mono-sized spheres each of a dimensionless diameter $d_{pp} = 1$ into a box with a quadratic cross-section of $50 d_{pp} \times 50 d_{pp}$ applying periodic boundary conditions (code McPack by Zeiser (2008)). As depicted in Fig. 5.1, the filling level reaches about $72 d_{pp}$. A huge number of iterations is carried out until the solution is converged. To evaluate the state of the resulting packing, the packing fraction and coordination number of the entire Monte Carlo cluster are evaluated. The former is found to be $f_{\text{pack}}^{\text{MC}} = 0.55$, which is computed based on Eq. (5.5) considering V_{ag} to be equal to the volume of the smallest box that encloses all particles. Furthermore, the coordination number of the packing is computed according to Eq. (5.7). For this purpose, the gap between the surfaces of any two particles is compared with the critical surface separation mentioned above (i.e., $l_{\text{max}} = 5 \cdot 10^{-2} d_{pp}$). If the critical separation l_{max} is not surpassed, the two particles are assumed to be in contact and the corresponding number of contacts for each of the two particles $N_{c,i}$ is increased by one. The resulting mean coordination number is $k_c^{\text{MC}} = 6.2$. The obtained packing fraction and coordination number lay in the upper range of properties for a typical random loose packing, which often intersects with the lower range of properties of the random close packing (Dong et al., 2006; German, 1989; Nolan and Kavanagh, 1992; Scott, 1962).

In the second step, agglomerates with increasing numbers of particles are gradually collected starting from a reference particle located near the center of the packing. The first agglomerate (i.e., a two-particle agglomerate) is formed by adding the particle which center is closest to the center of the reference particle. The collection of particles proceeds progressively by successively adding the closest particle to the center of mass of the present configuration to obtain the next agglomerate. At the end of the process, a continuous series of agglomerates comprising up to 1000 primary particles is generated and the position of each particle in every agglomerate is known. Examples for agglomerates consisting of $N_{\text{pp}}^{\text{tot}} = 5, 10, 30, 50$ and 1000 primary particles and generated by the procedure described are depicted in Fig. 5.2.

These artificially generated agglomerates are analyzed in terms of the packing fraction and the average coordination number. Here, the packing fraction is determined considering the volume of the agglomerate V_{ag} to be equal to the volume of the convex hull enveloping the primary particles as depicted in Fig. 5.2. The algorithm used to compute the volume of the convex hull is provided by Matlab[®] (function: `convhull`). The method of the convex hull for representing the volume of the agglomerate is a commonly used approach to determine the packing fraction of agglomerates (see, e.g., Dadkhah et al., 2012; Ernst et al., 2013).

Furthermore, adopting the approach of the convex hull for determining the packing fraction means that the resulting diameter of the agglomerate (see Eq. (5.6)) to be used in the Lagrangian tracking is compatible with the recommendations of Dietzel and Sommerfeld (2013) and Dietzel et al. (2016). Based on fully-resolved simulations they found that a sphere can be adequately used to represent the motion of an agglomerate provided that the diameter of the sphere is equal to that of a characteristic circle. This circle possesses a surface area equal to the projected surface of the convex hull enveloping

the original agglomerate perpendicular to the flow direction (see Section 2.1.2). Of course, it is not possible in the present work to compute the projected area of the convex hull, since the structure of agglomerates is not available in the Euler–Lagrange simulations. However, based on the assumed nearly-spherical shape of the agglomerates, the projected area of the agglomerates is mostly independent on the orientation of the agglomerate in the flow field. Hence, the diameter based on the projected surface of the convex hull in this case does not strongly differ from the diameter based on the volume of the convex hull considered in the present work.

The resulting packing fraction and coordination number of the extracted agglomerates are depicted as a function of the number of primary particles in Fig. 5.3 as black curves. Obviously, the properties of the agglomerates vary to a certain extent in the lower range of the agglomerate size and finally level off as the number of included particles increases. The asymptotic values approach the properties of the initial packing of $2 \cdot 10^5$ particles.

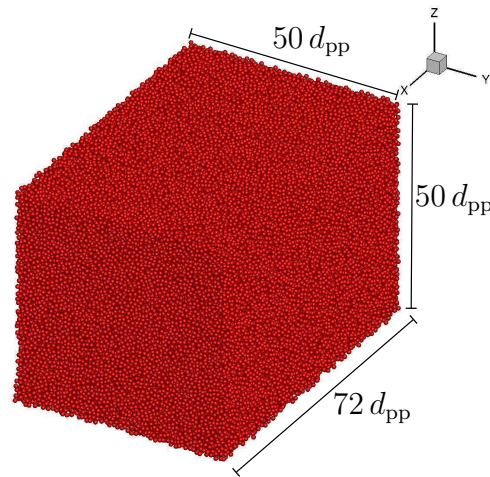


Fig. 5.1. Random loose packing of $2 \cdot 10^5$ particles within a box generated by a Monte Carlo simulation.

5.3 Scaling of the Structural Features of Agglomerates

A Monte-Carlo simulation is a numerical technique of stochastic nature, which does not require the calculation of the physical forces. However, in practice the characteristics of a packing of particles in the micrometer size range is known to be influenced by the interplay between two effects: The force bringing the particles together (e.g., gravity in vertical packing processes) and the inter-particle cohesive force (e.g., Yang et al., 2008; Yu et al., 2003). In particular, the role of the cohesive force is found to be important, since it hinders the further compression of particles upon reaching their first stable positions. In order to account for this physical circumstance, the results of the Monte-Carlo simulation are rescaled using the scaling formulas proposed by Yu et al. (2003) and Yang et al. (2008). Yu et al. (2003) performed an analysis on different experimental measurements available in the literature aiming at quantifying the relationship between the packing fraction and

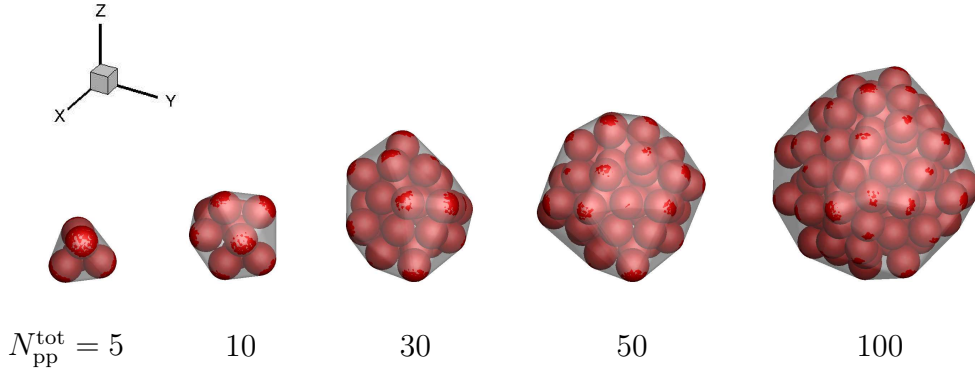


Fig. 5.2. Samples of the agglomerates artificially generated by a gradual accumulation of particles from the initial packing of $2 \cdot 10^5$ particles. The envelope containing the agglomerate is the corresponding convex hull used to represent the volume of the agglomerate V_{ag} .

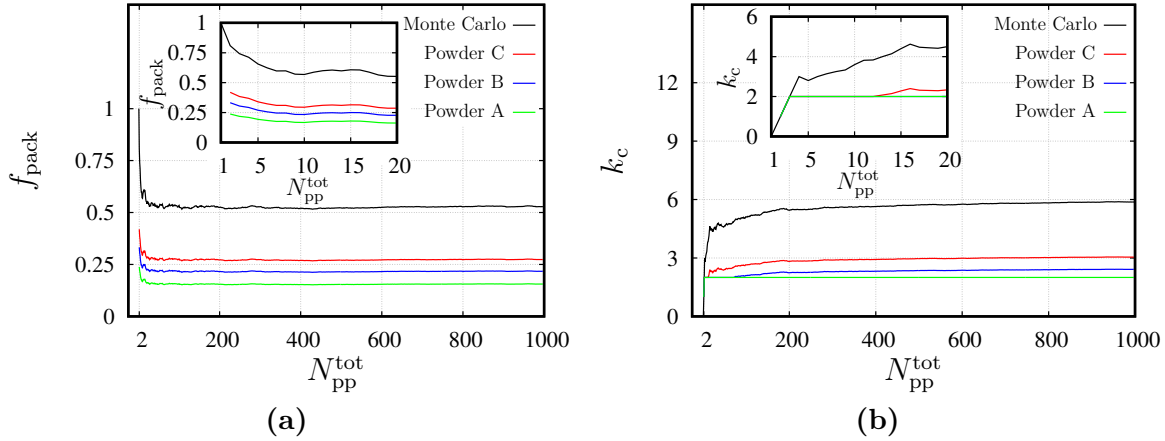


Fig. 5.3. Scaling the Monte Carlo results by Eq. (5.8) for (a) the packing fraction f_{pack} and (b) the average coordination number k_c . Here the properties of the powders defined in Table 9.2 are assumed.

the inter-particle forces for dry, monodisperse particles. They proposed the following correlation:

$$f_{\text{pack}} = f_{\text{pack},0} \left(1 - \exp(-m R_f^{-n}) \right), \quad (5.8)$$

where $f_{\text{pack},0}$ is the packing fraction in the limiting case of vanishing cohesion between particles. In addition, m and n are empirically determined parameters and R_f is the ratio between the magnitudes of the total inter-particle forces and the compression force. For dry, monodisperse particles falling in a column under the influence of gravity, R_f describes the ratio between the van-der-Waals force given in Eq. (4.34) and the gravitational force:

$$R_f = \frac{F^{\text{vdW}}}{m_{\text{pp}} g} = \frac{H}{4 \pi \delta_0^2 \rho_{\text{pp}} d_{\text{pp}}^2 g}. \quad (5.9)$$

The correlation (5.8) allows to mathematically predict the packing fraction under the influence of cohesion (i.e., non-negligible R_f) using the value of the case without cohesion $f_{\text{pack},0}$ as a reference.

Yang et al. (2008) carried out DEM simulations to generate a spherical packing by applying a centripetal force to drag particles randomly distributed in a spherical domain towards the center of the domain. While a range of the van-der-Waals force was considered, the magnitude of the centripetal force applied to each particle was fixed to the limit of the gravitational force. Hence, the ratio of forces R_f was varied over an interval spanning several orders of magnitude. The correlation (5.8) was found to be useful to represent the results. The fitting parameters in this spherical packing case were given as $m = 6.727$ and $n = 0.223$. Note that the packing fraction and coordination number of the agglomerate generated by DEM at the limit of a negligible cohesive force (i.e., $R_f \rightarrow 0$) are $f_{\text{pack},0} = 0.609$ and $k_{c,0} = 6$ (Yang et al., 2008). Such values roughly coincides with the aforementioned values of the initial Monte-Carlo packing (i.e., $f_{\text{pack}}^{\text{MC}} = 0.55$, $k_c^{\text{MC}} = 6.2$). This indicates that the present (stochastic) Monte-Carlo packing corresponds to a packing generated under physical conditions with weak inter-particle cohesion.

Consequently, the values of the packing fraction of the agglomerates extracted from the Monte-Carlo packing are adjusted by applying the correlation (5.8). In more detail, the packing fraction of an agglomerate containing a certain number of primary particles is determined by setting the packing fraction for the case without cohesion $f_{\text{pack},0}$ in Eq. (5.8) equal to that of the corresponding Monte-Carlo agglomerate and by applying the fitting parameters ($m = 6.727$ and $n = 0.223$) suggested by Yang et al. (2008) for the spherical packing case. The results of the rescaling of the packing fraction are depicted in Fig. 5.3(a) for the three different powders relevant for the present work. These are denoted powder **A** ($d_{\text{pp}} = 0.97 \mu\text{m}$), **B** ($d_{\text{pp}} = 2.47 \mu\text{m}$), and **C** ($d_{\text{pp}} = 5.08 \mu\text{m}$). Except the size of the primary particles, the three powders refer to silica particles of equal material properties listed in Table 9.2.

Moreover, owing to the lack of an analogous model specific for the coordination number k_c in the reference studies, the values of the coordination number k_c^{MC} of the agglomerates extracted from the initial Monte-Carlo packing are rescaled applying the same empirical relations and the same values m and n that are used for scaling the packing fraction. Fig. 5.3(b) depicts the scaled coordination number of the three aforementioned powders. Note that the minimal coordination number after rescaling is restricted to 2 for agglomerates consisting of three or more primary particles. This means that on average each primary particle is connected to at least two other particles. Such a restriction is imposed to ensure that the empirical scaling does not lead in extreme cases to the properties of chain-like agglomerates since compact sphere-like agglomerates are assumed in the present work.

5.4 Application of the Model in Euler–Lagrange Simulations

To summarize, the model for the structural features of the agglomerates applied in the Euler–Lagrange simulations is as follows: At the beginning of the simulation, the properties of the series of agglomerates resulting from the Monte-Carlo packing, i.e., $f_{\text{pack}}^{\text{MC}}(N_{\text{pp}}^{\text{tot}})$ and $k_{\text{c}}^{\text{MC}}(N_{\text{pp}}^{\text{tot}})$ are introduced as functions of the number of primary particles involved in the agglomerate. Subsequently, these properties are adjusted to take the effect of the cohesion between particles into account using the correlation (5.8) suggested by Yu et al. (2003) and applying the fitting parameters proposed by Yang et al. (2008):

$$f_{\text{pack}}(N_{\text{pp}}^{\text{tot}}) = f_{\text{pack}}^{\text{MC}}(N_{\text{pp}}^{\text{tot}}) \left(1 - \exp(-6.727 R_{\text{f}}^{-0.223}) \right), \quad (5.10)$$

$$k_{\text{c}}(N_{\text{pp}}^{\text{tot}}) = k_{\text{c}}^{\text{MC}}(N_{\text{pp}}^{\text{tot}}) \left(1 - \exp(-6.727 R_{\text{f}}^{-0.223}) \right). \quad (5.11)$$

The results of these scaling relationships differ depending on the properties of the primary particles, i.e., the ratio R_{f} of the cohesive to the gravitational force. Since in the present work solely a single powder (i.e., fixed properties and d_{pp}) is considered in a certain simulation, the rescaling is carried out once at the beginning of the simulation. The results are stored in look-up tables providing the packing fraction and the coordination number as functions of the number of primary particles within the agglomerate.

Overall, the packing fraction is used during the simulations to determine the diameter of the point-particle agglomerate (see Eq. (5.4)). In addition, both the packing fraction and the coordination number are used for evaluating the strength of the agglomerates (see Section 6.2).

The model discussed in this chapter is applicable for dry, monodisperse primary particles. In addition, the model assumes the structure of the agglomerates in the Euler–Lagrange simulations to be always compact and nearly spherical. In fact, for a certain number of primary particles of the same powder (i.e., equal $N_{\text{pp}}^{\text{tot}}$ and R_{f}), agglomerates possess the same structural properties regardless if these agglomerates appear as a result of the agglomeration of smaller fragments or due to the breakage of larger agglomerates.

6 Models for Breakup by Fluid Stresses

The cost-efficient modeling of the breakup of agglomerates attributed to the interactions with the surrounding fluid is a key objective of the present thesis. Building on the Euler–Lagrange simulation strategy explained in Chapters 3 and 4 and making use of the model for the structural features of agglomerates introduced in Chapter 5, approaches for modeling the fluid-induced breakup of agglomerates is discussed in detail in this chapter. Note that for convenience, the derivations presented in this chapter use the vector notation.

It is worth mentioning that the present modeling techniques were published in Breuer and Khalifa (2019a) and later improved in Breuer and Khalifa (2019b). In addition, the breakup model was applied in subsequent studies related to the present thesis (Khalifa and Breuer, 2021; Khalifa et al., 2022; Khalifa et al., 2021).

6.1 Overview on the Modeling Strategy

According to the literature review in Section 2.2, the deagglomeration of cohesive particles caused by the interactions with the surrounding fluid can be predicted based on a variety of methods. These methods are distinguished by the level of provided details and the computational expenses. As already pointed out, the present thesis aims at providing efficient solutions capable of modeling the agglomeration and breakup phenomena in highly-laden turbulent flows. To this end, the point-particle approximation is employed for modeling the fluid-particle interactions and the primary particles forming an agglomerate are represented by a single effective sphere. Within these efficiency-related considerations, a successful breakup model needs to reliably address three fundamental tasks: (i) the condition of breakage, (ii) the resulting fragment size distribution, and (iii) the velocities of the fragments after the disintegration.

To tackle the first two tasks, the stresses exerted by the fluid are continuously evaluated along the Lagrangian trajectories of agglomerates and compared with a critical threshold denoted the strength of the agglomerate. Referring to the literature review in Section 2.2.2.2, three kinds of stresses are accounted for: Turbulent stresses, drag (inertia) stresses, and rotary stresses. These stress mechanisms are described using first-principle models available in the literature, which rely on certain simplifying assumptions to allow analytical solutions. In particular, these models consider idealized flow conditions and treat agglomerates as homogeneous solid spheres. However, the theory behind these models is revisited and improvements are proposed where possible and expedient.

Furthermore, particular emphasis is put on the third modeling task, i.e., describing the velocities of the fragments arising due to the breakage. This issue has received little attention in the past despite its importance. Thus, in the present work special models

based on physical arguments and experimental observations are proposed to reasonably define the dynamics of the disintegrated fragments.

Lastly, a physically-motivated measure (i.e., breakup time lag) is applied to ensure that the prediction of breakage is independent of the typically small time-step size applied for LES.

6.2 Strength of Agglomerates

In the present study, the critical stress threshold beyond which an agglomerate breaks, is determined based on the well-known tensile strength model derived by Rumpf (1958, 1962). The model describes the tensile strength of an arbitrary plane within the agglomerate. The main assumption here is that all cross-sections within the agglomerate have identical packing fractions and identical average coordination numbers, which are equal to the average packing fraction f_{pack} and the average coordination number k_c of the entire agglomerate, respectively. To understand the considerations behind the model, the derivation by Rumpf (1958) is briefly discussed here.

The average number of mono-sized primary particles per unit area within a cross-section of the agglomerate is given by:

$$N_{\text{pp}}^{\text{avg}} = \frac{f_{\text{pack}}}{\frac{\pi}{4} d_{\text{pp}}^2}. \quad (6.1)$$

Accordingly, the average number of unique contacts per unit area reads:

$$N_{\text{uc}}^{\text{avg}} = N_{\text{pp}}^{\text{avg}} \frac{k_c}{2} = \frac{f_{\text{pack}}}{\frac{\pi}{4} d_{\text{pp}}^2} \frac{k_c}{2}, \quad (6.2)$$

where the average coordination number k_c is divided by 2 since each unique contact is shared by two particles. Assuming that the directions of the cohesive forces in the cross-section are isotropically distributed in space, Rumpf (1958) postulated that their projection in the tensile direction can be obtained by multiplying the magnitude of the cohesive force by the ratio between the cap surface area to the base surface area of a hemisphere, i.e., the factor 1/2. Consequently, the tensile strength in the case of dry particles for which cohesion is predominated by the van-der-Waals force can be expressed as:

$$S = \frac{1}{2} N_{\text{uc}}^{\text{avg}} F^{\text{vdW}} = k_c f_{\text{pack}} \frac{F^{\text{vdW}}}{\pi d_{\text{pp}}^2}. \quad (6.3)$$

Hence, the model relates the tensile strength S of an agglomerate to the van-der-Waals force defined in Eq. (4.34), the diameter of the primary particle d_{pp} , the average coordination number k_c , and the average volumetric packing fraction f_{pack} of the agglomerate, which is traditionally expressed in this model in terms of the porosity $\varepsilon = 1 - f_{\text{pack}}$.

Later, Cundall and Strack (1983) derived the same relationship following a different approach. They showed that the average stress tensor within an agglomerate comprising

isotropically packed particles of equal sizes can be obtained as (Cundall and Strack, 1983; Gröger et al., 2003; Yang et al., 2008):

$$\underline{\underline{\boldsymbol{\sigma}}}^{\text{avg}} = \frac{1}{V_{\text{ag}}} \sum_{p=1}^{N_{\text{pp}}^{\text{tot}}} \frac{d_{\text{pp}}}{2} \left(\sum_{c=1}^{k_c} \mathbf{n} \cdot \mathbf{F}_{\text{p-p}} \right), \quad (6.4)$$

where each particle within the agglomerate is assumed to possess the average number of contacts per particle inside the entire agglomerate, i.e., the coordination number k_c . In addition, \mathbf{n} is the normal unit vector connecting the center of the particle p and one of its contacting particles and $\mathbf{F}_{\text{p-p}}$ is their interaction force, which is assumed to be solely given by the cohesive van-der-Waals force \mathbf{F}^{vdW} . The latter acts solely in the contact normal direction, which means $\mathbf{F}^{\text{vdW}} \cdot \mathbf{n} = F^{\text{vdW}}$. As suggested by the continuum mechanics, the average tensile stress is equal to the average of the normal components of the stress tensor (Cundall and Strack, 1983; Gröger et al., 2003; Yang et al., 2008):

$$S = \frac{1}{3} \text{Tr}(\underline{\underline{\boldsymbol{\sigma}}}^{\text{avg}}) = k_c f_{\text{pack}} \frac{F^{\text{vdW}}}{\pi d_{\text{pp}}^2}, \quad (6.5)$$

where Tr denotes the trace of the tensor. The resulting relationship is identical to Eq. (6.3) derived by Rumpf (1958).

Overall, the above described strength model is simple, comprises accessible quantities, and stems from a clear theoretical analysis. Furthermore, it is argued that the model by Rumpf (1958) can be generally applied for characterizing the strength at the contact points of the particles independent of the nature of the acting stresses (tensile, compressive or shear) (Tsubaki and Jimbo, 1984). However, the model assumes large numbers of isotropically packed mono-sized particles. Namely, it considers that the average packing fraction and the average coordination number are generally applicable within the entire volume of the agglomerate, which might not be valid for agglomerates consisting of small numbers of particles.

6.3 Stress Mechanisms and Conditions for Breakup

In this section, models for determining the fluid stresses by turbulence, drag and rotation are introduced (see Fig. 6.1). In addition, breakup criteria are proposed taking the nature of the stress mechanism and the tensile strength into account. Note that since the stresses of the different physical mechanisms (turbulent, drag, and rotary) might act in different directions, an ordinary summation of their magnitudes can lead to physically incorrect results. Hence, the suggestion by Kusters (1991) is followed and solely the maximum of these stresses (i.e., the dominating stress) is considered for assessing the possibility of breakup.

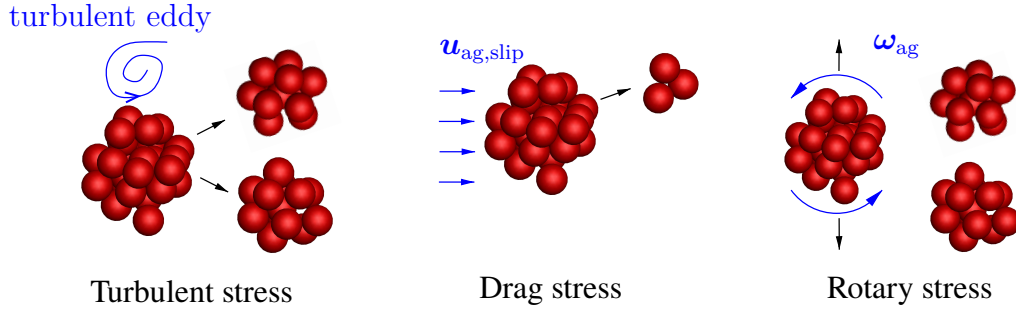


Fig. 6.1. Fluid-induced breakup mechanisms considered in the present work. Here, $\mathbf{u}_{\text{ag,slip}}$ is the relative velocity vector between the fluid and the agglomerate and $\boldsymbol{\omega}_{\text{ag}}$ is the angular velocity vector of the agglomerate.

6.3.1 Turbulent Stress

Turbulent stresses are the result of velocity fluctuations within a turbulent flow. Different velocity fluctuations on opposite sides of an agglomerate induce pressure differences and velocity gradients that may lead to the deformation or even rupture of the agglomerate (Thomas, 1964). The nature of the velocity fluctuations and the kind of the resulting stress depends on the size of the eddies effectively interacting with the agglomerate. In general, it is assumed that the strongest interaction takes place for eddies possessing sizes comparable to the diameter of the agglomerate d_{ag} .

To allow a simple description of the velocity fluctuations over the size of the agglomerate, (locally) isotropic turbulence is assumed. Accordingly, four different eddy-size subranges are distinguished in Table 6.1 based on the ratio of the agglomerate size d_{ag} to the Kolmogorov length scale η (Kusters, 1991; Lu et al., 1998; Neeße et al., 1987): **1.** viscous, **2.** transition (laminar preferred), **3.** transition (turbulent preferred), **4.** inertial. Consequently, the turbulent stress can be evaluated taking the relevant size range into account:

$$\sigma_{\text{turb}} = \mu_{\text{f}} \frac{\Delta v(d_{\text{ag}})}{d_{\text{ag}}} \quad \text{Viscous subrange,} \quad (6.6)$$

$$\sigma_{\text{turb}} = \rho_{\text{f}} \Delta u^2(d_{\text{ag}}) \quad \text{Transition and inertial subranges.} \quad (6.7)$$

Here, μ_{f} and ρ_{f} denote the dynamic viscosity and the density of the fluid, whereas $\Delta u(d_{\text{ag}})$ and $\Delta v(d_{\text{ag}})$ describe the corresponding root-mean-square fluctuating velocity differences in longitudinal and lateral direction, respectively. In addition, it is noted that the Kolmogorov length scale $\eta = (\nu_{\text{f}}^3/\epsilon)^{1/4}$ is defined in this work by the kinematic viscosity of the fluid ν_{f} and the local dissipation rate ϵ . The latter is given by:

$$\epsilon = 2 \nu_{\text{f}} \underline{\underline{\mathbf{S}}} \underline{\underline{\mathbf{S}}}, \quad (6.8)$$

with $\underline{\underline{\mathbf{S}}}$ being the strain rate tensor based on the local instantaneous (filtered) velocities given in Eq. (3.3) in index notation.

Tab. 6.1. Eddy subranges with corresponding expressions for the root-mean-square velocity difference (Δu) and the resulting fluid dynamic stresses acting on agglomerates of comparable size (Lu et al., 1998; Neeße et al., 1987).

Subrange	Agglomerate size d_{ag}	$\Delta u(d_{\text{ag}})$	Stress σ_{turb}
Viscous	$d_{\text{ag}}/\eta < 3$	$(1/15)^{1/2} (\epsilon/\nu_f)^{1/2} d_{\text{ag}}$	$(2/15)^{1/2} \mu_f (\epsilon/\nu_f)^{1/2}$
Transition (laminar preferred)	$3 \leq d_{\text{ag}}/\eta < 7$	$(1/15)^{1/2} (\epsilon/\nu_f)^{1/2} d_{\text{ag}}$	$(1/15) \rho_f (\epsilon/\nu_f) d_{\text{ag}}^2$
Transition (turbulent preferred)	$7 \leq d_{\text{ag}}/\eta < 58$	$0.7 \epsilon^{3/8} \nu_f^{-1/8} d_{\text{ag}}^{1/2}$	$0.49 \rho_f (\epsilon^3/\nu_f)^{1/4} d_{\text{ag}}$
Inertial	$d_{\text{ag}}/\eta > 58$	$1.38 (\epsilon d_{\text{ag}})^{1/3}$	$1.9 \rho_f (\epsilon d_{\text{ag}})^{2/3}$

Relation (6.7) indicates that agglomerates exhibit turbulent stresses in the form of normal stresses (pressure) in the transitional and turbulent subranges. However, in the viscous subrange, it is assumed that the smallest viscous eddies exert shear stresses on agglomerates of comparable sizes, which is attributed to the fluctuating velocity difference of the flow across the agglomerate in lateral direction. Hence, in Eq. (6.6) the root-mean-square of the lateral fluctuating velocity $\Delta v(d_{\text{ag}})$ appears, which in isotropic turbulence can be related to the longitudinal component $\Delta u(d_{\text{ag}})$ of the same subrange by $\Delta v(d_{\text{ag}}) = \sqrt{2} \Delta u(d_{\text{ag}})$ (Kusters, 1991).

To compute the turbulent stress σ_{turb} using Eqs. (6.6) and (6.7), the root-mean-square of the velocity fluctuations corresponding to the size of the agglomerate is required. For isotropic turbulence, these velocity fluctuations are obtained applying simple relations derived in the literature, which are listed in Table 6.1. In general, the given relations are functions of the local dissipation rate ϵ , the kinematic viscosity ν_f of the fluid and the diameter d_{ag} of the agglomerate. The resulting expressions for the turbulent stresses σ_{turb} are additionally provided in Table 6.1.

In the present model, the breakup by the turbulent stress mechanism occurs when the turbulent stress σ_{turb} is the dominant stress (i.e., surpasses the drag and the rotary stress) and exceeds the strength S of the agglomerate. In this case, agglomerates are assumed to break in the middle into two (nearly) equal parts (i.e., symmetric binary breakup). In more detail, if the agglomerate consists of an odd number of primary particles, the two resulting fragments deviate by one primary particle. Since the number of primary particles in both fragments are known, the densities of each fragment can be determined relying on the packing fraction, i.e., $\rho_{\text{fr1}} = \rho_{\text{pp}} f_{\text{pack}}(N_{\text{pp}}^{\text{fr1}})$ and $\rho_{\text{fr2}} = \rho_{\text{pp}} f_{\text{pack}}(N_{\text{pp}}^{\text{fr2}})$. The corresponding diameters are then computed based on a mass balance analogous to Eq. (5.6):

$$\begin{aligned}
 d_{\text{fr1}} &= \left(\frac{N_{\text{pp}}^{\text{fr1}}}{f_{\text{pack}}(N_{\text{pp}}^{\text{fr1}})} \right)^{1/3} d_{\text{pp}}, \\
 d_{\text{fr2}} &= \left(\frac{N_{\text{pp}}^{\text{fr2}}}{f_{\text{pack}}(N_{\text{pp}}^{\text{fr2}})} \right)^{1/3} d_{\text{pp}}.
 \end{aligned} \tag{6.9}$$

Lastly, the dynamics of the resulting fragments is described in Section 6.4.1.

6.3.2 Drag Stress

The theory behind the drag-induced stresses adapted in this work is based on the analysis carried out by Bagster and Tomi (1974). Therein, the simplified case of a fixed agglomerate suddenly released in a steady flow with an uniform fluid velocity \mathbf{u}_f is taken into account. Neglecting the effect of all fluid forces except the drag, the equation of motion of the agglomerate reads:

$$m_{\text{ag}} \frac{d\mathbf{u}_{\text{ag}}}{dt} = \mathbf{F}_D, \quad (6.10)$$

where \mathbf{F}_D stands for the drag force. Eq. (6.10) states that the agglomerate will accelerate in the direction of the flow until it reaches the flow velocity. The aim of the analysis here is to examine the tensile stress evolving in planes within the agglomerate by evaluating the inertial and fluid forces acting on portions of the accelerating agglomerate. The base of the spherical cap (dashed line) in Fig. 6.2 represents a plane inside the agglomerate on which the stress is examined. The orientation of this plane with respect to the direction of the relative velocity is defined by the angle θ . The size of the plane is specified by the diameter of the agglomerate d_{ag} and the angle ψ . Thus, the curved surface area $A_{\text{s,cap}}$ of the cap, the area of the base $A_{\text{b,cap}}$ and the volume of the cap V_{cap} can be determined applying the following geometric relations:

$$A_{\text{s,cap}} = \frac{\pi}{2} d_{\text{ag}}^2 (1 - \cos \psi), \quad (6.11)$$

$$A_{\text{b,cap}} = \frac{\pi}{4} d_{\text{ag}}^2 (1 - \cos^2 \psi), \quad (6.12)$$

$$V_{\text{cap}} = \frac{\pi}{8} d_{\text{ag}}^3 \left[\frac{2}{3} + \frac{\cos^3 \psi}{3} - \cos \psi \right]. \quad (6.13)$$

Considering the simplified case of a creeping flow, the normal stress of the fluid on the surface of the agglomerate is given by:

$$\sigma_{\text{surf}} = \frac{3 \mu_f}{d_{\text{ag}}} |\mathbf{u}_f - \mathbf{u}_{\text{ag}}| \cos \theta, \quad (6.14)$$

where $|\mathbf{u}_f - \mathbf{u}_{\text{ag}}|$ is the magnitude of the relative velocity between the fluid and the agglomerate (i.e., the slip velocity $u_{\text{ag,slip}}$). Eq. (6.14) can be used to determine the normal fluid forces acting on the outer surface of the cap:

$$F_{\text{D,n}}^{\text{cap}} = \sigma_{\text{surf}} A_{\text{s,cap}} = \frac{3}{2} \pi \mu_f d_{\text{ag}} |\mathbf{u}_f - \mathbf{u}_{\text{ag}}| \cos \theta (1 - \cos \psi). \quad (6.15)$$

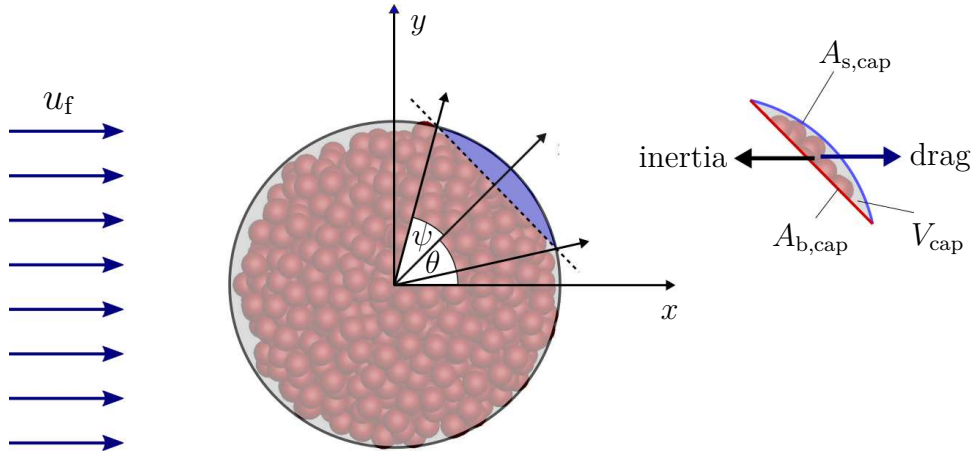


Fig. 6.2. Schematic sketch of an agglomerate in uniform flow. Erosion by drag stress (after Breuer and Khalifa, 2019a,b).

In addition, the inertial force of the cap in the base-normal direction is given by:

$$F_{I,n}^{\text{cap}} = \rho_{\text{ag}} V_{\text{cap}} \left| \frac{d\mathbf{u}_{\text{ag}}}{dt} \right| \cos \theta, \quad (6.16)$$

where the magnitude of the acceleration $|d\mathbf{u}_{\text{ag}}/dt|$ of the agglomerate can be analytically derived for the simple flow case presently considered, i.e., a rigid sphere accelerating in an uniform flow. The solution of the ordinary differential equation of motion of the agglomerate leads to the time-evolving velocity vector as a function of the steady fluid velocity (Sommerfeld et al., 2008) which reads:

$$\mathbf{u}_{\text{ag}} = \left(1 - \exp \left[-\frac{t}{\tau_{\text{ag}}} \right] \right) \mathbf{u}_f = f \mathbf{u}_f \quad \text{with} \quad \tau_{\text{ag}} = \frac{\rho_{\text{ag}} d_{\text{ag}}^2}{18 \mu_f}, \quad (6.17)$$

where f is the ratio of sphere-to-fluid velocity and τ_{ag} denotes the response time of the agglomerate. That allows to express the acceleration of the sphere as follows:

$$\frac{d\mathbf{u}_{\text{ag}}}{dt} = \mathbf{u}_f \dot{f} = \frac{1}{\tau_{\text{ag}}} (1 - f) \mathbf{u}_f. \quad (6.18)$$

Relying on the two aforementioned forces $F_{D,n}^{\text{cap}}$ and $F_{I,n}^{\text{cap}}$, the drag (tensile) stress acting on the base can be computed:

$$\sigma_{\text{drag}} = \frac{F_{D,n}^{\text{cap}} - F_{I,n}^{\text{cap}}}{A_{b,\text{cap}}}. \quad (6.19)$$

Inserting Eq. (6.18) into Eq. (6.16) and then Eqs. (6.15) and (6.16) into Eq. (6.19) leads to:

$$\sigma_{\text{drag}} = \frac{3 \mu_f}{d_{\text{ag}}} |\mathbf{u}_f - \mathbf{u}_{\text{ag}}| \cos \theta \cos \psi = \sigma_{\text{drag}}^{\text{max}} \cos \theta \cos \psi. \quad (6.20)$$

This solution postulates that the largest tensile stress is obtained at $\theta = 0^\circ$ and $\psi = 0^\circ$, i.e., on a negligibly small plane perpendicular to the direction of the relative velocity. Hence, applying $\theta = 0^\circ$ and $\psi = 0^\circ$ in Eq. (6.20) leads to the maximum drag stress $\sigma_{\text{drag}} = \sigma_{\text{drag}}^{\text{max}}$.

The validity of this model in turbulent flow conditions is discussed by Weiler (2008). Therein, it is argued that the time intervals over which the agglomerates maintain large relative velocities sufficient to induce breakup are small. Thus, the flow velocity can be assumed to be constant. Furthermore, Weiler et al. (2010) and Saha et al. (2015) applied the drag correction factor $\alpha = 1 + 0.15 \text{Re}_p^{0.687}$ (Schiller and Naumann, 1933) to extend the validity of expression (6.20) for the drag stress towards higher Re_p (see Section 4.2.1):

$$\sigma_{\text{drag}}^{\text{max}} = \frac{3 \mu_f}{d_{\text{ag}}} |\mathbf{u}_f - \mathbf{u}_{\text{ag}}| \alpha. \quad (6.21)$$

The drag stress model by Tomi and Bagster (1978) suffers from a shortcoming attributed to the simplifying assumption of $\psi = 0^\circ$ in Eq. (6.20). This assumption leads to the maximum magnitude of the stress and renders the model impractical in the context of breakup of agglomerates. The main reason is that such an assumption implies that the size of the spherical cap is infinitely small, and thus smaller than a single primary particle. In previous studies (Saha et al., 2015; Tomi and Bagster, 1978; Weiler et al., 2010) this issue was not further elaborated, i.e., the size of the affected portion of the agglomerate by the drag stress using Eq. (6.21) was not discussed.

In the current work, however, breakup by drag stresses is defined and handled as the split and detachment of primary particles. This requires that the computed stress should affect a single primary particle or more. Hence, in Eq. (6.20) the angle ψ must possess a finite value based on a reasonable argument in order to avoid the assumption of $\psi = 0^\circ$. This is especially important for agglomerates consisting of a small number of particles, since the angle of the cap covering one primary particle significantly deviates from 0° . For this reason, the drag stress model of Tomi and Bagster (1978) is extended in order to additionally predict the number of primary particles $n_{\text{p,break}}$ eligible for breakup.

The starting point is to retain the dependence of the stress on the cap angle ψ :

$$\sigma_{\text{drag}} = \sigma_{\text{drag}}^{\text{max}} \cos \psi. \quad (6.22)$$

The aim here is to derive a relation between the cap angle ψ and the number of primary particles $n_{\text{pp,cap}}$ enclosed in the cap. This can be achieved based on a mass balance:

$$N_{\text{pp}}^{\text{cap}} \rho_{\text{pp}} V_{\text{pp}} = \rho_{\text{ag}} V_{\text{cap}}, \quad (6.23)$$

where ρ_{pp} and V_{pp} denote the density and the volume of the primary particle, respectively. Inserting Eq. (6.23) into Eq. (6.13) yields:

$$N_{\text{pp}}^{\text{cap}} = \frac{f_{\text{pack}}}{4} \left(\frac{d_{\text{ag}}}{d_{\text{pp}}} \right)^3 [\cos^3 \psi - 3 \cos \psi + 2], \quad (6.24)$$

where the packing fraction f_{pack} represents $\rho_{\text{ag}}/\rho_{\text{pp}}$. The significance of Eq. (6.24) is that it relates the largest number of particles that can be eroded $N_{\text{pp}}^{\text{break}}$ under a given stress to a certain critical angle ψ_{cr} :

$$N_{\text{pp}}^{\text{break}} = \frac{f_{\text{pack}}}{4} \left(\frac{d_{\text{ag}}}{d_{\text{pp}}} \right)^3 \left[\cos^3 \psi_{\text{cr}} - 3 \cos \psi_{\text{cr}} + 2 \right]. \quad (6.25)$$

The critical angle ψ_{cr} describes the largest plane within the agglomerate on which the drag stress is greater than the strength, i.e., satisfies the breakup condition $\sigma_{\text{drag}} > S$. Therefore, the number of primary particles that can be eroded by the given stress is equal to the number of particles across this plane (i.e., inside the spherical cap). Applying these considerations in Eq. (6.22), the limiting value ψ_{cr} can be obtained:

$$\cos \psi_{\text{cr}} = \frac{S}{\sigma_{\text{drag}}^{\text{max}}}. \quad (6.26)$$

Provided that the drag stress is greater than the turbulent and the rotary stress, the breakup criterion takes the drag stress mechanism into account. In this case, two conditions need to be satisfied: The maximum drag stress must be greater than the strength of the agglomerate and the number of erodible particles under the given stress must be equal to or larger than unity:

$$\sigma_{\text{drag}}^{\text{max}} > S \quad \text{and} \quad N_{\text{pp}}^{\text{break}} \geq 1. \quad (6.27)$$

Note that the value of $N_{\text{pp}}^{\text{break}}$ resulting from Eq. (6.25) is a positive real number which is rounded to the next smaller integer. Upon fulfilling these conditions, agglomerates are split into two parts, one containing the number of erodible particles $N_{\text{pp}}^{\text{break}}$ and the other part comprises the remaining particles (i.e., an asymmetric binary breakup). Theoretically speaking, a breakup into two equal parts (i.e., symmetric binary breakup) by means of the drag stress is not possible. This is attributed to the fact that the drag force vanishes at the central cross-section of the spherical agglomerate. This condition corresponds to applying $\psi = 90^\circ$ in Eq. (6.22), which leads to a vanishing drag stress at the base of the cap representing the half of the agglomerate (i.e., a hemisphere). In general, it can be stated that for a given drag force, smaller cross-sections within the agglomerate encounter higher drag stresses. Thus, the erosion of a small number of particles is more likely to occur than the disintegration of fragments of comparable sizes.

Subsequent to the prediction of the number of primary particles in each fragment, the density and the diameter of each fragment can be determined relying on the mass conservation as explained by Eq. (6.9) for the turbulent stress mechanism. The motion of the resulting fragments is predicted based the model described in Section 6.4.2.

6.3.3 Rotary Stress

The third stress contribution originates from the rotation of agglomerates and is denoted rotary stress σ_{rotary} . Rumpf and Raasch (1962) proposed a formula to compute the stress

arising within an uniformly rotating sphere or cylinder, assuming a linear elastic behavior of the structure:

$$\sigma_{\text{rotary}} = A \rho_{\text{ag}} \omega_{\text{ag}}^2 r_{\text{ag}}^2 . \quad (6.28)$$

Here, ω_{ag}^2 is the angular velocity vector of the agglomerate, r_{ag} is the radius of the agglomerate and A is a constant with $A = A_{\text{sphere}} = 0.4$ for a sphere and $A = A_{\text{cylin}} = 0.41$ for a cylinder. The constants A were described to be solely valid for materials possessing a Poisson's ratio of $\nu_s = 0.3$ (Rumpf and Raasch, 1962). However, further details are lacking, since the derivation of the formula (6.28) is not provided in the reference.

In general, analytic solutions for the stresses in rotating cylinders or disks are well-established and frequently discussed in standard textbooks on the elasticity theory (e.g., Timoshenko and Goodier, 1970). Such stresses are of practical relevance for the application of rotating machinery. In addition, the simple geometry in the case of a cylinder and a disk allows to reduce the complexity of the stress problem to a plane (two-dimensional) stress, which encouraged adapting their cases in the literature. Accordingly, the solution in cylindrical coordinates for the normal stresses in a steadily rotating agglomerate of cylindrical structure reads:

$$\sigma_{\text{rr}} = \frac{3 + \nu_s}{8} \rho_{\text{ag}} \omega_{\text{ag}}^2 (r_{\text{ag}}^2 - r^2), \quad (6.29)$$

$$\sigma_{\theta\theta} = \frac{1}{8} \rho_{\text{ag}} \omega_{\text{ag}}^2 \left[(3 + \nu_s) r_{\text{ag}}^2 - (1 + 3\nu_s) r^2 \right] . \quad (6.30)$$

Based on Eqs. (6.29) and (6.30) it can be readily shown that the largest stress appears at the center of the agglomerate, i.e., at $r = 0$. In this case, the two stress components become identical:

$$\sigma_{\text{rotary}} = \underbrace{\frac{3 + \nu_s}{8}}_{A_{\text{cylin}}^*} \rho_{\text{ag}} \omega_{\text{ag}}^2 r_{\text{ag}}^2 , \quad (6.31)$$

which leads to $A_{\text{cylin}}^* = 0.4125$ for $\nu_s = 0.3$ and can explain Eq. (6.28) given by Rumpf and Raasch (1962) for the cylindrical case.

In contrast to the case of cylinders and disks, analytical solutions for the stresses in the case of the sphere are less common. Niedballa and Husemann (2000) offered an interpretation of Eq. (6.28) suggesting that it describes the centrifugal force acting on the largest cross-sectional area of the agglomerate multiplied by the Poisson's ratio:

$$\sigma_{\text{rotary}} = \frac{F_{\text{cent.}}}{A_{\text{cs}}} \nu_s = \frac{\frac{4}{3} \pi r_{\text{ag}}^3 \rho_{\text{ag}} \omega_{\text{ag}}^2 r_{\text{ag}}}{\pi r_{\text{ag}}^2} \nu_s = \underbrace{\frac{4}{3} \nu_s}_{A_{\text{sphere}}^*} \rho_{\text{ag}} \omega_{\text{ag}}^2 r_{\text{ag}}^2 , \quad (6.32)$$

which reduces to Eq. (6.28) with $A_{\text{sphere}}^* = 0.4$ when $\nu_s = 0.3$. However, this interpretation lacks a theoretical base.

In the present work, efforts are made to analytically derive the formula (6.28) of the rotary stress in a sphere. For this purpose, the solution provided in the context of planetary

science (Chree, 1895) for the stress field in a sphere steadily rotating around its axis is accounted for. These stresses in polar coordinates (r, θ, β) are given as:

$$\sigma_{rr} = \frac{\rho_{\text{ag}} \omega_{\text{ag}}^2 (r_{\text{ag}}^2 - r^2) [9 + 7\nu_s - 5(3 + 2\nu_s)(1 - \nu_s) \cos(2\beta)]}{10(7 + 5\nu_s)(1 - \nu_s)}, \quad (6.33)$$

$$\sigma_{\theta\theta} = \frac{\rho_{\text{ag}} \omega_{\text{ag}}^2 [2(12 + \nu_s - 5\nu_s^2) r_{\text{ag}}^2 - (13 + 14\nu_s + 5\nu_s^2) r^2 - 5(1 - \nu_s^2) r^2 \cos(2\beta)]}{10(7 + 5\nu_s)(1 - \nu_s)}, \quad (6.34)$$

$$\sigma_{\beta\beta} = \frac{\rho_{\text{ag}} \omega_{\text{ag}}^2 [5(3 + 2\nu_s)(1 - \nu_s)(r_{\text{ag}}^2 - r^2) \cos(2\beta) + (9 + 7\nu_s) r_{\text{ag}}^2 - (3 + 19\nu_s + 10\nu_s^2) r^2]}{10(7 + 5\nu_s)(1 - \nu_s)}, \quad (6.35)$$

$$\sigma_{\beta r} = \frac{\rho_{\text{ag}} \omega_{\text{ag}}^2 (3 + 2\nu_s)(r_{\text{ag}}^2 - r^2) \sin(2\beta)}{2(7 + 5\nu_s)}, \quad (6.36)$$

$$\sigma_{\theta r} = 0, \quad (6.37)$$

$$\sigma_{\theta\beta} = 0. \quad (6.38)$$

Following the approach by Kadish et al. (2005), the von Mises stress (equivalent uni-axial tensile stress) can be predicted based on these components as follows:

$$\sigma_E = \sqrt{\sigma_{rr}^2 + \sigma_{\theta\theta}^2 + \sigma_{\beta\beta}^2 - \sigma_{rr}\sigma_{\theta\theta} - \sigma_{\theta\theta}\sigma_{\beta\beta} - \sigma_{\beta\beta}\sigma_{rr} + 3\sigma_{\theta r}^2 + 3\sigma_{\theta\beta}^2 + 3\sigma_{\beta r}^2}. \quad (6.39)$$

Inserting Eqs. (6.33) to (6.38) into Eq. (6.39) gives:

$$\sigma_{\text{rotary}} = \sigma_E = \underbrace{\frac{(2\nu_s + 3)}{(5\nu_s + 7)}}_{A_{\text{sphere}}^{**}} \rho_{\text{ag}} \omega_{\text{ag}}^2 r_{\text{ag}}^2. \quad (6.40)$$

The newly derived relation (6.40) for the rotary stress can be generalized again in form of Eq. (6.28), where $A = A_{\text{sphere}}^{**}$ is a function weakly depending on the Poisson's ratio ν_s . It varies from $A_{\text{sphere}}^{**} = 0.4267$ at $\nu_s = 0.1$ to $A_{\text{sphere}}^{**} = 0.4211$ at $\nu_s = 0.5$. In the same range of ν_s values, A_{sphere}^* in Eq. (6.32) strongly increases from $= 0.1333$ to 0.6667 . For the Poisson ratio $\nu_s = 0.17$ considered in the present study (see Table 9.2) both relations significantly deviate. Since in contrast to the other expressions relation (6.40) is physically underpinned, the latter is used in the present work.

It is important to mention that agglomerates may acquire a high angular velocity either due to the torque induced by the fluid or due to collisions with other particles or walls. Hence, the breakup by the rotary stress is not strictly attributed to the direct interaction with the fluid.

The condition for breakup by this mechanism requires the rotary stress to be the largest among the other stresses acting on the agglomerate (i.e., the turbulent and the drag stress). In addition, the rotary stress must surpass the strength of the agglomerate, i.e., $\sigma_{\text{rotary}} \geq S$. When these conditions are fulfilled, agglomerates are assumed to split in the middle (i.e., a symmetric binary breakup) owing to the lack of further information. This

means that the two fragments might deviate in their sizes by a single primary particle only if the original agglomerate consists of an odd number of particles. Similar to the procedure explained for the other two breakup mechanisms, the density and the diameter of each fragment is determined based on a mass balance taking the number of particles within the fragment into account. Moreover, the velocities of the resulting fragments are determined based on the approach explained in Section 6.4.3.

6.4 Post-Breakup Kinetics

To finalize the modeling of the breakage, the velocities of the fragments and the spatial direction along which fragments are separated after breakup have to be determined. To ensure physically reasonable kinetics in the Euler–Lagrange simulations, post-breakup models are developed taking the nature of the responsible breakup mechanism into account.

6.4.1 Kinetics for Breakup by Turbulent Stress

In the experimental work by Saha (2013), the breakage of aggregates in homogeneous quasi-isotropic turbulence is investigated and an analysis for the post-breakage behavior of particles is presented. The experiment was performed inside a tank filled with deionized water. Polystyrene primary particles of 420 nm in diameter and a density close to that of water were used to prepare the aggregates which were found to have sizes up to $d_{ag}/\eta \sim 5$. The measurements allowed to determine the strain rate tensor $\underline{\underline{S}}$ (Eq. (3.3)) in the vicinity of the agglomerates. The tensor possesses three eigenvalues denoted Λ_i and the corresponding eigenvectors denoted λ_i which determine the principal axis of the strain rate tensor. Saha (2013) measured the separation vector between the fragments at the time of breakage due to turbulent stresses and found that this vector is consistently aligned with λ_1 ($\Lambda_1 > 0$), i.e., the most extensional (stretching) eigenvector along the Lagrangian trajectory. Consequently, the direction in which the two fragments separate after a breakup process due to turbulence (with negligible effects of drag and rotation) is given by λ_1 . Hence, the present model separates the two fragments in opposite directions along this axis.

The eigen vector λ_1 is determined by applying a three-step procedure provided in Numerical Recipes (Press et al., 2007). First, the matrix $\underline{\underline{S}}$ is reduced to a real, symmetric, tridiagonal matrix by a Householder reduction. Then the eigenvalues and eigenvectors of this new matrix are determined based on a QL algorithm with implicit shifts. Finally, the eigenvalues and the corresponding eigenvectors are sorted in descending order yielding the largest eigenvalue Λ_1 and the corresponding eigenvector λ_1 .

To determine the magnitudes of the post-breakup velocity, an energy balance is employed. Note that the idea behind the model is borrowed from the literature on the breakup of bubbles (Hoppe, 2020; Hoppe and Breuer, 2020). Here, it is assumed that the compact spherical agglomerate breaks down into a two-particle (doublet) structure before the two

fragments completely separate. The size of the doublet structure is predicted as the sum of the diameters of the two fragments:

$$d_{\text{doublet}} = d_{\text{fr1}} + d_{\text{fr2}} > d_{\text{ag}} . \quad (6.41)$$

This size is larger than the diameter of the original agglomerate. Consequently, velocity fluctuations in the turbulent flow, which are estimated differently for the four subranges (see Table 6.1):

$$\Delta w(d_{\text{ag}}) = \begin{cases} (2/15)^{1/2} (\epsilon/\nu_f)^{1/2} d_{\text{ag}} & \text{viscous} \\ (1/15)^{1/2} (\epsilon/\nu_f)^{1/2} d_{\text{ag}} & \text{transition (laminar preferred)} \\ 0.7 \epsilon^{3/8} \nu_f^{-1/8} d_{\text{ag}}^{1/2} & \text{transition (turbulent preferred)} \\ 1.38 (\epsilon d_{\text{ag}})^{1/3} & \text{inertial} \end{cases} \quad (6.42)$$

are larger on the doublet structure than on the agglomerate. Note that in Eq. (6.42) the root-mean-square velocity is generally called $\Delta w(d_{\text{ag}})$, since in the viscous subrange the lateral component $\Delta v(d_{\text{ag}})$ is relevant, whereas in the other subranges the longitudinal component $\Delta u(d_{\text{ag}})$ is considered as explained in Section 6.3.1. Hence, two specific turbulent kinetic energies can be computed. The first corresponds to the root-mean-square fluctuating velocity difference Δw over the size of the agglomerate d_{ag} before breakage. The second is similar but takes the size of the agglomerate d_{doublet} at the time of breakage (i.e., the doublet structure) into account. These two specific energies are expressed as:

$$E_{\text{kin}}^{\text{ag}} = \frac{1}{2} [\Delta w(d_{\text{ag}})]^2 , \quad (6.43)$$

$$E_{\text{kin}}^{\text{doublet}} = \frac{1}{2} [\Delta w(d_{\text{doublet}})]^2 . \quad (6.44)$$

Applying an energy balance, the difference between these two kinetic energies is assumed to be consumed by the fragmentation process:

$$\Delta E_{\text{kin}} = \frac{1}{2} [\Delta u_{\text{sep}}]^2 = E_{\text{kin}}^{\text{doublet}} - E_{\text{kin}}^{\text{ag}} . \quad (6.45)$$

The resulting magnitude of the separation velocity Δu_{sep} is a relative velocity in a frame of reference moving with the agglomerate. It denotes the relative change of the velocity of the new fragment 2 in relation to fragment 1, which is supposed to be the original agglomerate:

$$\Delta u_{\text{sep}} = \Delta u_{\text{fr2}} - \Delta u_{\text{fr1}} . \quad (6.46)$$

Accordingly, $\Delta u_{\text{fr}1}$ and $\Delta u_{\text{fr}2}$ stand for the change of the velocity of fragment 1 and fragment 2 after breakup, respectively. Applying the conservation equation of the translational momentum:

$$m_{\text{fr}1} \Delta u_{\text{fr}1} + m_{\text{fr}2} \Delta u_{\text{fr}2} = 0, \quad (6.47)$$

this velocity magnitude is split into contributions added to both fragments in opposite directions along the separation axis, i.e., the most extensional eigenvector $\boldsymbol{\lambda}_1$ of the strain rate tensor $\underline{\boldsymbol{S}}$ in the vicinity of the agglomerates. For this purpose, Eq. (6.46) is inserted into Eq. (6.47) yielding:

$$\Delta u_{\text{fr}2} = + \frac{m_{\text{fr}1}}{m_{\text{ag}}} \Delta u_{\text{sep}}, \quad (6.48)$$

$$\Delta u_{\text{fr}1} = - \frac{m_{\text{fr}2}}{m_{\text{ag}}} \Delta u_{\text{sep}}. \quad (6.49)$$

Consequently, the velocities of the fragments after breakup are set as follows:

$$\boldsymbol{u}_{\text{fr}1} = \boldsymbol{u}_{\text{ag}} + \frac{\boldsymbol{\lambda}_1}{|\boldsymbol{\lambda}_1|} \Delta u_{\text{fr}1}, \quad (6.50)$$

$$\boldsymbol{u}_{\text{fr}2} = \boldsymbol{u}_{\text{ag}} + \frac{\boldsymbol{\lambda}_1}{|\boldsymbol{\lambda}_1|} \Delta u_{\text{fr}2}, \quad (6.51)$$

where $\boldsymbol{u}_{\text{ag}}$ denotes the velocity of the agglomerate prior to breakup. Lastly, the rotational motion is assumed to be not affected during the breakup process. Thus, applying the conservation of the angular momentum gives $\boldsymbol{\omega}_{\text{fr}1} = \boldsymbol{\omega}_{\text{fr}2} = \boldsymbol{\omega}_{\text{ag}}$.

6.4.2 Kinetics for Breakup by Drag Stress

As explained in Section 6.3.1, the breakup by the drag stress mechanism gives rise to fragments possessing uneven sizes. In order to determine the velocity vectors of the arising fragments relative to the velocity of the original agglomerate (i.e., $\Delta \boldsymbol{u}_{\text{fr}1}$ and $\Delta \boldsymbol{u}_{\text{fr}2}$), the following assumptions are made: First, since the drag stress is attributed to the relative velocity vector between the fluid and the agglomerate $\boldsymbol{u}_{\text{ag,slip}} = \boldsymbol{u}_f - \boldsymbol{u}_{\text{ag}}$ (i.e., the slip velocity), it is reasonable to assume that the fragments are going to split along the axis of the slip velocity given by $\boldsymbol{r}_{\text{slip}}$ (see Fig. 6.3). Second, since the drag stress leads to erosion, where one or a small number of primary particles is detached from a large agglomerate ($m_{\text{fr}2}/m_{\text{fr}1} \ll 1$), the breakup process is assumed to influence solely the smaller fragment 2. Thus, no velocity contribution is added to the larger fragment as depicted in Fig. 6.3. Based on these two assumptions the relative velocity vectors read:

$$\Delta \boldsymbol{u}_{\text{fr}2} = \Delta u_{\text{fr}2} \boldsymbol{r}_{\text{slip}} = \Delta u_{\text{fr}2} \frac{\boldsymbol{u}_f - \boldsymbol{u}_{\text{ag}}}{|\boldsymbol{u}_f - \boldsymbol{u}_{\text{ag}}|}, \quad (6.52)$$

$$\Delta \boldsymbol{u}_{\text{fr}1} = 0. \quad (6.53)$$

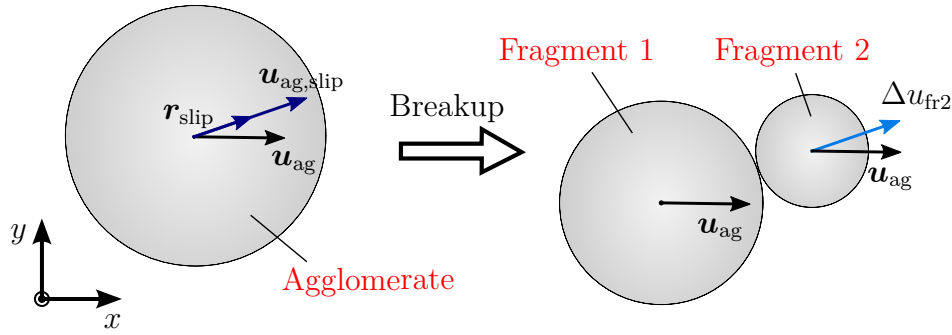


Fig. 6.3. Separation of two asymmetric fragments after breakage by the drag stress.

For the determination of the magnitude of the relative velocity Δu_{fr2} , an energy balance is employed. The balance assumes that a certain part of the relative translational kinetic energy of the agglomerate is dissipated due to breakup. This part is described by the critical slip velocity $u_{cr,slip}$. The remaining part raises the relative velocity between the fragments:

$$\Delta u_{fr2} = u_{ag,slip} - u_{cr,slip}, \quad (6.54)$$

with $u_{ag,slip} = |\mathbf{u}_f - \mathbf{u}_{ag}|$. The magnitude of the critical slip velocity $u_{cr,slip}$ results from equating the drag stress given by Eq. (6.22) and the strength of the agglomerate S :

$$u_{cr,slip} = \sqrt{\frac{8S}{C_D \cos(\psi_{N_{pp}^{break}})}}. \quad (6.55)$$

Here, $\psi_{N_{pp}^{break}}$ is the angle of the cap representing the exact number of particles N_{pp}^{break} eligible for breakup ($\psi_{N_{pp}^{break}} < \psi_{cr}$). It has to be clearly distinguished from the critical angle ψ_{cr} introduced in Section 6.3.2 to describe the largest plane on which the stresses are greater than the strength. The angle $\psi_{N_{pp}^{break}}$ is computed based on the mass balance equation (6.24) replacing N_{pp}^{cap} by N_{pp}^{break} and resolving the cubic equation for the angle $\psi_{N_{pp}^{break}}$. It can be shown that the cubic equation always has three real solutions and only the third solution with $0 < \cos(\psi_{N_{pp}^{break}}) < 1$ is relevant here.

In summary, the velocities of the fragments after breakup are set as follows:

$$\mathbf{u}_{fr1} = \mathbf{u}_{ag}, \quad (6.56)$$

$$\mathbf{u}_{fr2} = \mathbf{u}_{ag} + (u_{ag,slip} - u_{cr,slip}) \frac{\mathbf{u}_f - \mathbf{u}_{ag}}{|\mathbf{u}_f - \mathbf{u}_{ag}|}. \quad (6.57)$$

The sign of the additional velocity component in Eq. (6.57) is set positive since the tensile stress calculated on the plane between the two fragments pulls fragment 2 (the spherical cap) in the direction of the relative velocity. Similar to the case of the turbulent stress the model for the drag stress does not provide any information about the angular velocities of the fragments. Thus, it is again assumed that this quantity does not change during the breakup process, i.e., $\boldsymbol{\omega}_{fr1} = \boldsymbol{\omega}_{fr2} = \boldsymbol{\omega}_{ag}$.

6.4.3 Kinetics for Breakup by Rotary Stress

The breakup by the rotary stress occurs when the angular velocity of the agglomerate is large enough to generate stresses which exceed the strength of the agglomerate. Two fragments possessing (nearly) equal sizes are assumed to appear. To determine the post-breakup translational and angular velocities of the fragments, a critical angular velocity is introduced ω_{cr} . The idea behind the critical angular velocity ω_{cr} is to describe the angular momentum dissipated during the breakup process denoted $\mathbf{L}_{\text{break}}$. For this purpose, ω_{cr} is defined as the smallest angular velocity that provokes a rotary stress satisfying the breakup condition, i.e., equal or larger than the strength of the agglomerate. Thus, the expression for ω_{cr} can be derived by equating the rotary stress given by Eq. (6.40) with the strength S :

$$\omega_{\text{cr}} = \sqrt{\frac{S}{\sigma_{\text{rotary}}}} \frac{\omega_{\text{ag}}}{|\omega_{\text{ag}}|} = \sqrt{\frac{4S}{A_{\text{sphere}}^{**} \rho_{\text{ag}} d_{\text{ag}}^2}} \frac{\omega_{\text{ag}}}{|\omega_{\text{ag}}|}. \quad (6.58)$$

Furthermore, the conservation of the angular momentum is applied. Referring to Fig. 6.4, it is assumed that the sum of the angular momenta of the two fragments (i.e., $\mathbf{L}_{\text{fr1}}^A + \mathbf{L}_{\text{fr2}}^A$) about the center of mass (point A) of the two-fragment structure can be determined from the angular momentum of the agglomerate \mathbf{L}_{ag} reduced by $\mathbf{L}_{\text{break}}$ which describes the part consumed by the breakup process:

$$\mathbf{L}_{\text{fr1}}^A + \mathbf{L}_{\text{fr2}}^A = \mathbf{L}_{\text{ag}} - \mathbf{L}_{\text{break}}, \quad (6.59)$$

$$I_{\text{fr1}}^A \omega_{\text{fr1}} + I_{\text{fr2}}^A \omega_{\text{fr2}} = I_{\text{ag}} (\omega_{\text{ag}} - \omega_{\text{cr}}). \quad (6.60)$$

For simplicity and since the two resulting fragments might differ in their sizes by a maximum of one primary particle only (see Section 6.3.3), the two fragments will be henceforth assumed to be exactly identical. This implies equal moment of inertia of the two fragments, i.e., $I_{\text{fr1}}^A = I_{\text{fr2}}^A = I_{\text{fr}}^A$ and the same applies also for the angular velocity ω_{fr} . Accounting for these consideration in Eq. (6.60) and resolving for the angular velocity of the fragments ω_{fr} leads to:

$$\omega_{\text{fr}} = \frac{I_{\text{ag}} (\omega_{\text{ag}} - \omega_{\text{cr}})}{2 I_{\text{fr}}^A}, \quad (6.61)$$

where $I_{\text{ag}} = 1/10 m_{\text{ag}} d_{\text{ag}}^2$ denotes the moment of inertia of the spherical agglomerate about its center and $I_{\text{fr}}^A = 7/20 m_{\text{fr}} d_{\text{fr}}^2$ is the moment of inertia of one fragment about the axis of rotation of the two-particle structure, i.e., the center of mass of the structure denoted point A in Fig 6.4. The latter relation is derived using the parallel axis theorem.

The effect of the breakup event on the translational velocities of the fragments is investigated next. The rotary stress is understood to pull the fragments in centrifugal directions, which are perpendicular to the axis of rotation of the agglomerate. Since this condition does not uniquely define the direction, a random unit vector \mathbf{c} perpendicular to the axis of rotation is determined, which is uniformly distributed on the entire perimeter.

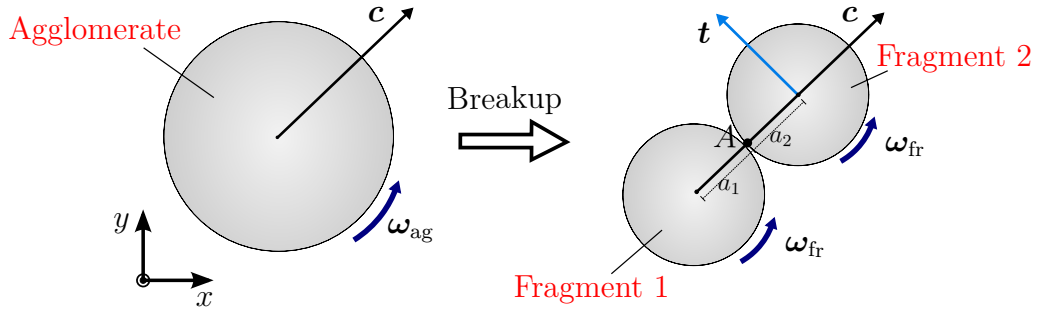


Fig. 6.4. Sketch of the spherical agglomerate and the two-fragment structure. Note that a_1 and a_2 are the radii of the first and second fragments, i.e., $d_{fr1}/2$, $d_{fr2}/2$, respectively.

Based on \mathbf{c} and $\boldsymbol{\omega}_{ag}$ the tangential direction, which is perpendicular to both $\boldsymbol{\omega}_{ag}$ and \mathbf{c} can be defined by the corresponding unit vector \mathbf{t} :

$$\mathbf{t} = \frac{\boldsymbol{\omega}_{ag}}{|\boldsymbol{\omega}_{ag}|} \times \mathbf{c}. \quad (6.62)$$

Now (relative) velocity components of the fragments in centrifugal and tangential direction have to be determined separately. The magnitude of the velocity component in centrifugal direction is obtained by means of an energy balance. For this purpose, it is assumed that the rotational energy of the agglomerate $E_{ag,rot} = 1/2 I_{ag} \boldsymbol{\omega}_{ag}^2$ is partially spent for the breakup process ($E_{ag,cr} = 1/2 I_{ag} \boldsymbol{\omega}_{cr}^2$) and partially transferred into a change of the translational $\Delta E_{fr,kin} = 1/2 m_{fr} \Delta u_{fr,c}^2$ and the rotational $E_{fr,rot} = 1/2 I_{fr}^A \boldsymbol{\omega}_{fr}^2$ kinetic energies of the two generated fragments:

$$E_{ag,rot} - E_{ag,cr} = 2 \Delta E_{fr,kin} + 2 E_{fr,rot}, \quad (6.63)$$

$$E_{ag,rot} - E_{ag,cr} = m_{fr} \Delta u_{fr,c}^2 + I_{fr}^A \boldsymbol{\omega}_{fr}^2. \quad (6.64)$$

Solving Eq. (6.64) for $\Delta u_{fr,c}$ gives:

$$\Delta u_{fr,c} = \sqrt{\frac{I_{ag} (\boldsymbol{\omega}_{ag}^2 - \boldsymbol{\omega}_{cr}^2) - 2 I_{fr}^A \boldsymbol{\omega}_{fr}^2}{2 m_{fr}}}. \quad (6.65)$$

Accordingly, the velocity of each fragment after breakup will be altered in centrifugal direction by $\Delta \mathbf{u}_{fr1,c} = \Delta u_{fr,c} \mathbf{c}$ and $\Delta \mathbf{u}_{fr2,c} = -\Delta u_{fr,c} \mathbf{c}$.

Furthermore, the change of the center of rotation from the center of mass of the two-particle structure (point A) to the center of each individual fragment requires to add a velocity component in tangential direction. The velocity components in tangential direction are thus computed as $\Delta \mathbf{u}_{fr1,t} = d_{fr}/2 (\boldsymbol{\omega}_{fr} \times \mathbf{c})$ and $\Delta \mathbf{u}_{fr2,t} = -d_{fr}/2 (\boldsymbol{\omega}_{fr} \times \mathbf{c})$.

Finally, the velocity of the fragments after breakup are obtained by superimposing the two new components on the velocity of the original agglomerates:

$$\mathbf{u}_{\text{fr1}} = \mathbf{u}_{\text{ag}} + \Delta\mathbf{u}_{\text{fr1,c}} + \Delta\mathbf{u}_{\text{fr1,t}} , \quad (6.66)$$

$$\mathbf{u}_{\text{fr2}} = \mathbf{u}_{\text{ag}} + \Delta\mathbf{u}_{\text{fr2,c}} + \Delta\mathbf{u}_{\text{fr2,t}} . \quad (6.67)$$

Hence, physically derived translational and angular velocities are found for the resulting fragments.

6.5 Breakup Time Lag

For unsteady turbulent flow simulations, the choice of the time-step size depends on physical and numerical issues. Physically, the applied time-step size has to ensure that all relevant time scales are resolved appropriately. For the large-eddy simulation technique applied, that typically leads to very small time-step sizes especially for wall-resolved simulations carried out in the present study. Numerically, the physically motivated time-step size are typically within the stability limits of explicit schemes (CFL number and diffusion number less than unity) and thus this does not lead to any further restrictions. The rule of thumb states: The higher the Reynolds number, the smaller the time step to be used. Since in the present methodology the Lagrangian time step does not differ from the Eulerian one, the evaluation of the breakup conditions (i.e., stress larger than strength) is repeatedly carried out at high frequencies not related to any physical time scale. As a consequence, the frequency of breakup processes is overpredicted. Furthermore, fragments being rapidly released in the vicinity of each other experience an unphysically high number of collisions and re-agglomerations.

In order to resolve these problems and to find a solution which is independent of the Eulerian time-step size, a physically motivated time lag is introduced. That means an agglomerate which experiences a breakup process at time t_0 is not allowed to further breakup within the subsequent time interval Δt_{lag} as depicted in Fig. 6.5. Another physical explanation is that breakup processes are not infinitely fast and thus require a certain breakup time which is accounted for by the time lag. It is determined based on the properties of the agglomerate and the local flow properties. When this time period expires, i.e., $t > t_0 + \Delta t_{\text{lag}}$, a further breakup is possible. This assumption is supported by numerical (Eggersdorfer et al., 2010) and experimental (Saha, 2013) results reported in the literature. Eggersdorfer et al. (2010) carried out DEM simulations of soft agglomerates in a simple shear flow and demonstrated that breakup does not happen immediately, even if the stress exceeds the strength of the agglomerate. Instead, the process lasts over the breakup duration. In addition, Saha (2013) studied the breakup of agglomerates in isotropic homogeneous turbulence and found that fragmentation takes place over a certain time scale.

To derive an expression for the breakup time lag, the nature of the breakup mechanism is taken into account. For the breakup processes purely promoted by the interactions with the fluid (i.e., turbulent and drag stresses), the time lag is attributed to the local flow

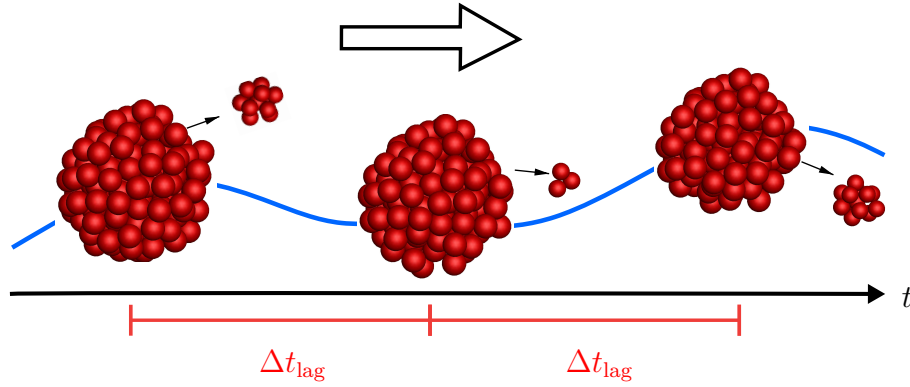


Fig. 6.5. Time lag Δt_{lag} defines the minimum period separating two successive breakup events of the same agglomerate in time.

properties at the scale of the agglomerate size. It is suggested that the time lag Δt_{lag} is equal to the turbulent time scale τ predicted based on the root-mean-square fluctuating velocity difference $\Delta w(d_{\text{ag}})$ over the size d_{ag} of the agglomerate:

$$\Delta t_{\text{lag}} = \tau = \frac{k}{\epsilon} = \frac{1/2 [\Delta w(d_{\text{ag}})]^2}{\epsilon}, \quad (6.68)$$

where the determination of $\Delta w(d_{\text{ag}})$ depends on the relevant sub-range of turbulence as given in Eq. (6.42). In the context of experimental investigations on the breakup of bubbles and droplets (Andersson and Andersson, 2006) the time scale for breakup was compared with the turbulent time scale $\tau = k/\epsilon$. The average breakup time was found to be in the range of 1/2 to 2/3 of the turbulent time scale, which is a clear hint that τ is a physically reasonable estimation of the time lag (Hoppe, 2020; Hoppe and Breuer, 2020).

For the breakup processes not directly provoked by fluid dynamic forces, i.e., the rotary stress, a different time lag is considered to be more appropriate. A dimensional analysis taking the rotary stress σ_{rotary} , the angular velocity ω_{ag} and the diameter d_{ag} of the agglomerate into account, yields that a characteristic velocity is given by $\sqrt{\sigma_{\text{rotary}}/\rho_{\text{ag}}}$. A characteristic length scale is defined by d_{ag} . Thus, a characteristic time scale defining the time lag Δt_{lag} in case of the rotary stress reads:

$$\Delta t_{\text{lag}} = \frac{d_{\text{ag}}}{\sqrt{\sigma_{\text{rotary}}/\rho_{\text{ag}}}} \simeq \frac{d_{\text{ag}}}{\sqrt{\omega_{\text{ag}}^2 d_{\text{ag}}^2}} = \frac{1}{\omega_{\text{ag}}} \quad (6.69)$$

Here, the rotary stress $\sigma_{\text{rotary}} \sim \rho_{\text{ag}} \omega_{\text{ag}}^2 d_{\text{ag}}^2$ described in Section 6.3.3 is taken into account in the derivation of Eq. (6.69).

Consequently, the time intervals Δt_{lag} between two successive breakup processes are determined relying on physical considerations. Hence, the time periods between two breakup processes of the same agglomerate are no longer related to the time-step size of the numerical method. Thus, the methodology is significantly enhanced even for the case

when the time-marching procedures for the continuous and the disperse phase would be fully decoupled.

By determining the ratio of the time delay Δt_{lag} to the time-step size Δt , the number of time steps, in which the agglomerate can not breakup, can be calculated as:

$$n_{\text{lag}} = \text{int} \left[\frac{\Delta t_{\text{lag}}}{\Delta t} \right]. \quad (6.70)$$

These values are stored as a property of the agglomerate and transported through the flow field in the subsequent time steps.

7 Models for Breakage due to Wall Impact

Besides the effect of fluid forces, the impact at walls is another cause for the deagglomeration of cohesive particles in wall-bounded particle-laden flow systems. In this chapter, data-driven wall-impact breakage models are developed and incorporated into the Eulerian–Lagrangian simulation methodology. Note that these breakage models were derived and applied in Khalifa and Breuer (2020, 2021), Khalifa et al. (2021), and Khalifa et al. (2022).

7.1 Overview on the Data-Driven Modeling Strategy

In Section 1.2 it was argued that efficient Euler–Lagrange techniques rely on a full or partial modeling of the intraphase and the interphase interactions occurring at small temporal and spatial scales instead of fully resolving them. However, the level of resolution of the two aforementioned types of interactions dictates the kind of techniques applicable for predicting the deagglomeration of cohesive particles. For instance, employing a single effective sphere to model the multi-particles structure of the agglomerate leads to a loss of knowledge on the inter-particle interactions occurring within the agglomerate. As a consequence, the disintegration of agglomerates cannot be governed by a balance of forces on the individual primary particles. Instead, models based on properties described at the agglomerate level have to be employed. As discussed before, in order to fully describe breakage events, these models need to tackle three main issues: **(i)** the condition (onset) of breakage, **(ii)** the number of fragments and the resulting fragment size distribution and **(iii)** the kinetics of the resulting fragments after breakage.

In general, the literature summarized in Section 2.3 contains theoretical and data-driven approaches for predicting the wall-impact breakage of agglomerates represented by perfect spheres. Theoretical models rely on a comparison between the (compressive) stress arising within the agglomerate with a critical threshold (e.g., Kousaka et al., 1979). In principle, this approach is equivalent to the one adopted in this thesis for describing the deagglomeration by fluid forces. Hence, a number of drawbacks can be pointed out. First, the available models for describing the distribution of the stresses propagating within solid structures consider agglomerates as perfect solid spheres, i.e., the effect of the heterogeneous morphology is not accounted for. In addition, the resulting fragment size distribution (modeling task **ii**) cannot be directly predicted due to the lack of knowledge on the development of the stresses within the internal network of particle contacts. Thus, additional assumptions such as the binary breakage need to be utilized.

The second option are data-driven modeling approaches, which are becoming increasingly important and involved in many fields of science and engineering (Montáns et al., 2019). Data-driven models offer descriptions for complex phenomena that can be applied in practical applications at low computational costs. These models rely on the knowledge captured by physics-based, typically expensive investigations. However, to ensure insightful and accurate data-driven predictions, a sufficient amount of data must be available. Moreover, appropriate analysis tools need to be applied in order to allow the derivation of predictive models using the collected data.

In the present work, a data-driven modeling strategy is followed to address the wall-impact breakage problem. The aim is to offer a reasonable forecasting for the three aspects (i to iii) defined above, without having to resolve the underlying physics in the Euler–Lagrange simulations itself. For this purpose, a huge number ($\mathcal{O}(10^4)$) of discrete element method (DEM) simulations are carried out to study the wall-impact behavior of agglomerates in an isolated (vacuum) environment (see Section 7.2.3). Wide ranges of different important impact conditions are taken into account. The investigated impact conditions include the impact velocity, the impact angle, the number of included primary particles, and the size of the primary particles. Subsequently, the obtained results are analyzed and quantified in terms of physical parameters (see Section 7.3). Lastly, relationships between the impact conditions and the physical parameters quantifying breakage are established. This is achieved in the present work based on two different strategies. The first follows the state-of-the-art literature (Moreno-Atanasio and Ghadiri, 2006; van Wachem et al., 2020) on the wall-impact breakage. More specifically, traditional regression functions are applied relying on dimensionality reduction techniques such as the concept of dimensionless numbers (see Section 7.4). The second uses multilayer perceptron (MLP), i.e., feed-forward artificial neural networks (ANN) to approximate functions relating the impact variables to the measures of the breakage (see Section 7.5). Hence, two different wall-impact breakage models are developed for the present Euler–Lagrange methodology.

The two proposed models are conceptually similar, i.e., they provide quantitative forecasting for the breakage of agglomerates based on the same parameters. However, they essentially differ in the type of the regression technique (traditional functions vs. ANN) and in the variety of cases covered in the corresponding DEM database. The latter difference is explained by the fact that the model based on traditional regression performed well on an initial, quite broad DEM database. However, an unsatisfactory performance was detected when the database was further extended in a later step to include more critical impact conditions such as flat impact angles (i.e., the shear impact case). In fact, this circumstance motivated the introduction of ANNs, which delivered generally better results taking the complete database into account. More details on this matter are provided in Sections 7.4 and 7.5.

7.2 DEM Wall-Impact Simulations

The data in the present data-driven modeling strategy refer to the results of a large number of DEM wall-impact simulations taking a variety of impact conditions into account. This section focuses on the details of the wall-impact simulations. Thus, the applied DEM methodology is explained in Section 7.2.1. The properties of the primary particles and the agglomerates are given in Section 7.2.2. Furthermore, the wall-impact setup and the general simulation procedure are described in Section 7.2.3.

7.2.1 Discrete Element Method (Soft-Sphere)

In DEM, primary particles are tracked by determining their trajectories in a Lagrangian frame of reference. The deformation of particles during their interactions with other particles or walls is allowed by assuming the acting surfaces to overlap (Cundall and Strack, 1979). Accordingly, the contact forces are continuously computed as a function of the deformation (overlap). For the present wall-impact simulations solely spherical particles are of interest. The equations of the translatory and rotary motions of a particle i interacting with a particle (or a wall) j are given by:

$$m_{\text{pp},i} \frac{d\mathbf{u}_{\text{pp},i}}{dt} = \sum_j \mathbf{F}_{ij}, \quad (7.1)$$

$$I_{\text{pp},i} \frac{d\boldsymbol{\omega}_{\text{pp},i}}{dt} = \sum_j (\mathbf{M}_{ij} + \mathbf{M}_{ij,r}), \quad (7.2)$$

respectively. Here, $m_{\text{pp},i}$ and $\mathbf{u}_{\text{pp},i}$ are the mass and velocity of particle i . $I_{\text{pp},i}$ and $\boldsymbol{\omega}_{\text{pp},i}$ are the moment of inertia and the angular velocity, respectively. The contact force \mathbf{F}_{ij} is decomposed into a normal $\mathbf{F}_{n,ij}$ and a tangential $\mathbf{F}_{t,ij}$ component. The latter results in a torque \mathbf{M}_{ij} at the contact point causing the particle to rotate, where the relative rotational motion between the two bodies gives rise to a rolling friction torque $\mathbf{M}_{ij,r}$.

The open-source DEM software LIGGGHTS (Kloss et al., 2012) is used as it provides a variety of contact models and the possibility to integrate additional ones. The employed models of the contact forces and torques are briefly explained next.

Based on a spring-dashpot analogy (see Fig. 7.1) the normal force is generally expressed as:

$$\mathbf{F}_{n,ij} = \mathbf{F}_{n,ij}^{\text{El}} + \mathbf{F}_{n,ij}^D = -k_n \boldsymbol{\delta}_n + c_n \Delta \mathbf{u}_n, \quad (7.3)$$

where k_n is the normal elastic coefficient, $\boldsymbol{\delta}_n$ is the normal overlap vector, c_n is the normal damping coefficient, and $\Delta \mathbf{u}_n$ is the normal relative velocity vector.

The normal overlap vector $\boldsymbol{\delta}_n$ refers to the distance vector between the surfaces of the two contacting particles along a line passing through their centers:

$$\boldsymbol{\delta}_n = [(R_i + R_j) - |\mathbf{x}_i - \mathbf{x}_j|] \cdot \frac{\mathbf{x}_i - \mathbf{x}_j}{|\mathbf{x}_i - \mathbf{x}_j|}, \quad (7.4)$$

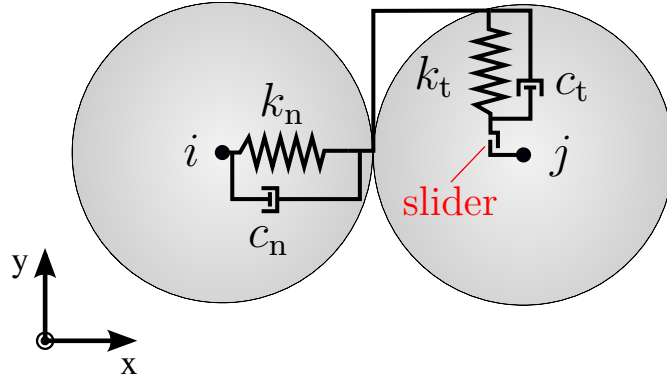


Fig. 7.1. Spring-dashpot analogy for the normal and the tangential forces in DEM.

where R_i and R_j denote the radius of particle i and j , respectively. In case of a particle-wall contact, the normal overlap vector δ_n refers to the distance vector between the two surfaces along the line connecting the center of particle i with the point of contact at the wall:

$$\delta_n = [R_i - |\mathbf{x}_i - \mathbf{x}_{c,w}|] \cdot \frac{\mathbf{x}_i - \mathbf{x}_{c,w}}{|\mathbf{x}_i - \mathbf{x}_{c,w}|}. \quad (7.5)$$

Here, \mathbf{x}_i , \mathbf{x}_j and $\mathbf{x}_{c,w}$ stand for the position vectors of the center of particle i , the center of particle j , and the particle-wall contact point, respectively.

Coming back to Eq. (7.3), the negative sign in the present notation stands for the repulsive nature of the elastic force. The normal elastic coefficient is given based on the theory of Hertz (1882):

$$k_n = \frac{4}{3} E^* \sqrt{R^* \delta_n}, \quad (7.6)$$

where δ_n is the magnitude of the normal overlap vector. Moreover, the normal damping coefficient is given as a function of the normal restitution coefficient e (Tsuji et al., 1992):

$$c_n = -2 \sqrt{\frac{5}{6}} \frac{\ln(e)}{\ln(e)^2 + \pi^2} \sqrt{S_n m^*}, \quad (7.7)$$

with:

$$S_n = 2 E^* \sqrt{R^* \delta_n}. \quad (7.8)$$

Here, R^* is the effective radius, E^* is the effective Young's modulus of elasticity and m^* is the effective mass (see Appendix A).

Similar to the normal force, the tangential force is accounted for based on a spring-dashpot analogy (see Fig. 7.1) proposed by Tsuji et al. (1992):

$$\mathbf{F}_{t,ij} = \begin{cases} -k_t \delta_t + c_t \Delta \mathbf{u}_t & \text{for } |k_t \delta_t| \leq \mu_s |\mathbf{F}_{n,ij}|, \\ -\mu_s |\mathbf{F}_{n,ij}| \cdot \frac{\delta_t}{|\delta_t|} & \text{for } |k_t \delta_t| > \mu_s |\mathbf{F}_{n,ij}|. \end{cases} \quad (7.9a)$$

$$(7.9b)$$

which represents a simplified version of the model suggested by Mindlin and Deresiewicz (1953). The model suggests that in case of sticking the tangential force is given by the sum of the elastic and damping tangential forces (Eq. (7.9)). However, a sliding contact is assumed to take place once the limit by Coulomb's law of static friction is undershot. In this case, the tangential force is set equal to the friction force computed based on the coefficient of static friction μ_s (Eq. (7.9)) assuming that it is valid also for dynamic conditions (Di Renzo and Di Maio, 2005). The mechanism of the tangential force is mimicked in the tangential spring-damper system in Fig. 7.1 by the introduction of the slider which is activated (i.e., fix the tangential force) when the limit by Coulomb's law is undershot. Moreover, the tangential elastic coefficient k_t in Eq. (7.9a) is given as (Mindlin, 1949):

$$k_t = 8 G^* \sqrt{R^* \delta_n}, \quad (7.10)$$

where G^* is the effective shear modulus (see Appendix A). The tangential overlap vector δ_t is computed by integrating the relative tangential velocity $\Delta \mathbf{u}_t$ over the contact time Δt_c (Cleary et al., 1998):

$$\delta_t = \int_{\Delta t_c} \Delta \mathbf{u}_t dt. \quad (7.11)$$

The tangential damping coefficient c_t is computed based on a relation analogous to that of the normal counterpart given in Eq. (7.7). Hence, the tangential coefficient reads:

$$c_t = -2 \sqrt{\frac{5}{6}} \frac{\ln(e)}{\ln(e)^2 + \pi^2} \sqrt{S_t m^*}, \quad (7.12)$$

with:

$$S_t = 8 G^* \sqrt{R^* \delta_n}. \quad (7.13)$$

As previously mentioned, the tangential force is used to determine the contact torque acting on particle i :

$$\mathbf{M}_{ij} = \mathbf{F}_{t,ij} R_i. \quad (7.14)$$

In practice, a particle rolling on a surface experience a rolling resistance from various sources such as friction, viscous hysteresis, and shape effect among others (Ai et al., 2011). As a result, a relative rotational velocity arises even between particles rotating with a common contact point. To account for this behavior, an additional torque resisting the rolling of the particle i is considered. In the present work, a simple constant torque model is used (Zhou et al., 1999):

$$\mathbf{M}_{ij,r} = -\mu_r |\mathbf{F}_{n,ij}^{El}| R^* \frac{\boldsymbol{\omega}_{rel}}{|\boldsymbol{\omega}_{rel}|}, \quad (7.15)$$

where μ_r is the rolling friction coefficient, and $\boldsymbol{\omega}_{rel}$ is the relative angular velocity between particles i and j . It is worth mentioning that the rolling friction torque is not considered for the particle-wall interaction (see Section 7.2.3 for the motivation).

The cohesion between primary particles is taken into account relying on the van-der-Waals force model by Hamaker (1937), which guarantees a smooth transition between the touch and non-touch state (Dong et al., 2012; Parteli et al., 2014):

$$\mathbf{F}_{n,ij}^{\text{vdW}} = \begin{cases} \frac{H R^*}{6 \delta_0^2} \cdot \frac{\delta_n}{|\delta_n|} & \text{for } \delta_n \geq 0, \\ \frac{H R^*}{6 (\delta_n - \delta_0)^2} \cdot \frac{\delta_n}{|\delta_n|} & \text{for } -l_{\text{max}} \leq \delta_n < 0, \\ 0 & \text{for } \delta_n < -l_{\text{max}}. \end{cases} \quad (7.16)$$

If particles are in physical contact ($\delta_n \geq 0$), the cohesive force contribution is computed based on the Hamaker constant H and the minimum separation distance δ_0 between the surfaces attributed to the surface roughness. As particles depart from each other, the cohesive force smoothly damps down to zero. However, to reduce the computational burden, the van-der-Waals force cut-off distance l_{max} is introduced into the equation describing the maximum separation distance at which the cohesion between two particles decays to effectively zero. Subsequently, the computed van-der-Waals force contribution $\mathbf{F}_{n,ij}^{\text{vdW}}$ is superimposed on the normal contact force in Eq. (7.3).

The motivation for choosing the van-der-Waals cohesion model by Hamker is twofold. First, the model accounts for the attraction between (non-touching) neighboring particles, which has a non-negligible effect on particles in the micrometer size range (Parteli et al., 2014) relevant for the present work. In addition, considering the properties of the particles (see Table 7.1), the dimensionless Tabor parameter $\mu_{\text{Ta}} = (4R^* \gamma_s^2 / E_s^{*2} \delta_0)^{1/3}$ varies between 0.03 and 0.06 justifying the application of a model based on the Derjaguin-Muller-Toporov (DMT) theory (Derjaguin et al., 1975) such as the present van-der-Waals force model (Dong et al., 2012). The Tabor parameter is frequently used in the literature to describe the influence of the cohesive force expressed by means of the surface energy γ_s on the contact area predicted by Hertz (1882). For small particles with low surface energies and large modulus of elasticity (i.e., $\mu_{\text{Ta}} < 1.0$, Liu et al. (2010), Li et al. (2011)), the deviation of the contact area due to cohesion from the Hertzian solution is negligible. Hence, the current contact model, where the normal elastic force is independent of the cohesive force, is suitable. Thus, the DEM code LIGGGHTS was extended by incorporating the van-der-Waals force model described. Note, however, that the cohesion between the particles and the wall is not taken into account as will be explained in Section 7.2.3.

In order to obtain the velocities and the positions of the particles, the equation of motion of each particle is numerically solved based on the velocity Verlet scheme (Swope et al., 1982). The scheme solves for the velocity and the position of the individual particles with

a second-order and a fourth-order temporal accuracy, respectively, and can be summarized as follows (Scherer, 2013):

$$\begin{aligned}
1.) \quad & \mathbf{u}_{\text{pp},i}^{(n+\frac{1}{2})} = \mathbf{u}_{\text{pp},i}^{(n)} + \frac{\Delta t_{\text{DEM}}}{2} \mathbf{a}_{\text{pp},i}^{(n)}, \\
2.) \quad & \mathbf{x}_{\text{pp},i}^{(n+1)} = \mathbf{x}_{\text{pp},i}^{(n)} + \Delta t_{\text{DEM}} \mathbf{u}_{\text{pp},i}^{(n+\frac{1}{2})}, \\
3.) \quad & \text{Compute } \mathbf{a}_{\text{pp},i}^{(n+1)} \text{ from the inter-particle interactions,} \\
4.) \quad & \mathbf{u}_{\text{pp},i}^{(n+1)} = \mathbf{u}_{\text{pp},i}^{(n+\frac{1}{2})} + \frac{\Delta t_{\text{DEM}}}{2} \mathbf{a}_{\text{pp},i}^{(n+1)}.
\end{aligned} \tag{7.17}$$

First, the velocities $\mathbf{u}_{\text{pp},i}^{(n+\frac{1}{2})}$ are determined at an intermediate time step using the velocities $\mathbf{u}_{\text{pp},i}^{(n)}$ and the accelerations $\mathbf{a}_{\text{pp},i}^{(n)}$ in the current time step t^n . Subsequently, the positions of the particles at the next time step $\mathbf{x}_{\text{pp},i}^{(n+1)}$ are determined by means of the calculated intermediate velocities. Since the positions of the particles $\mathbf{x}_{\text{pp},i}^{(n+1)}$ are now known, the distance between each two contacting particles δ_n can be determined facilitating the computation of the interaction forces described above and thus the accelerations of the particles $\mathbf{a}_{\text{pp},i}^{(n+1)}$. Finally, the velocities $\mathbf{u}_{\text{pp},i}^{(n+1)}$ at the new time step are determined with the help of the intermediate velocities $\mathbf{u}_{\text{pp},i}^{(n+\frac{1}{2})}$ and the accelerations $\mathbf{a}_{\text{pp},i}^{(n+1)}$.

An appropriate choice of the time-step size Δt_{DEM} is important in DEM to ensure that collisions between particles are properly detected and resolved. For this purpose, the elastic-response (Hertz) time scale (Li et al., 2011) and the Rayleigh-wave time scale (Li et al., 2005) are commonly used in the literature to determine the time-step size. The former considers the duration of a collision between two elastic spheres and the latter determines the time step based on the Rayleigh wave velocity. In this work, the time step is restricted to a maximum of 5% of any of the two characteristic time scales.

Owing to the different sizes of the primary particles and the wide range of the impact velocities, a broad spectrum of time-step sizes can be utilized. However, the time-step size in all DEM simulations is fixed at a small value of $\Delta t_{\text{DEM}} = 10^{-11}$ s. Unifying the time-step size eases the preprocessing of the extensive number of simulations. In addition, such a small value is needed for some cases with a relatively small particle diameter and a high impact velocity due to the high modulus of elasticity considered (see Table 7.1). Based on this time-step size, the displacement (normalized by the particle diameter) of a particle within a single time step varies between $2 \cdot 10^{-9}$ and $3 \cdot 10^{-4}$ depending on the total impact velocity.

7.2.2 Properties of the Particles and the Agglomerates

The objective of the present reference DEM simulations is to devise wall-impact breakage models to be applied in the intended Euler–Lagrange computations. Hence, the properties of the primary particles and the agglomerates used in the reference simulations are inspired by the conditions to be considered in the Euler–Lagrange simulations.

The primary particles are assumed to possess the properties of dry silica particles. In order to investigate the influence of cohesion on the breakage behavior, the magnitude of the cohesive van-der-Waals force is regulated by considering different sizes of the primary particles over a certain range instead of varying the material-specific Hamaker constant. Accordingly, the diameter of the primary particles is varied between 0.97, 2.47 and 5.0 μm . The corresponding cohesive agglomerates are denoted as powder **A**, **B** and **C**, respectively. The motivation for choosing silica particles with the given particle sizes is an experimental investigation on the breakage of agglomerates in a lab-scale disperser (Weiler, 2008). This experimental setup will be numerically simulated in the present work (see Section 9.1), and the same particle properties will be applied for the two remaining test cases (see Sections 9.2 and 9.3). The mechanical properties and other characteristic parameters used are listed in Table 7.1. Here, the cut-off distance l_{\max} for the van-der-Waals force $\mathbf{F}_{n,ij}^{\text{vdW}}$ (see Section 7.2.1) is set to $5 \cdot 10^{-2} d_{\text{pp}}$. This condition is chosen since according to Eq. (7.16) it can be readily shown that for the given material properties and particle size range the van-der-Waals force already drops several orders of magnitudes over this distance.

A prerequisite for the DEM wall-impact simulation is the generation of agglomerates with properties equivalent to those considered in the Euler–Lagrange methodology (see Chapter 5). More specifically, agglomerates possessing a nearly spherical structure and consisting of monodisperse particles are needed. In order to generate such agglomerates, a three-step procedure is carried out.

In the *first step*, the spherical packing process (e.g., Yang et al., 2008, among others) is applied. The packing process starts with a random placement of 10^4 non-overlapping monodisperse particles in a spherical domain of a certain size leading to an overall porosity of 0.92. Under the absence of gravity, the particles are dragged towards the center of the spherical domain by steadily imposing a centripetal force equal to the particle’s weight. The van-der-Waals force between particles is taken into account from the beginning of the process to effectively realize the influence of cohesion on the resulting structure. The packing process continues until all particles are found at stable positions, whereby the kinetic energy of the system drops to zero due to damping by dissipation.

To validate the DEM technique including the implementation of the van-der-Waals force, the structures of the generated agglomerates are compared against those reported by Yang et al. (2008) for comparable particle properties. The comparison takes the average coordination number k_c and the packing fraction f_{pack} (see the definitions in Section 5.1) into account.

The results depicted in Fig. 7.2 indicate that the structural properties of the generated agglomerates and those by Yang et al. (2008) agree quite well both qualitatively and quantitatively. This is in particular true considering the (slight) differences between the two studies with respect to the material properties, the models of the contact interactions, and other simulation parameters. From a physical point of view, the final structure of the agglomerate is dictated by the competition between the compression by the packing (centripetal) force and other mechanisms hindering the restructuring and compaction (Yang et al., 2008). The latter includes the friction enhanced by the cohesion between

Tab. 7.1. Properties and other characteristic parameters of the considered silica particles (SiO_2) used in the DEM wall-impact simulations.

Parameter	Unit	Powder A	Powder B	Powder C
Primary particle diameter d_{pp}	m	$0.97 \cdot 10^{-6}$	$2.47 \cdot 10^{-6}$	$5.08 \cdot 10^{-6}$
Primary particle density ρ_{pp}	$\text{kg}\cdot\text{m}^{-3}$		2000	
Poisson's ratio ν_s	-		0.17 ^e	
Modulus of elasticity E_s	N/m^2		$7.2 \cdot 10^{10}$ ^e	
Normal restitution coefficient e	-		0.97 ^c	
Static friction coefficient μ_s	-		0.94 ^f	
Rolling friction coefficient μ_r	-		$2 \cdot 10^{-3}$ ^d	
Hamaker constant H	J		$2.148 \cdot 10^{-20}$ ^a	
Min. inter-particle distance δ_0	m		$4.0 \cdot 10^{-10}$ ^b	
Cut-off distance l_{max}	m		$5 \cdot 10^{-2} d_{\text{pp}}$	

^aSchubert (2003) for the interaction between two pure silica spheres in vacuum, ^bKrupp (1967), ^cFoerster et al. (1994) for soda-lime-silica glass, ^dYang et al. (2008) for a material with comparable properties, ^eAzomaterials.com (2018), ^fSerway and Vuille (2007) approximated for glass on glass.

particles. During the packing process the centripetal force is set equal to the weight of the particle and thus scales with the cube of the particle diameter d_{pp} , whereas the van-der-Waals force varies linearly with d_{pp} as apparent in Eq. (7.16). Thus, by enlarging the particle diameter higher packing fractions and coordination numbers are obtained. At larger d_{pp} , the cohesive force becomes negligible with respect to the weight of the particle. Consequently, the friction force is no longer affected by cohesion and the packing process is solely constrained by the limit introduced due to friction. As visible in Fig. 7.2, for the particle properties and parameters used in the present study, a further increase of the particle diameter raises the packing fractions and coordination numbers towards the maximum theoretical values of a random packing in a weaker manner than in Yang et al. (2008).

Since the influence of the size of the agglomerate on the impact breakage is of specific interest, agglomerates of varying numbers of primary particles are required. For this purpose, in the *second step* of the three-step procedure mentioned above the repetition of the time-consuming DEM packing process for generating many agglomerates of varying size is avoided. Instead, the initial packing consisting of 10^4 particles is post-processed in order to artificially extract a series of smaller agglomerates. This is done by a gradual accumulation of particles starting from a single particle located at the center of the 10^4 particle agglomerate. Subsequently, the particles which are in contact with at least one particle of the current configuration are detected, and the nearest among them to the center of mass of the current configuration is sampled to obtain the next larger agglomerate. The described procedure is applied to the agglomerates of powders **A**, **B** and **C** to

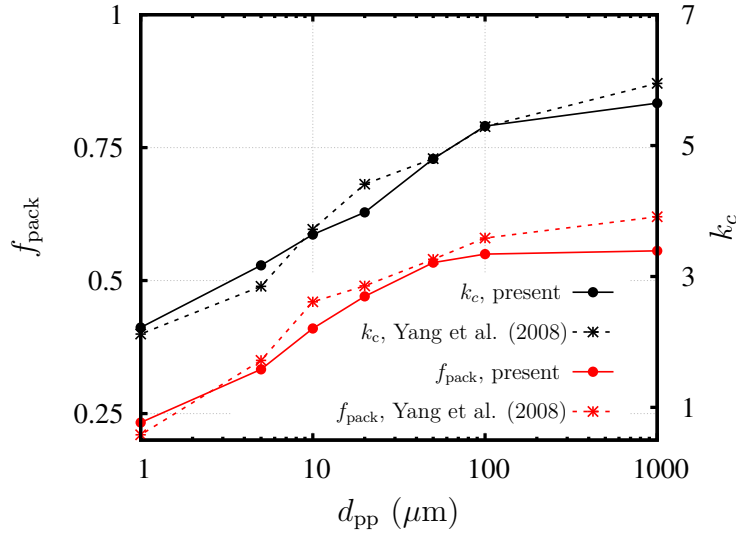


Fig. 7.2. Comparison between the agglomerates obtained in the present study and those reported in Yang et al. (2008) concerning the packing fraction f_{pack} and the coordination number k_c . The data refer to seven agglomerates consisting of 10^4 equally-sized primary particles possessing the size d_{pp} given by the abscissa. As previously pointed out, in the present work a contact is detected if two particles are within the force cut-off distance l_{max} (i.e., $\delta_n/d_{\text{pp}} \leq -5 \cdot 10^{-2}$). However, the values of k_c here are computed restricting the criterion for counting a contact to $\delta_n/d_{\text{pp}} \leq -5 \cdot 10^{-3}$ in order to match the condition in Yang et al. (2008). The packing fraction $f_{\text{pack}} = N_{\text{pp}}^{\text{tot}} V_{\text{pp}}/V_{\text{ag}}$ of the agglomerates generated in the present work are computed assuming that the total volume of the agglomerate V_{ag} is equal to the volume of the convex hull closely wrapped around the primary particles (Dadkhah et al., 2012; Dietzel and Sommerfeld, 2013). The volume of the convex hull is computed using the built-in function `convhull` available in MATLAB®.

generate smaller agglomerates to be used in the analysis of the impact breakage.

In the *third step*, the agglomerates obtained are loaded into the DEM impact simulation environment and positioned at a certain distance to the target wall. The distance is chosen sufficiently far away from the wall to allow the agglomerates to relax and find a stable state under their new network of interactions before reaching the wall.

7.2.3 Wall-Impact Simulation Setup and Procedure

The impact simulations are carried out inside a 3D cuboid domain possessing a wall-type boundary condition on two opposite sides and periodic boundary conditions on the other four sides. In general, the size of the domain is chosen based on a compromise between the associated computational costs and the size of the investigated agglomerate. Nevertheless, it is taken into account that secondary impact events of the fragments bouncing from the impact wall towards the opposite wall are prevented. In addition, it is ensured that the influence on the results by artificial collisions between particles crossing the periodic

boundaries is negligible. As an example, the dimensions of the domain in the case of the agglomerates with 10^4 particles of powder **C** is set to $235 d_{pp} \times 235 d_{pp} \times 135 d_{pp}$ in the two periodic directions and the wall-normal direction, respectively.

The parameters of the target wall, such as the elastic properties (i.e., E_s , ν_s), the static wall friction coefficient μ_s and the wall-normal restitution coefficient e are set equal to those of the silica particles given in Table 7.1. However, the wall is assumed to be cohesionless in order to eliminate the influence of the particle-wall deposition phenomenon on breakage. In addition, the particle-wall rolling friction (see Eq. (7.15)) is neglected. This assumption is due to the lack of information on the particle-wall rolling friction coefficient. To evaluate the influence of the latter assumption on the breakage, additional simulations were conducted while considering a rolling friction coefficient of the wall equal to that of the particles ($\mu_r = 2 \cdot 10^{-3}$). As expected, very marginal deviations are found which do not lead to any change in the trends or the conclusions drawn, which justifies neglecting the rolling friction for the particle-wall contact.

The DEM simulations are carried out in a vacuum environment ignoring the gas drag on the agglomerates and their impact events. The motivation is to focus on the breakage behavior arising due to the kinetics of the agglomerate, isolated from other external effects. Note, however, that within the multiphase simulation framework in which the derived models are finally applied, the fluid forces acting on the agglomerate and the resulting fragments are of course taken into account. Consequently, the assumption of a vacuum environment solely applies to the pure breakage event of the reference DEM simulations and not to the LES Euler–Lagrange simulations.

The general DEM wall-impact setup is depicted in Fig. 7.3. The simulations start by placing the agglomerate within a certain distance from the target wall which, as mentioned before, still allows a relaxation and stabilization phase of the agglomerate before reaching the wall. A pre-defined impact velocity is imposed on the agglomerate and the effect of gravity is neglected. In order to reproduce the whole spectrum of breakage patterns from an unrecognizable damage to a complete deagglomeration, the range of the wall-normal impact velocities $v_{imp,n}$ is varied between 0.01 and 150 m/s depending on the other parameters. Seven different impact angles Θ_{imp} are considered covering the range of a flat angle (0.2°) to a normal impact (90°). For each of the described cases agglomerates incorporating a specific number of primary particles N_{pp}^{tot} varying between 2 and 10^4 are investigated. In addition, the influence of cohesion between the particles is accounted for by changing the size of the primary particles according to the different powders **A**, **B** and **C**. Note that the impact cases taken into account for the derivation of the breakage model based on typical regression (see Section 7.4) and the ANN-based model (see Section 7.5) slightly differ. The details of the considered cases and the motivation for the selection of the cases are given in the corresponding sections.

The breakage process is assumed to be completed when no more changes in the kinetic energy of the system and in the number of generated fragments take place (Moreno-Atanasio, 2012). To ensure meaningful statistics, each impact event is repeated multiple times while changing the location of the impact point on the surface of the agglomerate. This is achieved by rotating the agglomerates by a certain angle prior to the start of the simulation. For the spherical packing procedure adopted for generating the agglomerates,

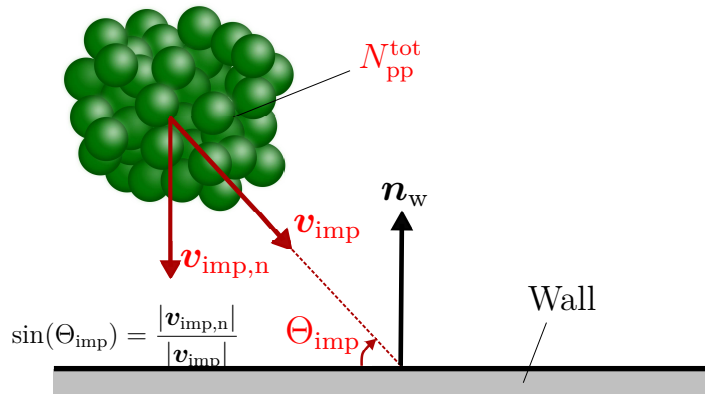


Fig. 7.3. General setup of the DEM wall-impact simulations (Khalifa and Breuer, 2021).

the larger the agglomerate is, the higher is its sphericity. Thus, the role of the orientation of the agglomerate with respect to the impact wall becomes less significant. Accordingly, the number of investigated impact points for each agglomerate size decreases with an increasing number of particles in the agglomerate. For this reason and due to the large associated computational costs, solely a single impact point is considered for agglomerates consisting of 10^4 particles.

7.3 Breakage Parameters

The typical outcomes of a DEM simulation are instantaneous quantities such as the velocity and position vectors as well as the number of contacts for each primary particle. In order to characterize phenomena like the wall-impact breakage, additional parameters describing the change of the properties of the agglomerates (e.g., velocity and number of contacts) as a result of the impact at the wall must be introduced and evaluated. In Section 7.3.1, the parameters considered to quantify the results with respect to the number of fragments and the fragment size distribution (modeling tasks **i** and **ii**) are given. In addition, the parameters describing the post-breakup velocity of the fragments (modeling tasks **iii**) are explained in Section 7.3.2.

7.3.1 Number of Fragments and Fragment Size Distribution

The main parameter used to quantify the outcome of breakage is based on the number of generated fragments (Moreno et al., 2003) providing a first hint on the resulting fragment size distribution. Therefore, the fragmentation ratio (FR) is introduced, which is defined as the maximum number of fragments generated by breakage divided by the maximum number of attainable fragments (excluding the donating agglomerate from both numbers):

$$FR = \frac{N_{fr}^{max} - 1}{N_{pp}^{tot} - 1}. \quad (7.18)$$

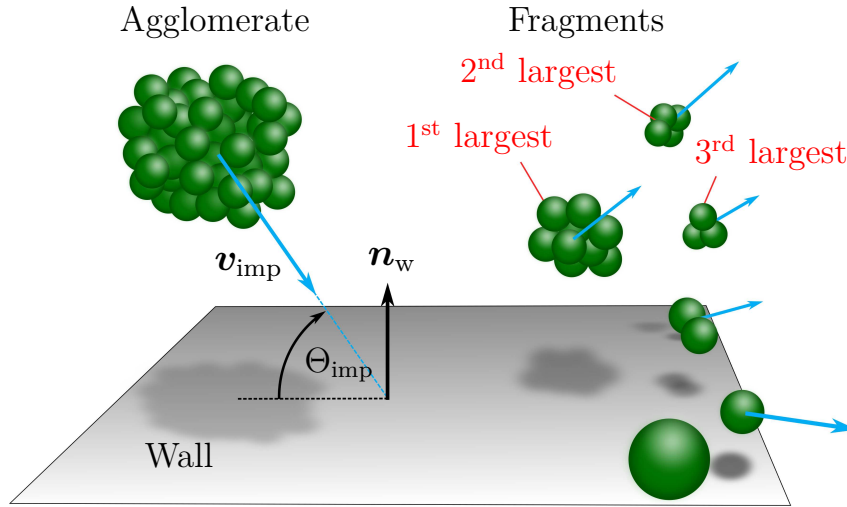


Fig. 7.4. Characterization of the results of wall-impact events using the number of fragments and the size of the three largest fragments (Khalifa and Breuer, 2021).

Here, $N_{\text{fr}}^{\text{max}}$ stands for the largest number of fragments (including the donating agglomerate) detected over the course of the DEM simulation since the number of fragments varies in time due to reagglomeration. Note that the maximum number of fragments ($N_{\text{fr}}^{\text{max}}$) is chosen instead of the steady-state value because agglomeration is accounted for by a separate model the Euler–Lagrange simulations. Hence, the definition (7.18) of the fragmentation ratio focuses on the breakage. In this context, a fragment denotes a structure moving as a single entity. Hence, as illustrated in Fig. 7.4 a fragment can be a single detached primary particle or a cluster of particles, in which each particle is within the force cut-off distance l_{max} of at least one other particle.

Furthermore, the sizes of the individual fragments can be characterized using a cumulative parameter:

$$\zeta_i = \frac{N_{\text{pp}}^{\text{tot}} - \sum_{j=1}^i N_{\text{pp}}^j}{N_{\text{pp}}^{\text{tot}} - i}. \quad (7.19)$$

Its numerator expresses the number of primary particles of the agglomerate excluding the particles belonging to the first i largest fragments. The denominator represents the maximum possible number of particles which can exist beside the first i largest fragments assuming that all fragments are single primary particles (full fragmentation). Note that the analysis is restricted to the three largest fragments so that i runs from 1 to 3 (see Fig. 7.4).

If ζ_1 is zero, the number of particles in the largest fragments N_{pp}^1 is equal to the total number of particles in the original donating agglomerate $N_{\text{pp}}^{\text{tot}}$ indicating no breakage. A value of unity of ζ_1 denotes that the largest fragment is a primary particle suggesting a full deagglomeration. For any intermediate value the number of particles in the largest fragment (i.e., the donating agglomerate) can be calculated based on Eq. (7.19). Concerning ζ_2 , a zero value means that the impact leads to two fragments only, whereas ζ_2

equal unity tells that both the first and second largest fragments are primary particles and thus a full deagglomeration is taking place. For values of ζ_2 between zero and unity the number of particles in the second largest fragment can be computed based on the number of particles in the first largest fragment. In this case, the second largest fragment can be a single particle so that the rest of the fragments are also primary particles. The same logic applies to ζ_3 . Note that for the case of a two-particle agglomerate the values of ζ_2 and ζ_3 for the second and third largest fragments are no longer defined. Similarly, ζ_3 is not defined for an agglomerate consisting of three primary particles.

The introduction of the above described four parameters (i.e., FR, ζ_1 , ζ_2 , ζ_3) leads to a useful modeling concept. Namely, if relationships for predicting the fragmentation ratio FR and the size ratios (ζ_1 , ζ_2 and ζ_3) as functions of the impact conditions are available, the resulting number of fragments and the sizes of the three largest fragments generated by an impact event can be adequately determined. If more than three fragments arise due to the impact and the third largest fragment is not a primary particle, the rest of the fragments can exist in the form of multiple-particle fragments, single particles, or a mixture of both. The size distribution of the remaining fragments can then be statistically described by, e.g., a random distribution function (details in Section 7.4.1.3). Consequently, the number of resulting fragments due to wall impact and the size distribution of the fragments can be reasonably forecasted in the Euler–Lagrange simulation framework. Since full DEM simulations for particle-laden flows with high mass loadings are too CPU-time intensive, the proposed model allows to bridge this gap.

7.3.2 Post-Breakage Kinetics

The starting point of the analysis is to collect the velocity vectors of the fragments after a breakage event at the same time instant at which the fragmentation ratio and the fragment size parameters are analyzed for deriving the size distribution model discussed above. That is the time instant at which the largest number of fragments appears for the first time. This ensures that the overall description of breakage is consistent and limits the influence of inter-particle collisions after breakage on the obtained statistics.

Consequently, the post-breakage velocity of the fragments is described with reference to the impact velocity vector of the original agglomerate based on three quantities: A velocity ratio v_{ratio} and two characteristic angles α and β depicted in Fig. 7.5. Here, the velocity ratio refers to the ratio between the magnitude of the velocity of the center of mass of the fragment $v_{\text{cm}}^{\text{fr}}$ to the velocity magnitude of the agglomerate v_{imp} before impact:

$$v_{\text{ratio}} = \frac{|\mathbf{v}_{\text{cm}}^{\text{fr}}|}{|\mathbf{v}_{\text{imp}}|} = \frac{v_{\text{cm}}^{\text{fr}}}{v_{\text{imp}}} . \quad (7.20)$$

The angle α denotes the reflection angle, which describes the inclination of the velocity vector of a fragment with respect to the wall. The second angle β is referred to as the spreading angle and measures the angular displacement of the post-breakage velocity vector of a fragment with respect to the velocity vector of the original agglomerate in the

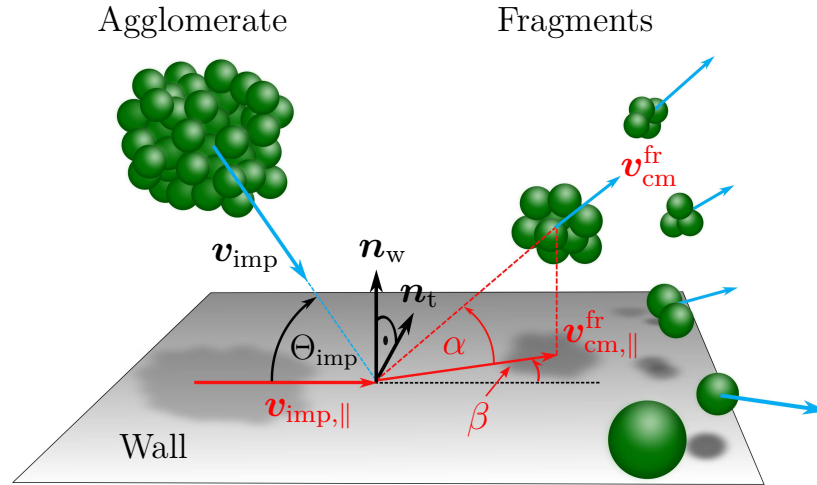


Fig. 7.5. Schematic representation of the reflection angle α , the spreading angle β , and the velocity of the center of mass of a fragment $\mathbf{v}_{\text{cm}}^{\text{fr}}$, respectively. Note that \mathbf{n}_t , $\mathbf{v}_{\text{imp},\parallel}$, and $\mathbf{v}_{\text{cm},\parallel}^{\text{fr}}$ are spanning the wall plane (Khalifa and Breuer, 2021; Khalifa et al., 2022).

wall plane. Thus, for determining the angle β , the projection $\mathbf{v}_{\text{imp},\parallel}$ of the impact velocity vector of the original agglomerate onto the plane of the wall is introduced:

$$\mathbf{v}_{\text{imp},\parallel} = \mathbf{v}_{\text{imp}} - (\mathbf{v}_{\text{imp}} \cdot \mathbf{n}_w) \mathbf{n}_w, \quad (7.21)$$

where \mathbf{n}_w is the wall-normal unit vector. In addition, the projection of the fragment velocity vector $\mathbf{v}_{\text{cm}}^{\text{fr}}$ onto the wall plane is required. The latter reads:

$$\mathbf{v}_{\text{cm},\parallel}^{\text{fr}} = \mathbf{v}_{\text{cm}}^{\text{fr}} - (\mathbf{v}_{\text{cm}}^{\text{fr}} \cdot \mathbf{n}_w) \mathbf{n}_w. \quad (7.22)$$

The spreading angle β is then obtained based on the definition of the scalar product as follows:

$$\beta = \arccos \left(\frac{\mathbf{v}_{\text{cm},\parallel}^{\text{fr}} \cdot \mathbf{v}_{\text{imp},\parallel}}{|\mathbf{v}_{\text{cm},\parallel}^{\text{fr}}| |\mathbf{v}_{\text{imp},\parallel}|} \right), \quad (7.23)$$

leading to values between 0° and 180° . This means that the analysis of this angle does not account for a possible spreading in all directions covering only half of the potential physical range of this angle. To represent the full range, i.e., $\beta \in [-180^\circ, 180^\circ]$, the sign of the angle β has to be adjusted according to the sign obtained by the scalar product between the projected velocity vector of the fragment $\mathbf{v}_{\text{cm},\parallel}^{\text{fr}}$ and the tangential unit vector \mathbf{n}_t . The latter is determined by the cross-product $\mathbf{n}_t = \mathbf{n}_w \times \mathbf{v}_{\text{imp},\parallel}$. As expected, however, the analysis of the DEM results confirms that for a certain breakage event, the distribution of β for the arising fragments is (nearly) symmetric with respect to the direction of $\mathbf{v}_{\text{imp},\parallel}$. This observation is exploited to neglect the sign of β again (i.e., $\beta \in [0^\circ, 180^\circ]$), since the distributions are represented in a later modeling step (see Section 7.4.2.2) by a two-parameters Weibull probability density function (PDF), which is not defined for negative

values. To retrieve the full range of angles in the Euler–Lagrange computations intended by the breakage model, the sign of β predicted by the Weibull PDF is alternately inverted (more details in Section 7.4.1.3).

Lastly, the reflection angle α varies between 0° and 90° and is computed as:

$$\alpha = \arccos \left(\frac{\mathbf{v}_{\text{cm}}^{\text{fr}} \cdot \mathbf{v}_{\text{cm},\parallel}^{\text{fr}}}{|\mathbf{v}_{\text{cm}}^{\text{fr}}| |\mathbf{v}_{\text{cm},\parallel}^{\text{fr}}|} \right). \quad (7.24)$$

It is worth pointing out that v_{ratio} , α , and β are defined for each fragment separately. This means that a single breakage event leads to a range of values of these three parameters. Consequently, probability density distributions can be used to describe the collective behavior of the fragments arising under certain breakage circumstances.

7.4 Model Based on Traditional Regression Techniques

The wall-impact breakage model discussed in this section relates the breakage parameters (see Section 7.3) to the impact conditions relying on conventional techniques. The first part of the model is devoted to the number and size distribution of the fragments (see Section 7.4.1), whereas the second part addresses the post-breakage velocity issue (see Section 7.4.2).

7.4.1 Fragmentation Ratio and Fragment Size Parameters

The first part of the breakage model focuses on establishing mathematical relations describing the breakage parameter, i.e., the fragmentation ratio FR and the fragment size parameter ζ_i as functions of the impact conditions. After the clarification of the impact cases considered for the analysis in Section 7.4.1.1, the general trends obtained are analyzed in Section 7.4.1.2 and the corresponding model is proposed in Section 7.4.1.3.

7.4.1.1 Wall-Impact Database

The analysis of the fragmentation ratio FR and the fragment size parameter ζ_i accounts for the breakage behavior of agglomerates consisting of $N_{\text{pp}}^{\text{tot}}$ particles varying between 10 and 10^4 of each powder **A**, **B**, and **C** while varying the impact angle Θ_{imp} between 7° and 90° . Table 7.4 lists the conditions in detail. The normal impact velocity $v_{\text{imp},n}$ is given by a range leading to cases varying between no breakage (FR = 0) to full deagglomeration (FR = 1). Note that any combination of parameters (i.e., d_{pp} , $N_{\text{pp}}^{\text{tot}}$, Θ_{imp}) in Table 7.4 with a certain impact velocity defines a separate impact case. Each case is repeated up to eight times considering different impact points on the surface of the agglomerate to ensure reliable statistics. In total, about 15,000 independent simulations are carried out delivering almost 2500 averaged cases to be used in the analysis.

Tab. 7.2. Overview of the impact conditions used for analyzing the breakage behavior concerning the fragmentation ratio FR and the fragment size parameter ζ_i .

Parameter	Investigated values
d_{pp}	0.97 μm (A), 2.47 μm (B), 5.08 μm (C)
N_{pp}^{tot}	10, 25, 50, 100, 200, 500, 10^3 , 10^4
Θ_{imp}	7° , 15° , 30° , 45° , 60° , 75° , 90°

7.4.1.2 Trend Analysis

In order to investigate the dependence of the breakage behavior on key impact conditions, the fragmentation ratio is plotted against the normal component of the impact velocity in Fig. 7.6 for a set of selected cases in which N_{pp}^{tot} and $v_{\text{imp},n}$ are varied. The values depicted represent the fragmentation ratio obtained for agglomerates of powder **A**, **B** and **C** consisting of 50 to 10^4 primary particles averaged over multiple impact events to improve the statistics (as explained in Section 7.2.3), and the bars refer to the standard deviations.

First, increasing the impact velocity leads to higher fragmentation ratios for all considered cases as expected. This trend is well established in the literature and is mainly attributed to the higher incident kinetic energy available for inducing breakage. Furthermore, Fig. 7.6 reveals that for a fixed impact angle, impact velocity and number of particles included in the agglomerate, a decrease of the size of the primary particles (**C** to **A**) results in a lower fragmentation ratio. This behavior can be explained referring to the theories on the strength of agglomerates, e.g., Rumpf (1962) and Kendall (1988). In these theories and the subsequent literature an inverse relationship between the strength of the agglomerate and the diameter of the primary particles is concluded. Practically, the breakage of agglomerates is ruled by the ratio between the cohesive van-der-Waals force and the external forces acting on the particles such as the repulsive force. The latter is proportional to the inertia of the agglomerate. Since the dependence of the inertia force on the particle diameter (cubic relationship) is stronger than that of the van-der-Waals force (linear relationship), the larger the diameter is the less significant the cohesive force is. Consequently, a higher possibility for breakage exists for agglomerates consisting of larger primary particles.

Moreover, the influence of the number of constituting particles N_{pp}^{tot} on the breakage behavior shall be analyzed. In principle, the incident kinetic energy of the agglomerate increases linearly with the number of constituting particles (mass) implying a higher potential for breakage. However, when the number of particles increases, a larger amount of work is dissipated by the internal collisions and friction between the particles, since the number of bonds also approximately increases linearly with the number of primary

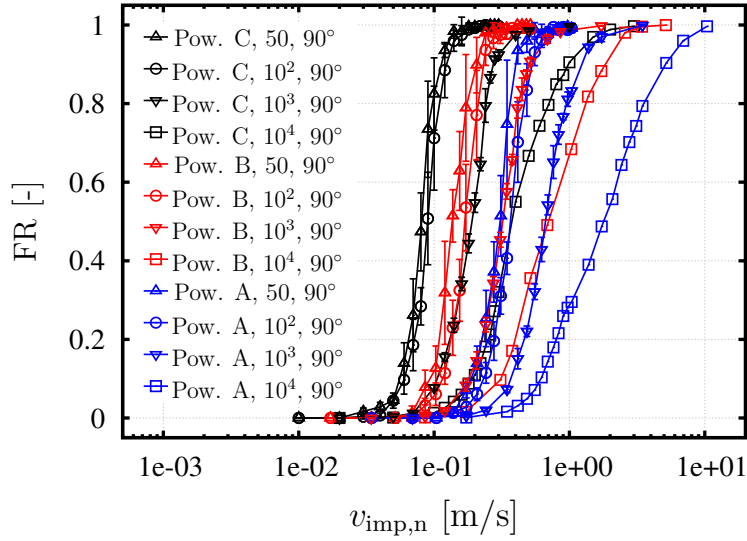


Fig. 7.6. Fragmentation ratio FR as a function of the impact velocity $v_{\text{imp},n}$ for a normal impact of agglomerates of powder **A**, **B** and **C** consisting of 50 to 10^4 primary particles. No error bars appear for the 10^4 particle agglomerates since solely a single impact was considered (see Section 7.2.3).

particles. For this reason, it is difficult to make a general statement on the effect of the number of particles on the breakage behavior. This is especially true since other relevant structural properties such as the coordination number and the packing fraction vary with the number of included particles as well. The results depicted in Fig. 7.6 show that for the same impact velocity and primary particle diameter the fragmentation ratio decreases with the number of particles included in the agglomerate. However, since the fragmentation ratio is a function of the number of primary particles included in the agglomerate (see Eq. (7.18)), different insights can be obtained by comparing the number of detached fragments (the numerator in Eq. (7.18)) for the different cases.

Fig. 7.7 depicts this quantity ($N_{\text{fr}}^{\text{max}} - 1$) as a function of the number of particles in the agglomerate. The results suggest that the onset of breakage occurs for all agglomerates at a similar velocity. In fact, the smallest agglomerate ($N_{\text{pp}}^{\text{tot}} = 10$) starts to break up at a slightly higher velocity than the larger agglomerates. Looking at Fig. 7.7 it can be seen that for a given velocity in the lower velocity range the number of detached fragments is roughly constant. Thus, only a negligible variation of $N_{\text{fr}}^{\text{max}}$ with the number of particles in the original agglomerates is observed. However, at larger impact velocities the number of detached fragments ($N_{\text{fr}}^{\text{max}} - 1$) for smaller agglomerates ($N_{\text{pp}}^{\text{tot}} < 200$) reaches its asymptotic value. For larger agglomerates, the number of detached fragments starts to increase with the number of particles, whereby the slope increases with the impact velocity. This behavior is consistent with the observations by Moreno (2003) and Moreno-Atanasio (2012) who based on DEM simulations found a linear relationship between the number of broken contacts and the number of included primary particles with a slope increasing with the impact velocity. Overall it can be concluded from Fig. 7.7 that the relationship between the number of detached fragments and the size of the original agglomerate is

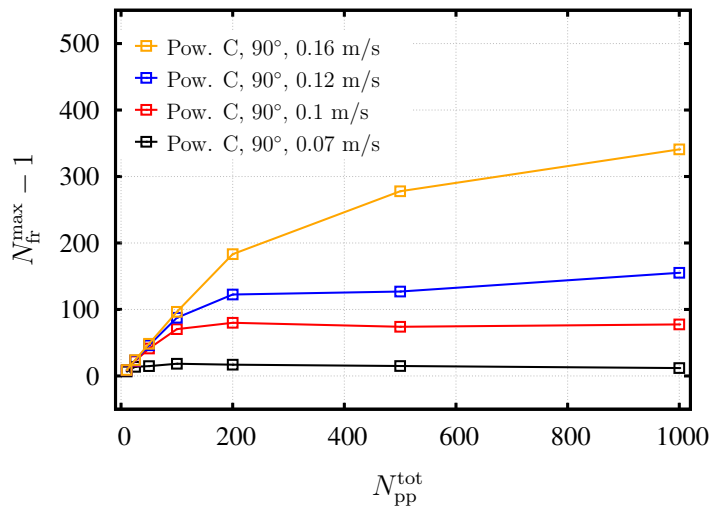


Fig. 7.7. Number of detached fragments (the numerator in Eq. (7.18)) as a function of the impact velocity $v_{imp,n}$ for agglomerates of powder **C** consisting of 25 to 10^3 primary particles undergoing a normal impact.

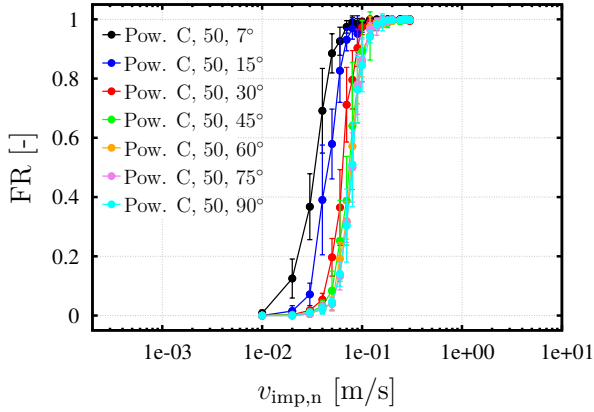
complex since it differs based on the impact velocity.

Next, the role of the impact angle Θ_{imp} is investigated. For this purpose, simulations of oblique impacts are carried out, in which the normal components of the impact velocity are fixed to the values considered for the normal impact cases. Thus, to achieve a certain impact angle, a corresponding tangential velocity component is added to the normal component. Fig. 7.8 presents exemplary results corresponding to two agglomerates of powder **C** consisting of 50 and 10^3 particles impacting with varying angles Θ_{imp} . The results depicted in Figs. 7.8(a) and 7.8(c) indicate that at a certain normal component of the impact velocity, identical agglomerates experience a stronger fragmentation when decreasing the impact angle, which is accompanied by an increase of the total impact velocity magnitude. The effect becomes more pronounced for impact angles smaller than 45° , where the tangential component of the impact velocity is equal to the normal component.

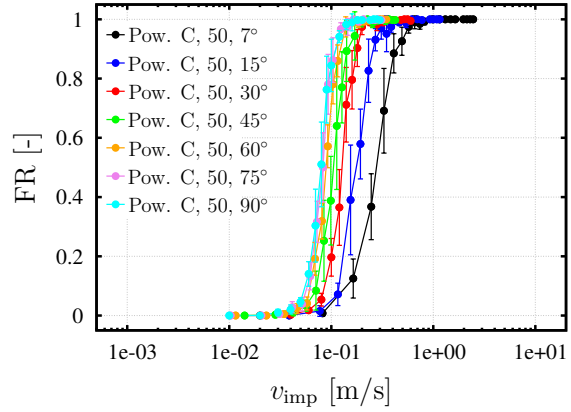
Alternatively, plotting the same data based on the total velocity as presented in Figs. 7.8(b) and 7.8(d) leads to a reversed trend. Specifically, the fragmentation ratio increases effectively with the impact angle for an equal magnitude of the total impact velocity until $\Theta_{imp} = 45^\circ$. Beyond this angle, the increase becomes clearly less significant.

In general, the obtained trends coincide with numerical DEM predictions by Moreno et al. (2003), who found that for impact events with the same normal component of the impact velocity, the number of detached fragments decreases with an increasing impact angle. In addition, for an increasing total impact velocity Moreno et al. (2003) found that the number of broken contacts inside the agglomerates generally increases.

According to these conclusions, both the tangential and the normal component of the impact velocity play certain roles in the breakage process. Hence, both components should be considered in the subsequent modeling (see Section 7.4.1.3).



(a) Normal component of the impact velocity, agglomerates consisting of 50 particles



(b) Total impact velocity, agglomerates consisting of 50 particles

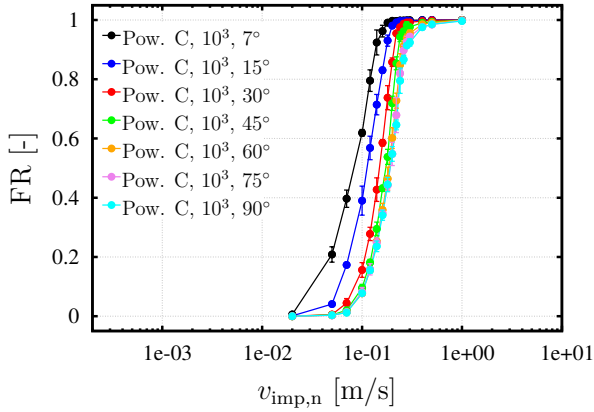
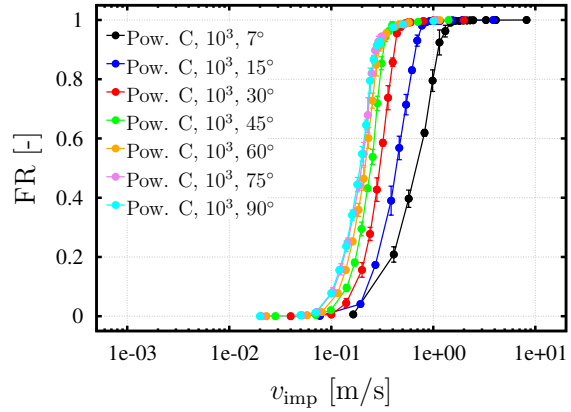
(c) Normal component of the impact velocity, agglomerates consisting of 10^3 particles(d) Total impact velocity, agglomerates consisting of 10^3 particles

Fig. 7.8. Fragmentation ratio FR as a function of the normal component of the impact velocity $v_{\text{imp},n}$ (a, c) and as a function of the total impact velocity v_{imp} (b, d) for two exemplary agglomerates of powder **C** consisting of 50 or 10^3 primary particles impacting with varying impact angles Θ_{imp} .

7.4.1.3 Derived Model

The wide scattering of the results depicted in Figs. 7.6 and 7.8 illustrates the multivariate nature of the wall-impact breakage problem. In other words, it is obvious that the outcome of an impact event is influenced by multiple factors (impact conditions). A common approach to deal with such problems utilizes dimensionless numbers. For this

purpose, a dimensional analysis of the relevant parameters is carried out leading to two dimensionless numbers:

$$\pi_1 = \frac{\rho_{\text{pp}} v_{\text{imp}}^2 d_{\text{pp}}^3}{H}, \quad (7.25)$$

$$\pi_2 = \frac{\rho_{\text{pp}} v_{\text{imp}}^2}{E_s}, \quad (7.26)$$

expressed based on the quantities of the primary particles and the total impact velocity v_{imp} . The former (π_1) represents a variant of the Weber number describing the ratio of the impact kinetic energy to the van-der-Waals interaction energy, whereas the latter (π_2) relates the specific kinetic energy of the impact to the elasticity of the particle interactions.

It is found that the deviations between the fragmentation ratios obtained for different primary particle sizes (powders **A**, **B** and **C**) can be strongly reduced by plotting the fragmentation ratio as a function of the product of π_1 and π_2 ($\pi^* = \pi_1 \cdot \pi_2$). In other words, the deviating fragmentation ratio curves obtained for agglomerates of different primary particle sizes nearly collapse onto a general curve when plotted as a function of $v_{\text{imp}}^4 \cdot d_{\text{pp}}^3$.

Furthermore, the proposed dimensionless number should improve the discrepancy of the breakage results obtained for agglomerates possessing different numbers of primary particles (see Fig. 7.6). For this purpose, the initial number of particles in the agglomerate $N_{\text{pp}}^{\text{tot}}$ has to be incorporated into π^* . To provide a base for this incorporation, the numbers of fragments ($N_{\text{fr}}^{\text{max}} - 1$) detached by a normal impact (i.e., numerator of FR) of agglomerates comprising 50 to 10^3 primary particles are plotted exemplarily for powder **C** in Fig. 7.9 as a function of the combined dimensionless number π^* .

Fig. 7.9 shows that at low values of the combined dimensionless number (corresponding to small impact velocities since all other material properties are fixed), a quasi-linear relationship between the number of detached fragments and π^* is obtained, in which the slope for all different agglomerates is nearly equal. This linear behavior continues up to a certain velocity threshold, after which the rate of increase starts to show a dependence on the velocity and the number of included particles. Finally, the number of detached fragments tends to approach the maximum number of attainable fragments in an asymptotic manner. It is worth mentioning that this kind of mixed trends has been reported before by Moreno (2003) concerning the evolution of the number of broken contacts depending on the impact velocity. Note that the range of π^* , where the transition to the non-linear behavior occurs, is relevant solely for large agglomerates since smaller ones experience a nearly full fragmentation within the linear range (see the black, red and blue curves in Fig. 7.9). In general, it is evident that for a specific agglomerate size, the number of detached fragments is a function of the dimensionless number π^* :

$$(N_{\text{fr}}^{\text{max}} - 1) = f_1(\pi^*). \quad (7.27)$$

Consequently, dividing both sides by the maximum number of attainable fragments

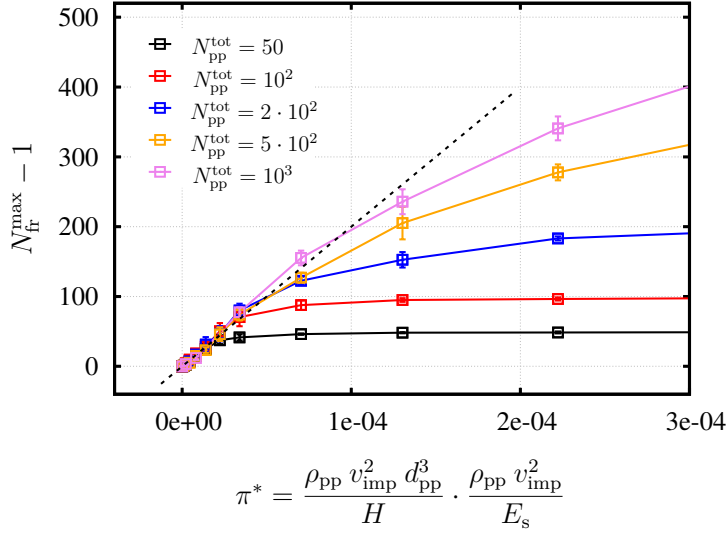


Fig. 7.9. Number of detached fragments (the numerator in Eq. (7.18)) as a function of the dimensionless number π^* for normally impacting agglomerates of powder **C** consisting of 50 to 10^3 primary particles. The dashed line refers to the slope of the number of detached fragments ($N_{fr}^{max} - 1$) at low values of π^* .

$(N_{pp}^{tot} - 1)$ leads to:

$$FR = f_2 \left(\pi^*, \frac{1}{N_{pp}^{tot} - 1} \right). \quad (7.28)$$

Hence, the fragmentation ratio can be expressed as a function of π^* and $1/(N_{pp}^{tot} - 1)$. Accordingly, a modified dimensionless number π^{**} is proposed based on the product of the latter two quantities:

$$\pi^{**} = \frac{\rho_{pp} v_{imp}^2 d_{pp}^3}{H} \cdot \frac{\rho_{pp} v_{imp}^2}{E_s} \cdot \frac{1}{(N_{pp}^{tot} - 1)}. \quad (7.29)$$

This dimensionless number, i.e., π^{**} is postulated to improve the representation of the breakage results obtained for agglomerates consisting of widely differing numbers of particles. However, the expression (7.29) suggests a proportionality between the square of the kinetic energy ($\sim v_{imp}^4$) and the fragmentation ratio FR. Such a formulation might be misleading since it refutes the fact that a fraction of the incident kinetic energy is consumed by the breakage process. Relying on the fact that the exponentiation of a dimensionless number does not alter the functional form, taking the square root of π^{**} leads to the new dimensionless number π^{***} :

$$\pi^{***} = \sqrt{\frac{\rho_{pp} v_{imp}^2 d_{pp}^3}{H} \cdot \frac{\rho_{pp} v_{imp}^2}{E_s} \cdot \frac{1}{(N_{pp}^{tot} - 1)}}. \quad (7.30)$$

To demonstrate the advantage of the proposed dimensionless number π^{***} , the fragmentation ratio for the cases presented in Figs. 7.6 are re-plotted as a function of π^{***}

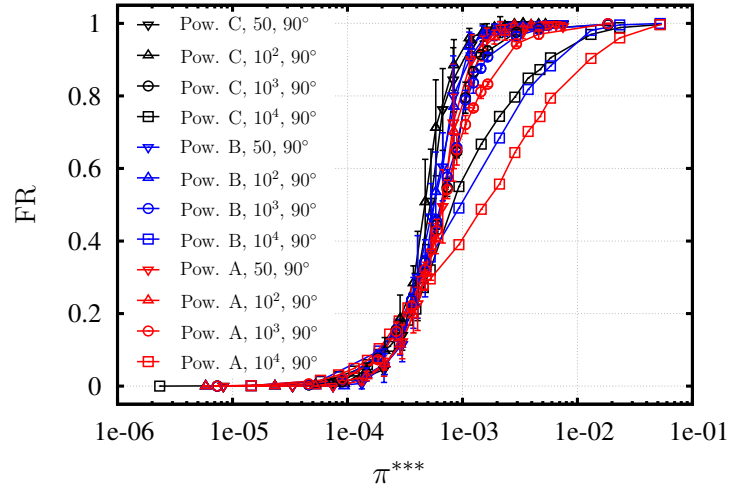


Fig. 7.10. Fragmentation ratio FR as a function of the proposed dimensionless number π^{***} (Eq. (7.30)) for selected agglomerates related to powders **A**, **B** and **C** comprising 50 to 10^4 primary particles for a fixed impact angle of $\Theta_{\text{imp}} = 90^\circ$ (Note that in this case $\pi^{***} = \pi_{\text{imp}}$).

in Fig. 7.10. Except the obvious deviations appearing for agglomerates comprising 10^4 primary particles for large values of π^{***} , an overall reasonable unification of the fragmentation ratio is achieved based on π^{***} . The observed deviations are evidently attributed to extensive re-agglomeration processes of the detached fragments in these cases, justifying their willful negligence as tackled in detail below.

Lastly, the effect of the impact angle has to be addressed. As discussed in Section 7.4.1.2, both the normal component of the impact velocity and the total velocity are contributing to breakage with a varying effectiveness (see Fig. 7.8). The total velocity and accordingly the tangential velocity component starts to play a notable role solely when its magnitude exceeds that of the normal component. The dimensionless number π^{***} is essentially formed out of the square root of the product of two numbers (π_1 and π_2). Each scales with the square of the impact velocity corresponding to the incident kinetic energy. The effect of the different velocity components and thus the impact angle can be appropriately accounted for by supposing that one of the two numbers refer to the kinetic energy in the direction normal to the impact instead of the total kinetic energy. Since the total and the normal velocities are related to each other by the sine of the impact angle, the dimensionless number π^{***} is modified leading to the final expression:

$$\begin{aligned} \pi_{\text{imp}} &= \sqrt{\frac{\rho_{\text{pp}} v_{\text{imp}}^2 d_{\text{pp}}^3}{H} \cdot \frac{\rho_{\text{pp}} v_{\text{imp}}^2}{E_s} \cdot \frac{\sin^2(\Theta_{\text{imp}})}{(N_{\text{pp}}^{\text{tot}} - 1)}} \\ &= \rho_{\text{pp}} v_{\text{imp}}^2 \sin(\Theta_{\text{imp}}) \sqrt{\frac{d_{\text{pp}}^3}{H E_s} \cdot \frac{1}{(N_{\text{pp}}^{\text{tot}} - 1)}}. \end{aligned} \quad (7.31)$$

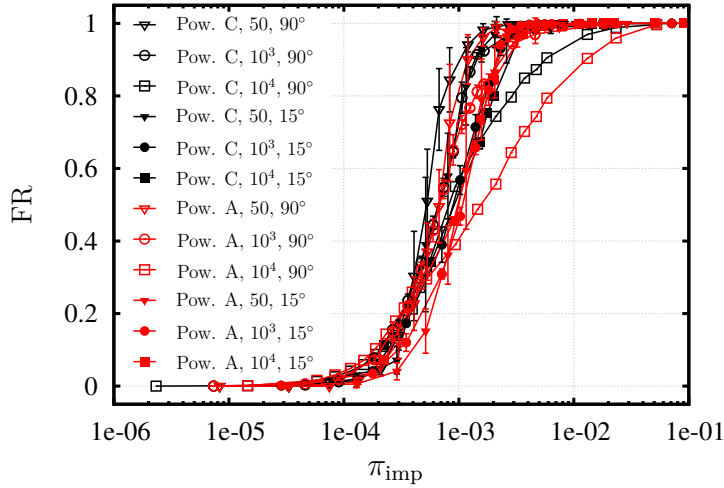


Fig. 7.11. Fragmentation ratio FR as a function of the proposed dimensionless number π_{imp} (Eq. (7.31)) for selected agglomerates related to powders **A** and **C** comprising 50 to 10^4 primary particles for two different impact angles Θ_{imp} (90° vs. 15°).

Note that for a normal impact the dimensionless numbers π^{***} and π_{imp} (Eq. (7.30)) are identical and thus the results shown in Fig 7.10 are still relevant. Fig. 7.11 shows the enhancement achieved by π_{imp} regarding the unification of the results obtained for strongly deviating impact angles (90° and 15°), especially when compared to the representation based on the total or the normal impact velocity shown in Fig. 7.8. Nevertheless, some deviations are detected especially for large impact angles π_{imp} and for large agglomerates as already discussed based on Fig. 7.10.

In summary, it is concluded that the proposed dimensionless number π_{imp} can be successfully utilized for providing a statistically reasonable description of the fragmentation ratio. Nevertheless, constraints are found. In particular, larger deviations appear with a recognizable pattern suggesting a growing disagreement for (1) an increasing number of constituting primary particles, (2) an increasing impact angle, and (3) a decreasing primary particle diameter. The discrepancies under these three conditions are attributed to a higher rate of re-agglomeration between particles and fragments after breakage decreasing the number of resulting fragments and thus the fragmentation ratio. In more detail, re-agglomeration events extensively take place when large numbers of small fragments and particles are released in the vicinity of each other. This is the case for large agglomerates impacting with a high velocity sufficient to break out a considerable number of particles, typically from the side of the agglomerate confronting the wall. At large impact angles, the released particles are naturally reflected back towards the center of the agglomerate promoting re-agglomerations. In addition, as explained before a stronger cohesion and thus an enhanced tendency to clustering is found for particles with smaller primary particle diameters.

In order to further investigate this issue, Fig. 7.12 shows the time evolution of the ratio between the bonds generated during the impact (i.e., excluding the original ones) normalized by the number of bonds in the original agglomerate (B_{imp}) at $\pi_{\text{imp}} = 2.12 \cdot 10^{-3}$

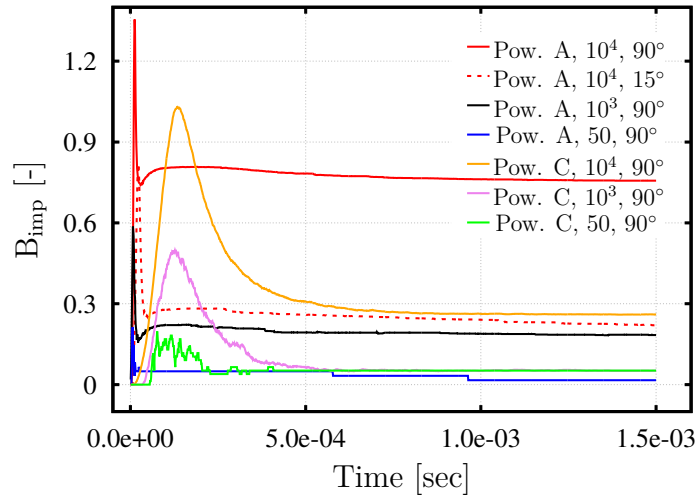


Fig. 7.12. History of the number of bonds generated during an impact normalized by the number of bonds in the original agglomerate at $\pi_{\text{imp}} = 2.12 \cdot 10^{-3}$ for agglomerates of powders **A** and **C** consisting of 50 to 10^4 primary particles.

for some of the investigated cases. Indeed, it can be confirmed that the number of new bonds generated due to the impact increases with a decreasing size of the primary particle, an increasing number of included primary particles, and an increasing impact angle. For instance, Fig. 7.12 shows that the highest peak and steady-state value of the number of new bonds is found for a 10^4 primary particle agglomerate of powder **A** impacting the wall at 90° .

Accordingly, an important conclusion can be drawn: Since agglomeration is typically separately accounted for in the Euler–Lagrange simulation framework for which the breakage model is intended, the results obtained for the cases highly influenced by re-agglomeration should not be further considered in the modeling process, i.e., for data fitting purposes as will be discussed next. However, this does not restrict the validity range of the derived impact breakage model especially if models for the re-agglomeration are separately considered.

Another intriguing outcome is that similar to FR, each of the fragment size parameters ζ_1 , ζ_2 and ζ_3 (see Eq. (7.19)) depend on π_{imp} . This includes the same kind of relationship and a similar unification behavior concerning the results obtained under different impact conditions. Consequently, the following two-parameter (here γ_1 and γ_2) relations (Le Bouteiller and Naaïm, 2011):

$$\text{FR}(\pi_{\text{imp}}) = \frac{1}{1 + (\gamma_1/\pi_{\text{imp}})^{\gamma_2}}, \quad (7.32a)$$

$$\zeta_{i \rightarrow 3}(\pi_{\text{imp}}) = \frac{1}{1 + (\gamma_1/\pi_{\text{imp}})^{\gamma_2}}, \quad (7.32b)$$

are fitted to the results in Fig. 7.13 obtained for agglomerates of powders **A**, **B** and **C** comprising 10 to 10^3 primary particles using a nonlinear least-squares method. Again, the

data correspond to impact events, where the impact angle Θ_{imp} is varied between 7° and 90° . In total, about 2500 data points are depicted in Fig. 7.13. The values of the most appropriate fitting parameters for FR and ζ_i are listed in Table 7.3. It is remarkable that these parameters are of the same order for the different quantities and generally close to each other.

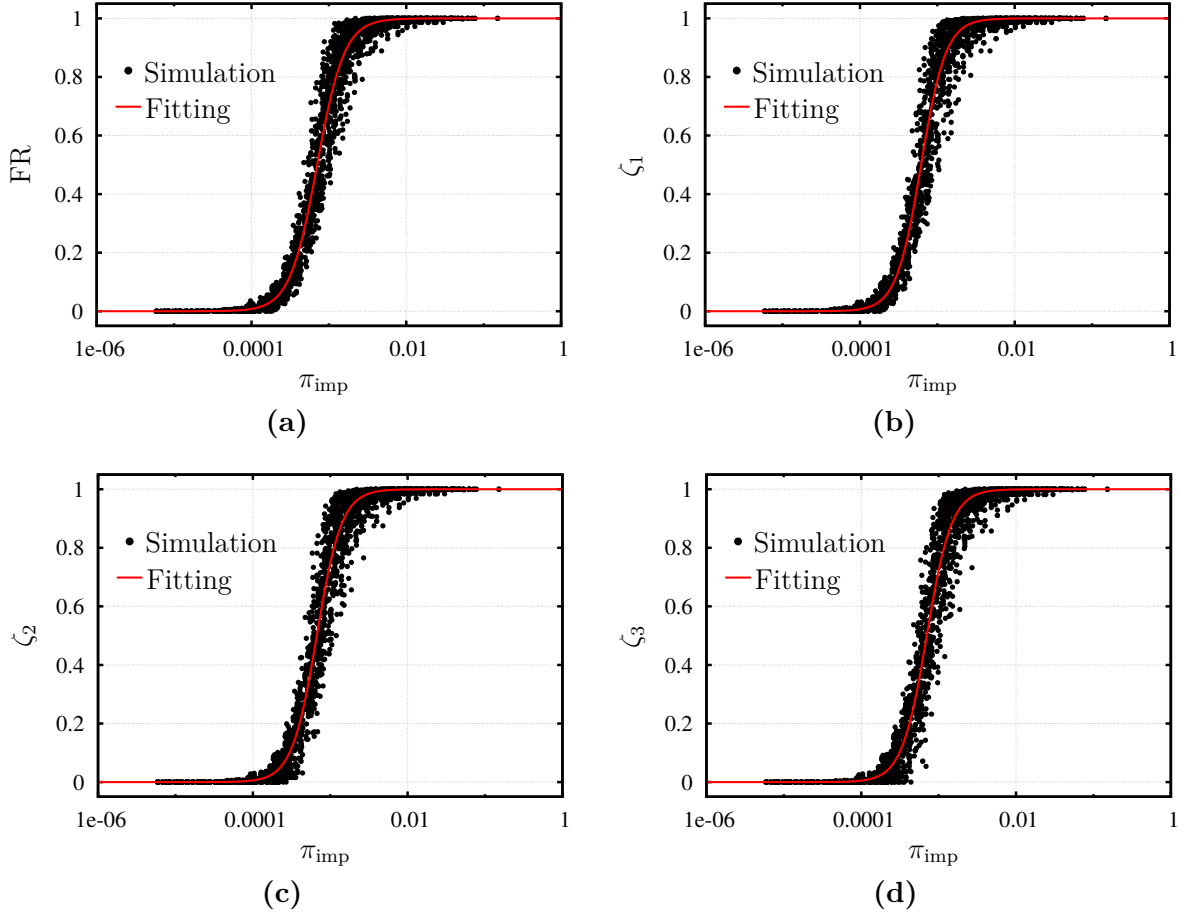


Fig. 7.13. Simulation results and fitting curves by Eqs. (7.32) for (a) the fragmentation ratio FR and the particle size parameters (b) ζ_1 , (c) ζ_2 and (d) ζ_3 as functions of the proposed dimensionless number π_{imp} . The included simulation data refer to all impact events carried out based on agglomerates of powders **A**, **B** and **C** comprising 10 to 10^3 primary particles with an impact angle Θ_{imp} varying between 7° and 90° . The most appropriate fitting parameters are given in Table 7.3.

A possible explanation for the smooth transition of the fragment size parameter ζ_i from zero to unity might be attributed to the ductile failure mode of the agglomerates. This mode is related to the low value of the surface energy of the particles (Moreno, 2003; Moreno-Atanasio, 2012) and implies that solely single particles and small fragments are detached from the agglomerate, so that the first largest fragment is always much larger than the second one in the mentioned transitional regime.

Tab. 7.3. Values of the fitting parameters γ_1 and γ_2 introduced in Eqs. (7.32), and the root-mean-square of the residuals. Note that the first value was corrected in comparison to the original value in Khalifa and Breuer (2020).

	γ_1	γ_2	RMS Error
FR	$7.04 \cdot 10^{-4}$	2.47	$6.17 \cdot 10^{-2}$
ζ_1	$6.17 \cdot 10^{-4}$	2.73	$6.48 \cdot 10^{-2}$
ζ_2	$6.70 \cdot 10^{-4}$	2.72	$6.90 \cdot 10^{-2}$
ζ_3	$7.01 \cdot 10^{-4}$	2.71	$7.37 \cdot 10^{-2}$

The derived model for forecasting the number of fragments and the fragment size distribution is applied in the Euler–Lagrange hard-sphere methodology as follows: If an agglomerate collides with a wall, the dimensionless number π_{imp} is computed. Subsequently, the fragmentation ratio is determined which allows to calculate the number of generated fragments using Eq. (7.32a). If the number of fragments is smaller than or equal to unity, breakage does not occur and the agglomerate bounces back based on the hard-sphere treatment. If the number of fragments is larger than one, the agglomerate is replaced by the computed number of fragments. The number of particles in the fragments up to the third largest fragment is determined based on Eq. (7.32b).

If more than three fragments arise and the third fragment is a single particle, all remaining fragments are understandably single particles. If the third fragment is not a single particle, the difference between the total number of primary particles in the original agglomerate and the number of particles in the first three largest fragments is determined. These particles are then stepwise distributed to the remaining fragments based on random numbers generated by a uniform distribution. However, there are two conditions which need to be checked while assigning the randomly predicted number of particles to each fragment before progressing to the next one. The first condition is that the fragment can not have more particles than the third largest fragment. The second condition requires that after filling the current fragment, the number of remaining particles is ensured to be sufficient to endow the remaining number of fragments by a single particle at least. In case any of these two conditions is not satisfied, the randomly predicted number of particles is repeated respectively. At the end of this procedure it can happen that some particles are left out without being assigned to any of the fragments. In this case, these extra particles are redistributed in a second (or more) iteration step to the fragments evenly starting from the first largest fragment in order not to heavily affect the predicted fragment size distributions of the first iteration step.

7.4.2 Spreading and Reflection Angles and Fragment Velocity Ratio

In the second part of the breakage model, the parameters describing the post-breakage motion of the individual fragments, i.e., the reflection angle α , the spreading angle β , and the velocity ratio v_{ratio} are proposed as functions of the impact conditions of the

original agglomerate. For this purpose, a statistical analysis by means of probability density functions is carried out focusing on a rather restricted set of impact cases, which are detailed and justified in Section 7.4.2.1. Subsequently, the resulting distributions for the three parameters (α , β , and v_{ratio}) are analyzed in Section 7.4.2.2 and a respective model is proposed in Section 7.4.2.3.

7.4.2.1 Considered Impact Cases

Owing to the fact that a single breakage event entails a range of velocity ratios v_{ratio} and reflection α and spreading β angles, the collective behavior of the fragments is statistically analyzed. Such an analysis necessitates a large number of fragments under similar impact conditions. Therefore, each impact case is repeated up to 64 times while changing the relative orientation of the agglomerate with respect to the wall. However, this large number of necessary repetitions restricts the analysis of the post-breakage motion to a narrower set of impact conditions in comparison to the fragmentation ratio and the fragment size distribution. The sets of impact cases considered are listed in Table 7.4. Solely powder **C** is taken into account. In addition, only three agglomerates are investigated possessing $N_{\text{pp}}^{\text{tot}} = 50, 100, \text{ and } 200$ particles. However, all seven impact angles are considered and a number of impact velocities is chosen to achieve partial ($\text{FR} < 1$) as well as complete fragmentation ($\text{FR} = 1$) scenarios.

Tab. 7.4. Description of the cases considered in the analysis of the post-breakage kinetics of the fragments predicted by DEM. All provided cases refer to powder **C**.

$N_{\text{pp}}^{\text{tot}}$	FR	$v_{\text{imp},n}$ [m/s]	Θ_{imp}	Repeated events
200	1.0	0.22	7°, 15°, 30°, 45°, 60°, 75°, 90°	5
200	[0.05,0.85]	[0.14,17.0]	7°, 30°	up to 64
100	1.00	0.18	7°, 15°, 30°, 45°, 60°, 75°, 90°	16
100	[0.05,0.85]	[57.3,0.1]	7°, 30°	up to 64
50	1.0	0.18	7°, 15°, 30°, 45°, 60°, 75°, 90°	16

7.4.2.2 Probability Distribution Analysis

The quantities analyzed by means of probability distributions are the dimensionless reflection angle $\alpha/\Theta_{\text{imp}}$, the dimensionless spreading angle $\beta/\Theta_{\text{imp}}$, and the velocity ratio v_{ratio} . Exemplary histograms normalized by the number of counts times the width of the bins are depicted in Fig. 7.14. Obviously, probability density functions of different shapes are required to achieve a proper fitting of the data. For example, a log-normal distribution function seems to be appropriate for describing the dimensionless angles $\alpha/\Theta_{\text{imp}}$ and $\beta/\Theta_{\text{imp}}$, whereas a skew-normal distribution is more suitable for describing the velocity

ratio v_{ratio} . For this purpose, the commonly used two-parameter Weibull distribution function (PDF) is chosen:

$$f(x) = \begin{cases} \frac{k}{\lambda} \left(\frac{x}{\lambda}\right)^{k-1} e^{-(x/\lambda)^k} & x \geq 0, \\ 0 & x < 0, \end{cases} \quad (7.33)$$

where $\lambda > 0$ and $k > 0$ are the scale and shape parameters, respectively. This choice is motivated by the versatility of the Weibull PDF since it can represent the characteristics of other distributions based on the chosen value of the shape parameter. The Weibull PDFs obtained for the exemplary case ($\Theta_{\text{imp}} = 7^\circ$, $N_{\text{pp}}^{\text{tot}} = 100$ and $\text{FR} = 1$) depicted in Fig. 7.14 are superimposed on the histograms. Note that compared to other functions, the Weibull distribution is found to provide the overall best fitting taking into account the complete dataset considered in the analysis.

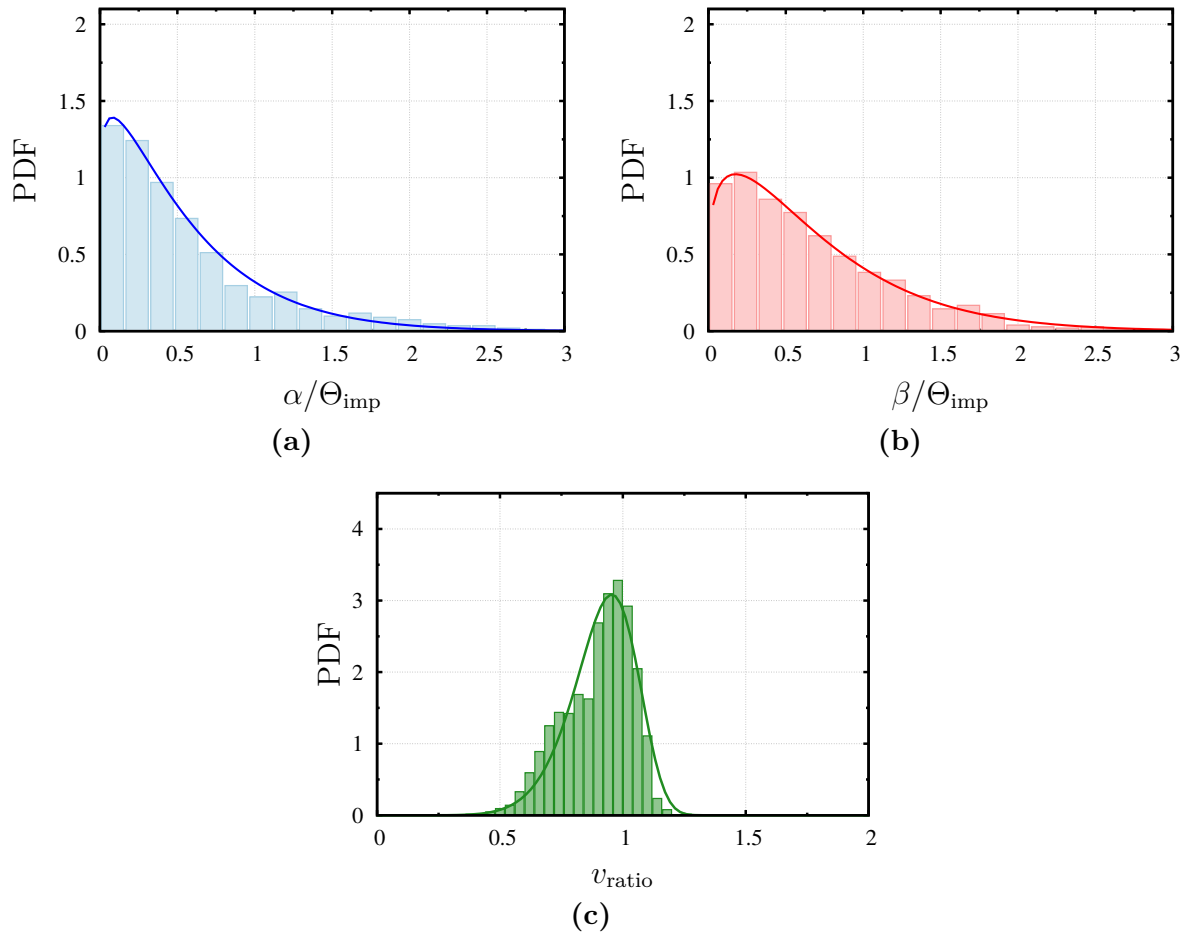


Fig. 7.14. Results based on 16 different impact events with $\Theta_{\text{imp}} = 7^\circ$ and $N_{\text{pp}}^{\text{tot}} = 100$ and full fragmentation (i.e., 1600 fragments): (a) reflection angle $\alpha/\Theta_{\text{imp}}$; (b) spreading angle $\beta/\Theta_{\text{imp}}$; (c) velocity ratio v_{ratio} . The solid line is fitted to the data by the Weibull distribution given by Eq. (7.33).

The Weibull fitting curves for the complete set of considered cases are compared in Fig. 7.15. The figures of the first column (Figs. 7.15(a), 7.15(c) and 7.15(e)) depict the DEM simulation data obtained for agglomerates consisting of 50 or 100 primary particles, whereas the second column presents the results for agglomerates including 100 or 200 particles. Note that the number of fragments analyzed for each case can be calculated based on the number of particles in the agglomerate N_{pp}^{tot} , the fragmentation ratio FR and the number of repeated impact events as provided in Table 7.4.

Several important conclusions can be drawn based on the results depicted in Fig. 7.15:

- First, the shapes of the distributions for the dimensionless reflection angle $\alpha/\Theta_{\text{imp}}$ are qualitatively similar but the amount of spreading of the data varies depending on the impact conditions as seen in Figs. 7.15(a) and 7.15(b). A careful inspection of the trends of the discrepancies reveals that the shapes of the distributions are strongly influenced by the magnitude of the impact angle Θ_{imp} . The effect of other conditions such the number of particles and the fragmentation ratio is less pronounced.
- Second, similar findings apply to the results obtained for the spreading angle $\beta/\Theta_{\text{imp}}$. However, here it has to be noted that since the analysis deals with fitting curves which are associated with certain errors, the tails of the Weibull distributions can exceed physical values (i.e., $\beta > 180^\circ$). This is mainly detected in some of the normal impact cases (e.g., the yellow curves in Figs. 7.15(c) and 7.15(d)) due to the fact that the spreading angles β obtained by normal impacts ($\Theta_{\text{imp}} = 90^\circ$) naturally tend to be uniformly distributed. This uniform distribution of β in the limit of normal impact events can not be accurately reproduced by a Weibull distribution. However, describing the angle β based on a single distribution function (i.e., Weibull) for all impact angles Θ_{imp} simplifies the upcoming model. Here it is important to note that normal impact events are not very common to particle-laden flows due to the effect of the near-wall shear layer. Thus, the Weibull distribution is accepted for modeling the distribution of the spreading angle β for all impact angles Θ_{imp} , since it overall delivers the best fitting accuracy and avoids using different models for the normal and the nearly normal impact cases. Nevertheless, the issue of the non-physical values will be addressed later on by restricting the predicted values for any of the two angles (α and β) to their physical ranges (see Section 7.4.2.3).
- Third, a stronger dependence on the impact angle Θ_{imp} is found for the shapes of the Weibull PDFs obtained for the velocity ratio v_{ratio} . A significantly less pronounced dependence on the number of primary particles N_{pp}^{tot} and the fragmentation ratio FR is observable. Overall, the distributions of v_{ratio} obtained at equal impact angles are fairly similar although they correspond to cases with different numbers of primary particles or different fragmentation ratios.

In summary, the distributions of the reflection and spreading angles and the velocity ratio significantly depend on the impact angle. This can be further demonstrated based on the values of the scale (λ) and shape (k) parameters of the obtained Weibull PDFs, which are plotted in Fig. 7.16 as functions of the impact angle. The figures confirm the

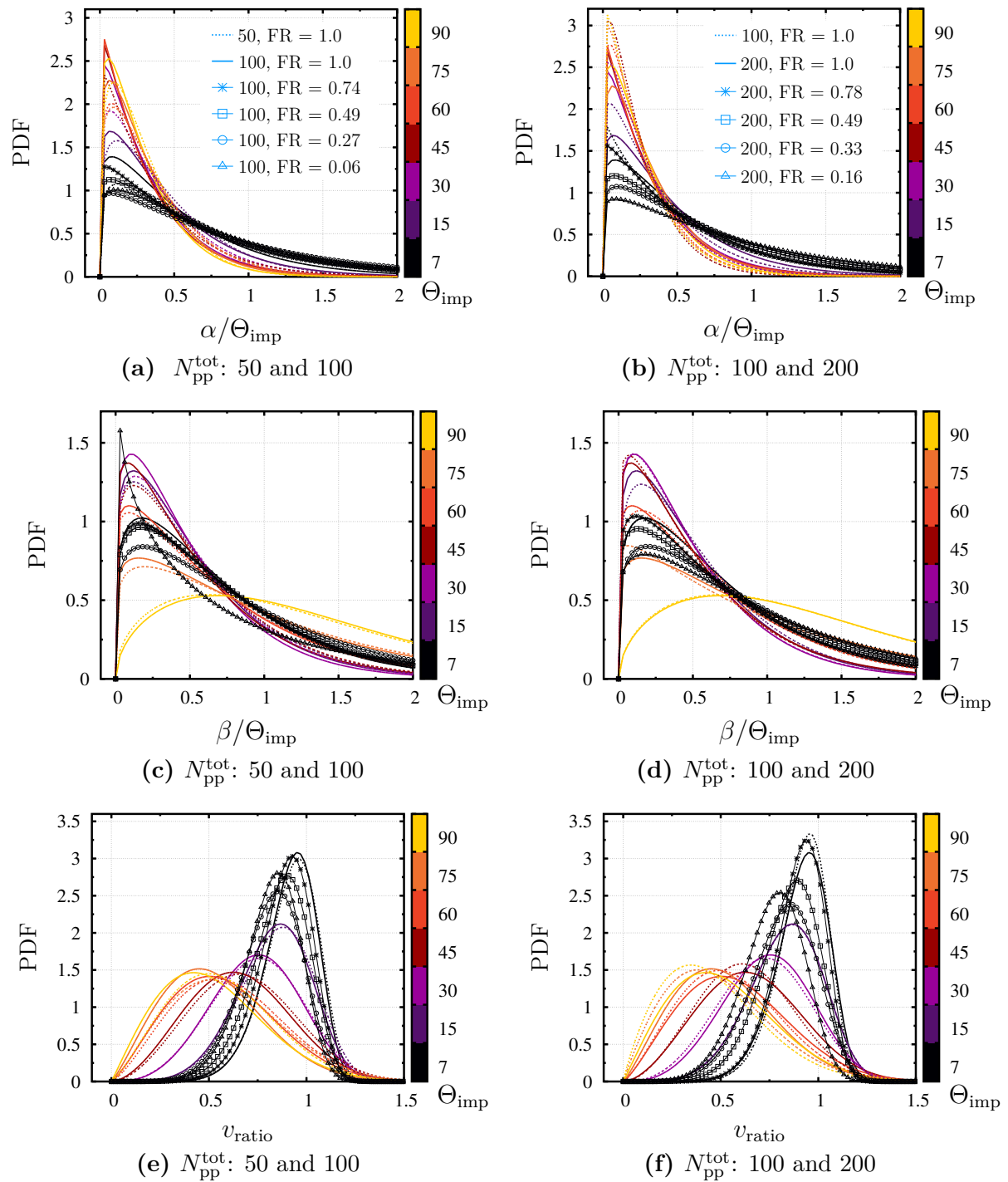


Fig. 7.15. Comparison between the Weibull PDFs obtained for the full set of investigated cases. Again the reflection angle $\alpha/\Theta_{\text{imp}}$, the spreading angle $\beta/\Theta_{\text{imp}}$ and the velocity ratio v_{ratio} are depicted. The key legend provided in the first subfigure of a column applies to all subfigures of the same column. The (discrete) color bar refers to the impact angle Θ_{imp} .

conclusions drawn for the three investigated quantities discussed above, suggesting that the impact angle is the most important factor for describing the behavior of the fragments after breakage. However, at certain impact angles some discrepancies between the data obtained for different agglomerate sizes and fragmentation ratios still exist. Since no clear trend is observed, these deviations are neglected.

7.4.2.3 Derived Model

Building on the conclusion made in the previous section, the parameters of the Weibull PDFs (k and λ) are assumed to be solely functions of the impact angle. The relationships between the impact angle Θ_{imp} and the parameters k and λ are established by applying a fourth-order polynomial regression:

$$f_i(\Theta_{\text{imp}}) = a_i \cdot \Theta_{\text{imp}}^4 + b_i \cdot \Theta_{\text{imp}}^3 + c_i \cdot \Theta_{\text{imp}}^2 + d_i \cdot \Theta_{\text{imp}} + e_i. \quad (7.34)$$

Here, Θ_{imp} is expressed in radians and $f_i(\Theta_{\text{imp}})$ refers to k and λ for each of the investigated quantities, i.e., $\alpha/\Theta_{\text{imp}}$, $\beta/\Theta_{\text{imp}}$ and v_{ratio} . The fitting curves are depicted in Fig. 7.17, and the most appropriate fitting coefficients are listed in Table 7.5. The datasets used for generating the fitting curves in Fig. 7.17 exclude the results obtained for the partial fragmentation cases ($\text{FR} < 1$), although most of the results of these cases fit very well to the data obtained for the full fragmentation cases as depicted in Fig. 7.16. The motivation behind this procedure is that polynomials of high order are sensitive to data outliers. Therefore, a small number of events associated with clear deviations might strongly affect the coefficients (i.e., the form) of the fitting functions.

The proposed model is applied in the Euler–Lagrange simulations as follows: When a breakage event due to a wall-impact occurs, the impact angle Θ_{imp} and the impact velocity v_{imp} are determined. Based on the magnitude of the impact angle the parameters k and λ of the Weibull PDFs of $\alpha/\Theta_{\text{imp}}$, $\beta/\Theta_{\text{imp}}$ and v_{ratio} are obtained relying on the proposed fourth-order relationship (7.34) and the coefficients in Table 7.5. Subsequently, the magnitude

Tab. 7.5. Values of the fitting coefficients obtained by a nonlinear least-squares regression for the relationship between Θ_{imp} and the parameters k and λ of the Weibull PDFs (Fig. 7.17), and the root-mean-square errors.

Parameter		a_i	b_i	c_i	d_i	e_i	RMS Error
$\alpha/\Theta_{\text{imp}}$	λ	$3.27 \cdot 10^{-1}$	-1.56	2.62	-1.85	$7.87 \cdot 10^{-1}$	$5.40 \cdot 10^{-2}$
	k	$-8.08 \cdot 10^{-1}$	2.77	-3.03	1.16	$9.95 \cdot 10^{-1}$	$6.37 \cdot 10^{-2}$
$\beta/\Theta_{\text{imp}}$	λ	$1.01 \cdot 10^{-1}$	$-5.29 \cdot 10^{-1}$	1.71	-1.46	$8.94 \cdot 10^{-1}$	$3.38 \cdot 10^{-2}$
	k	1.03	-2.70	2.30	$-8.00 \cdot 10^{-1}$	1.28	$3.66 \cdot 10^{-2}$
v_{ratio}	λ	$8.84 \cdot 10^{-2}$	$-2.47 \cdot 10^{-1}$	$3.16 \cdot 10^{-1}$	$-5.12 \cdot 10^{-1}$	1.03	$3.33 \cdot 10^{-2}$
	k	10.67	-42.06	59.79	-37.72	11.89	$2.90 \cdot 10^{-1}$

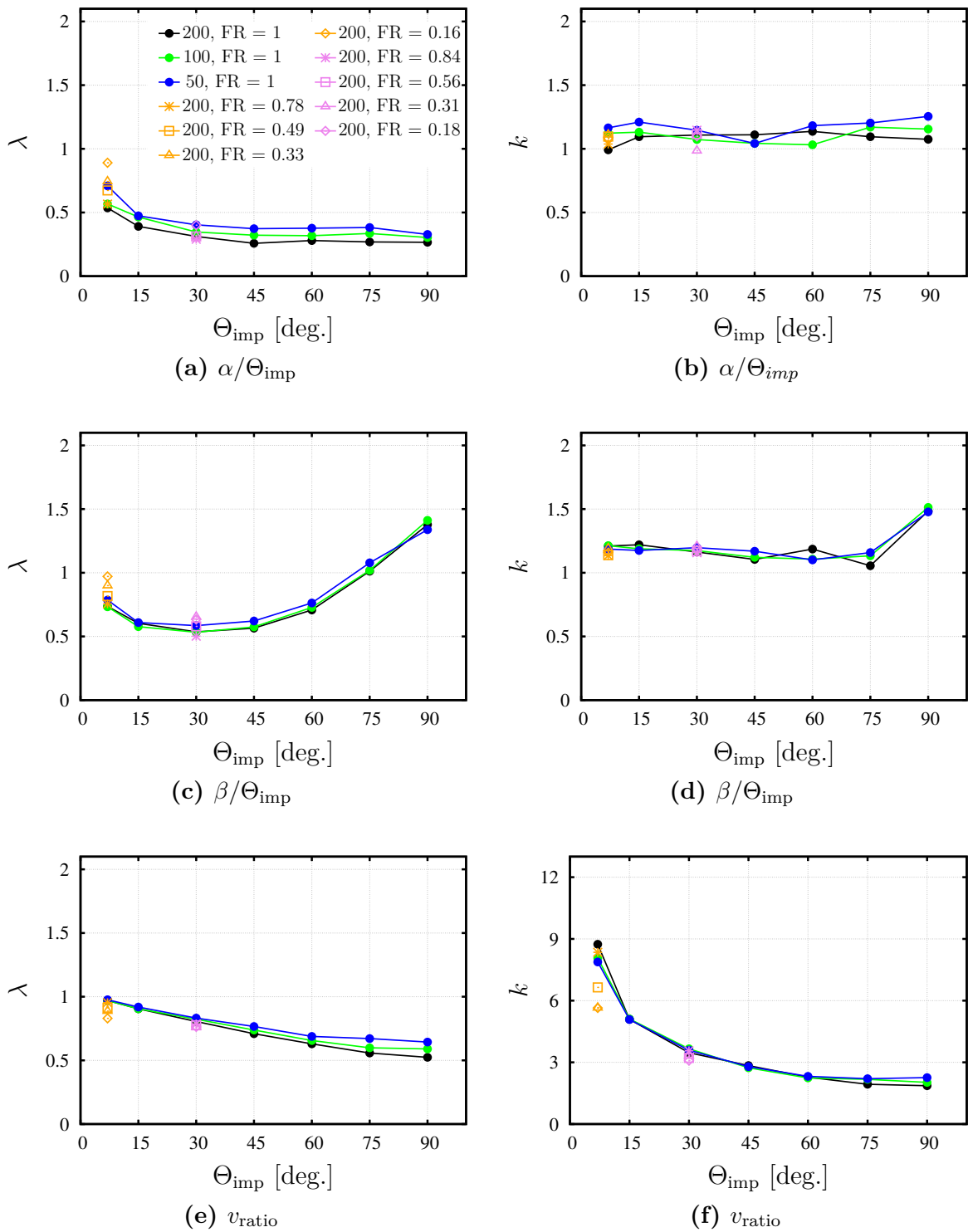


Fig. 7.16. Scale and shape parameters λ and k of the Weibull PDFs (Fig. 7.15) as functions of the impact angle Θ_{imp} .

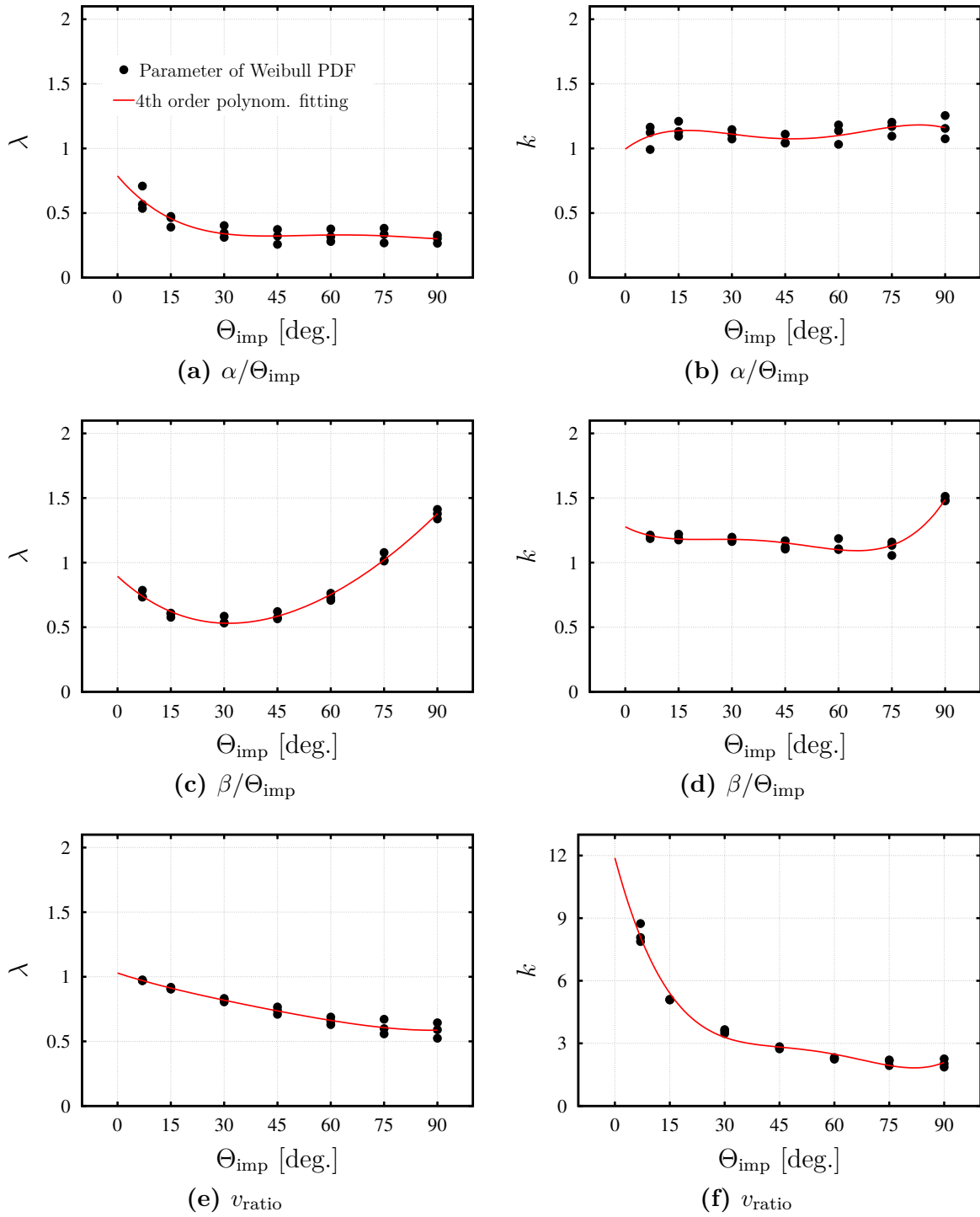


Fig. 7.17. Fitting curves for the parameters λ and k used in the Weibull PDFs as functions of the impact angle Θ_{imp} . The values of the coefficients of the fourth-order relationships are given in Table 7.5.

of the velocity of each fragment is determined based on a random number according to the corresponding Weibull PDF (7.34) applying the inverse sampling transformation method (Devroye, 1986). The angles α and β are determined in the same manner, and the obtained values are ensured to be within the physical ranges as described in Section 7.3.2. This is done by truncating the predicted values of the angles α and β to 90° and 180° , respectively. However, since the angle β is mathematically defined in the range $0 \leq \beta \leq 180^\circ$, it covers only half of the possible range for the spreading directions of the fragments (see Section 7.3.2). Therefore, the sign of the randomly predicted angle β is alternated between positive and negative values to reproduce the full physical spectrum of spreading.

Consequently, the fragments are now fully described concerning their post-breakage velocities and axes of separation. The proposed model leads to reliable results as long as the number of arising fragments is large since it is based on statistical descriptions. In the limiting case of breakage resulting in a handful number of resulting fragments, the full spectrum of the Weibull PDFs can not be correctly reproduced. This might be not critical with respect to the determination of the axis of separation (defined by α and β). However, it can lead to an over- or underestimation of the amount of kinetic energy of the fragments, yielding in the latter case an accumulation of particles in the near-wall region. This is a critical issue since the velocities of the fragments have to be reasonably predicted in order to minimize the number of non-physical collisions and re-agglomerations between the newly introduced fragments.

To overcome this drawback, the predicted kinetic energy of the fragments is corrected according to an additional model developed for this purpose. The model for the kinetic energy is based on an energy balance, which is carried out to quantify the ratio of the translational kinetic energy of the particles after breakage to the incident kinetic energy of the agglomerate:

$$\text{ER}_{\text{trans}} = \frac{\sum_{i=1}^{N_{\text{pp}}^{\text{tot}}} \frac{1}{2} m_{\text{pp},i} v_{\text{pp},i}^2}{\frac{1}{2} m_{\text{ag}} v_{\text{imp}}^2} , \quad (7.35)$$

where $m_{\text{pp},i}$ and $v_{\text{pp},i}$ are the mass and velocity of the primary particle i . The same is done for the rotational kinetic energy of the particles leading to:

$$\text{ER}_{\text{rot}} = \frac{\sum_{i=1}^{N_{\text{pp}}^{\text{tot}}} \frac{1}{2} I_{\text{pp},i} \omega_{\text{pp},i}^2}{\frac{1}{2} m_{\text{ag}} v_{\text{imp}}^2} , \quad (7.36)$$

where $I_{\text{pp},i}$ and $\omega_{\text{pp},i}$ are the moment of inertia and the angular velocity of the primary particle i around its own axis. Note that the analyzed agglomerates did not possess an angular velocity prior to the impact so that solely the translational kinetic energy of the agglomerate appears in the denominator of both energy ratios. Interestingly, based on the outcome of the DEM simulations it is found that the energy ratio ER_{trans} can be also described as a function of the impact angle, where the influence of the number of included primary particles $N_{\text{pp}}^{\text{tot}}$ can be neglected. Fig. 7.18 depicts the average energy ratios for

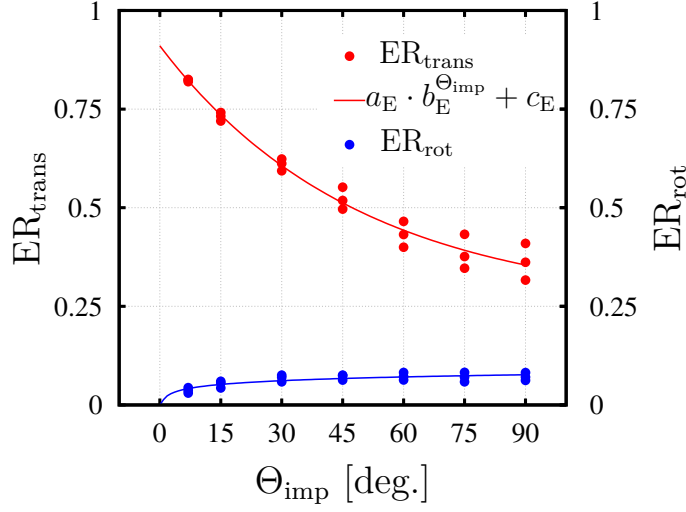


Fig. 7.18. Ratios of energies ER_{trans} and ER_{rot} as functions of the impact angle Θ_{imp} . The blue solid line is a logarithmic fitting function, which is added here for guidance only.

agglomerates including 50, 100 and 200 particles considering all investigated cases with $FR = 1$. The fitting curve provided for ER_{trans} is based on an exponential function:

$$ER_{\text{trans}} = a_E \cdot b_E^{\Theta_{\text{imp}}} + c_E, \quad (7.37)$$

where the impact angle Θ_{imp} is expressed in radians and the fitting coefficients a_E , b_E and c_E are given in Table 7.6.

Tab. 7.6. Values of the fitting coefficients for ER_{trans} depicted in Fig. 7.18.

Quantity	a_E	b_E	c_E	RMS Error
ER_{trans}	$6.59 \cdot 10^{-1}$	$3.07 \cdot 10^{-1}$	$2.52 \cdot 10^{-1}$	$2.74 \cdot 10^{-2}$

Consequently, the translational velocities of the fragments predicted by the Weibull PDFs are adjusted using an energy correction factor ϵ_{cor} . This factor is defined as the ratio of the reference ER_{trans} and the translational kinetic energy of the fragments resulting from the Weibull PDF of v_{ratio} :

$$\epsilon_{\text{cor}} = \sqrt{\frac{ER_{\text{trans}}}{ER_{\text{PDF}}}}. \quad (7.38)$$

Note that ϵ_{cor} is applied to each component of the velocity vector of each fragment adjusting their velocities evenly (i.e., $\mathbf{v}_{\text{new}}^{\text{fr}} = \epsilon_{\text{cor}} \cdot \mathbf{v}^{\text{fr}}$). In case of a sufficiently large number of fragments this correction step has a negligible effect ($\epsilon_{\text{cor}} \approx 1$) since the energy is already taken into account based on v_{ratio} . Thus, this step does not influence the nature of the Weibull distribution of the velocities.

Concerning the rotational motion of the fragments after breakage, the angular velocity of the original agglomerate is assigned to each fragment. This is a simplifying assumption

motivated by the observation that the part of the incident kinetic energy of the agglomerate which due to breakage is transferred to the rotational kinetic energy is not high as suggested by the small values of ER_{rot} in Fig. 7.18. Thus, relation (7.36) is not applied in the model. Finally, the implementation of the model into the Euler–Lagrange methodology is verified as described in Appendix B.

7.5 Model Based on Artificial Neural Networks

In Section 7.4 it has been illustrated that the outcome of wall-impact events depends on a variety of impact conditions. Consequently, data-driven breakage models have been formulated after simplifying the problem using techniques for variable reduction. For the description of the fragmentation ratio FR and the fragment size parameters ζ_i (modeling tasks **i** and **ii**), a dimensionless number π_{imp} combining all impact conditions has been used to construct relationships for the parameters quantifying the breakage. For the post-breakage motion of fragments (modeling task **iii**), the translational energy ratio ER_{trans} and the Weibull PDF parameters of the velocity ratio v_{ratio} , the reflection α angle, and the spreading angle β have been found to mostly depend on the impact angle Θ_{imp} . Hence, the aforementioned parameters were proposed as functions of the impact angle and the effect of other impact conditions was ignored.

The modeling strategy proposed in Section 7.4 did not perform well when additional DEM impact cases defining shear impact events (i.e., $\Theta_{\text{imp}} = 0.2^\circ$ and 3°) were considered. However, wall impacts at flat angles are very important for particle-laden flows due to the effect of the near-wall shear layer. For this purpose, an alternative approach based on artificial neural networks (ANNS) is introduced in this section. The approach utilizes two feed-forward ANNs to estimate the unknown functions relating the breakage parameters to the impact conditions. A brief description of this type of neural networks is given. In addition, the specific details and the performance of each network are discussed. Note that two networks are needed since the second modeling task, i.e., the prediction of the kinetics of the fragments is addressed by a restricted DEM database as elaborated in Section 7.5.3.1.

7.5.1 Theoretical Background of Artificial Neural Networks

ANNs of various designs are applied to tackle different problems. In the case of regression problems, feed-forward networks with fully connected layers are the simplest and the most common choice among other types of ANNs. Feed-forward networks allow to find a function to approximate the underlying mapping between a set of inputs and outputs (Hagan et al., 2014). In this type of networks, the information solely travels in forward direction without any cycles or loops, i.e., from the input layer through optional (one or more) hidden layers to the output layer. A typical network of this kind with a single hidden layer is schematically depicted in Fig. 7.19. Such a configuration is denoted a multilayer perceptron (MLP) since it has a hidden layer between the input and the output layers. Each connection has a weighting value w representing the relative importance of its input

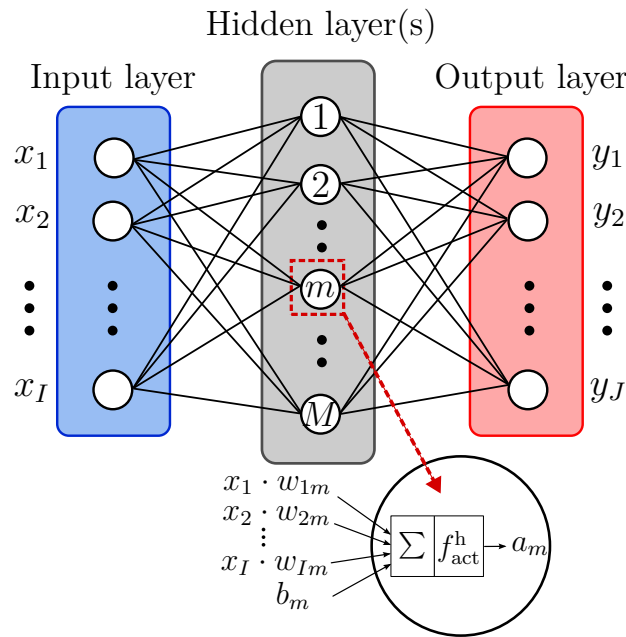


Fig. 7.19. Schematic representation of a multilayer feed-forward artificial neural network. The symbols x_I , a_m and y_J stand for the network input, the activation of a hidden node, and the network output, respectively. The indices I , M , and J stand for the number of nodes in the respective layers and m is an arbitrary node in the hidden layer. w and b refer to the weight of a connection (artificial synapse) and the bias in a particular node, respectively. f_{act}^h denotes the activation function of the hidden layer.

node (artificial neuron). Hence, the configuration is described by a linear matrix-vector operation. In addition, the bias b is assigned to each node to add the intercept to the linear neuron. The weight and the bias are both free parameters which need to be tuned in the training process. As depicted in the zoomed node within Fig. 7.19, the sum of the weighted inputs and the bias of the node m located in the hidden layer is passed through a predefined activation function f_{act}^h leading to a certain output value a_m , which is forwarded to the following (output) layer as an input. A variety of linear and nonlinear activation functions can be used depending on the nature of the database and the specifications of the problem. In general, nonlinear mapping relations between the inputs and the outputs can be achieved by the appropriate choice of the activation functions and the number of hidden layers. Determining the optimum number of hidden nodes is an important issue for which a general rule does not exist. For instance, using too few nodes might lead to underfitting, i.e., predictions of low accuracy. Excessive numbers of nodes, on the other hand, lead to more critical issues such as overfitting of the dataset. Furthermore, this would cause high computational costs during the training process and later on in the application. Note that overfitting is a situation which occurs when a network delivers poor predictions for the testing dataset despite being able to predict the training dataset very well.

A typical supervised training method combines the backpropagation algorithm (Rumelhart et al., 1986) with the Levenberg-Marquardt optimization (Scales, 1985). In this

method the loss function, which is chosen here as the mean squared error (MSE), is minimized by adjusting the weights and the biases in all layers. The mean squared error is a measure for the quality of predictions, which for the present application reads:

$$\text{MSE} = \frac{1}{N_{\text{data}}} \sum_{n=1}^{N_{\text{data}}} \left(y_n^{\text{DEM}} - y_n^{\text{ANN}} \right)^2, \quad (7.39)$$

where N_{data} is the total number of the DEM breakage events available in the dataset, and y^{DEM} and y^{ANN} stand for the actual DEM output and the output predicted by the ANN. In the present thesis the training is carried out in MATLAB® R2020a based on the available DEM database and prior to the Euler–Lagrange computations. The Bayesian regularization method (MacKay, 1992) is applied which builds on the backpropagation with Levenberg–Marquardt optimization and improves the generalization of the network by introducing regularization parameters. These regularization parameters penalize large weights during the training to ensure a smooth mapping, i.e., minimize the likelihood of overfitting the training database (MacKay, 1992). The training procedure is briefly summarized as follows (Hagan et al., 2014):

1. The weights and the biases are randomly initialized based on the Nguyen–Widrow method (Nguyen and Widrow, 1990) and the regularization parameters are computed.
2. A single step of the Levenberg–Marquardt algorithm towards minimizing the regularized MSE function at the output layer is carried out, leading to new weights and biases in all layers.
3. The number of effective weights and biases is computed. Subsequently, the regularization parameters, which are functions of number of effective weights and biases, are updated. Note that the effective weights and biases are defined as those effectively used in reducing the error function. Their number can range between zero and the total number of weights and biases in the network (Hagan et al., 2014).
4. Steps 2 and 3 are iterated until convergence, i.e., until any of the following conditions is reached: A performance gradient below 10^{-7} , a damping factor μ of the Levenberg–Marquardt algorithm exceeding 10^{-10} , or a MSE equal to or smaller than 10^{-8} . Further details on the adopted training algorithm can be found in the relevant literature (see, e.g., Hagan et al., 2014; MacKay, 1992, 2003).

Note that the training is carried out prior to the Euler–Lagrange simulations and solely the details of the trained networks are transferred to the simulation methodology as will be explained in Section 7.5.4.

7.5.2 Fragmentation Ratio and Fragment Size Parameters

The first ANN focuses on describing the number of fragments and the fragment size distributions resulting from a wall-impact breakage event. The additional impact cases

accounted for in the ANN-based model are highlighted in Section 7.5.2.1 and the details of the ANN are explained 7.5.2.2.

7.5.2.1 Extended Database

The motivation behind extending the wall-impact breakage database is to provide results for impact conditions frequently encountered in particle-laden flow simulations. First, the range of impact angles is enriched by adding two small angles of 0.2° and 3° for all seven agglomerate size classes (see Table 7.7). This measure is necessary in order to expand the study from the normal or oblique impact cases discussed so far to the shear case. Second, the breakage behavior is explored for two additional agglomerate sizes, which are the two-particle (doublet) and the five-particle agglomerates impacted at four selected angles (see Table 7.7). Considering agglomerates with such a small number of particles is especially advantageous in the context of ANN, since they widen the interpolation zone of the corresponding neural networks. Note, however, that the results of the two-particle agglomerates are not considered in the training of the corresponding ANN since they strongly deviate from the results of all other cases as depicted in Figs. 7.20 and 7.21. The reasons for these deviations will be addressed in the discussion of the aforementioned figures provided below. Furthermore, as previously mentioned the fragment size parameter of the second and third largest fragments ζ_2 and ζ_3 (see Eq. (7.19)) are not defined for the two-particle agglomerate. This is an additional reason for ignoring the results of the two-particle agglomerate in the present model.

The new cases are limited to powders **A** and **C**. A summary of the additional impact conditions is given in Table 7.7, where combinations between the elements in each row form separate cases. As usual, a range of impact velocities is considered for each case to achieve the full spectrum of breakage from an intact rebound of the original agglomerate to a full fragmentation. In addition, the location of the impact point is varied multiple times and the obtained results are averaged to attain realistic measures. In sum, the original DEM database is extended by a total of about 570 averaged cases.

Tab. 7.7. Impact conditions of the newly investigated cases. Note that the results of the two-particle agglomerates ($N_{pp}^{\text{tot}} = 2$) are not considered in the training of the ANN.

d_{pp} [μm]	Θ_{imp} [deg]	N_{pp}^{tot} [-]
0.97 (pow. A), 5.08 (pow. C)	0.2, 3	10, 25, 50, 100, 200, 10^3
0.97 (pow. A), 5.08 (pow. C)	0.2, 7, 45, 90	2, 5

To assess the results of the new cases, the fragmentation ratio FR and the fragment size parameters ζ_i are plotted as functions of the dimensionless number π_{imp} in Figs. 7.20 and 7.21. Both figures contain exactly the same set of data and they only differ by the variable used for coloring the symbols as indicated by the color bar. While the

coloring scheme indicates the impact angle Θ_{imp} in Fig. 7.20, it characterizes the number of comprised primary particles $N_{\text{pp}}^{\text{tot}}$ in Fig. 7.21. Note that the fragment size distribution parameters ζ_i for the two-particle agglomerates are eliminated since breakage in this case always leads to two particles. To allow a direct comparison with the cases in the original database, the DEM results and the corresponding fitting curves reported in Section 7.4.1.3 are added as a reference. Note that the fitting parameters of the relationships (7.32) are not adjusted to account for the new cases presented in this section.

Fig. 7.20 shows that the results obtained for the impact angle 3° are consistent with the trend established by the other larger angles, i.e., a shift towards a curve with a lower slope for decreasing impact angles. This behavior can be easily seen by comparing the development of the data points corresponding to $\Theta_{\text{imp}} = 3^\circ$ with the fitted curves. Concerning the impact angle of 0.2° , a broad scattering of the results obtained at nearly equal values of π_{imp} is observed. Roughly speaking, the results corresponding to this angle tend to form multiple curves with slopes deviating strongly from the fitted reference curves. This discrepancy has to be expected. As mentioned before, for very low impact angles another physical mechanism is responsible for the breakup of agglomerates denoted as shear breakage.

To study the scattering of the results at the smallest impact angle 0.2° in more detail, Fig. 7.21 depicts the results with colors based on the number of comprised primary particles $N_{\text{pp}}^{\text{tot}}$. Fig. 7.21(a) shows that the data points with the largest deviations from the majority are attributed to the two-particle agglomerates. Nevertheless, significant discrepancies also exist for all larger agglomerates at this nearly flat impact angle as can be deduced from Figs. 7.21(a) to 7.21(d).

The results depicted in Figs. 7.20 and 7.21 indicates that the data of the two-particle agglomerates remarkably deviate from all other agglomerates for all investigated impact angles. This can be explained by the fact that the two-particle agglomerates are characterized by a binary mode of breakage: A full fragmentation ($\text{FR} = 1$) or no breakage ($\text{FR} = 0$). In the present study, the location of the impact point on the surface of these two-particle agglomerates is varied six times by changing the orientation of the agglomerate with respect to the wall. However, for some configurations the impact at certain angles does not lead to breakage regardless of the impact velocity, e.g., when the two particles arrive at the wall (almost) simultaneously, they bounce off with similar accelerations. In general, a large number of additional impact events, in which the location of the impact point is further varied, is needed to improve the statistics. Hence, the results of the two-particle agglomerates are excluded from the training of the corresponding network. This applies for the fragmentation ratio FR as well as the three fragment size parameters ζ_1 , ζ_2 and ζ_3 . Accordingly, the smallest agglomerate size used in the training is $N_{\text{pp}}^{\text{tot}} = 5$.

Overall, it can be stated that the dimensionless number π_{imp} does not deliver an appropriate unification of the results, when the shear breakage case given by the smallest impact angle of 0.2° is taken into account, even when the results of the critical two-particle agglomerates are omitted. This implies that the π_{imp} model is not well suited for shear breakage events. However, such impact angles are expected to be important for particle-

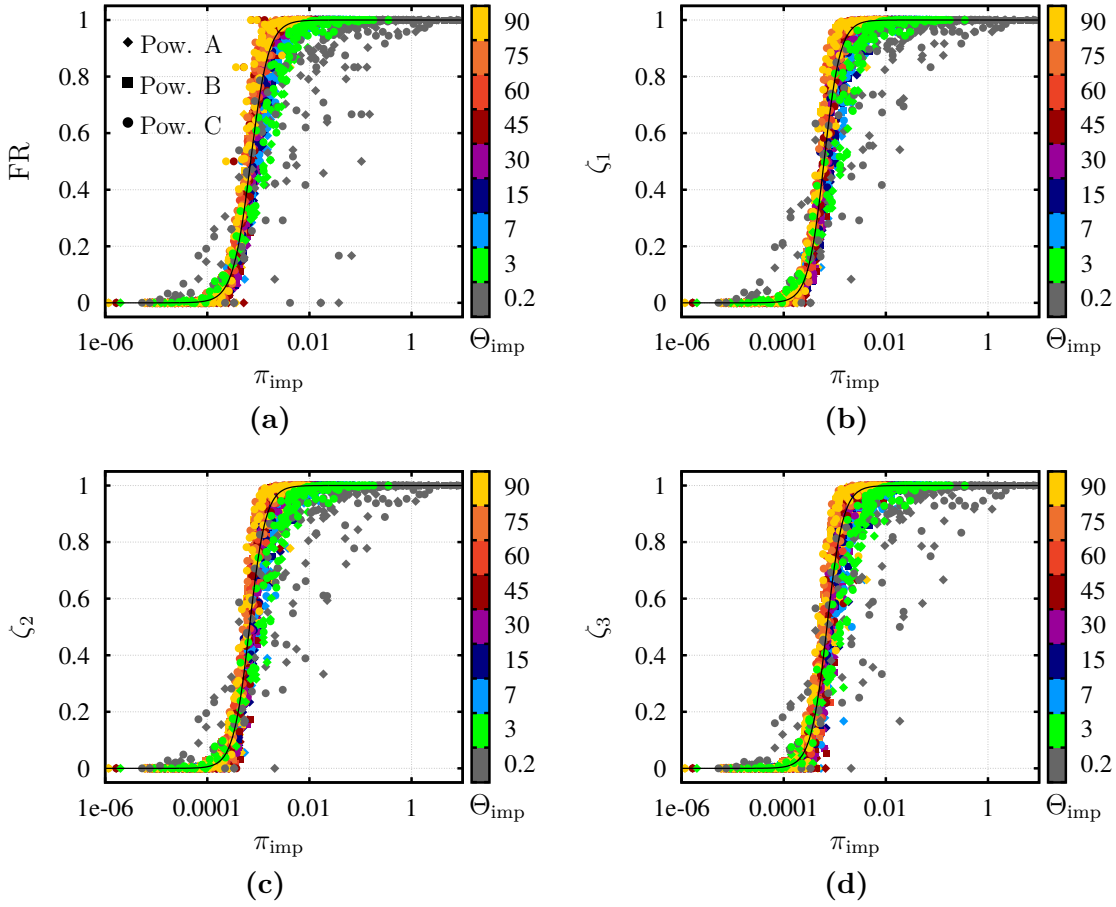


Fig. 7.20. Results for (a) the fragmentation ratio FR and the fragment size parameters (b) ζ_1 , (c) ζ_2 and (d) ζ_3 as functions of the dimensionless number π_{imp} for varying impact angles Θ_{imp} . The black curves refer to the regression relationships proposed in Section 7.4.1.3 before extending the DEM database and are solely added here as a reference. Note that for the two-particle agglomerates solely the fragmentation ratio is provided.

laden flows. That is an additional argument why an alternative approach relying on ANN is worth exploring.

7.5.2.2 Derived ANN

The first network is concerned with predicting the number of fragments and the fragment size distribution. The input parameters are (1) the total impact velocity v_{imp} , (2) the diameter of the primary particles d_{pp} , (3) the impact angle Θ_{imp} , and (4) the total number of primary particles in the agglomerate $N_{\text{pp}}^{\text{tot}}$. The output parameters are the fragmentation

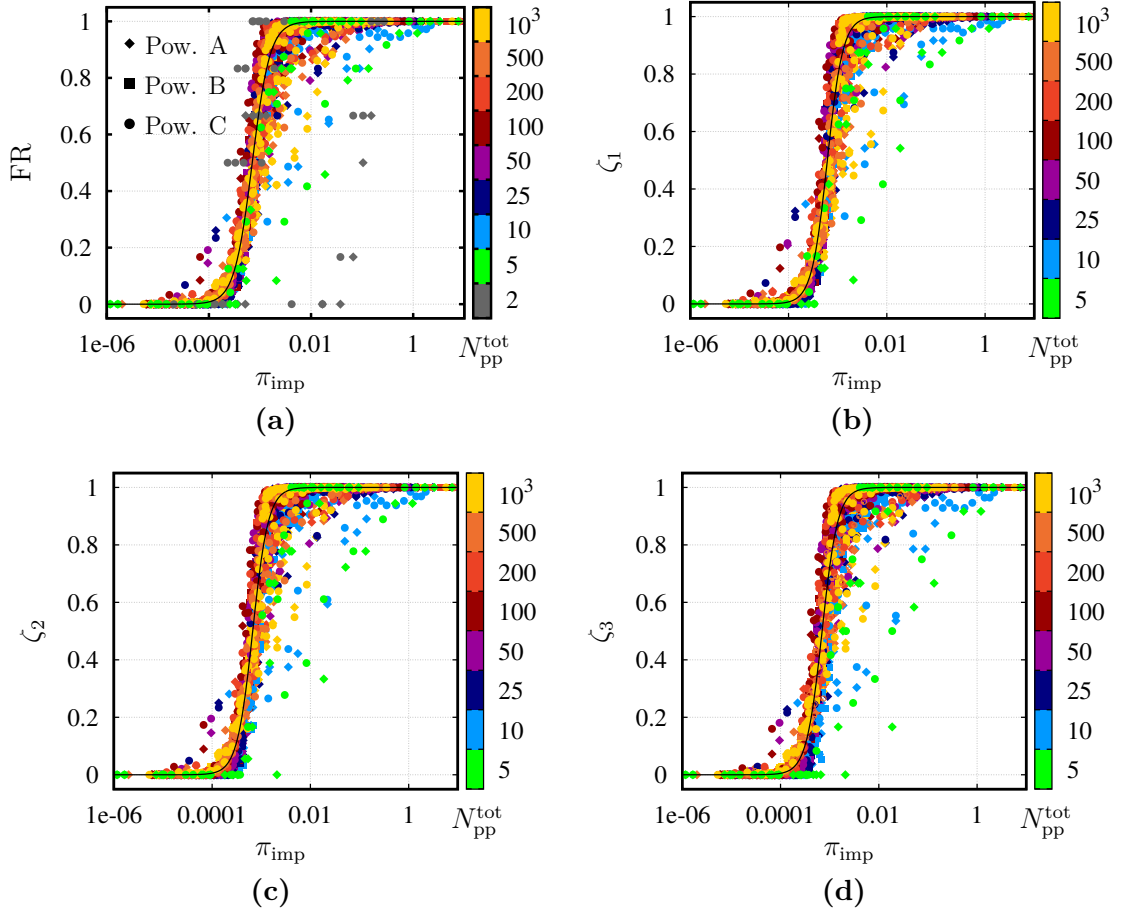


Fig. 7.21. Results for (a) the fragmentation ratio FR and the fragment size parameters (b) ζ_1 , (c) ζ_2 and (d) ζ_3 as functions of the dimensionless number π_{imp} for varying numbers of primary particles $N_{\text{pp}}^{\text{tot}}$ in the agglomerate. The black curves refer to the regression relationships proposed in Section 7.4.1.3 before extending the DEM database and are solely added here as a reference. Note that for the two-particle agglomerates solely the fragmentation ratio is provided.

ratio FR and the fragment size parameters ζ_1 , ζ_2 , and ζ_3 . To facilitate the training, the input data are normalized bringing them into the range between 0 and 1 as follows:

$$x_i = \frac{x_i^* - x_i^{*,\min}}{x_i^{*,\max} - x_i^{*,\min}}, \quad (7.40)$$

where x_i^* and x_i stand for the network input i and its normalized counterpart, respectively. In addition, $x_i^{*,\min}$ and $x_i^{*,\max}$ are the normalization parameters referring to the minimum and the maximum of the input i , respectively. The output parameters are not further normalized since they represent dimensionless quantities (FR, ζ_i), which vary per definition solely between a minimum of zero and a maximum of unity. Two hidden layers are found to be needed to capture the complex dependencies between the impact conditions and the

breakage results. Based on several tests described below, the number of nodes in the first and the second hidden layer is set to 10 and 6, respectively. Hence, the topology of the network is 4–10–6–4. The logistic sigmoid activation function is applied in all three layers (two hidden and one output):

$$f_{\text{act}}(x) = \frac{1}{1 + e^{-x}} \quad , \quad (7.41)$$

which is a nonlinear bounded function leading to values in the interval $[0,1]$. While such a function is typical for hidden layers, a linear activation function is generally more adequate in the output layer of regression networks to allow unbounded predictions. However, considering that the output quantities in the present case are solely defined in the interval $[0,1]$, a logistic sigmoid activation function in the output layer does not lead to any limitations.

The described setup is adopted after testing several different configurations, including different activation functions with appropriate normalization schemes of the inputs/outputs, the variation of the number of hidden layers, the number of nodes in these layers, and the random initial values of the weights and biases. To evaluate and compare the performance of the examined network configurations, the database is split into training (90%) and testing (10%) datasets. The latter has more than 300 data points representing distinctly different impact cases and breakage scenarios. Note that the testing part is not used at all during the training and solely serves to evaluate how reliable the network is for predicting new data. It is worth mentioning that a validation dataset is not needed, since the generalization of the network is achieved by the Bayesian regularization and not by early stopping based on validation (Hagan et al., 2014). Besides the MSE, the quality of the predictions is quantified based on the coefficient of determination R^2 , which is another widely used measure to assess the quality of the fitting provided by ANNs. It reads:

$$R^2 = 1 - \frac{\sum_{n=1}^{N_{\text{data}}} (y_n^{\text{DEM}} - y_n^{\text{ANN}})^2}{\sum_{n=1}^{N_{\text{data}}} (y_n^{\text{DEM}} - \bar{y}^{\text{DEM}})^2} \quad , \quad (7.42)$$

where \bar{y}^{DEM} is the mean of the DEM results in the corresponding dataset. A perfect match between the actual and the predicted data leads to R^2 of unity, whereas R^2 equal to zero indicates a model that always predicts the mean value \bar{y}^{DEM} of the actual data.

In general, the chosen network configuration yields the best compromise between the accuracy in predicting the training and the testing dataset. The predictions achieved by the network for the training and the testing dataset are depicted in Figs. 7.22(a) and 7.22(b), respectively. The mean values of the training MSE ($5.49 \cdot 10^{-4}$) and the testing MSE ($5.63 \cdot 10^{-4}$) are adequately small and very close to each other implying a well-trained network which generalizes well. This can be also inferred from the obtained mean value of $R^2 = 0.997$ for each of the training and the testing datasets indicating high prediction accuracy for both datasets. Note that the detailed values for each output parameter are

given in Table 7.8. It is worth mentioning that the training of this network stops when the gradient of the error function falls below the convergence limit of 10^{-7} . The last value of the damping coefficient of the Levenberg–Marquardt algorithm is 0.05. In addition, the number of the effective parameters (i.e., weights and biases which were used in to reduce the error function in the last iteration) is 140 out of 144 trainable parameters.

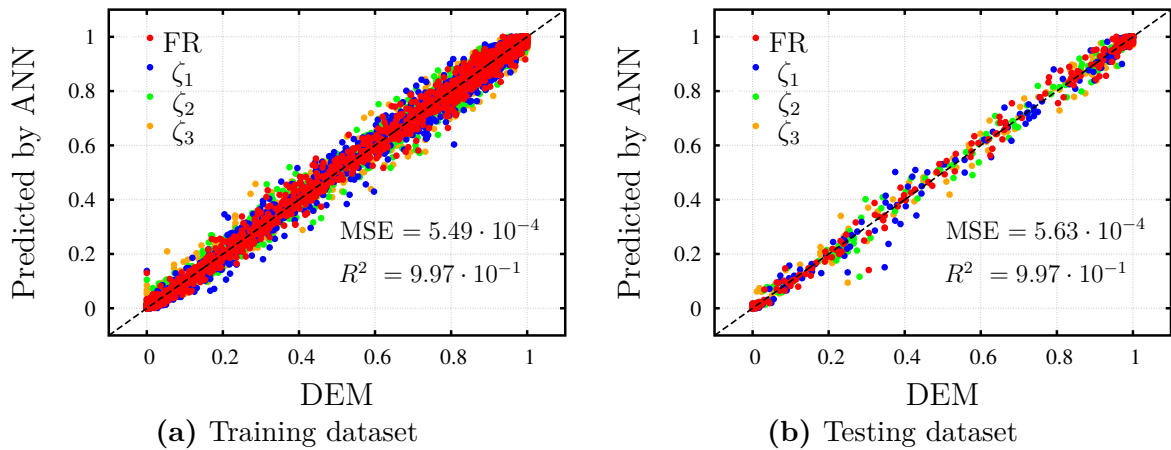


Fig. 7.22. ANN predictions of the fragmentation ratio FR and the fragment size parameters ζ_i for (a) the training dataset and (b) the testing dataset. The reference line is dashed and has a slope of unity.

Tab. 7.8. MSE and R^2 values of the outputs of the ANN predicting the fragmentation ratio FR and the fragment size parameters ζ_i .

	Training		Testing	
	MSE	R^2	MSE	R^2
FR	$4.54 \cdot 10^{-4}$	0.997	$4.99 \cdot 10^{-4}$	0.997
ζ_1	$6.23 \cdot 10^{-4}$	0.996	$6.97 \cdot 10^{-4}$	0.996
ζ_2	$5.16 \cdot 10^{-4}$	0.997	$4.94 \cdot 10^{-4}$	0.997
ζ_3	$6.01 \cdot 10^{-4}$	0.997	$5.71 \cdot 10^{-4}$	0.997

7.5.3 Spreading and Reflection Angles and Fragment Velocity Ratio

The second ANN is involved with the post-breakage motion of the fragments. The considered set of impact cases is detailed in Section 7.5.3.1 and the development of the corresponding ANN is discussed in Section 7.5.3.2.

7.5.3.1 Considered Impact Cases

Besides the cases considered in the development of the model based on the polynomial regression function (see Section 7.4.2.1), additional cases related to the shear breakage scenario are taken into account. Those correspond to the 50-, 100-, and 200-particle agglomerates of powder **C** accounting for both newly investigated impact angles of 0.2° and 3° of the shear impact case. In addition, five impact velocities achieving a fragmentation ratio varying between 0.08 and 1 are considered for each case. Consequently, the number of fragments corresponding to each set of impact conditions was nearly 3000 except for the cases associated with the smallest FR, where the number of analyzed fragments was about 500.

As previously pointed out, the obtained reflection angle α , spreading angle β , and velocity ratio v_{ratio} for the individual fragments in the DEM simulations are statistically described by means of PDFs.

Fig. 7.23 depicts the histograms of α , β , and v_{ratio} and the fitted Weibull PDFs for one of the newly added shear breakage cases. In addition, the distributions of the complete set of cases compared in terms of their scale λ and shape k parameters are shown in Fig. 7.24. The results depicted suggest a strong dependence of the distributions for all three measures (i.e., α , β , and v_{ratio}) on the impact angle. However, significant deviations are present between some cases of different fragmentation ratios or numbers of primary particles especially at the newly investigated angles of 0.2° and 3° of the shear impact case. This implies inevitable errors if the Weibull distribution parameters are expressed as functions of solely the impact angle in order to allow the usage of common regression techniques (see Section 7.4.2.3). Thus, a multivariate approach based on an ANN is a viable alternative.

It is noteworthy that the histograms used in the development of the model based on the polynomial regression function (see Fig. 7.14) refer to the angles α and β normalized by the impact angle Θ_{imp} . This kind of normalization is not necessary for training the corresponding ANN. Thus, the absolute ranges of the angles α and β are used in the present analysis. Consequently, different trends and ranges are observed for the scale parameter λ of the angles α and β in both analyses.

Furthermore, in Fig. 7.25 the energy ratios ER_{trans} obtained for the newly investigated angles ($\Theta_{\text{imp}} = 0.2^\circ$ and 3°) are depicted. For completeness, the results for the larger angles and their exponential fitting curve are added. It can be stated that the new results are consistent with the trend obtained for the larger angles, i.e., a negative exponential relationship exist between the energy ratio ER_{trans} and the impact angle (Khalifa and Breuer, 2021). However, the values of the energy ratio ER_{trans} approach unity at the smallest angle of 0.2° , indicating almost no kinetic energy losses during the breakage event. This can be understood considering that with a decreasing impact angle, a higher total impact velocity is required to induce breakage (see Section 7.4.1.2). Hence, the incident kinetic energy of the agglomerate in the case of $\Theta_{\text{imp}} = 0.2^\circ$ is much higher than the dissipated work during the disintegration of particles, e.g., through friction and breakage of bonds. In general, it is also noticeable that at any impact angle certain deviations appear between

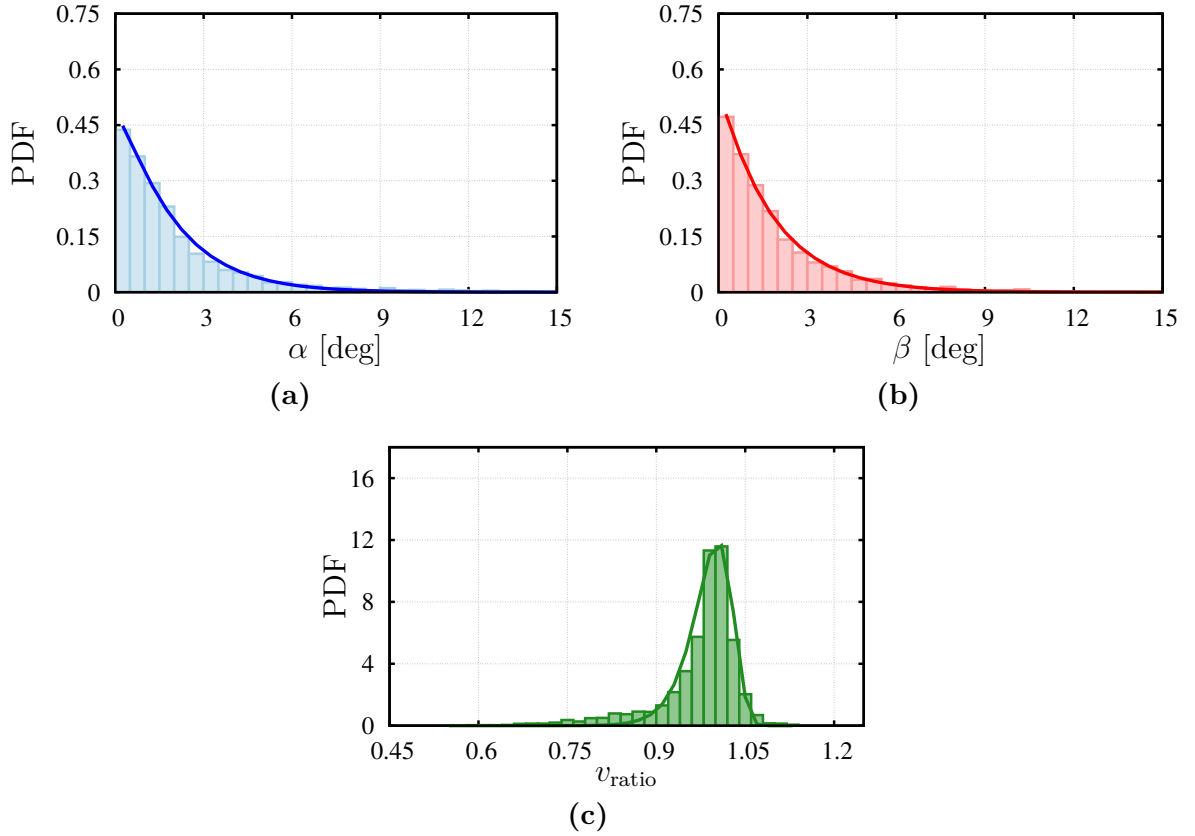


Fig. 7.23. Results based on 64 different impact events with $\Theta_{\text{imp}} = 0.2^\circ$ and $N_{\text{pp}}^{\text{tot}} = 100$ achieving a mean fragmentation ratio of $\text{FR} = 0.47$: (a) reflection angle α ; (b) spreading angle β ; (c) velocity ratio v_{ratio} . The solid line is fitted to the data by the Weibull distribution given by Eq. (7.33).

the values of ER_{trans} for a varying fragmentation ratio or number of primary particles, suggesting non-trivial roles of these factors.

In summary, the complete database provided for training the ANN concerning the post-breakage kinetics of the fragment consists of 6 Weibull distribution parameters (scale λ and shape k parameter for α , β and v_{ratio}) and the kinetic energy ratio ER_{trans} , all obtained under 67 different sets of impact conditions.

7.5.3.2 Derived ANN

The second ANN aims at predicting the post-breakage behavior of the fragments. The input parameters are the impact angle Θ_{imp} , the total number of primary particles in the agglomerate $N_{\text{pp}}^{\text{tot}}$ and the fragmentation ratio FR . The number of nodes in the output layer is seven corresponding to six Weibull distribution parameters (scale λ and shape k parameter for the reflection angle α , the spreading angle β and the fragment velocity ratio v_{ratio}) and the kinetic energy ratio ER_{trans} . Since the Weibull parameters λ and k

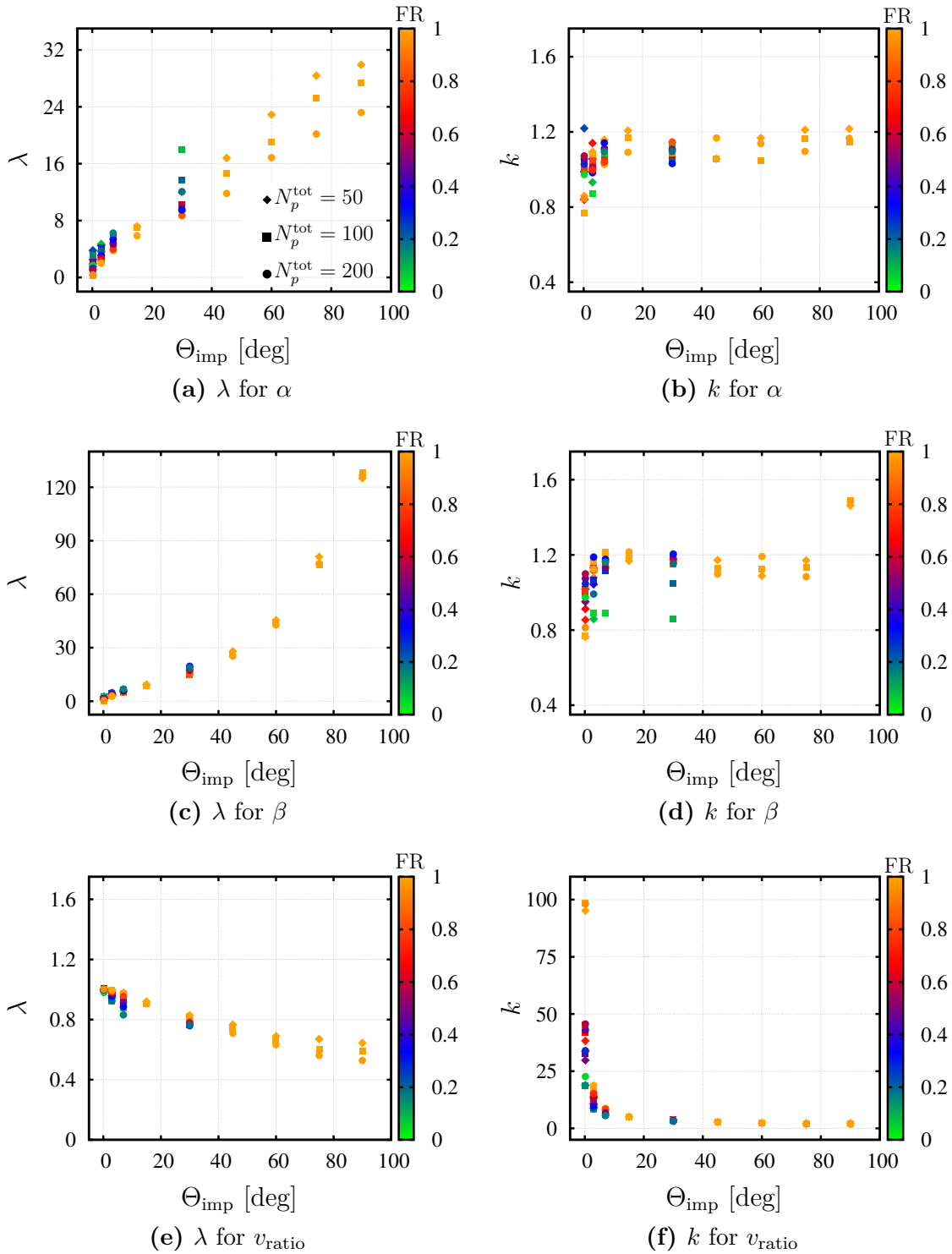


Fig. 7.24. Scale and shape parameters λ and k of the Weibull PDFs as functions of the impact angle Θ_{imp} .

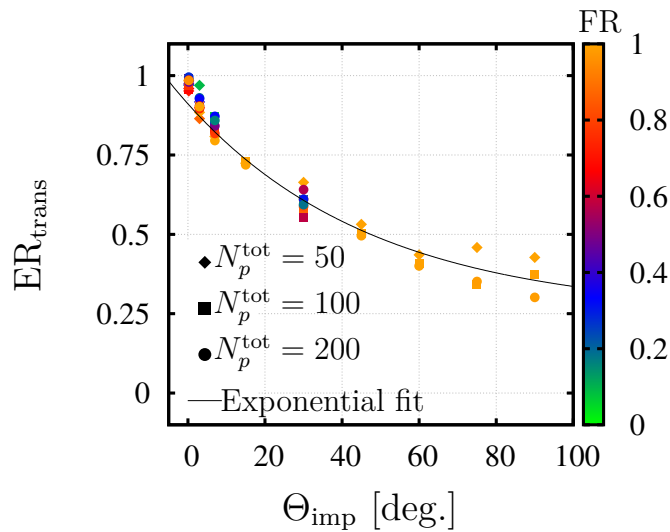


Fig. 7.25. Ratio of translational kinetic energy of the fragments ER_{trans} as a function of the impact angle Θ_{imp} .

are always greater than zero and ER_{trans} varies in the range $[0, 1]$, the second network deals with a non-negative regression problem. In this network solely a single hidden layer consisting of 6 nodes is used leading to the topology of 3–6–7. The activation function in the hidden layer is the logistic sigmoid function, whereas a rectified linear activation function is applied at the output layer. The latter is a piecewise function that returns the input directly if it is positive, and a zero if the input is negative. Adopting such a function for the output layer of this network is an appropriate choice since the output parameters are naturally bounded in the positive range. However, to allow the network to extrapolate beyond the minimum values of the output parameters of the training dataset, a linear normalization scheme is generally adopted which transfers the input ($x_i = x_i^*/x^{*,\text{max}}$) and the output ($y_i = y_i^*/y^{*,\text{max}}$) data into the range $(0, 1]$. As an exception, a logarithmic scaling is applied to the output parameter k for v_{ratio} to reduce the skewness of the data (see Fig. 7.24(f)):

$$y_{k,v_{\text{ratio}}} = \frac{\ln(y_{k,v_{\text{ratio}}}^* + 1)}{\ln(y_{k,v_{\text{ratio}}}^{*,\text{max}} + 1)}, \quad (7.43)$$

which also transfers the data into the range $(0, 1]$. Note that if the network is utilized in Euler–Lagrange simulations and has to extrapolate the data, it is still possible to obtain non-physical predictions of the Weibull distribution parameters (i.e., k or $\lambda = 0$) or the kinetic energy ratio (i.e., $ER_{\text{trans}} > 1$). Thus, the outputs of the network need to be checked and restricted to their physical ranges if necessary. This issue will be revisited in Section 7.5.4.

Analogous to the first ANN, the database of the second network is split into training and testing datasets with 58 (87%) and 9 (13%) breakage cases, respectively. Furthermore, several configurations are checked and the combination of the settings described above

leads to the best trade-off between the predictions of the training and the testing datasets, which are depicted in Figs. 7.26(a) and 7.26(b), respectively. Note that the training of this network stops when the damping coefficient of the Levenberg–Marquardt algorithm exceeds the convergence threshold of 10^{-10} and the performance gradient is $1.16 \cdot 10^{-6}$. In addition, the number of effective parameters (weights and biases) is 66 out of 73 trainable parameters. The mean MSE of the training and testing datasets averaged over the seven output parameters are $8.21 \cdot 10^{-4}$ and $8.80 \cdot 10^{-4}$, respectively. Again, the individual values for each output parameter are provided in Table 7.9.

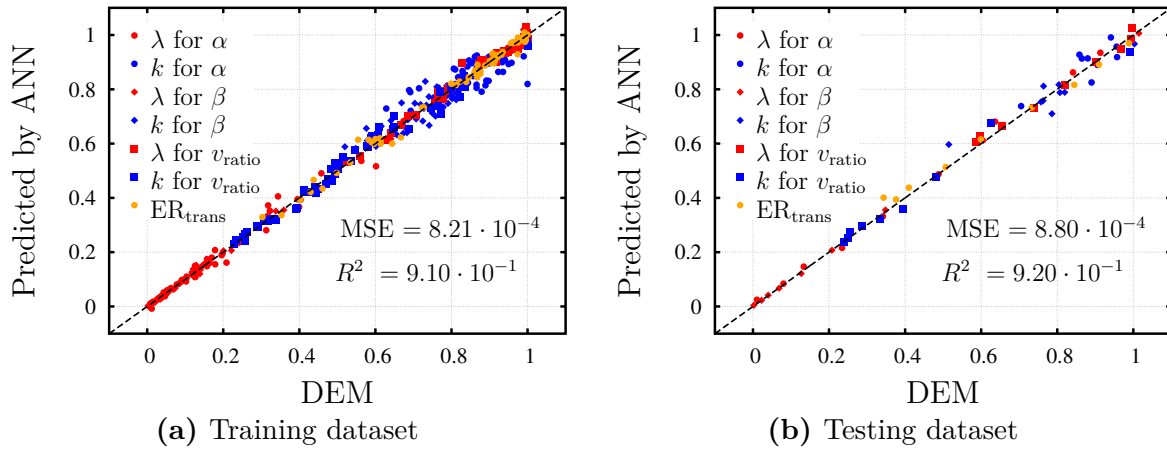


Fig. 7.26. ANN predictions of the six Weibull distribution parameters (scale λ and shape k parameter for the reflection angle α , the spreading angle β and the fragment velocity ratio v_{ratio}) and the kinetic energy ratio ER_{trans} for (a) the training dataset and (b) the testing dataset. The reference line is dashed and has a slope of unity.

Overall, these numbers suggest a good agreement between the actual and predicted data in both datasets. A larger number of testing cases would allow a better assessment of the generality of the network. Unfortunately, increasing the number of testing cases is not possible for the present network without undermining the required diversity of cases in the training dataset due to the overall small number of cases in the whole database. Furthermore, the corresponding mean values of R^2 are 0.91 and 0.92. Considering the output parameters individually reveals that R^2 of the training and testing datasets is about 0.98 if the results of k for α are excluded. The predictions of this output parameter cannot be improved without affecting the accuracy of the prediction of other output parameters (e.g., by changing the normalization scheme or tuning other network parameters). An alternative solution would be to split the network into multiple networks of smaller numbers of outputs. However, the current form and the obtained performance of the network are acceptable for the sake of keeping the modeling procedure compact and efficient. Nevertheless, the high capability of this network to deliver reasonable predictions for all output parameters will be demonstrated in the duct flow case in Section 9.2.4.

Tab. 7.9. MSE and R^2 values of the outputs of the ANN predicting the kinetics of the fragments.

		Training		Testing	
		MSE	R^2	MSE	R^2
α	λ	$4.42 \cdot 10^{-4}$	0.992	$4.07 \cdot 10^{-4}$	0.996
	k	$2.78 \cdot 10^{-3}$	0.550	$1.98 \cdot 10^{-3}$	0.624
β	λ	$7.14 \cdot 10^{-5}$	0.998	$2.15 \cdot 10^{-5}$	0.999
	k	$1.29 \cdot 10^{-3}$	0.834	$1.94 \cdot 10^{-3}$	0.859
v_{ratio}	λ	$2.72 \cdot 10^{-4}$	0.982	$3.10 \cdot 10^{-4}$	0.988
	k	$5.61 \cdot 10^{-4}$	0.986	$8.02 \cdot 10^{-4}$	0.985
ER _{ratio}		$3.24 \cdot 10^{-4}$	0.992	$6.95 \cdot 10^{-4}$	0.987

7.5.4 Realization of the Model in the Euler–Lagrange Approach

The ANN-based wall-impact breakage model is incorporated into the particle-laden flow simulations as follows. When an agglomerate consisting of $N_{\text{pp}}^{\text{tot}}$ primary particles of a certain particle diameter d_{pp} impacts a wall, the total impact velocity v_{imp} and the impact angle Θ_{imp} are computed. To predict the occurrence of breakage, the resulting fragment size distributions, and the velocities of the fragments using the two pre-trained ANNs, the feed-forward procedures of the networks have to be fully replicated in the simulation framework. This measure is necessary in order not to endanger the high-performance efficiency of the parallelized Euler–Lagrange solver. The implementation includes the number of hidden layers and hidden nodes, the activation functions, the trained weights and biases, and the normalization parameters of the input and output data used in the training. The predictions in form of the normalized outputs are then obtained by applying the mathematical procedure behind each network on the corresponding set of inputs.

Concerning the first network tackling the number of evolving fragments and the fragment size distribution, the relevant impact conditions are scaled based on Eq. (7.40) using the same parameters as those employed to normalize the DEM data in the training stage. This step is necessary since the impact conditions in the application must be consistent with the normalized training inputs in order to obtain comparable predictions. Then, the output of the first hidden layer for an arbitrary node m is computed as follows:

$$a_m^{\text{h1}} = f_{\text{act}}^{\text{h1}} \left(\sum_{i=1}^I [x_i \cdot w_{im}^{\text{h1}} + b_m^{\text{h1}}] \right), \quad (7.44)$$

where I is the total number of input nodes in the network and the superscript h_1 refers to the first hidden layer. In an analogous way the output of the node k belonging to the

second hidden layer is predicted. Subsequently, the predictions of the network output j is obtained as follows:

$$y_j^{\text{ANN}} = f_{\text{act}}^{\text{out}} \left(\sum_{k=1}^K [a_k^{\text{h2}} \cdot w_{kj}^{\text{out}} + b_j^{\text{out}}] \right). \quad (7.45)$$

Here, K is the total number of nodes in the second hidden layer and the superscript *out* denotes the output layer. Furthermore, j is an index running between 1 and 4 referring to the fragmentation ratio FR and the fragment size parameters ζ_1 , ζ_2 , and ζ_3 . Breakage is detected when FR leads to more than one fragment. The sizes of the three largest fragments are computed based on the definition of ζ_i given by Eq. (7.19). If more than three fragments exist and the third largest fragment is not a single primary particle, the sizes of the remaining fragments are randomly obtained satisfying the mass conservation of the original agglomerate and the condition that none of these fragments is larger than the third largest fragment.

Since FR is obtained in the first network, the inputs of the second network are complete allowing to predict the velocity of the fragments. The procedure is analogous to that of the first network with the sole difference that only one hidden layer exists in this network.

Hence, the kinetic energy ratio ER_{trans} and the Weibull distribution parameters λ and k of α , β , and v_{ratio} are obtained in a normalized form. To determine the natural values of these parameters, the normalization step used in the training (e.g., Eq. (7.43)) is reversed. Since the Weibull parameters k and λ must per definition always be greater than zero, the predicted values are restricted to a small limit of 0.1 during the feed-forward procedure to avoid numerical problems. This limiting value is still smaller than the smallest value found in the reference DEM database (i.e., $y_{\lambda, \alpha}^{\text{min}} = 0.25$) allowing for a reasonable range of extrapolation for all output parameters. Next, a value of α , β and v_{ratio} computed based on random numbers according to the corresponding Weibull PDFs is assigned to each fragment. However, since the Weibull PDF of the angle β accounts solely for the positive range of the angle, the sign of β is alternately inverted leading to a symmetric distribution between the positive and the negative range which fits well to the real situation. Furthermore, if the number of fragments is not large, the statistical predictions of v_{ratio} might lead to an over- or underestimation of the amount of the translational kinetic energy of the fragments. This may cause a non-physical accumulation of particles in the near-wall region or may lead to too high bouncing velocities. Thus, the velocities of the fragments are slightly adjusted using ER_{trans} to ensure that the kinetic energy of the fragments is comparable to those obtained in the reference DEM simulations for similar impact conditions. To achieve that, the energy correction factor ϵ_{cor} defined in Eq. (7.38) is applied to each component of the velocity vector of each fragment adjusting their velocities evenly (i.e., $\mathbf{v}_{\text{new}}^{\text{fr}} = \epsilon_{\text{cor}} \cdot \mathbf{v}^{\text{fr}}$). In case of a sufficiently large number of fragments this correction step has a negligible effect ($\epsilon_{\text{cor}} \approx 1$) since the energy is already taken into account based on v_{ratio} .

8 Numerical Methodology

In the preceding chapters the physical aspects of the present Euler–Lagrangian approach have been the main focus. However, the numerical procedure is another important aspect since it allows solutions of the mathematical systems describing the underlying physics.

The particle-laden flow simulations in the present thesis are carried out using the in-house Euler–Lagrange code *LESOC* (Breuer, 1998a,b, 2000, 2002). The code utilizes curvilinear body-fitted block-structured grids allowing to predict flows in complex geometries based on a technique combining large-eddy simulation for the fluid with point-particle tracking for the particles.

The present chapter introduces the numerical framework employed in this thesis for the solution of the equations governing the Euler–Lagrange system. To this end, the most important features of the finite-volume method applied to solve the incompressible fluid flow are briefly outlined in Section 8.1. In addition, Section 8.2 gives a brief overview on the numerical techniques applied for the particulate phase.

8.1 Numerical Methods for the Continuous Phase

Curvilinear, non-orthogonal, and block-structured grids are known to offer a balance between flexibility and complexity. The structured curvilinear arrangement enables efficient solution procedures by mapping complex physical domains into simpler computational ones (see Fig. 8.1), while offering a fixed general scheme to describe the connectivity between the grid points. That is an advantage compared to unstructured grids, where a list of node connectivities has to be stored and recovered. Furthermore, the multi-block arrangement allows to achieve fine grid resolutions in flow regions of interest without exaggerations in the total number of grid cells. However, adopting curvilinear coordinates entails the transformation of the governing equations from the physical to the computational (curvilinear) coordinate system. For instance, the curvilinear form of the dimensionless conservation equation of mass (Eq. (3.1)) and momentum (Eq. (3.7)) for an incompressible fluid read (Ferziger and Perić, 2002):

$$\frac{\partial (\bar{U}_j J^{-1})}{\partial \xi_j} = 0, \quad (8.1)$$

$$J^{-1} \frac{\partial \bar{u}_i}{\partial t} + \frac{\partial (\bar{u}_i \bar{U}_j J^{-1})}{\partial \xi_j} = -\frac{\partial \bar{P}}{\partial \xi_j} \beta_{ji} + \frac{\partial}{\partial \xi_j} \left[\left(\mu_T + \frac{1}{\text{Re}} \right) \left(\frac{\partial \bar{u}_i}{\partial \xi_m} J \beta_{mi} \beta_{ji} \right) \right] + J^{-1} f_j^{\text{PSIC}}, \quad (8.2)$$

respectively. Here, \bar{P} stands for the modified filtered pressure defined in Eq. (3.6) and \bar{U}_i is the filtered contravariant velocity of the fluid, which will be explained below. In

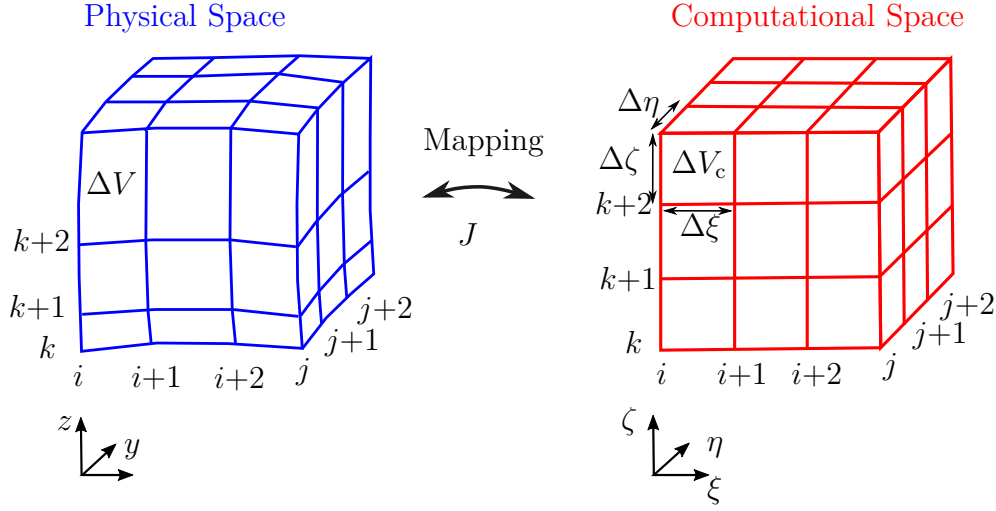


Fig. 8.1. Transformation of the coordinate system between the physical and the computational space.

addition, $\xi_i = (\xi, \eta, \zeta)$ denotes the coordinates in the computational space and J and J^{-1} are the determinants of the Jacobian matrix \mathbf{J} and its inverse \mathbf{J}^{-1} , respectively. The Jacobian matrix consists of the following first-order partial derivatives:

$$\mathbf{J} = \begin{pmatrix} \frac{\partial \xi}{\partial x} & \frac{\partial \xi}{\partial y} & \frac{\partial \xi}{\partial z} \\ \frac{\partial \eta}{\partial x} & \frac{\partial \eta}{\partial y} & \frac{\partial \eta}{\partial z} \\ \frac{\partial \zeta}{\partial x} & \frac{\partial \zeta}{\partial y} & \frac{\partial \zeta}{\partial z} \end{pmatrix}. \quad (8.3)$$

The determinant J defines the ratio between the volume of cells in the physical (ΔV) to the computational space (ΔV_c), i.e., $J = \Delta V_c / \Delta V$ (Ferziger and Perić, 2002). Fig. 8.1 depicts a computational domain in which all control volumes are assumed to be equally sized and have the dimensions $\Delta \xi = \Delta \eta = \Delta \zeta = 1$, i.e., the volume of the cell is equal to unity $\Delta V_c = 1$. Hence, the determinant of the Jacobian matrix and its inverse are given by $J = 1 / \Delta V$ and $J^{-1} = \Delta V$, respectively. Moreover, the coefficient $\beta_{ij} = J^{-1} (\partial \xi_i / \partial x_j)$ is introduced. Using these definitions, the contravariant velocity of the fluid can be expressed as $\bar{U}_i = (\bar{U}, \bar{V}, \bar{W}) = J (\bar{u}_k \beta_{ik})$.

The code *LESOC* applies the finite-volume method to predict the solution of the partial differential equations (8.1) and (8.2). For this purpose, the domain is discretized by a grid. Furthermore, the governing equations need to be discretized to enable a solution. For simplicity, the solution technique is briefly discussed based on a general conservation equation for an arbitrary transport quantity ϕ related to an incompressible fluid and expressed in curvilinear coordinates:

$$J^{-1} \left(\frac{\partial \phi}{\partial t} \right) + \frac{\partial (\phi U_j J^{-1})}{\partial \xi_j} = \frac{\partial}{\partial \xi_j} \left(\Gamma_\phi \frac{\partial \phi}{\partial \xi_m} J \beta_{mi} \beta_{ji} \right) + S_\phi J^{-1}. \quad (8.4)$$

Here, Γ_ϕ denotes the diffusion coefficient and S_ϕ is a source term for the quantity ϕ . Note that with respect to the conservation of mass given by Eq. (8.1), the transport quantity ϕ corresponds to the dimensionless density of the fluid which does not appear in the equation since it is equal to unity (i.e., $\rho_f = 1$). In the momentum conservation equation (8.2) the transport quantity ϕ corresponds to the components of the (filtered) velocity field. By integrating Eq. (8.4) over the control volume V_c in the computational space (see Fig. 8.1) and applying Gauss's theorem, the integral form of the general transport equation (8.4) is obtained:

$$\underbrace{\int_{V_c} J^{-1} \left(\frac{\partial \phi}{\partial t} \right) dV_c}_{\text{local change}} + \underbrace{\int_{S_c} (\phi U_j J^{-1}) \cdot n_j dS_c}_{\text{convective fluxes}} = \underbrace{\int_{S_c} \left(\Gamma_\phi \frac{\partial \phi}{\partial \xi_m} J \beta_{mi} \beta_{ji} \right) \cdot n_j dS_c}_{\text{diffusive fluxes}} + \underbrace{\int_{V_c} S_\phi J^{-1} dV_c}_{\text{sources}}. \quad (8.5)$$

Here, S_c stands for the surface of the control volume in the computational space and n_j is the corresponding unit vector normal to S_c . The terms appearing in Eq. (8.5) are discretized as follows. The volume integrals are approximated by applying the second-order accurate midpoint rule (Ferziger and Perić, 2002). Here the volume-averaged value for each cell is approximated by the corresponding value at the center of the control volume. Since *LESOCC* adopts a collocated (i.e., non-staggered) variable arrangement, all variables are available at the center of the cells. Hence, no additional interpolation is necessary in the discretization of the volume integrals.

Furthermore, both surface integrals appearing in Eq. (8.5) are split into a sum of integrals (fluxes) over the six faces of the hexahedral control volumes used in structured grids. For each surface, the flux is obtained by multiplying the surface-averaged value of the integrand with the corresponding surface area which describes the midpoint rule. The surface-averaged values are approximated by the corresponding values at the center of the surface. However, since all variables are stored at the center of the control volumes in collocated grids, an interpolation to the centers of the six surfaces is mandatory.

For the convective fluxes in Eq. (8.5), a linear interpolation is used to evaluate the velocity at the surface based on the known velocities at the two cell centers laying across the surface. This type of interpolation scheme, which is known as the linear interpolation is second-order accurate and represents the counterpart of the central finite-differences in the finite-difference context. However, it may generate oscillatory solutions. That is also an important issue for grids with a collocated variable arrangement. In this case, the prediction of the mass fluxes at the cell faces based on the midpoint rule and a linear interpolation of the velocities to the cell faces is problematic and can lead to a decoupling of the velocity and the pressure field. This problem is prevented in the present work by applying the momentum interpolation technique by Rhie and Chow (1983).

Moreover, the gradient of the quantity ϕ appearing in the diffusive fluxes in Eq. (8.5) is approximated at the six surfaces of the control volume using a second-order accurate central finite-difference scheme.

It should be noted that the pressure term in Eq. (8.2) has no direct analog in the generic conservation equation (8.5). However, the pressure term is expressed in the form of a surface force (conservative treatment).

Applying the finite-volume method described above to the momentum conservation equation (8.2) delivers a non-linear differential equation in time for the filtered fluid velocity at the center of the computational cells. In the present methodology, the time-marching is achieved by the second-order accurate low-storage Runge-Kutta method (Binniger, 1989) within a predictor-corrector scheme. In a first step, the temporal integration of the momentum equation is carried out to predict the value of the velocity (prediction step). Note that the pressure of the new time step is not known and thus approximated by the pressure from the previous time step. The resulting velocity field does not satisfy the mass conservation equation, i.e., is not necessarily divergence-free. For this reason, a corrector step is subsequently carried out, in which the obtained velocity is considered as an intermediate value between the old and the new time step. To this end, a Poisson equation for the pressure correction is numerically solved by means of the incomplete lower-upper decomposition (ILU) method (Stone, 1968). Owing to the iterative nature of ILU, five to ten (inner) iterations are typically carried out. As a result, a new (corrected) pressure is obtained, which is subsequently inserted in the momentum equation to obtain an improved estimation of the velocity. In the present collocated variable arrangement, the improved velocity field can still be not divergence free. Therefore, the entire correction step is repeated (five to ten outer iterations) until a predefined convergence threshold ($\mathcal{O}(10^{-8})$) of the mass conservation is reached. For more details the reader is referred to (Breuer, 1998a,b, 2000, 2002) and Ferziger and Perić (2002).

8.2 Numerical Methods for the Dispersed Phase

The present section describes some of the essential features of the numerical method used for the Lagrangian tracking. Different issues are discussed including the techniques applied for (1) interpolating quantities from the Eulerian grid to the particle position (and vice versa) (Section 8.2.1), (2) integrating the equation of motion (Section 8.2.2), and (3) detecting particle collisions and wall impacts (Section 8.2.3).

8.2.1 Interpolation of Fluid Quantities to Particle Positions

As earlier stated in Section 4.2, the fluid forces and the torque exerted on the point-particles are given by closure models. These closures mainly rely on the velocity of the fluid computed at the position of the particle. Similarly, the relationships used for evaluating the turbulent and the drag stress in the fluid-induced breakup model (Section 6.3) depend on the local fluid velocity and the local dissipation rate ϵ of the fluid kinetic energy.

For this purpose, it is necessary to interpolate some fluid quantities represented on the computational grid to arbitrary particle positions.

In the present thesis, the aforementioned interpolation is accomplished using two different methods. The first is the second-order accurate trilinear interpolation. This method uses the results available on the eight grid points surrounding the interpolation point, taking the distance between the grid and the interpolation point into account based on weighting factors. Examples of quantities which are computed on the Eulerian grid first and then interpolated to the particle position by the trilinear scheme include (1) the rotation of the velocity field $\nabla \times \mathbf{u}_f$ needed for computing the relative rotation of particles (see Eq. (4.16)), and (2) the local strain rate tensor $\underline{\mathbf{S}}$ required for determining the local energy dissipation rate ϵ (see Eq. (6.8)). In addition, as clarified in Section 4.2.4 a trilinear scheme is also applied in the opposite direction to determine the weighting factors used for projecting the feedback force from the particles back to the Eulerian grid, in case two-way coupling is taken into account.

The second interpolation method is the second-order accurate Taylor series expansion (Marchioli et al., 2007), which is specifically used for determining the fluid velocity at the position of the particles. The reason for abandoning the trilinear scheme for this important task is the significant unphysical filtering of the velocity field associated with the trilinear interpolation (Alletto, 2014; Marchioli et al., 2007).

8.2.2 Solution of the Particle Equations of Motion

In order to obtain the velocities and displacements of particles, the governing equation of the translatory and the rotational motion of the individual particles need to be solved. The solution methods are briefly explained next.

8.2.2.1 Translatory Motion

In Section 4.2 it was explained that the equation of motion for the translatory motion of particles accounts for various physical effects including gravity and buoyancy \mathbf{F}_{G+B} , drag \mathbf{F}_D , lift $\mathbf{F}_L^{\text{Saf+Mag}}$, and added-mass and pressure-gradient forces \mathbf{F}_{AM+PG} :

$$m_p \frac{d\mathbf{u}_p}{dt} = \mathbf{F}_{G+B} + \mathbf{F}_D + \mathbf{F}_L^{\text{Saf+Mag}} + \mathbf{F}_{AM+PG}. \quad (8.6)$$

The expressions for calculating these forces are summarized as follows:

$$\mathbf{F}_{G+B} = m_p \mathbf{g} \left[1 - \frac{\rho_f}{\rho_p} \right], \quad (8.7a)$$

$$\mathbf{F}_D = \frac{C_D}{8} \pi \rho_f d_p^2 |\mathbf{u}_f - \mathbf{u}_p| (\mathbf{u}_f - \mathbf{u}_p), \quad (8.7b)$$

$$\mathbf{F}_L^{\text{Saf+Mag}} = \frac{\rho_f}{2} \frac{\pi}{4} d_p^3 \left[C_{LS} [(\mathbf{u}_f - \mathbf{u}_p) \times \boldsymbol{\omega}_f] + \frac{C_{LR}}{d_p} |\mathbf{u}_f - \mathbf{u}_p| \frac{\boldsymbol{\Omega}_{\text{rel}} \times (\mathbf{u}_f - \mathbf{u}_p)}{|\boldsymbol{\Omega}_{\text{rel}}|} \right], \quad (8.7c)$$

$$(8.7d)$$

In order to commence a solution for Eq. (8.6), some rearrangements are useful. Since the second term on the r.h.s. of Eq. (8.9d) contains the acceleration of the particle, this term can be added to the l.h.s. of Eq. (8.6). In addition, Eq. (8.6) is divided by the mass of the particle m_p yielding:

$$\underbrace{\left(1 + C_m \frac{\rho_f}{\rho_p}\right)}_{f_m} \frac{d\mathbf{u}_p}{dt} = \mathbf{f}_D + \mathbf{f}_{G+B} + \mathbf{f}_L^{\text{Saf+Mag}} + \mathbf{f}_{AM+PG}^*, \quad (8.8)$$

where the symbol \mathbf{f} stands for the force normalized by the mass (i.e., acceleration term). These acceleration terms are given as follows:

$$\mathbf{f}_{G+B} = \mathbf{g} \left[1 - \frac{\rho_f}{\rho_p}\right], \quad (8.9a)$$

$$\mathbf{f}_D = \frac{3}{4} \frac{C_D}{d_p} \frac{\rho_f}{\rho_p} |\mathbf{u}_f - \mathbf{u}_p| (\mathbf{u}_f - \mathbf{u}_p), \quad (8.9b)$$

$$\mathbf{f}_L^{\text{Saf+Mag}} = \frac{\rho_f}{\rho_p} \frac{3}{4} \left[C_{LS} [(\mathbf{u}_f - \mathbf{u}_p) \times \boldsymbol{\omega}_f] + \frac{C_{LR}}{d_p} |\mathbf{u}_f - \mathbf{u}_p| \frac{\boldsymbol{\Omega}_{\text{rel}} \times (\mathbf{u}_f - \mathbf{u}_p)}{|\boldsymbol{\Omega}_{\text{rel}}|} \right], \quad (8.9c)$$

$$\mathbf{f}_{AM+PG}^* = \frac{\rho_f}{\rho_p} (1 + C_{AM}) \frac{D\mathbf{u}_f}{Dt}. \quad (8.9d)$$

Note that the superscript '**' in \mathbf{f}_{AM+PG}^* indicates the modification of the term related to the shift of the particle acceleration part to the l.h.s. of equation (8.8). Finally, the governing equation (8.8) of the particle's translatory motion can be formulated as:

$$\frac{d\mathbf{u}_p}{dt} = f_D (\mathbf{u}_f - \mathbf{u}_p) + \frac{1}{f_m} \underbrace{(\mathbf{f}_{G+B} + \mathbf{f}_L^{\text{Saf+Mag}} + \mathbf{f}_{AM+PG}^*)}_a, \quad (8.10)$$

which constitutes a non-linear ordinary differential equation requiring numerical solution. The factor f_D appearing in the non-linear term is given by:

$$f_D = \frac{1}{f_m} \frac{3}{4} \frac{C_D}{d_p} \frac{\rho_f}{\rho_p} |\mathbf{u}_f - \mathbf{u}_p|. \quad (8.11)$$

By integrating Eq. (8.10), the velocity of the particle is obtained (first integration). Subsequently, the actual position of the particle can be determined based on the definition of the particle velocity:

$$\frac{d\mathbf{x}_p}{dt} = \mathbf{u}_p, \quad (8.12)$$

applying a second integration.

The first integration is carried out based on the fourth-order accurate Runge–Kutta scheme.

$$\mathbf{u}_p^{(n+1)} = \mathbf{u}_p^{(n)} + \frac{1}{6} (\mathbf{k}_1 + 2\mathbf{k}_2 + 2\mathbf{k}_3 + \mathbf{k}_4), \quad (8.13)$$

with $\mathbf{u}_p^{(n+1)}$ denoting the particle velocity at the new time step. The coefficients of the four sub-steps of Eq. (8.13) are defined by:

$$\mathbf{k}_1 = \Delta t \left\{ f_D^{(n)} \left[\mathbf{u}_f - \mathbf{u}_p^{(n)} \right] + \mathbf{a}^{(n)} \right\}, \quad (8.14a)$$

$$\mathbf{k}_2 = \Delta t \left\{ f_D^{(n)} \left[\mathbf{u}_f - \left(\mathbf{u}_p^{(n)} + \frac{1}{2} \mathbf{k}_1 \right) \right] + \mathbf{a}^{(n)} \right\}, \quad (8.14b)$$

$$\mathbf{k}_3 = \Delta t \left\{ f_D^{(n)} \left[\mathbf{u}_f - \left(\mathbf{u}_p^{(n)} + \frac{1}{2} \mathbf{k}_2 \right) \right] + \mathbf{a}^{(n)} \right\}, \quad (8.14c)$$

$$\mathbf{k}_4 = \Delta t \left\{ f_D^{(n)} \left[\mathbf{u}_f - \left(\mathbf{u}_p^{(n)} + \mathbf{k}_3 \right) \right] + \mathbf{a}^{(n)} \right\}. \quad (8.14d)$$

Ideally, the acceleration term $\mathbf{a}^{(n)}$ should also be updated within the four sub-steps of the Runge–Kutta method since it includes forces (see Eq. (8.10)), which are functions of the particle velocity. However, for the sake of simplicity and since these forces are typically smaller than the drag by orders of magnitude, the acceleration term $\mathbf{a}^{(n)}$ is determined only once.

The stability of the Runge–Kutta scheme (8.14) is determined based on a condition defined by the parameter $\beta^{\text{tran}} = f_D \Delta t$, where Δt is the time-step size (Antia, 2002; Breuer et al., 2006). If the condition $0 < \beta^{\text{tran}} \leq 2.78$ is satisfied, the numerical solution (8.14) is always stable. Since in wall-resolved LES the time-step sizes are quite small (in the order of $\text{CFL} = \mathcal{O}(1)$ or less), the fluid time step can be also applied to the Lagrangian tracking (Breuer et al., 2006). This condition is especially reasonable, since in the present work the collisions of particles are not resolved in time but modeled based on the hard-sphere approach. However, in order to avoid using the numerical solution outside its stability range, a simplified analytical solution of Eq. (8.10) is considered in the rare case of $\beta^{\text{tran}} > 2$:

$$\mathbf{u}_p^{(n+1)} = \mathbf{u}_f + \left(\mathbf{u}_p^{(n)} - \mathbf{u}_f \right) \exp \left(-\beta^{\text{tran}} \right) + \frac{1}{f_D^{(n)}} \mathbf{a}^{(n)} \left[1 - \exp \left(-\beta^{\text{tran}} \right) \right], \quad (8.15)$$

which is derived assuming a Stokes flow regime, i.e., $\text{Re}_p < 1$. In this case, the drag force scales linearly with the slip velocity of the particle, i.e., f_D in Eq. (8.10) is independent on the velocity. That renders Eq. (8.10) a linear ordinary differential equation, for which an exact solution is given by Eq. (8.15). Of course, this analytical solution does not hold for higher particle Reynolds numbers. However, taking into account that the analytical solution is used in seldom cases, the introduced error is not critical.

The second integration delivering the position of the particles (see Eq. (8.12)) is carried out in the computational space:

$$\frac{d\xi_p}{dt} = \mathbf{U}_p, \quad (8.16)$$

where $\boldsymbol{\xi}_p$ and \mathbf{U}_p are the position and the contravariant velocity of the particle, respectively (Alletto, 2014; Breuer et al., 2006). The motivation behind performing the second integration in the computational space is to enable an efficient tracking procedure capable to predict millions of particles. This is related to the fact that in the computational space an explicit relation between the coordinates of the particle location and the accommodating control volume exist (Breuer et al., 2006). Hence, CPU-time extensive search algorithms for the new position of the particles can be avoided (Breuer et al., 2006; Schäfer and Breuer, 2002).

Eq. (8.16) is integrated using the same Runge–Kutta numerical scheme as applied for the first integration:

$$\boldsymbol{\xi}^{(n+1)} = \boldsymbol{\xi}^{(n)} + \frac{1}{6} (\mathbf{k}_1 + 2\mathbf{k}_2 + 2\mathbf{k}_3 + \mathbf{k}_4), \quad (8.17)$$

with the coefficients of the four sub-steps given by:

$$\mathbf{k}_1 = \Delta t \mathbf{U}_p, \quad (8.18a)$$

$$\mathbf{k}_2 = \Delta t \left(\mathbf{U}_p + \frac{1}{2} \mathbf{k}_1 \right), \quad (8.18b)$$

$$\mathbf{k}_3 = \Delta t \left(\mathbf{U}_p + \frac{1}{2} \mathbf{k}_2 \right), \quad (8.18c)$$

$$\mathbf{k}_4 = \Delta t (\mathbf{U}_p + \mathbf{k}_3). \quad (8.18d)$$

8.2.2.2 Rotational Motion

The governing equation of the rotational motion discussed in Section 4.2 can be summarized as:

$$I_p \frac{d\boldsymbol{\omega}_p}{dt} = C_R \frac{\rho_f}{2} \left(\frac{d_p}{2} \right)^5 |\boldsymbol{\Omega}_{\text{rel}}| \boldsymbol{\Omega}_{\text{rel}}. \quad (8.19)$$

Substituting the definition of the torque coefficient $C_R = 64 \pi / \text{Re}_r$ and the definitions of Re_r (see Eq. (4.18)) and $\tau_p = \rho_p d_p^2 / (18 \mu_f)$ yields a linear ordinary differential equation:

$$\frac{d\boldsymbol{\omega}_p}{dt} = \frac{10}{3\tau_p} \boldsymbol{\Omega}_{\text{rel}} = \frac{10}{3\tau_p} \left(\frac{1}{2} \nabla \times \mathbf{u}_f - \boldsymbol{\omega}_p \right). \quad (8.20)$$

Hence, Eq. (8.20) is analytically integrated to obtain the actual angular velocity of the particles:

$$\boldsymbol{\omega}_p^{(n+1)} = \boldsymbol{\omega}_p^{(n)} \exp(-\beta^{\text{rot}}) + \left(\frac{1}{2} \nabla \times \mathbf{u}_f \right) [1 - \exp(-\beta^{\text{rot}})], \quad (8.21)$$

where the factor β^{rot} is given by:

$$\beta^{\text{rot}} = \left(\frac{10}{3\tau_p} \Delta t \right). \quad (8.22)$$

8.2.3 Detection of Particle Collisions and Wall Impacts

As argued in Section 4.1, in the present methodology the motion of particles determined by solving the equation of motion is subsequently adjusted in case inter-particle or particle-wall collisions take place. For this purpose, deterministic approaches for detecting collisions (Breuer and Alletto, 2012) are available in the code *LESOC*, which are briefly explained next.

The search for inter-particle collisions is carried out within virtual cells dividing the whole computational domain into smaller sub-domains. The advantage of this procedure is to avoid a brute-force method by examining collisions between particles which are widely distanced from each other. In other words, solely particles separated by a certain distance range defined by the size of the virtual cells are considered as potential collision partners. As a result, the dependence of the computational costs related to the collision detection on the total number of particles in the domain decreases by at least an order of magnitude (Breuer and Alletto, 2012).

The size of the virtual cells is dynamically optimized during the simulation. The adjustment of the virtual cell size depends on the ratio between the desired maximum number of particles in a virtual cell to the actual maximum number of particles in a virtual cell in the previous time step (Breuer and Alletto, 2012). In addition, in each time step the search for likely collision partners is repeated while increasing the size of the virtual cells by a factor of $17/13 \approx 1.3$ to assure capturing closely-placed particles laying across the edges of two different cells in the first virtual-cell arrangement.

After identifying the potentially colliding particles using the concept of virtual cells, the occurrence of collisions are pairwise examined based on two conditions (Breuer and Alletto, 2012). First, the two collision partners have to approach each other, i.e., their separation is decreasing. Solely for the pairs satisfying the first condition, the second condition is checked. The second condition requires the minimum separation between the centers of the two particles within a single time step to be equal or smaller than the sum of their radii. Note that the minimum separation is calculated assuming that the particles are moving with constant relative velocity (Chen et al., 1998; Tanaka and Tsuji, 1991) during the period of the search. Further details on the presently used collision detection algorithm are provided in Alletto (2014) and Breuer and Alletto (2012).

The detection of particle-wall collisions is conceptually similar. However, the search for particles potentially colliding with the wall is significantly simpler since the location of walls is known and fixed. Consequently, solely the particles existing in the vicinity of the wall are examined. Two conditions need to be satisfied to detect a particle-wall collision. First, the separation between the particle and the wall is decreasing within the time interval investigated. Second, the wall-normal distance between the particle center and the wall is less than or equal to the distance of the cell-center from the wall in the wall-normal direction.

8.2.4 Treatment of Agglomerate Breakage

When a breakage event is detected due to fluid-induced stresses or wall impacts, the number, the sizes, and the velocities of the resulting fragments are predicted by the corresponding model as explained in Chapters 6 and 7.

In the present methodology, all fragments are initially placed at the last position of the original agglomerate after undergoing breakage. This implies that the new fragments are entirely overlapping, which does not resemble the real physical behavior and might lead to quick re-agglomerations. However, such an assumption is necessary to prevent two problems associated with the sudden spatial separation of fragments in the computational domain. First, the newly generated fragments can overlap with other neighboring particles or agglomerates. Second, since block-structured grids are typically utilized for such simulations, a fragment might be placed in a different computational block if breakup takes place near the border of two or more blocks. This is especially challenging if the blocks are treated by different processors. The solutions to these problems are computationally expensive which motivates the present choice of allowing the fragments to initially overlap. However, if the post-breakage separation velocities of the fragments are adequately set, the problem of non-physical collisions and re-agglomerations can largely be prevented since in the present method collision are detected if particles are approaching each other (see Section 8.2.3). For this purpose, special attention is paid in this work to the modeling of the post-breakage kinetics of the fragments.

9 Test Cases and Results

This chapter presents the results of various particle-laden flow simulations, in which the Euler–Lagrange simulation methodology explained in the preceding chapters is applied taking the breakage of agglomerates based on the developed models into account.

The first investigation (Section 9.1) is concerned with the flow in a generic lab-scale disperser, which is inspired by the experimental setup by Weiler (2008). Note that in the disperser case the investigation of breakage solely considers the role of the fluid-induced stresses, i.e., the deagglomeration due to wall impacts is not accounted for. The reason for this limitation is twofold: (1) the configuration of the disperser is designed to intensify the effect of the fluid-induced stresses by exposing agglomerates to critical flow conditions (i.e., abrupt acceleration and a shear layer) before arriving at walls, (2) the chronological order of the development of the breakage models, i.e., this test case was studied to evaluate the breakup models for the fluid-induced stresses (Breuer and Khalifa, 2019a,b) prior to the introduction of the wall-impact breakage models.

The second investigation deals with the deagglomeration of particles in duct flows taking a wide range of Reynolds numbers into account (Section 9.2). Such a setup is relevant for a range of practical applications. It should be noted that the results of the duct flow simulations were published in Khalifa and Breuer (2021) and Khalifa et al. (2022).

Lastly, the third investigation focuses on the breakage of agglomerates in various pipe bend configurations (Section 9.3). The considered geometries and flow Reynolds numbers stem from an experimental study by Adi et al. (2010) and a related numerical investigation by Tong et al. (2011) devoted to explore the effect of design parameters on the performance of dry powder inhalers. It is worth mentioning that the results of the bend pipe simulations were published in Khalifa et al. (2021).

9.1 Powder Disperser

In order to study the three fluid-induced breakup mechanisms (turbulence, drag and rotation) considered in this thesis in a single configuration, a versatile setup is sought. The generated flow field must provide the prerequisites for all deagglomeration mechanisms with manageable computational demands. This requires the establishment of a turbulent flow characterized by regions of high shear rates, high vorticity, and zones, where agglomerates are suddenly accelerated. For this purpose, a configuration resembling a simple disperser consisting of two interleaving ducts is chosen. As depicted in Fig. 9.1, the setup consists of a main square duct with a hydraulic diameter of $d_h = 4.3 \cdot 10^{-3} \text{m}$ crossed up to its midplane by a vertical square duct denoted as funnel. This is crucial for generating the flow

characteristics desired for breakup by fluid-induced mechanisms. The dimensions of both ducts are given in the sketch. An important geometric factor for generating these specific flow features is the blockage ratio $B = 0.4048$ describing the ratio of the penetrating area of the funnel and the cross-section of the main duct. Agglomerates released in the upper part of the funnel are falling in the direction normal to the duct due to gravitational acceleration. They are expected to experience severe conditions (shear/vorticity/strong velocity differences) when entering the main duct.

The entire setup is derived from an experimental investigation carried out by Weiler (2008) for studying the disintegration of dry powders. The main geometric difference is that the dry powder disperser of Weiler (2008) consisted of two pipes instead of square ducts. Otherwise the geometric setup as well as the flow conditions and powder properties are inspired by this study. As depicted in Fig. 9.2, the simplification of the geometry from a circular pipe to a square duct arrangement retains the same hydraulic diameter ($d_h = d_{\text{pipe}}$) and the same blockage ratio, i.e., $B = A_{\text{pf1}}/A_{\text{pipe}} = A_{\text{pf2}}/A_{\text{duct}} = 0.4048$. Since in the original configuration the funnel ranges to the midplane of the main pipe, the funnel in the simplified setup also extends to the midplane of the square duct yielding a width of $w_{\text{fe}} = 3.48 \cdot 10^{-3}$ m.

The main objective is to investigate the effect of two physical influences on the breakup phenomena:

1. The flow conditions specified by different volumetric flow rates leading to different Reynolds numbers, and
2. The cohesion between particles adjusted by varying the size of the primary particles forming the agglomerates.

9.1.1 Flow Configuration

The effect of the Reynolds number is examined by considering two different flow cases. Table 9.1 summarizes the flow properties of the two cases taken into account. Assuming a statistically fully developed flow at the main inlet for both cases, a low volumetric flow rate of $\dot{V}_{\text{f,in}} = 25$ norm-liter/min leads to a low Reynolds number of $\text{Re}_L = 8698$ based on the bulk velocity U_b and the hydraulic diameter d_h . Increasing the volumetric flow rates eight times results in the high-Re case of $\text{Re}_H = 69,584$.

Tab. 9.1. Flow properties for the powder disperser.

Case	Re	$\dot{V}_{\text{f,in}}$ [norm-liter/min]	U_b [m/s]	ρ_f [kg/m ³]	μ_f [kg · s ⁻¹ m ⁻¹]
Low-Re	8698	25	31	1.196	$1.833 \cdot 10^{-5}$
High-Re	69,584	200	248	1.196	$1.833 \cdot 10^{-5}$

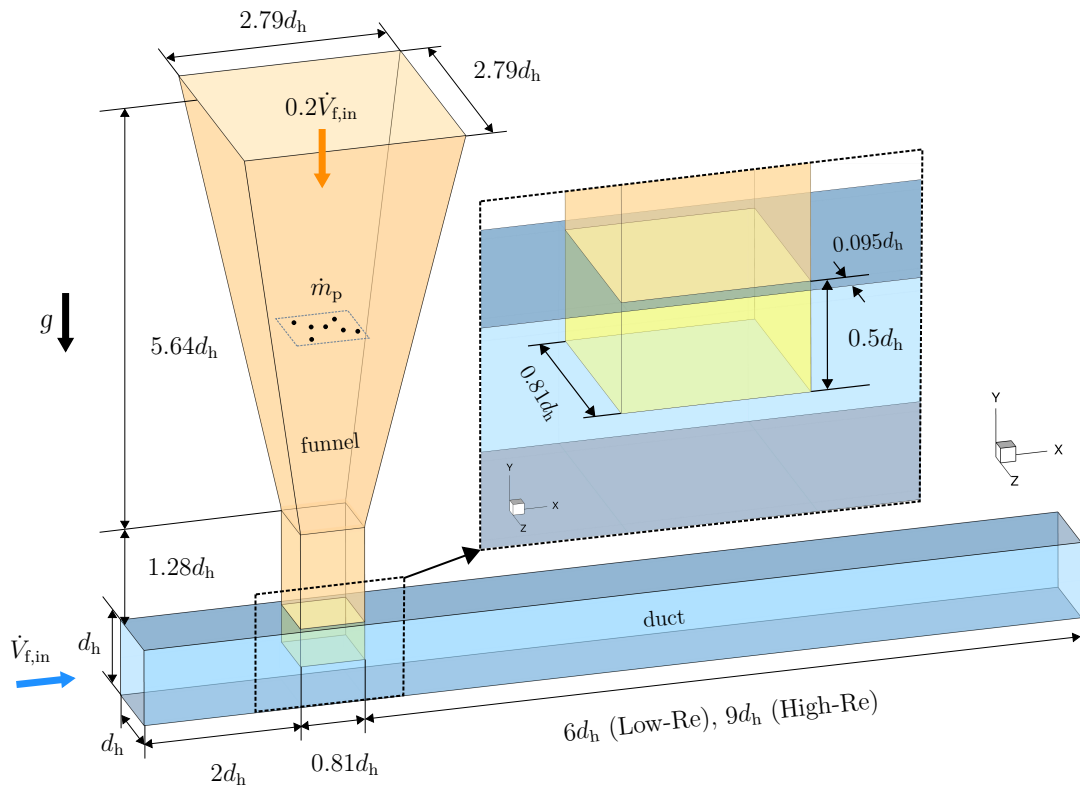


Fig. 9.1. Schematic sketch of the dry powder disperser (deagglomerator) (Breuer and Khalifa, 2019b).

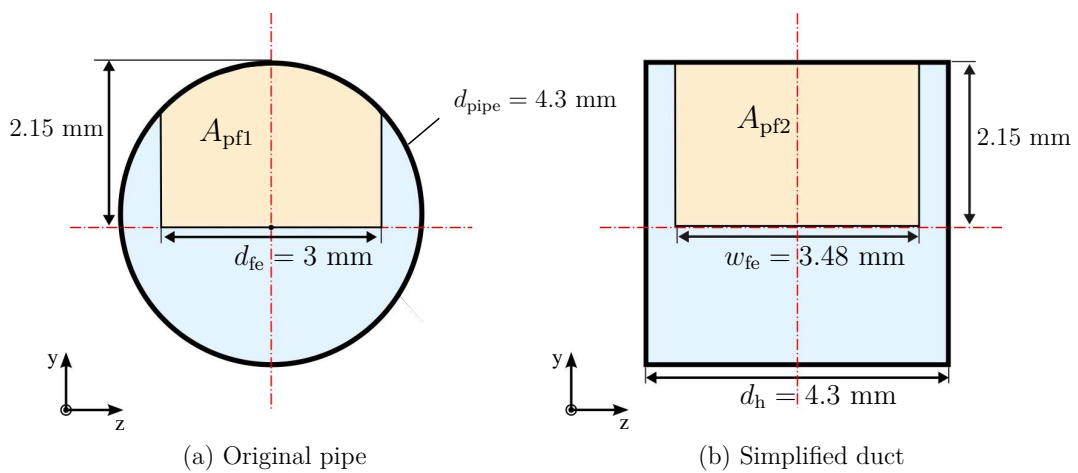


Fig. 9.2. Cross-sections of the (a) main pipe in the original configuration (Weiler, 2008) and (b) the square duct in the simplified configuration (Breuer and Khalifa, 2019a,b).

At the open top of the funnel, an inlet velocity is assumed according to a volumetric flow rate of 20% of the flow rate at the main inlet. This condition is imposed in order to mimic the air flow sucked through the funnel as the result of the pressure difference. It prevents the formation of large recirculation regions in the funnel, which hinder the transport of the agglomerates towards the main duct.

To evaluate the influence of the size of the primary particles forming an agglomerate and therefore the cohesive forces between the particles on the breakage behavior, three different size classes of monodisperse silica (SiO_2) particles are investigated. The diameter of the primary particles varies between 0.97, 2.47 and 5.08 μm and the corresponding agglomerates are denoted powder **A**, **B** and **C**, respectively. All other properties and impact parameters of the primary particles are listed in Table 9.2.

In the model for the fluid-induced breakup explained in Section 6.3, the strength S of the agglomerate is an essential quantity. According to the formula by Rumpf (1962) (see Section 6.2), the strength of agglomerates consisting of monodisperse dry primary particles bonded together by the van-der-Waals force depends on the average coordination number k_c , the packing fraction f_{pack} and the binding force (see Eq. (6.3)). As explained in Section 5.4, the two former quantities are available in the CFD code as look-up tables depending on the number of primary particles included in the agglomerates. Thus, the strength of agglomerates comprising $N_{\text{pp}}^{\text{tot}}$ primary particles of powder **A**, **B** and **C** can be determined. The outcome is depicted in Fig. 9.3. Obviously, the strength varies for small agglomerates but levels off for large ones. Furthermore, the inverse dependence of the strength on the diameter d_{pp} of the primary particles is visible. Hence, the agglomerates of powder **A** generally possess a larger strength than the agglomerates built up by the

Tab. 9.2. Properties and other characteristic parameters of the considered silica particles (SiO_2).

Parameter	Unit	Powder A , B , C
Primary particle diameter d_{pp}	m	0.97, 2.47, 5.08 $\cdot 10^{-6}$
Primary particle density ρ_{pp}	kg/m^3	2000
Poisson's ratio ν_s	-	0.17 ^d
Modulus of elasticity E_s	N/m^2	$7.2 \cdot 10^{10}$ ^d
Surface energy γ_s	J/m^2	$1.78 \cdot 10^{-3}$ ^a
Hamaker constant H	J	$2.148 \cdot 10^{-20}$ ^a
Min. inter-particle distance δ_0	m	$4.0 \cdot 10^{-10}$ ^b
Normal restitution coefficient e_n	-	0.97 ^c
Tangential restitution coefficient e_t	-	0.44 ^c
Static friction coefficient μ_s	-	0.94 ^e
Kinetic friction coefficient μ_{kin}	-	0.092 ^c

^aSchubert (2003), ^bKrupp (1967), ^cFoerster et al. (1994) for soda-lime-silica glass,

^dAzomaterials.com (2018), ^eSerway and Vuille (2007) approximated for glass on glass.

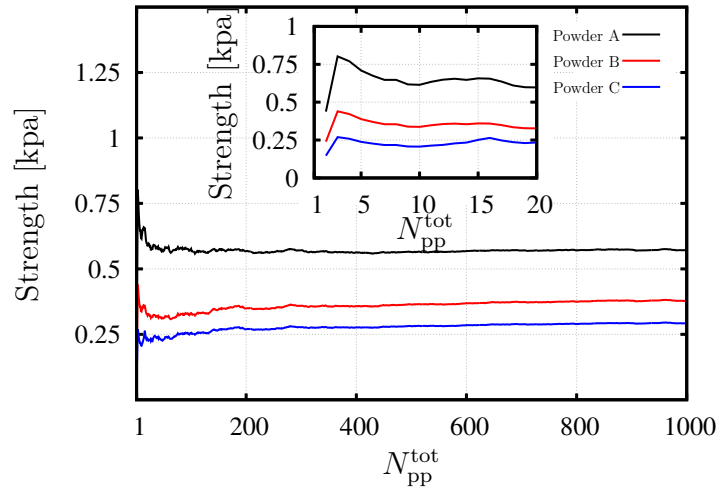


Fig. 9.3. Variation of the strength S with the size of the agglomerate (number of primary particles N_{pp}^{tot} included).

larger primary particles. However, the factor between powder **A** and **C** is not about five as expected from the diameter ratio, but only about two, since the diameter d_{pp} also affects k_c and f_{pack} .

Compact agglomerates idealized by spheres each consisting of 100 primary particles are released inside the funnel at a fixed height of about $4d_h$ measured from the central axis of the main duct. The mass flow rate is set to $\dot{m}_p \approx 10$ mg/s to match the experimentally investigated case (Weiler, 2008). The reason for not discharging the agglomerates at the top of the converging funnel is to avoid a very long settling process imposed by the considerably weak flow at the due to the large cross-section. However, to mimic realistic feeding conditions, the release positions are randomly chosen within a centered rectangular region of the extension $0.46d_h \times 0.92d_h$ in the $x-z$ plane. The initial velocities of the agglomerates are set equal to the flow velocity at the release positions. Since the feeding mass flow rate of the powder is fixed for both Reynolds numbers and all three powders, the number of released agglomerates per dimensionless time unit is different for all six cases. Namely, for the low-Re case the number of released agglomerates per dimensionless time unit is 17,778, 833, and 101 for powders **A**, **B**, and **C**, respectively. The corresponding numbers in the high-Re case are 1786, 109, and 13 in the same order.

9.1.2 Computational Setup

9.1.2.1 Boundary Conditions

The dry powder disperser sketched in Fig. 9.1 consists of two inlets (main duct and funnel) and one outlet. As mentioned above, a statistically fully developed flow at the main inlet is assumed mimicking the situation that the turbulent flow passes through a long entrance duct before reaching the disperser. In order to generate appropriate instantaneous inflow data, supplementary simulations of a single duct flow with the dimensions of $2\pi d_h \times d_h \times d_h$ are carried out. Assuming a statistically fully developed flow, periodic boundary conditions

can be applied in these auxiliary simulations, which sole task is to guarantee reliable inflow data for the main simulations. Two auxiliary simulations are carried out for the low and the high-Re cases considered. After the flow is fully developed, the velocities extracted from a selected plane normal to the streamwise direction are stored over a sufficiently long time interval and used as inflow velocities in the main configuration. For the low-Re case, this time interval $\Delta T_{\text{inlet}}^* = \Delta T_{\text{inlet}} U_b/d_h$ comprises 90 time units. Owing to the higher temporal and spatial resolution applied for the high Reynolds number, it has to be restricted to about 16 time units for this case. Since the grid point distribution in the cross-section of the grids of the auxiliary and the main simulations are chosen to match and the time-step sizes are also adjusted accordingly, no interpolation in space or time is required for the data transfer.

For the second inlet at the top of the funnel, a constant velocity distribution is chosen. Owing to the ratio of the cross-sections of the funnel inlet and the main duct, the inlet velocity corresponding to $0.2 \check{V}_{\text{f,in}}$ (i.e., $0.128 U_b$) is quite low.

Concerning the outlet of the disperser configuration, a classic convective boundary condition with U_b as the constant convection velocity is applied. As depicted in Fig. 9.1, the length of the downstream part of the main duct is $9 d_h$ for the high-Re case. This length guarantees that no backflow is present at the outlet. For the low Reynolds number a shorter length of $6 d_h$ is found to be sufficient.

All other boundaries are solid smooth walls at which the Stokes no-slip and the impermeability conditions are set. This choice is justified by the fact that wall-resolved LES predictions are performed. Thus, the grids are generated with a refined near-wall resolutions allowing the viscous sublayer to be well resolved. The latter statement is proved for the single duct flow which possesses the same near-wall spacing as the main configuration as will be discussed next.

Furthermore, since walls are assumed to be made of glass, the parameters of the particle-wall collision model ($e_n, e_t, \mu_{\text{kin}}$, and μ_{st}) are set equal to the (silica) particle-particle counterparts given in Table 9.2.

9.1.2.2 Computational Grids

The computational domain is discretized by block-structured grids as depicted in Fig. 9.4. With the exception of the converging part of the funnel, Cartesian grids are applied. Generally, grid points are clustered towards the walls of the main duct and the walls of the funnel protruding into the duct. Furthermore, the regions below and behind the obstructing part of the funnel are especially well resolved, since these are the areas where most of the breakup processes are expected to occur. The applied near-wall resolution fulfills the recommendation of Piomelli and Chasnov (1996) for wall-resolved LES defined in terms of $y_{1\text{st}}^+ < 2$, $\Delta x^+ = \mathcal{O}(50\text{--}150)$ and $\Delta z^+ = \mathcal{O}(15\text{--}40)$. Here, the index "1st" denotes the center of the first cell near the wall. In addition, the superscript "+" refers to dimensionless quantities (e.g., $y_{1\text{st}}^+ = y_{1\text{st}} \cdot u_\tau/\nu_f$) normalized by the kinematic viscosity of

the fluid ν_f and the shear velocity u_τ . The latter is predicted separately for each of the two Reynolds numbers using:

$$u_\tau = \sqrt{\frac{\tau_w}{\rho_f}}. \quad (9.1)$$

The shear stress at the wall τ_w is given by:

$$\tau_w = \frac{f_D \rho_f U_b^2}{8}, \quad (9.2)$$

where the Darcy friction factor f_D is obtained based on the formula proposed by Moody (1947), which is widely used as a design formula for turbulent pipe flows and reads:

$$f_D = 0.0055 \left[1 + \left(2 \times 10^4 \cdot \frac{\varepsilon_{sr}}{D} + \frac{10^6}{\text{Re}} \right)^{\frac{1}{3}} \right], \quad \text{for: } \begin{array}{l} 4000 \leq \text{Re} \leq 5 \times 10^8, \\ 0 \leq \varepsilon_{sr}/d_h \leq 0.01. \end{array} \quad (9.3)$$

Note that the surface roughness ε_{sr} is assumed to be negligible (i.e., $\varepsilon_{sr} = 0$) for the present ducts.

Of course, due to a factor of eight between both Reynolds numbers, the grid spacing in the vicinity of the walls and the total numbers of grid points are significantly different for both cases.

Low-Re case

The grid for the low Reynolds number case consists of 186×200 grid points in the y - z cross-section. Geometric and bi-geometric grid clustering with a maximum stretching ratio of 1.05 is applied towards the outer walls of the main duct and towards the inner walls of the obstructing part of the funnel. The center of the first cell in wall-normal direction is $\Delta y_{1st}^+ = \Delta z_{1st}^+ \approx 0.5$ in wall units (based on the wall shear stress velocity u_τ of the periodic duct case and the kinematic viscosity of the fluid). Owing to the matching conditions of the grids in the y - z cross-section of the auxiliary and the main simulation, identical grid resolutions are applied in this plane. Accordingly, solely the resolution in the streamwise (x) direction is different for both cases. For the periodic duct flow an equidistant grid spacing is appropriate in the streamwise (x) direction applying 130 grid points. That leads to a resolution of $\Delta x^+ \approx 15$ expressed in wall units. The total number of grid points in x -direction in the main simulation is 445. Stretched grids are applied in different blocks in order to cluster the points in regions of specific interest.

The first cell spacing at the main inlet boundary is set to have a comparable size in streamwise direction as the grid of the periodic duct. Furthermore, the block-structured nature of the grid facilitates the application of different geometric stretching functions in different parts. Specifically, the grid is clustered towards the inner walls in the upstream (E_4) and downstream parts (E_6) of the obstructing funnel, whereas a bi-geometric stretching is applied on the intersection part (E_5) with a maximum stretching ratio of 1.05. In the upper part of the funnel, the number of grid points along the y -direction (E_7+E_8) is 116, which are clustered towards the bottom. The details of the grid applied

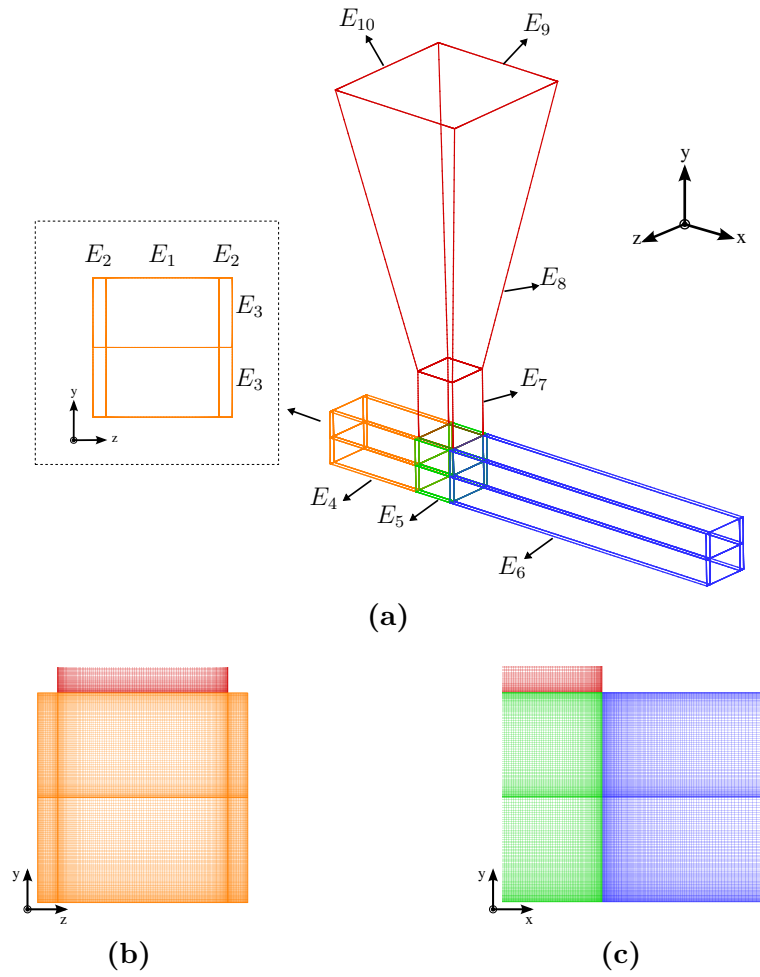


Fig. 9.4. Computational grid for the duct-funnel case. (a) 3-D view of the multi-block structure; (b) Zoom of the cross-section in the y - z plane; (c) Zoom of the cross-section in the x - y plane.

for the low-Re case are summarized in Table 9.3. The resulting total number of control volumes for this case is about 17.6 millions. The grid is split up into 158 blocks allowing the application of a high-performance computing cluster with the same number of cores (6 nodes each possessing 28 cores).

High-Re case

The grid of the high Reynolds number case possesses the same geometric block structure and the same clustering functions as the low-Re case. Nonetheless, the grid resolution is further refined to address the steeper gradients of the flow in the vicinity of the walls. However, to keep the corresponding grid of the main simulation affordable, a compromise has to be made: The first cell centers in the wall-normal directions are set according to $\Delta y_{1st}^+ = \Delta z_{1st}^+ \approx 0.8$. In addition, the resolution in the streamwise direction applied for the periodic duct flow is increased to $\Delta x^+ \approx 50$. This results in a grid containing 280×320 grid

Tab. 9.3. Summary of the grid details for the duct-funnel low-Re case. The first and last cells are defined with respect to the coordinate system. The edges E_1 to E_{10} are depicted in Fig. 9.4. The grid spacing is normalized by d_h .

Edge	Length in d_h	Number of nodes	Mesh stretching	Stretching factor	First spacing	Last spacing
E_1	0.81	120	bi-geometric	1.05	$1.57 \cdot 10^{-3}$	$1.57 \cdot 10^{-3}$
E_2	0.095	40	bi-geometric	1.05	$1.57 \cdot 10^{-3}$	$1.57 \cdot 10^{-3}$
E_3	0.50	93	bi-geometric	1.05	$1.57 \cdot 10^{-3}$	$1.57 \cdot 10^{-3}$
E_4	2.0	130	geometric ($-x$)	1.028	$5.68 \cdot 10^{-2}$	$1.57 \cdot 10^{-3}$
E_5	0.81	120	bi-geometric	1.05	$1.57 \cdot 10^{-3}$	$1.57 \cdot 10^{-3}$
E_6	6.0	195	geometric ($+x$)	1.024	$1.57 \cdot 10^{-3}$	$1.39 \cdot 10^{-1}$
E_7	1.28	78	geometric ($+y$)	1.05	$1.57 \cdot 10^{-3}$	$6.18 \cdot 10^{-2}$
E_8	5.64	38	geometric ($+y$)	1.045	$6.18 \cdot 10^{-2}$	$3.03 \cdot 10^{-1}$
E_9	2.79	120	bi-geometric	1.05	$5.42 \cdot 10^{-3}$	$5.42 \cdot 10^{-3}$
E_{10}	2.79	120	bi-geometric	1.05	$5.42 \cdot 10^{-3}$	$5.42 \cdot 10^{-3}$

points in the y - z cross-section for both the auxiliary and the main simulations fulfilling the matching condition for the transfer of the inflow data.

To avoid disturbances at the outlet of the duct, the length of the downstream part (E_6) is set to $9d_h$, which is longer than the corresponding part in the low-Re case where a length of $6d_h$ is found to be sufficient. Accordingly, the number of grid points in the x -direction ($E_4+E_5+E_6$) is in total 1240 and thus significantly larger than for the low-Re case.

Similar to the low-Re grid, different geometric stretching functions are applied in different blocks of the high-Re grid. For instance, the grid is geometrically clustered towards the inner walls in the upstream (E_4) and downstream (E_6) parts of the obstructing funnel and a bi-geometric stretching function is used for the intersection part (E_5). Along the y -direction in the upper non-intersecting part of the funnel (E_7+E_8) the grid is again geometrically stretched towards the bottom applying 235 grid points. The full details of the grid applied for the high-Re case are provided in Table 9.4. The total number of control volumes is quite large with about 114.9 millions. Again, the grid is split up into a parallel block structure but this time with 392 blocks allowing the application of 14 nodes each consisting of 28 cores.

9.1.2.3 Time-Step Size

As explained above, the employed grids apply very fine near-wall resolutions, which are also used in the streamwise direction for the inner walls where the funnel intersects the main duct. Therefore, small time-step sizes have to be used. The dimensionless time-step sizes are $\Delta t^* = \Delta t U_b/d_h = 1.5 \cdot 10^{-4}$ and $\Delta t^* = 3.5 \cdot 10^{-5}$ for the low and high Reynolds number cases, respectively. The corresponding CFL numbers are 0.49 and 0.40. That

Tab. 9.4. Summary of the grid details for the duct-funnel high-Re case. The first and last cells are defined with respect to the coordinate system. The edges E_1 to E_{10} are depicted in Fig. 9.4. The grid spacing is normalized by d_h .

Edge	Length in d_h	Number of nodes	Mesh stretching	Stretching factor	First spacing	Last spacing
E_1	0.81	160	bi-geometric	1.05	$4.8 \cdot 10^{-4}$	$4.8 \cdot 10^{-4}$
E_2	0.095	80	bi-geometric	1.05	$4.8 \cdot 10^{-4}$	$4.8 \cdot 10^{-4}$
E_3	0.50	140	bi-geometric	1.05	$4.8 \cdot 10^{-4}$	$4.8 \cdot 10^{-4}$
E_4	2.0	280	geometric ($-x$)	1.015	$3.0 \cdot 10^{-2}$	$4.8 \cdot 10^{-4}$
E_5	0.81	160	bi-geometric	1.05	$4.8 \cdot 10^{-4}$	$4.8 \cdot 10^{-4}$
E_6	9.0	800	geometric ($+x$)	1.006	$4.8 \cdot 10^{-4}$	$5.34 \cdot 10^{-2}$
E_7	1.28	120	geometric ($+y$)	1.05	$4.8 \cdot 10^{-4}$	$4.98 \cdot 10^{-2}$
E_8	5.64	115	geometric ($+y$)	1.0	$4.94 \cdot 10^{-2}$	$4.94 \cdot 10^{-2}$
E_9	2.79	160	bi-geometric	1.05	$1.65 \cdot 10^{-3}$	$1.65 \cdot 10^{-3}$
E_{10}	2.79	160	bi-geometric	1.05	$1.65 \cdot 10^{-3}$	$1.65 \cdot 10^{-3}$

shows that the stability of the explicit time-marching scheme is dictated by diffusion in the present case as expected for a wall-resolved simulation.

9.1.3 Simulation Procedure

The funnel-duct flow simulations are carried out applying the considered four-way coupled Euler–Lagrange methodology based on LES, which is explained in Chapters 3 and 4. In the funnel-duct simulations the dynamic subgrid-scale model by Germano et al. (1991) is used for both Re cases. However, it should be pointed out that the inflow data (auxiliary duct simulations) were generated earlier using the classical Smagorinsky subgrid-scale model (Smagorinsky, 1963) extended by the van Driest damping function for the near-wall region ($C_S = 0.065$).

The particle-related models applied are as follows: The stochastic Langevin particle subgrid-scale model (see Section 4.2.2), the feedback effect of the particles on the fluid (i.e., the two-way coupling), and the inter-particle collisions are taken into account. Furthermore, the agglomeration (see Section 4.3) and the fluid-induced breakup (see Chapter 6) are accounted for. As previously mentioned, the wall-impact breakage is not considered in this investigation.

Initially, the unladen flow simulation is carried out for a time interval of several flow-through times to develop the continuous phase. Afterwards, the particle-laden simulation is conducted until the disperse phase also reaches a statistically steady state. The results are sampled and analyzed over time intervals which are proven to provide nearly stable statistics. Details are given in Section 9.1.7.

9.1.4 Continuous Flow in the Auxiliary Duct

To evaluate the inflow data, some statistics of the fully developed duct flow driven by an external pressure gradient are calculated. This is done by time-averaging the instantaneous flow over more than 250 and 50 flow-through times for the low-Re and the high-Re case, respectively. Simultaneously, the flow variables are additionally averaged in the homogeneous streamwise direction. The contour lines of the mean streamwise velocity shown in Fig. 9.5 are bended towards the corners of the duct complying with the expected effects of the secondary motions (Prandtl, 1925, 1927). The secondary flow can be described as a mean weak cross-flow velocity field, which appears in the form of counter-rotating pairs of eddies located in each of the corners of the cross-section (see Fig. 9.5). In turbulent non-circular duct flows this secondary flow is attributed to the arising streamwise vorticity, which in turn is generated by the gradients of the Reynolds stresses (Bradshaw, 1987). This phenomenon is commonly referred to as Prandtl's secondary flow of second kind. As a result, high-momentum fluid is carried from the core of the duct towards the corners leading to the distortion of the contour lines of the streamwise velocity (Gavrilakis, 1992). The magnitude of the generated cross-flow velocity is low. In the present case it is about 2.5% of the bulk velocity for both cases. Larger differences between both Re numbers are visible in the Reynolds stress distributions, which are not depicted here for the sake of brevity.

Although a completely anti-symmetric distribution of all statistics is not yet reached, the qualitative characterization of the mean and secondary flows at both Reynolds numbers are in general agreement with the data available in the literature. A longer time-averaging would improve the symmetry of the results. However, that is beyond the scope of the

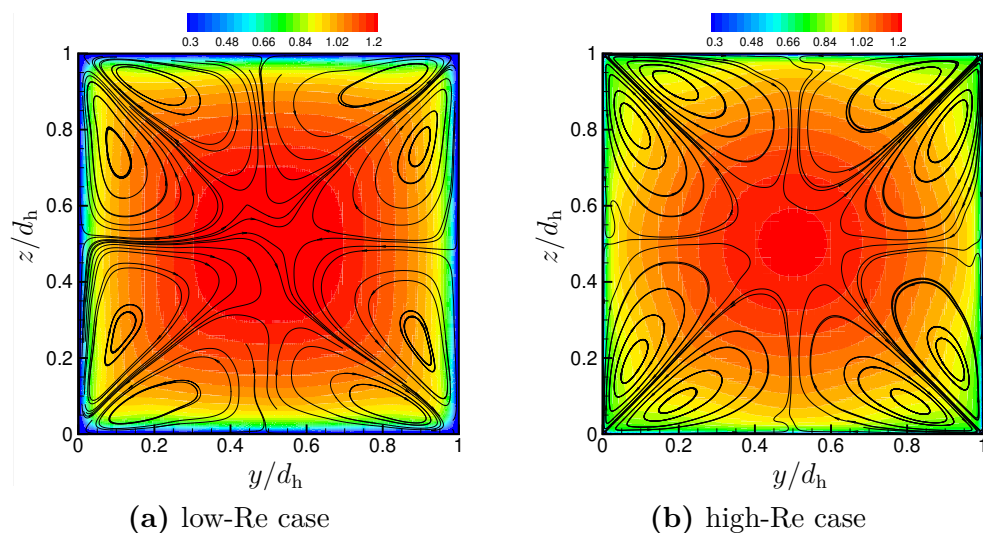


Fig. 9.5. Contours of the mean streamwise velocity u/U_b in the cross-section of the duct with superimposed streamlines of the mean secondary flow for the (a) low-Re and the (b) high-Re case.

present work, since the intrinsic goal is to generate instantaneous inflow data for the disperser flow.

9.1.5 Continuous Flow in the Disperser

In this section, the flow patterns occurring due to the protrusion of the funnel exit into the main duct are presented. In addition, their relevance to the breakup processes is explained. From a practical point of view, the walls of the funnel inside the duct can be seen as a bluff body obstructing the duct flow, which gives rise to two well-known phenomena captured by the instantaneous u/U_b and the time-averaged $\langle u \rangle / U_b$ streamwise velocity in the symmetry plane ($z/d_h = 0$) depicted in Figs. 9.6(a) and 9.6(c) for the low-Re case and Figs. 9.6(b) and 9.6(d) for the high-Re case, respectively.

The first phenomenon observed is the acceleration of the flow below the funnel exit. Due to the abruptly contracted cross-sectional area the fully developed duct flow is diverted and the streamwise velocity increases quickly below the exit of the funnel. In the downstream region, the streamwise velocity slowly decreases again. The second phenomenon is the flow separation occurring behind the obstacle. Consequently, a separating shear layer develops. Owing to the sucked air flow leaving the funnel with velocities in the negative y -direction, no recirculation is detected directly below the exit. However, a small recirculation zone is formed in the upstream region (corner vortex) which appears in front of the funnel exit (blue region in the corner) in Figs. 9.6(c) and 9.6(d). As expected a large recirculation is found behind the obstacle where its size varies by the oscillating movement of the shear layer. Naturally, strong velocity gradients appear across the shear layer and within the recirculation zone. Not surprisingly, the resolved Reynolds stresses are high in these regions as visible in Figs. 9.6(e) to 9.6(j) depicting the distribution of the resolved normal Reynolds stresses $\langle u'u' \rangle$ and $\langle v'v' \rangle$ and the Reynolds shear stress $\langle u'v' \rangle$ for both Re. For both cases an increased level of turbulent fluctuations is observed at the end of the recirculation region induced by the back-and-forth and lateral movement of the separation region. The strong velocity fluctuations can also be seen by the distribution of the resolved turbulent kinetic energy $\langle k \rangle = 1/2 (\langle u'u' \rangle + \langle v'v' \rangle + \langle w'w' \rangle)$ exemplary depicted in Fig. 9.7(a) for the high-Re case.

To illustrate the strong velocity gradients established within the flow in a context directly related to the stress mechanisms leading to breakup, two quantities derived from the velocity gradient tensor are presented in Figs. 9.7(b) and 9.7(c): The magnitude of the strain rate tensor $|\underline{\underline{S}}|$, and the magnitude of the fluid vorticity vector ω_f , both calculated based on the time-averaged velocity field in the high-Re case. However, it has to be noted that since breakup results from the interaction of agglomerates with the instantaneous and not the time-averaged flow field, these figures should only serve as qualitative maps highlighting the most critical regions. Both quantities are found to possess large values in the shear layer, the recirculation zone and in the vicinity of the walls including the walls inside the funnel.

In Section 6.3.1 it was explained that the breakup of agglomerates by the turbulent stress requires the presence of large velocity differences at length scales comparable to

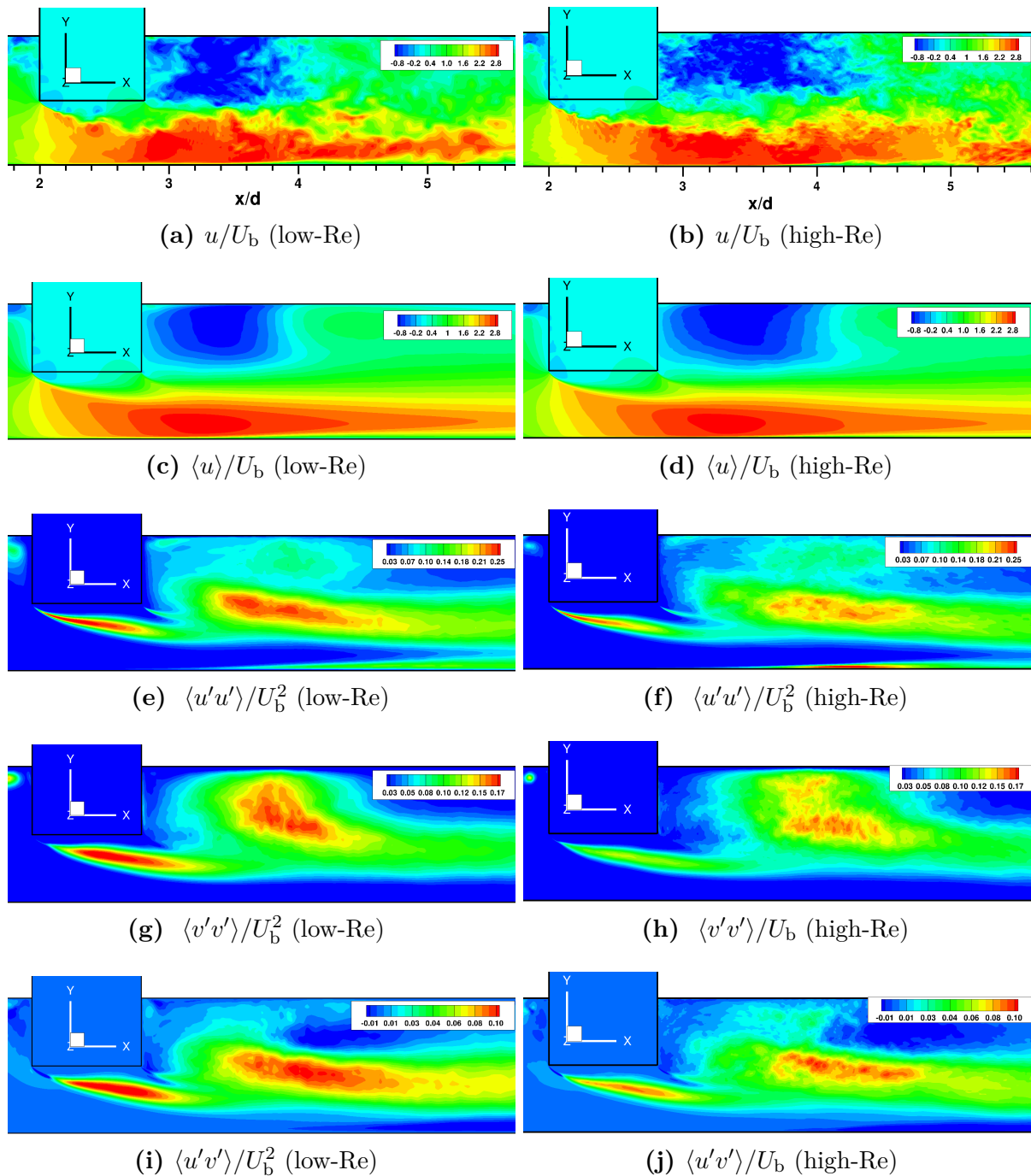


Fig. 9.6. Contour plots of the instantaneous streamwise velocity u/U_b for the (a) low-Re case and the (b) high-Re case; time-averaged streamwise velocity $\langle u \rangle / U_b$ for the (c) low-Re case and the (d) high-Re case; time-averaged resolved Reynolds stress in streamwise direction $\langle u'u' \rangle / U_b^2$ for the (e) low-Re case and the (f) high-Re case; time-averaged resolved Reynolds stress in y -direction $\langle v'v' \rangle / U_b^2$ for the (g) low-Re case and the (h) high-Re case; and time-averaged resolved Reynolds shear stress $\langle u'v' \rangle / U_b^2$ for the (i) low-Re case and the (j) high-Re case. All results are depicted in the x - y symmetry plane ($z/d_h = 0$).

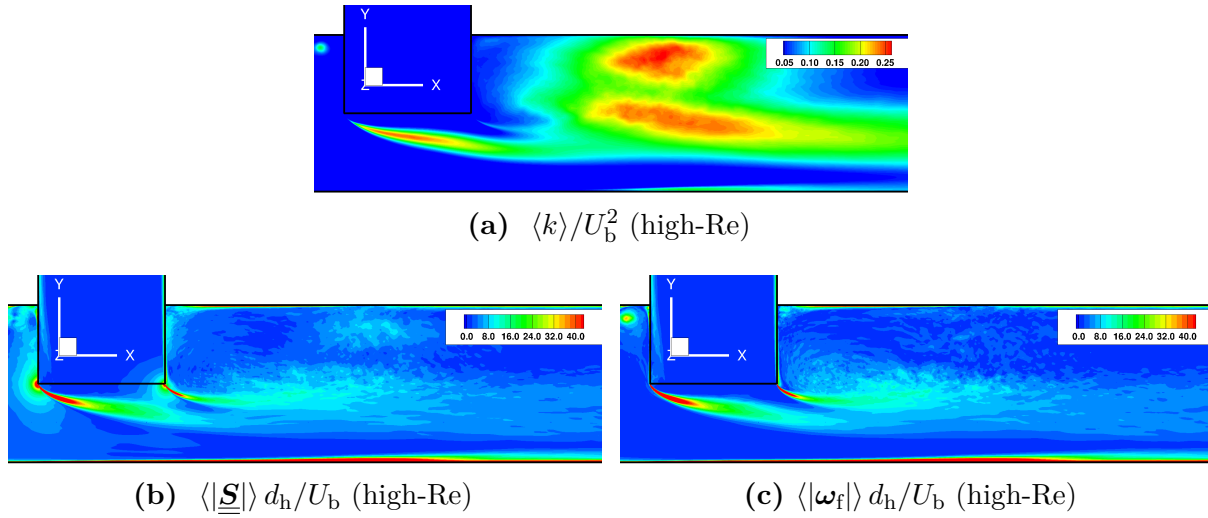


Fig. 9.7. Contour plots of (a) the turbulent kinetic energy $\langle k \rangle / U_b^2$, (b) the magnitude of the strain rate tensor computed based on the mean velocities, and (c) the magnitude of the vorticity vector based on the mean velocities. All results are depicted in the x - y symmetry plane ($z/d_h = 0$) in the high-Re case.

the diameter of the agglomerates. The model adapted in this study computes this velocity difference based on relations strongly depending on the dissipation rate ϵ of the turbulent kinetic energy, which in turn is a function of the strain rate tensor $\underline{\underline{S}}$. Hence, it is indicated that agglomerates are likely to experience breakup by turbulence in the regions with large values of $|\underline{\underline{S}}|$ visible in Fig. 9.7(b). The results obtained for the low-Re case show no contribution at all of the turbulent stress mechanism to the total breakup statistics. As expected, however, the situation is different for the high-Re case as it starts to play a role although marginal in comparison to the other mechanisms (see Section 9.1.7).

The drag-induced breakup mechanism takes place when the magnitude of the relative velocity between the agglomerate and the surrounding fluid exceeds a certain threshold. The considered configuration facilitates the fulfillment of this condition. The agglomerates released in the upper part of the funnel drop downwards due to gravity and the weak fluid forces inside the funnel. Eventually, they emerge with negligible streamwise velocities into the main duct, where the flow is much faster. Consequently, agglomerates reaching the shear layer are exposed to a fast erosion process. This scenario is valid for the low-Re and the high-Re case. However, at high Re the magnitudes of the relative velocity in the lower part of the funnel near the exit are found to be higher. This is related to the fact that at a higher Re number, a certain agglomerate needs longer time to adjust its velocity in response to disturbances of the flow taking place near the outlet of the funnel. In other words, the Stokes number (see Eq. (4.2)) characterizing the motion of the agglomerate increases with Re, indicating less responsiveness to the changes in the flow velocity and hence a higher drag force. Thus, the erosion process starts to take place shortly before agglomerates are entrained into the main duct and continues thereafter.

More attention has to be paid to the breakup by the rotary stress since the rotational motion of the agglomerates can be induced by two means: The vorticity of the fluid flow, and the particle-particle or the particle-wall interactions taking friction into account. Concerning the former, Fig. 9.7(c) depicts the potential regions for the breakup due to rotation induced by the flow (shear layer, recirculation zone and vicinity of walls). Comparing these regions with the breakup positions due to rotation depicted in Fig. 9.8(d), it is obvious that a large portion of the breakup events takes place outside the regions of large fluid vorticity. Consequently, they are induced by particle-particle or particle-wall collisions. In order to find out the relative importance of fluid vorticity and collisions, additional simulations were conducted in which either the rotation of agglomerates due to the fluid torque was neglected or frictionless particle-wall collisions were assumed while keeping all other conditions identical to the standard simulation. Note, however, that the inter-particle collisions with friction was considered since it is part of the momentum-based agglomeration model applied in this work.

The evaluation of these additional simulation data turned out to be very difficult, as there is a complex interaction between the mechanisms causing rotational motion for the agglomerates. For example, agglomerates mainly experience a counterclockwise rotation (with respect to the x - y plane) when entering the duct due to the fluid shear. Later on they hit the bottom wall and acquire a clockwise rotation. Thus, both effects are counteracting when simultaneously taken into account, which renders the results separately obtained for each rotation mechanism less helpful. However, since the rotational velocities induced by the wall impacts are generally much higher than those imposed by the fluid torque, the role of the fluid forces seems to be less significant than the collisions.

From another point of view, the high percentage of the collision-induced breakup events by rotation asserts the importance of taking agglomeration into account, since it is another possible outcome of inter-particle collisions. The current simulations confirm that agglomeration plays a non-negligible role since an appreciable number of agglomeration events is found to take place. The majority of these events are actually re-agglomerations between disintegrated fragments, whereas only a small number of agglomeration events between initial agglomerates is detected.

9.1.6 Breakup Positions for Powder A

To get insight into the breakage behavior inside the disperser, powder **A** is studied as an illustrative example before providing a comparison of the breakup statistics obtained for the three powders at the two Reynolds numbers considered in Section 9.1.7.

Agglomerates of powder **A** are the most breakage resistant since they comprise the smallest primary particles among the three powders and thus possess the highest strength S (see Fig. 9.3). For this reason, it is expected to see variations in the breakage behavior by intensifying the interactions between the flow and the agglomerates realized by the eight-times enlargement of the Reynolds number.

Figures 9.8(a) and 9.8(b) depict the locations of the breakup events by the drag stress mechanism at the low-Re and the high-Re case, respectively. Although the drag stress is found to be prevailing in both cases as it is responsible for 59.3% and 81.2% of the total

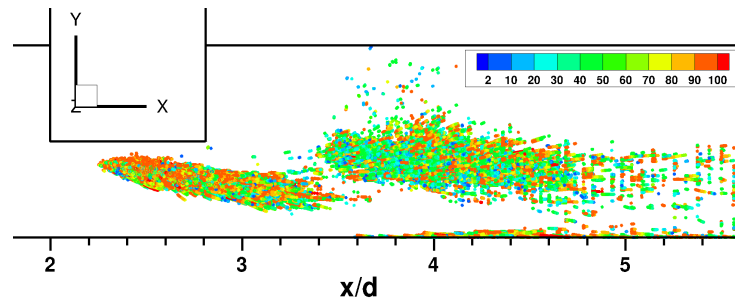
number of breakup events in the low-Re and high-Re cases, respectively, several differences are clearly visible. For instance, in the low-Re case breakup by drag starts to take place shortly below the funnel exit when the agglomerates pass through the shear layer, where the drag force increases rapidly. However, at this Re number the agglomerates are only partially eroded due to the competition between the drag stress and the strength. That is visible from the size-based coloring of the data points, where agglomerates of varying sizes are able to reach larger distances in the streamwise direction before the first or a subsequent breakup process occurs. In general, small agglomerates are likely entrained into the recirculation zone since they tend to trace the fluid streamlines. Contrarily, the larger ones move along the shear layer separating the recirculation zone from the main flow in the duct or reach the bottom wall of the duct. In all situations a sudden alteration in the fluid velocity occurs leading to increased relative velocities between the fluid and the agglomerates and thus breakage due to drag appears.

In the high-Re case, the relative velocities between the fluid and the agglomerates increase over a shorter distance compared to the low-Re case. To a certain extent, the velocity gradients required to initiate the erosion process are already large enough in the funnel itself. Approaching the outlet of the funnel the velocity differences further increase so that the agglomerates undergo a nearly complete deagglomeration by the drag stress mechanism shortly after entering the duct. Note that a breakup of a fragment consisting solely of two primary particles is not possible by the drag stress, since the inertia and drag forces acting on both parts are the same. Consequently, a complete disintegration purely based on the drag stress is not feasible.

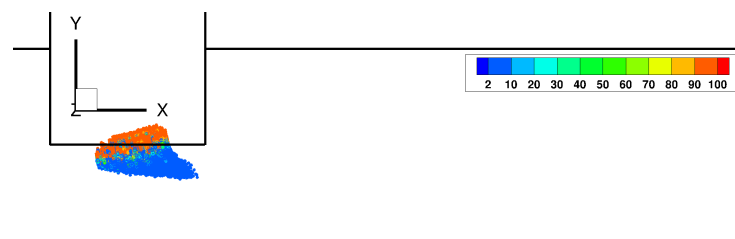
The second significant mechanism is the rotary stress as it contributes to 40.7% and 18.8% of the cumulative number of events in the low-Re and high-Re cases, respectively. Figures 9.8(c) and 9.8(d) show that breakup due to rotation occurs along the trajectories of the agglomerates in both flow cases. As expected, when agglomerates start to break up by the drag mechanism, new particles and fragments are released generating a denser particle distribution which increases the possibility of collisions between agglomerates or agglomerates and particles. Eventually, the interplay between the fluid vorticity in critical regions, inter-particle collisions and wall impactions induce high angular velocities resulting in breakup due to rotary stresses. It is noticed, however, that in the high-Re case, mostly only the two-particle agglomerates are affected by the rotary stress, since all larger structures are already disassembled by the drag stresses. This is not the same in the low-Re case. A wider distribution of agglomerate sizes experiences breakup due to rotation.

Finally, breakup by the turbulent stresses is deemed the least influential mechanism among all. In the low-Re case not a single breakup process by this mechanism is observed. The situation slightly changes for the high-Re case, where at least a few events are found. These breakup processes are located in the near-wall regions (side and bottom walls), where the dissipation rate of the turbulent kinetic energy is magnified. Nevertheless, the contribution of breakup by turbulent stresses is overall very marginal.

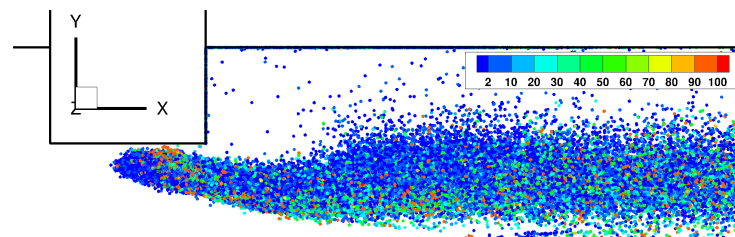
Note that the breakup positions for powders **B** and **C** are generally similar to those discussed for powder **A**. However, in order to explore the influence of the cohesive forces



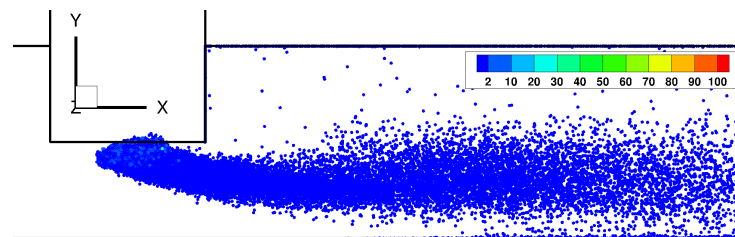
(a) Drag stress, low-Re



(b) Drag stress, high-Re



(c) Rotary stress, low-Re



(d) Rotary stress, high-Re

Fig. 9.8. Positions of the breakup events of powder **A** in the low-Re and high-Re number cases by the drag stresses ((a) & (b)) and the rotary stresses ((c) & (d)), respectively. The locations are depicted for the central region $-0.1 \leq z/d_h \leq 0.1$ over a dimensionless time period of about $\Delta T^* = 15$. The color levels describe the number of primary particles included in the agglomerate at the time of its breakage.

on the breakage phenomena, a more detailed comparison between the statistics obtained for each powder is carried out in the next section.

9.1.7 Breakup Statistics

As mentioned in Section 9.1.3, the simulations are performed over a sufficiently long time period in order to provide stable statistics. This is ensured by carrying out a sequence of simulation runs each with a time period of $\Delta T^* = 2.625$ and $\Delta T^* = 15$ for the high-Re and low-Re cases, respectively. Then, the breakup statistics are evaluated at the end of each run and compared with the preceding set of results. After several simulation runs only insignificant alterations of the statistics are observed. In the following solely the data accumulated from the simulations after reaching converged statistics are considered.

Table 9.5 provides a comparison of the statistical results for all six cases. At first the percentage contribution of the different mechanisms found in the entire domain are evaluated. As found for powder **A**, the drag stress mechanism makes the largest contributions to the total number of breakup events for powder **B** followed by the rotary stress mechanism. This trend applies also for powder **C** in the low-Re case. However, for the high-Re case the situation is different for powder **C** since the rotary stress mechanism slightly dominates over the drag stress. It is remarkable that the turbulent stresses only play a minor role for all powders. Specifically, this breakup mechanism is limited to the high-Re cases and does not appear in the low-Re cases. Since the agglomerates of powder **C** possess the lowest strength, the effect of the turbulent stresses is found to be largest.

Comparing the percentage contributions of the different breakup mechanisms for the three powders in Table 9.5, the trends vary between the high and the low-Re case. At the high Reynolds number the percentage of breakup by drag stresses increases with increasing strength of the agglomerate (i.e., from **C** to **B** to **A**). Accordingly, the percentage of breakup by rotation decreases. Contrarily, at the low-Re case the largest contribution of breakup by drag stresses and the lowest contribution of breakup by rotation is found for powder **B** of intermediate strength. Thus, such a clear trend as observed for the high-Re case is not visible in the low-Re case.

Furthermore, the total numbers of breakup $N_{\text{break}}^{\text{tot}}$, agglomeration $N_{\text{ag}}^{\text{event}}$ and collision N_{coll} events¹ are listed in Table 9.5. Since the mass flow rate of the particles is equal for all powders, but the particle size strongly varies, the number of released agglomerates is different in each case. Thus, for a reasonable comparison the values are normalized by the number of released agglomerates $N_{\text{ag}}^{\text{rel}}$. Obviously, for each powder the number of breakup events increases from the low-Re to the high-Re cases. The largest jump occurs for powder **A**, where the stresses in the low-Re case do not reach the high strength thresholds quite often. Looking at the three powders at the low-Re condition, it is evident that the number of breakup events increases with the size of the primary particles since the strength decreases. This trend is straightforward to understand. Less intuitive, however, is the opposite trend found at the high-Re case. This can be explained by the fact that at high Re overall much more breakup events take place than for the low-Re case. Consequently, more

¹Note that for collision and agglomeration no distinction is made between the original agglomerates, fragments and individual particles in the counting of the respective events.

small fragments and primary particles are released holding a higher potential for collisions and re-agglomeration. Due to the fixed mass flow rate of the released agglomerates and the resulting larger numbers of agglomerates, this trend is especially relevant for the powders with small primary particles. Hence, collision and re-agglomeration events of the newly formed agglomerates occur more often as evidenced by Table 9.5. A larger number of re-agglomeration events for a decreasing primary particle size also leads to larger numbers for the breakup processes per released agglomerate. Consequently, the interpretation of the results requires to take the complicated interplay of the different physical phenomena into account.

Tab. 9.5. Summary of the statistical results obtained in the disperser.

	powder A		powder B		powder C	
	low-Re	high-Re	low-Re	high-Re	low-Re	high-Re
$\frac{N_{\text{break}}^{\text{drag}}}{N_{\text{break}}^{\text{tot}}} \cdot 100\%$	59.3	81.2	77.4	55.6	69.1	47.6
$\frac{N_{\text{break}}^{\text{rot}}}{N_{\text{break}}^{\text{tot}}} \cdot 100\%$	40.7	18.8	22.6	44.4	30.9	51.4
$\frac{N_{\text{break}}^{\text{turb}}}{N_{\text{break}}^{\text{tot}}} \cdot 100\%$	0	0.0002	0	0.01	0	1.0
$N_{\text{break}}^{\text{tot}}/N_{\text{ag}}^{\text{rel}}$	10.6	106.4	65.9	95.6	84.3	97.6
$N_{\text{ag}}^{\text{event}}/N_{\text{ag}}^{\text{rel}}$	0.1	14.8	2.9	2.5	1.4	0.7
$N_{\text{coll}}/N_{\text{ag}}^{\text{rel}}$	36.8	742.9	822.0	377.9	485.6	130.6

To assess the capability of the present simulation methodology, the particle sizes at the outlet of the disperser are additionally studied. For this purpose, the arithmetic mean diameter d_{10}/d_{pp} and the Sauter mean diameter d_{32}/d_{pp} are calculated for the particles and agglomerates $N_{\text{p}}^{\text{out}}$ passing the outlet boundary of the disperser. Note that the Sauter mean diameter is defined as the mean diameter possessing the same ratio of volume to surface area as the entire ensemble (Sauter, 1926). Mathematically, the Sauter mean diameter is given by:

$$d_{32} = \frac{\sum_i^{N_{\text{p}}^{\text{out}}} d_{\text{p}}^3}{\sum_i^{N_{\text{p}}^{\text{out}}} d_{\text{p}}^2} . \quad (9.4)$$

The obtained results are presented in Fig. 9.9(a) for all cases. Obviously, the trends fit well with the expectations. By increasing the Reynolds number (blue to red) or the primary particle size (**A** to **C**) smaller agglomerate sizes are found at the outlet.

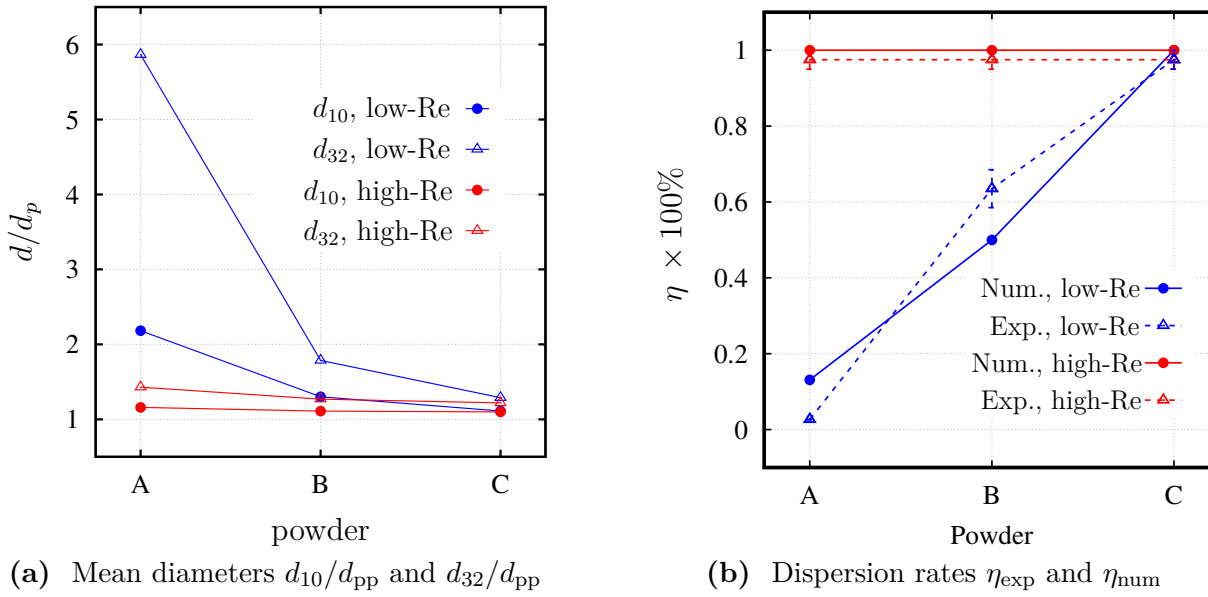


Fig. 9.9. (a) Characteristic diameters at the outlet of the disperser and (b) dispersion rates (numerical and experimental data by Weiler (2008) for all six cases.

Unfortunately, in the original experimental work (Weiler, 2008) solely an integral quantity denoted the dispersion efficiency η_{exp} is provided to describe the particle distribution at the outlet of the disperser. It is defined as the ratio of the median diameter $d_{50,3}^{\text{CD}}$ of the cumulative volumetric distribution Q_3 (Schubert, 2003) achieved in a high-end commercial disperser (CD) (see Table 9.6) to the median diameter $d_{50,3}^{\text{exp}}$ obtained in the considered lab-scale funnel-duct disperser ($\eta_{\text{exp}} = d_{50,3}^{\text{CD}}/d_{50,3}^{\text{exp}}$). A complete dispersion is assumed in the study when $\eta_{\text{exp}} \geq 95\%$ is attained. Accordingly, Fig. 9.9(b) shows a comparison between the experimental and the numerically predicted values for all cases considered. In addition the values are provided in Table 9.6. Note that the dispersion rates in the simulations are based on the available experimental values of $d_{50,3}^{\text{CD}}$ and the numerically determined median diameters $d_{50,3}^{\text{num}}$. For powder C, a close agreement is found for both flow cases, since the experiments and the simulations predict a full deagglomeration. For the other two powders the results qualitatively agree but deviations are visible concerning the values of the dispersion rate.

In fact, the encountered deviations are not surprising since several potential sources for discrepancy exist between the experimental and the numerical setups. These include the simplifications of the geometry, the assumptions made concerning some of the material properties of the agglomerates and the restriction to the fluid and rotational stresses in the present work neglecting the stresses arising due to the inter-particle and particle-wall collisions. Furthermore, the size distribution of the agglomerates at the inlet is not given in the experiments so that an assumption of equally sized 100-particle agglomerates has to be made in the simulations. Lastly and probably most important, the volumes of the agglomerates are computed in the present work based on the packing fraction modeled under certain assumptions including, e.g., the type of the packing force (see Section 5.2).

Tab. 9.6. Comparison of the numerical and experimental values (Weiler, 2008) of the dispersion rate at the outlet of the disperser. The values in the last row are the median volumetric diameters $d_{50,3}^{\text{CD}}$ achieved in a high-end commercial disperser provided by Weiler (2008).

	powder A		powder B		powder C	
	low-Re	high-Re	low-Re	high-Re	low-Re	high-Re
$\eta_{\text{num}}[\%]$	13.1	80.0	50.0	100.0	100.0	100.0
$\eta_{\text{exp}}[\%]$	2.65	97.5 ± 2.5	63.5 ± 5	97.5 ± 2.5	97.5 ± 2.5	97.5 ± 2.5
$d_{50,3}^{\text{CD}}[\mu\text{m}]$	0.91 ± 0.01		2.49 ± 0.05		4.87 ± 0.01	

Since the quantity η_{exp} used for the comparison is directly associated with the volume distribution, certain errors are inevitable.

Nevertheless, the results can be interpreted in a different manner by using the number size distribution. That allows to eliminate the dependence on the way the median size $d_{50,3}$ of the agglomerates is determined. The numerically predicted distribution for powder **A** is shown in Fig. 9.10. A very wide distribution is found in the low-Re case, which comprises agglomerate structures ranging from primary particles up to large agglomerates with 300 primary particles. The situation in the high-Re case is substantially different, since the distribution solely consists of primary particles and two-particle agglomerates. From a practical point of view such a distribution can be seen as a complete disintegration of the powder. That demonstrates that the numbers of the dispersion rates in Table 9.6 have to be interpreted with caution as they falsely give the impression that the deviations between the predictions and the measurements are still large.

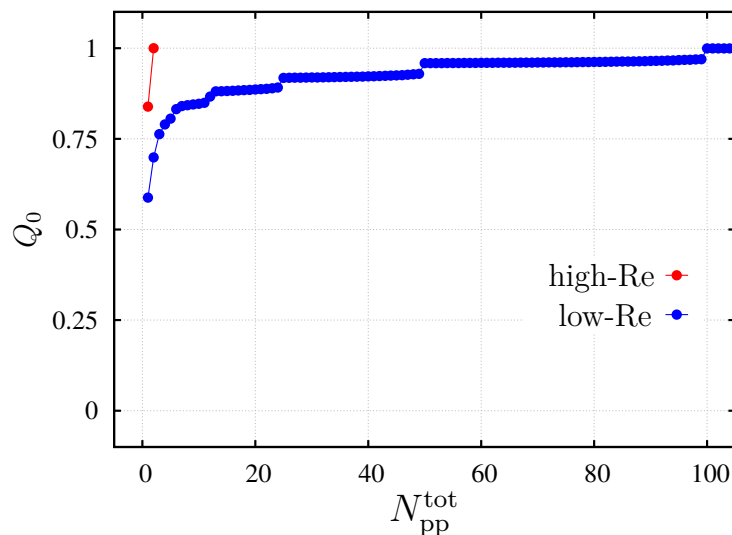


Fig. 9.10. Cumulative number size distribution of powder **A** at the outlet of the disperser for both Reynolds numbers.

9.1.8 Influence of the Breakup Time Lag

The significance of the breakup time lag proposed in this study is demonstrated taking powder **A** again as an example. In Table 9.7 the average time lag periods $\overline{\Delta t}_{\text{lag}}$ computed after breakup are listed for each mechanism separately. Here the time intervals are shown with dimensions, since the dimensionless values would be normalized by different bulk velocities for the two Reynolds numbers hindering a direct comparison. As expected the time delays in the high-Re case are smaller than for the low-Re case. For the breakup processes provoked by fluid dynamic forces, the chosen turbulent time scale is expected to decrease with increasing Re. For the characteristic time scale defining the time lag in case of the rotary stress, the inverse of the angular velocity was chosen (see Section 6.5). Here it is also obvious that due to collisions with walls or other agglomerates the angular velocity increases with increasing Re and thus shorter time delays are found.

The introduction of the time lag renders the occurrence of breakup events independent of the time-marching procedure and the time-step size applied. It serves to prevent the occurrence of a very fast consecutive series of breakup events of the same agglomerate generating a dense particle distributions in a very restricted region promoting unphysical collisions and associated re-agglomerations and breakup events. This is visible based on the statistics provided in Table 9.7 comparing the outcomes of a simulation with and without the time lag model. Again, the numbers of the breakup, agglomeration and collision events normalized by the number of released agglomerates are depicted. Obviously, more reasonable numbers are obtained with the time lag model. Without this measure the numbers of collisions and re-agglomerations are beyond physically reasonable values, which also influences the breakup statistics. As expected the differences are higher in the high-Re case, since the time-step size is smaller and therefore the advancement achieved by the time lag is more recognizable.

Tab. 9.7. Influence of the breakup time delay on the statistics of powder **A**.

	low-Re		high-Re	
	with Δt_{lag}	without Δt_{lag}	with Δt_{lag}	without Δt_{lag}
$\overline{\Delta t}_{\text{lag,drag}}$	0.19 μs	-	0.07 μs	-
$\overline{\Delta t}_{\text{lag,rot}}$	0.45 μs	-	0.14 μs	-
$\overline{\Delta t}_{\text{lag,turb}}$	-	-	0.007 μs	-
$N_{\text{break}}^{\text{tot}}/N_{\text{ag}}^{\text{rel}}$	10.6	23.3	106.4	236.4
$N_{\text{ag}}^{\text{event}}/N_{\text{ag}}^{\text{rel}}$	0.1	0.2	14.8	155.5
$N_{\text{coll}}/N_{\text{ag}}^{\text{rel}}$	36.8	334.8	742.9	2860.2

9.1.9 Summary and Conclusions

The Euler–Lagrange method extended to predict the fluid-induced breakup of agglomerates is evaluated. Based on six different operating conditions of an idealized dry powder disperser the entire range from mild dispersion rates to a full disintegration is covered. The main results are:

- Breakup of agglomerates by turbulent stresses plays a marginal role in the present application. In the low-Re case it is not present at all. However, increasing the Re number by a factor of eight at least a few breakup events by this mechanism are observed. Nevertheless, turbulence as a source of agglomerate breakup can not be generally ruled out, since turbulence increases the collision rate. Although particle-agglomerate and agglomerate-agglomerate collisions are considered in the simulations, they are presently not taken into account as a possible breakup mechanism.
- Breakup by drag stresses and rotary stresses are observed in the foreseeable areas, where either the velocity differences between the fluid and the agglomerates are large or high angular velocities are expected to be induced by the fluid, by inter-particle collisions or by particle-wall collisions. A particularly noteworthy region is the shear layer developing below the exit of the funnel. For the rotary stresses also the collisions of the agglomerates with the bottom and side walls play an important role.
- As shown for powder **A** an increase of the Reynolds number shifts the location for breakup slightly upstream and closer to the funnel exit. For the drag stress at the high-Re case breakup partially already appears within the funnel.
- Breakup by the drag stress is found to be the dominant mechanism for the present application. This statement holds true for all three powders and both Re considered with the exception of powder **C** at high Re. In this case breakup by rotary stress contributes at a maximum share of more than one half. However, for certain cases (e.g., powder **A** at high Re) the percentage is a factor of about three smaller.
- Although the determination of the dispersion rate is associated with numerous uncertainties, the comparison of the predicted and measured values allows to assess the capability of the present simulation methodology. Overall a reasonable coincidence of the simulation results with the measurements was found and all trends were correctly predicted.
- Finally, it was demonstrated that the introduction of the time lag between successive breakup events of the same agglomerate is strongly advantageous. The measure assures that the breakup model is independent on the numerical time-step size. On the contrary the time delay is purely based on physical considerations.

9.2 Duct Flows

The second investigation in this work aims at providing insight into the wall-impact breakage phenomenon in turbulent flows. For this purpose, simulations of a particle-laden duct under varying flow and particle conditions are carried out. The following three objectives are tackled: First, to identify the conditions under which agglomerates are breaking due to wall-impact in the presence of the fluid flow. Second, to assess the influence of the Reynolds number of the fluid and the strength of the agglomerates on the wall-impact breakage phenomenon. Third, to explore the interplay between the wall-impact breakage phenomenon and other related phenomena such as the breakage by fluid stresses and rotation as well as agglomeration.

To achieve these goals, the volumetric flow rate of the fluid within the duct with a square cross-section (edge length and hydraulic diameter of $d_h = 4.3 \cdot 10^{-3}$ m) is varied leading to five different bulk Reynolds numbers defined as $Re = \rho_f U_b d_h / \mu_f$. Assuming that the fluid medium is air with a density of $\rho_f = 1.196 \text{ kg} \cdot \text{m}^{-3}$ and a dynamic viscosity of $\mu_f = 1.833 \cdot 10^{-5} \text{ kg} \cdot (\text{s} \cdot \text{m})^{-1}$, the different cases are given in Table 9.8. In addition, the shear Reynolds number $Re_\tau = \rho_f u_\tau d_h / \mu_f$ and the ratio of the mean shear velocity u_τ to the bulk velocity U_b are provided. Note that the gravitational acceleration is neglected in all cases. Furthermore, three different primary particle diameters according to the introduced powders **A**, **B** and **C** are taken into account. The full description of the properties and parameters of the primary particles is provided in Table 9.2. In general, the values of the Reynolds number and the particle diameters are inspired by the experiments by Weiler (2008) who studied the breakage of silica particle agglomerates in a lab-scale disperser. Overall, the combination of the flow and particle parameters leads to 15 independent cases.

As will be further elaborated below, the present duct flow investigation is divided into two parts. In part **I**, the wall-impact breakage model based on the regression methods (see Section 7.4) is applied for all 15 simulation cases, whereas in part **II** the ANN-based wall-impact breakage model is used to simulate six of the cases presented in part **I**, which allows a comparison between the results of both models.

9.2.1 Computational Setup

The three-dimensional computational domain has the dimensions of $2 \pi d_h \times d_h \times d_h$ in the streamwise and the two wall-normal directions, respectively. Periodic boundary conditions are applied in the streamwise direction. To ensure a constant mass flux through the duct, the pressure gradient is permanently adapted by a dynamic procedure (Benocci and Pinelli, 1990; Breuer, 2002). All other boundaries are solid smooth walls at which the impermeability and Stokes no-slip conditions are set. The latter choice is justified since wall-resolved LES is considered relying on an appropriate grid resolution for each of the investigated flow cases as explained next.

The computational domain is discretized by block-structured grids which are generated following the recommendations of Piomelli and Chasnov (1996) for achieving a

wall-resolved LES. Accordingly, the dimensionless spacing of the first cell center in the wall-normal direction needs to be located at y_{1st}^+ and $z_{1st}^+ < 2$, where the superscript "+" refers to dimensionless quantities (e.g., $y_{1st}^+ = y_{1st} \cdot u_\tau / \nu_f$) normalized by the kinematic viscosity of the fluid ν_f and u_τ . The latter is predicted separately for each Reynolds number based on the friction factor formula proposed by Moody (1947) (see Eq. (9.3)), used as a design formula for turbulent pipe flows. Please note, however, that the dimensionless shear velocities ($u_\tau^* = u_\tau / U_b$) provided in Table 9.8 are the values predicted in the simulations and not those pre-computed based on the formula by Moody (1947). Furthermore, the grid spacing in the streamwise direction has to fulfill the condition $\Delta x^+ = \mathcal{O}(50\text{--}150)$. In the present simulations, these spacings are set to y_{1st}^+ and $z_{1st}^+ = 0.5$ and $\Delta x^+ = 40$ for all of the five grids corresponding to the different Reynolds numbers.

The grid points are uniformly distributed in the streamwise direction. However, a bi-geometrical clustering with a stretching factor of 1.05 is applied in the wall-normal directions. This means that the grid is coarsened towards the center of the square cross-section, where the largest dimensionless spacing varies between ≈ 12 and 60 for the cases Re_1 and Re_5 , respectively. Taking into account that these are the maximum values, which appear in a very limited region in the middle of the cross-section of the corresponding flow case, good compliance with the specification of Piomelli and Chasnov (1996) concerning the spanwise resolution $\Delta z^+ = \mathcal{O}(15\text{--}40)$ of a plane channel flow is achieved. Since the Reynolds numbers are different, the number of grid points for each flow case needs to be adjusted to fulfill the resolution requirements. The details are provided in Table 9.8.

In addition, the time-step size needs to address the refined resolution of the grid and the increase of the flow velocity with the Reynolds number. Table 9.8 also summarizes the dimensionless value of the time-step size ($\Delta t^* = \Delta t U_b / d_h$) for each of the flow cases considered. The provided values guarantee CFL numbers less than unity.

Tab. 9.8. Flow properties and domain (spatial and temporal) discretization settings for all duct flow cases.

Case	Re	U_b [m/s]	Re_τ	u_τ / U_b	Grid points			Δt^*
					x	y	z	
Re_1	8698	$3.10 \cdot 10^1$	552	$6.88 \cdot 10^{-2}$	116	112	112	$2 \cdot 10^{-3}$
Re_2	17,397	$6.20 \cdot 10^1$	1005	$6.34 \cdot 10^{-2}$	211	135	135	$1 \cdot 10^{-3}$
Re_3	34,794	$1.24 \cdot 10^2$	1839	$5.74 \cdot 10^{-2}$	385	160	160	$4.5 \cdot 10^{-4}$
Re_4	52,190	$1.86 \cdot 10^2$	2624	$5.47 \cdot 10^{-2}$	412	175	175	$3 \cdot 10^{-4}$
Re_5	69,584	$2.48 \cdot 10^2$	3380	$5.24 \cdot 10^{-2}$	531	185	185	$1.5 \cdot 10^{-4}$

9.2.2 Simulation Procedure

The duct flow simulations are carried out applying the Euler–Lagrange methodology based on LES explained in Chapters 3 and 4. The dynamic subgrid-scale model by Germano et al. (1991) and the Langevin-type particle subgrid-scale model are generally applied for the fluid and the particle phase, respectively. Since the wall-impact breakage is the scope of this investigation, the model describing this phenomenon is applied. Specifically, the regression model is used in part **I**. In this part, 15 simulation cases defining three powders (i.e., **A**, **B**, and **C**) and five flow Reynolds numbers (see Table 9.8) are investigated. Note that the results obtained in this part (Khalifa and Breuer, 2021) has motivated the development of the ANN-based approach. Thus, in part **II** the more recent ANN-based wall-impact breakage model is applied to simulate six cases referring to two powders (i.e., **A** and **C**) and three fluid Reynolds numbers (i.e., Re_1 , Re_2 , and Re_3) (Khalifa et al., 2022). The goal is to compare the results obtained by the two different wall-impact breakage models under otherwise equal conditions.

The simulation of each Reynolds number starts by establishing a fully developed unladen flow within a time interval corresponding to about 100 flow-through times of the duct setup. Afterwards, the averaging procedure of the instantaneous flow in time and in the streamwise direction is started in order to compute the flow statistics for each Re (details in Section 9.2.3). In parallel, agglomerates of a certain powder each consisting of 100 primary particles are gradually released into the domain by distributing them uniformly over the cross-section. This injection process is completed within a single flow-through time. The number of released agglomerates of each powder depends on the goals of the simulations set as will be explained next. Note that the presence of the agglomerates does not affect the averaged flow field since the two-way coupling is not taken into account in any of the simulations carried out in this investigation as will be motivated below.

In each part (i.e., part **I** and **II**) of the present investigation, two sets of simulations are considered. The simulations in the first set are one-way coupled. This means that the inter-particle collisions and the feedback effect of the disperse phase on the fluid phase are neglected. In addition, the agglomeration and the breakup processes due to fluid stresses are not taken into account. Thus, solely the wall-impact breakage model is applied. The idea behind this set of simulations is to investigate the pure effect of the Reynolds number of the fluid and the size of the primary particles forming an agglomerate on the wall-impact breakage phenomenon, completely isolated from the influence of other mechanisms. That is possible since in the hard-sphere point-particle methodology every particle-related phenomenon is incorporated by a separate model. This possibility is exploited here since it allows to better understand the role of individual mechanisms.

Since the simulations in the first set are one-way coupled, the volume fraction Φ_p of the disperse phase does not play a role and can be chosen to obtain proper statistics of the wall-impact breakage results. For this purpose, about 10^5 agglomerates are injected for each powder. After the injection, the agglomerates are allowed to disperse until they reach a statistically steady-state. To prove this condition, the position of the center of

mass of the agglomerates is monitored over time. Within a limited time interval of about 64 flow-through times the value settles at an asymptotic limit ensuring that a statistically steady-state is reached. Afterwards, the wall-impact breakup model is activated and the accumulation of the statistics starts.

In the second set of simulations the inter-particle collisions, the agglomeration and all breakup models (flow-induced and wall impact) are taken into account. To keep the influence of the inter-particle collisions similar in all cases, the number of released agglomerates is set to achieve a volume fraction of $\Phi_p = 10^{-5}$ based on the total volume of the primary particles. This leads to about 10^5 , 6400 and 730 agglomerates of powders **A**, **B** and **C**, respectively. Again the agglomerates are first allowed to disperse while neglecting the inter-particle collisions, the agglomeration, and the breakage. This process continues until the agglomerates reach a statistically steady-state in a similar manner as explained for the first set. Afterwards, the breakage and agglomeration models are activated and the results are reported from this instant in time as will be discussed in Section 9.2.5.2. Obviously, the main purpose of this set of simulations is to assess the role of the wall-impact breakage under practically relevant conditions.

It is noted that the feedback effect of the particle phase on the fluid phase (two-way coupling) is also not accounted for in the second set of simulations. The main motivation for this choice stems from the fact that the impact-breakage behavior needs to be compared for three powders of different primary particle sizes but with the overall same volume fraction ($\Phi_p = 10^{-5}$). This means that for each powder a different number of agglomerates must be taken into account, which are also different in their diameters. Consequently, the feedback of the particles on the fluid and eventually the fluid-particle interactions will be affected. Thus, to keep the number of influencing parameters on the breakage behavior small, the two-way coupling is ignored. However, such an assumption is not very critical, since the chosen volume fraction ($\Phi_p = 10^{-5}$) is close to the threshold suggested by Elghobashi (1991) ($\Phi_p = 10^{-6}$), above which the two-way coupling becomes worth to be taken into account.

A summary of the particular models applied for the different cases is provided in Table 9.9.

9.2.3 Continuous Flow in the Duct

Since it is crucial to ensure that the turbulent carrier phase is well predicted before moving on to the results of the particulate phase, the analysis starts with the fluid flow field.

For this purpose, averaged quantities of the flow fields are considered. Figs. 9.11(a) to 9.11(c) depict the projected streamlines of the secondary flow in the y - z cross-section for the cases Re_1 , Re_3 and Re_5 , respectively. Furthermore, the contours of the streamwise velocity $\langle u \rangle / U_b$ are superimposed. Both quantities are flow statistics obtained by averaging the instantaneous flow in the homogeneous streamwise direction and in time over periods of 650, 400 and 245 flow-through times, respectively. The shorter averaging times for the higher Re numbers are due to CPU-time restrictions, since the grids in these cases

Tab. 9.9. Summary of the particle-related models considered in the different set of simulations.

	Part I		Part II	
	First set	Second set	First set	Second set
Particle subgrid-scale	✓	✓	✓	✓
Two-way coupling	×	×	×	×
Inter-particle collisions	×	✓	×	✓
Agglomeration	×	✓	×	✓
Fluid-induced breakup	×	✓	×	✓
Wall-impact breakage	✓ (Regression)	✓ (Regression)	✓ (ANN)	✓ (ANN)

are much finer and the time-step sizes are smaller. Thus, in the case of Re_5 entirely anti-symmetric distributions for all statistics might not be guaranteed. However, since the present discussion is restricted to describing the most important features of the turbulent duct flow including the influence of the Reynolds number, this is not a critical issue. Note that for the wall impact simulations in the subsequent sections the averaged flow field is not of relevance at all. Thus, no quantitative validation of the averaged flow field is carried out here being beyond the scope of the present study. Studies applying similar LES technique (see, e.g., Yao et al., 2015) have already proven that LES predictions of turbulent duct flows are in good agreement with direct numerical simulations and experimental data for a large range of Reynolds numbers.

The projected streamlines in Fig. 9.11 illustrate a cross-flow motion which is known as Prandtl's secondary motion of the second kind (Prandtl, 1925, 1927). This phenomenon is also referred to as stress-induced secondary flow, since it arises due to local gradients of the Reynolds stresses in the corners of the cross-section leading to mean streamwise vortices (Bradshaw, 1987). Consequently, a pair of counter-rotating vortices appears in each quadrant causing the visible deformation of the streamwise velocity contours (Bradshaw, 1987). However, it is well known that this kind of stress-induced secondary flow is very weak. In the present simulations the magnitudes of the cross-sectional averaged flow velocity are found to be between 2.3% and 2.5% of the bulk velocity for the highest and lowest Re number, respectively. That fits well to the reported literature (see, e.g., Yao et al., 2015). Nevertheless, the effect of these secondary vortices on the particulate phase is not negligible. Based on DNS and LES, the turbulence-driven secondary motion was found to play a crucial role in the accumulation of particles in the near-wall regions of the duct, enhancing the interaction between particles and walls (see, e.g., Noorani et al., 2016; Yao and Fairweather, 2012; Yao et al., 2014).

Furthermore, Fig. 9.11 shows that the streamwise velocity profiles and the structures of the secondary vortices are influenced by the Reynolds number. Note that by increasing Re the centers of the vortices are shifted from the corners towards the wall bisectors as observed in Zhang et al. (2015). Moreover, the vortices extend deeper into the corner

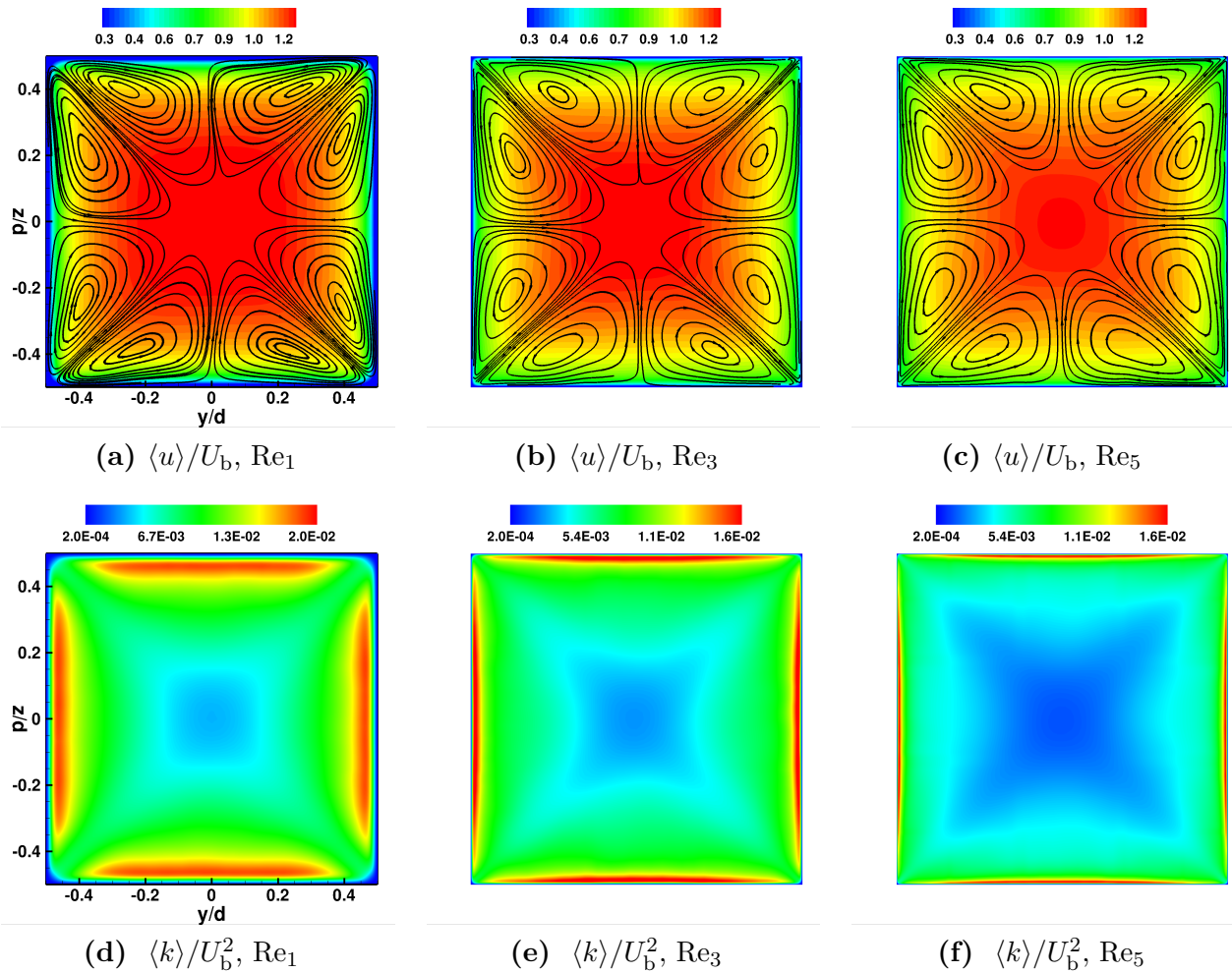


Fig. 9.11. Contour plots of the averaged streamwise velocity $\langle u \rangle / U_b$ and the resolved turbulent kinetic energy $\langle k \rangle / U_b^2$ for the cases Re_1 , Re_3 and Re_5 . The lines in subfigures (a)–(c) represent the projected streamlines of the secondary flow in the duct cross-section.

regions (see, e.g., Yao et al., 2015). The latter effect leads to a stronger transfer of the fluid from the center of the duct towards the corners pulling the high velocity zones more towards the corners (Zhang et al., 2015) as visible in the contours of the streamwise velocity.

In fact, the secondary flow also affects the higher-order turbulent statistics. Figs. 9.11(d)–9.11(f) depict the distributions of the resolved turbulent kinetic energy $\langle k \rangle$ for the same Reynolds numbers Re_1 , Re_3 and Re_5 , respectively. As expected, with increasing Reynolds number the velocity gradients in the vicinity of the rigid walls become steeper leading to thinner regions of high turbulent kinetic energy close to the walls. Obviously, the turbulence intensity is especially high in the near-wall region at the middle of the duct wall. Since the secondary vortices are pushing fluid into the corners, the velocity gradient and consequently the energy production is much lower there than at the wall bisectors.

9.2.4 Part I: Traditional Regression Wall-Impact Breakage Model

9.2.4.1 First Set of Simulations: Pure Wall-Impact Breakage

In this section, the results of the first set of simulations, where solely the wall-impact breakage model is applied (see Section 9.2.2) are discussed.

A very common parameter used to characterize the particle dynamics in turbulent flows is the dimensionless particle response time, i.e., the Stokes number, which describes the responsiveness of the disperse phase to changes in the motion of the carrier phase. The Stokes number $St^+ = \tau_{ag}/\tau_f^+$ considered here is given by the response time of the agglomerate $\tau_{ag} = \rho_{ag} d_{ag}^2 / (18 \mu_f)$ normalized by the viscous time scale $\tau_f^+ = \mu_f / (\rho_f u_\tau^2)$. Considering the mean shear velocity u_τ computed in the simulations (see Table 9.8), the values of the Stokes numbers of the initially injected 100-particle agglomerates are listed in Table 9.10 for all cases considered. Two quantities describing the results concerning the wall-impact breakage are included in the table. These are the number of wall-impact breakage events per released agglomerate, $N_{break}^{wall}/N_{ag}^{rel}$, and the rate of reduction of the Sauter mean diameter, $R_{d_{32}} = (d_{32}^{init} - d_{32}) / (d_{32}^{init} - d_{pp})$ expressing the percentage by which the initial Sauter mean diameter d_{32}^{init} collapses towards the diameter of the primary particle. This implies that for small values of $R_{d_{32}}$ approaching zero the reduction of the mean particle size is insignificant. On the contrary, larger values of $R_{d_{32}}$ tending towards unity express an effective reduction of the mean particle size and thus an effective breakage. It is noted that the results presented in Table 9.10 correspond to a dimensionless time interval of $\Delta T^* = 100$.

Comparing the results of powders **A** and **B** in Table 9.10, it can be generally concluded that with increasing Reynolds number a smaller number of breakage events per released agglomerate and a weaker reduction of the Sauter mean diameter are observed. Moreover, when comparing the results of both powders a less pronounced breakage behavior is found for powder **B** in comparison with powder **A**. Both conclusions might be confusing since at higher flow velocities one expects higher impact velocities and hence more effective breakage. In addition, powder **B** is characterized by smaller values of the agglomerate strength than powder **A** due to the larger primary particles and is therefore anticipated to experience more breakage. However, the obtained trends can be explained as follows. For rising Stokes numbers, i.e., increasing Re (Re_1 to Re_5) or increasing the diameter of the primary particles (powder **A** to **B**), the agglomerates possessing high inertia become even less responsive to secondary flow structures. These flow structures are understood to play an important role in transporting the particles towards the walls of the square duct (Wang et al., 2019; Yao and Fairweather, 2012).

An exception to the reported trends is obvious for powder **A** at the smallest Reynolds number Re_1 , where $R_{d_{32}}$ is smaller than the one predicted for Re_2 . This deviation is attributed to the fact that this specific case (i.e., powder **A**, Re_1) combines the mildest flow conditions and the highest agglomerate strength. Under these circumstances, agglomerates are harder to break and thus undergo only a partial fragmentation more frequently than in any other case. By contrast, a full disintegration of the agglomerate typically takes place

Tab. 9.10. Breakage results due to wall impact only (first set of simulations). The results are accumulated over a time interval of $\Delta T^* = 100$. The number of released agglomerates $N_{\text{ag}}^{\text{rel}}$ is 10^5 for all powders. Note that the value of $R_{d_{32}}$ for powder **A** at Re_3 and for powder **C** at Re_1 are slightly corrected in comparison to the corresponding value given in Khalifa and Breuer (2021).

Powder	Case	St^+	$N_{\text{break}}^{\text{wall}}/N_{\text{ag}}^{\text{rel}}$	$R_{d_{32}}$
A	Re_1	20	1.40	90.32%
A	Re_2	67	1.09	97.88%
A	Re_3	219	1.02	96.15%
A	Re_4	448	0.94	93.13%
A	Re_5	731	0.84	84.33%
B	Re_1	143	1.18	99.36%
B	Re_2	484	1.07	96.96%
B	Re_3	1586	0.61	66.38%
B	Re_4	3246	0.23	29.01%
B	Re_5	5295	0.18	21.83%
C	Re_1	652	1.19	93.49%
C	Re_2	2214	0.37	47.61%
C	Re_3	7248	0.39	51.09%
C	Re_4	14,830	0.37	48.09%
C	Re_5	24,195	0.58	71.83%

at the first breakage event for all other cases. This argument will be further supported in the discussion of Fig. 9.13(a) later on.

The observations for powder **C** are different. Here, the number of breakage events and the reduction rate decrease with Re from Re_1 to Re_2 . Then the values level off up to Re_4 before they increase again for Re_5 . Apparently, despite the weakened effect of the secondary flow for increasing Re and thus increasing Stokes number, other effects driving the agglomerates towards the walls are amplified for powder **C**. These include the turbophoresis leading to higher near-wall concentrations as the Stokes number increases (Esmaily et al., 2020; Kuerten, 2016; Phares and Sharma, 2006). In addition, based on additional simulations carried out in this study, the shear-induced lift (i.e., Saffman force) is found to be another cause enhancing the wall-impact breakage. The shear-induced lift-force model adopted in this work (Mei, 1992) scales with the cube of the particle diameter and the cross-product between the relative fluid-particle velocity vector and the vorticity vector of the fluid. When the particle is faster than the fluid, the lift force acts against the direction of a positive velocity gradient (i.e., towards the wall) and vice versa. These conditions concerning the turbophoresis and the reversed effect of the lift force

apply for powder **C**, since it has the largest primary particles. Thus, the agglomerates of this powder are those with the highest inertia as obvious from the Stokes numbers (improved turbophoresis). Besides, as Re increases the shear rates become larger. Consequently, agglomerates tend to reach the high-shear near-wall regions with velocities similar to the bulk velocity of the fluid, which is much higher than the fluid velocity in the near-wall regions. Thus, a rapidly increasing lift force acts on the agglomerates of powder **C** towards the walls as Re increases. This results in an enhanced appearance of breakage, unlike the cases of powders **A** and **B**, where the lift force does not play a dominant role in breakage as could be proven by further simulations. The high velocities of powder **C** in the near-wall regions will be demonstrated in the discussion of Fig. 9.12(a).

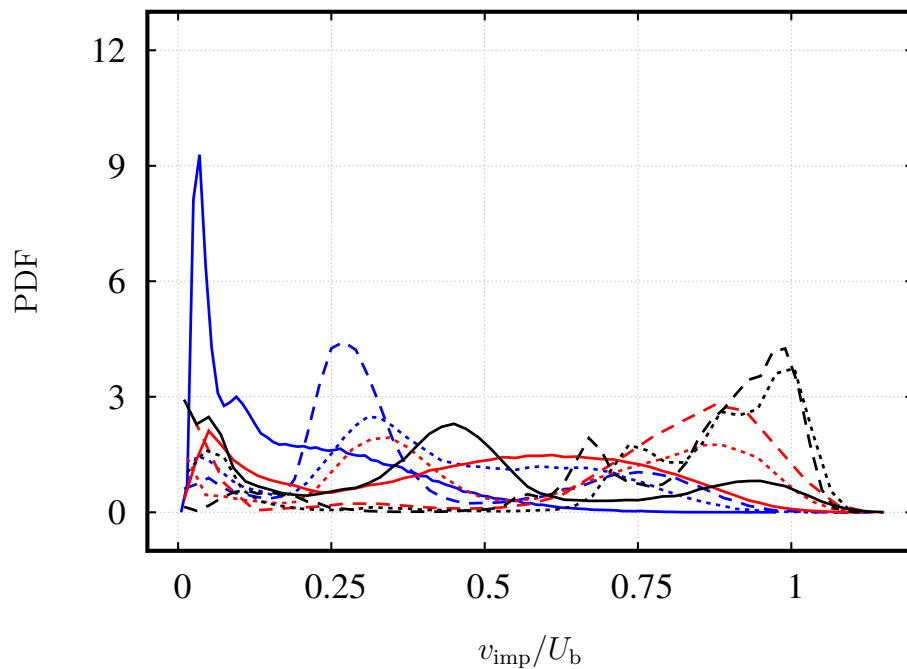
Besides the rate of breakage, it is of a considerable interest to highlight the conditions at which wall-impact breakage events take place. Such information delivers closer insights into the process allowing a better understanding.

Figs. 9.12 and 9.13 depict some statistics concerning the impact-breakage events for nine cases including three powders (**A**, **B** and **C**) and three selected Reynolds numbers: Re_1 , Re_3 and Re_5 . These statistics are collected over a time interval of $\Delta T^* = 100$. In Fig. 9.12(a) the probability density functions of the total impact velocity v_{imp} normalized by the bulk velocity are compared. Obviously, with increasing the Stokes number (i.e., the agglomerate diameter or Re increases) the breakage events take place at higher impact velocities. This behavior expresses the free-flight wall-impact mechanism (Brooke et al., 1994) known for inertial agglomerates with high Stokes numbers.

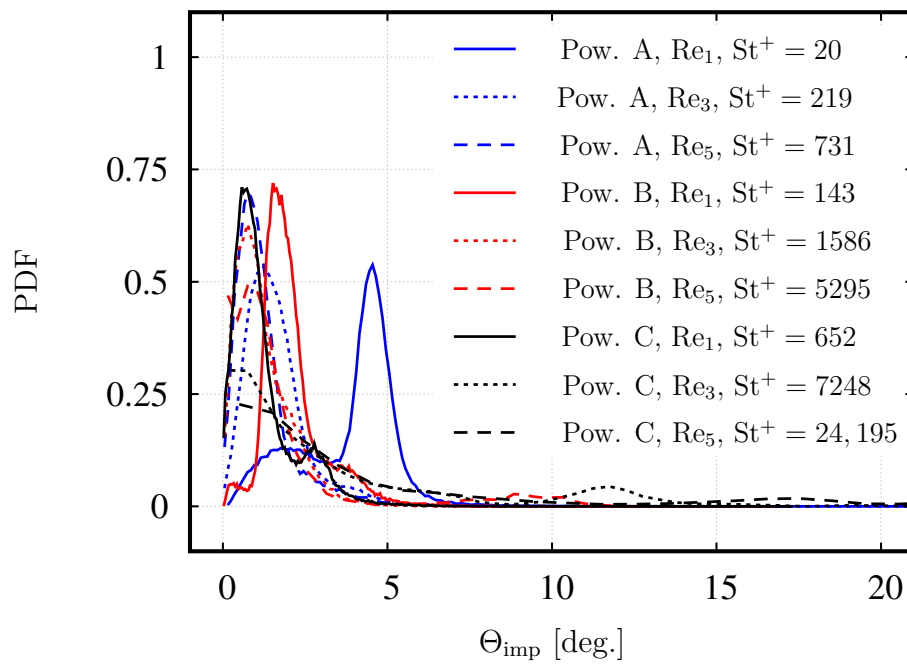
The PDFs of the impact angle Θ_{imp} associated with the breakage events are presented in Fig. 9.12(b). It is found that the impact angle varies in a very limited range not exceeding 7° for most of the considered cases except for powder **C** at Re_3 and Re_5 , where some breakage events take place at higher impact angles up to 18° . This can also be attributed to the free-flight impact mechanism, where the velocities of the agglomerates strongly deviate from the velocity of the fluid in the near-wall region. Overall, it is clear that in wall-bounded flows breakage events predominantly occur at small impact angles. Thus, as postulated in Section 7.4 for realistic predictions the effect of the impact angle must be taken into account in modeling the wall-impact breakage phenomenon.

Furthermore, the cumulative distribution function (CDF) of the fragmentation ratio FR is depicted in Fig. 9.13(a). The results demonstrate that due to the relatively high strength of powder **A** and the weak flow conditions in the case Re_1 about 40% of the breakage events lead to partial fragmentation (i.e., $FR < 1$). In the rest of the cases, i.e., for increasing Re and thus higher impact velocities or decreasing cohesion by increasing the primary particle diameter, the full fragmentation mechanism predominates. This means that a full disintegration of the agglomerate takes place by a single impact with the wall.

Lastly, it is explored whether breakage preferentially occurs at certain locations along the circumference of the duct. For this purpose, the locations of the breakage events as a function of the distance l/d_h from the duct corner are collected from the eight half edges, and the resulting distributions are compared in Fig. 9.13(b). Due to the absence of gravity in the present setup, the results are not expected to favor any of the two

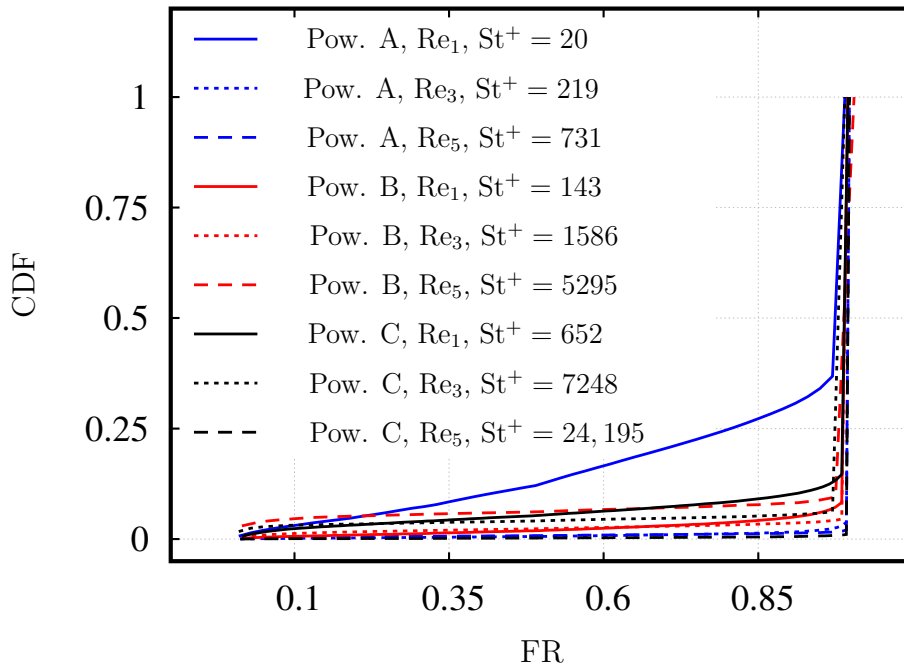


(a) Impact velocity

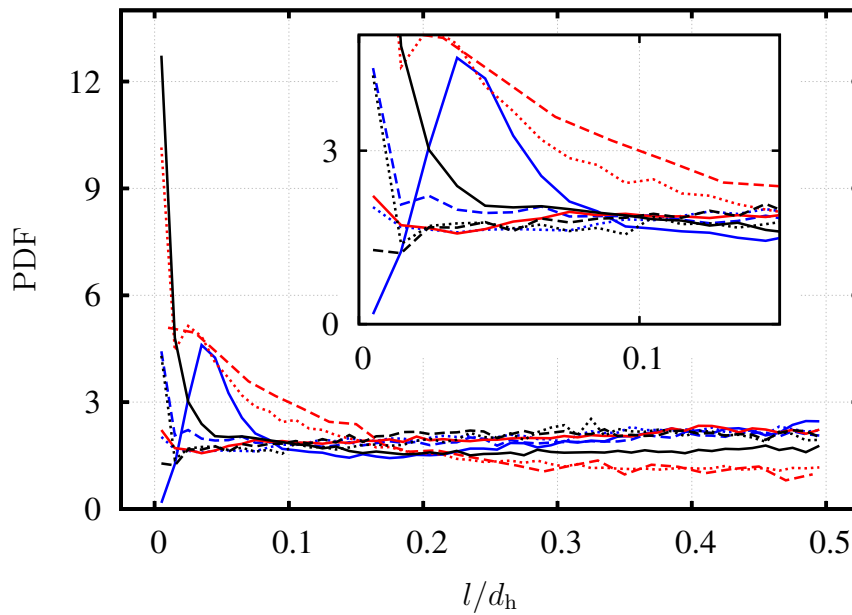


(b) Impact angle

Fig. 9.12. Impact-breakage events in the first set of simulations accumulated over a time interval of $\Delta T^* = 100$: Distribution functions for (a) the dimensionless impact velocity and (b) the impact angle. The data are collected for wall-impact events leading to breakage.



(a) Fragmentation ratio



(b) Wall-impact breakup positions

Fig. 9.13. Impact-breakage events in the first set of simulations accumulated over a time interval of $\Delta T^* = 100$: (a) Cumulative distribution functions of the fragmentation ratio, (b) Distribution functions of the breakage positions as a function of the distance from the corner, averaged over all four (cross-sectional) edges and all cross-sections.

cross-sectional directions, which allows averaging the distributions of the impact-breakage positions over all half edges. However, before going into the details of these distributions, it is helpful to describe the status of the agglomerates in the vicinity of the walls at the end of the initialization phase, i.e., before activating the breakage (see Section 9.2.2). For this purpose, the distributions of the near-wall population, which includes agglomerates within 2 wall units from the nearest wall (y^+ or $z^+ < 2$) are investigated. It is found that in 13 of the 15 cases (three powders times five Re numbers) considered, agglomerates are preferentially concentrated close to the duct corner. This finding is consistent with the literature reported on the deposition of inertial agglomerates in duct flows (Phares and Sharma, 2006; Yao and Fairweather, 2012). In the two remaining cases, which correspond to the two highest Stokes numbers, i.e., powder **C** at Re_4 and Re_5 , relatively high concentrations are also found near the corner but additionally around the wall bisector. This behavior can be attributed to the strongly reduced effect of the secondary flow on the agglomerates at such very high Stokes numbers which has not been handled in a relevant study before. Furthermore, the distributions of the velocity magnitudes of the agglomerates in the vicinity of the duct corner are analyzed. It is observed that with increasing St^+ agglomerates possess higher velocities. However, the velocity magnitudes are overall very small reaching a maximum of about $|\mathbf{u}_{ag}|/U_b < 0.08$.

With reference to the aforementioned trends of the near-wall agglomerates at the end of the initialization phase, the locations of the breakage events can be elucidated. Three main scenarios are distinguished based on the Stokes number:

1. In the relatively low St^+ range ($St^+ \leq 219$), the distributions of the breakage locations over the edge of the duct are found to be nearly uniform, except for powder **A** at Re_1 ($St^+ = 20$) as will be detailed below. In general, this observation implies that the high concentration of agglomerates near the corner does not necessarily lead to high breakage statistics in the corner region, if the velocities of the agglomerates in the corner are not sufficiently high. Thus, breakage takes place at arbitrary locations, whenever the breakage condition is fulfilled leading to the nearly uniform distributions.

The odd distribution for powder **A** at Re_1 ($St^+ = 20$), which has a peak close to the duct corner is an exception. This peak is attributed to the partial fragmentation mechanism regularly taking place for powder **A** at Re_1 since it is found that a large portion of the breakage events near the duct corner refers to (small) agglomerates generated by previous breakage events, each consisting of less than 10 primary particles.

In other words, the breakage of the initial agglomerates occurs at arbitrary locations along the circumference of the duct similar to all other cases in the low St^+ range. However, since for powder **A** at Re_1 the full deagglomeration at the first impact is not prevailing, small fragments bounce back from the wall towards the duct core supported by other mechanisms such as the near-wall fluid ejection (Esmaily et al., 2020; Robinson, 1991) and the lift force. As explained before, in this case the lift force acts in the direction away from the wall due to the small relative fluid-particle velocity as can be inferred from Fig. 9.12(a). Consequently, these small fragments

might be later entrained by the secondary vortices transporting them in the direction of the duct corner, where they eventually break again.

2. The second case corresponds to the range $219 < St^+ \leq 7248$. Within this range, agglomerates tend to favorably break close to the duct corners (i.e., $l/d_h \approx 0$). This can be attributed to the higher velocity magnitudes of the duct corner population at the end of the initialization phase as explained above, leading to more breakage events as soon as breakage is enabled.
3. The third case refers to powder **C** at Re_5 where St^+ is very high. In this case the distribution appears nearly uniform again, which is explained by the weakened role of the secondary flow on agglomerates (i.e., weaker transport towards the corners) in comparison to other mechanisms such as the turbophoresis or the lift force, leading to a more uniform breakage distribution.

It is worth noting that the above-mentioned patterns of breakage are not necessarily consistent with those found in the literature on the deposition of particles in turbulent duct flows. This is expected since the wall-impact breakage and deposition are two distinctly different phenomena. That means breakage takes place at the first location, where a highly energetic impact occurs, whereas deposition is expected when the impact is so weak that the particles stick to the wall due to adhesive forces (Almohammed and Breuer, 2016b). In addition, unlike the statistics of breakage which are collected for a finite number of discrete events, the patterns of depositions found in the literature are typically concluded by analyzing the stable positions of the deposited particles after the near-wall population reaches stable positions (see, e.g., Yao and Fairweather, 2012), which happens after a long simulation time.

9.2.4.2 Second Set of Simulations: Interaction with Other Phenomena

The results described in this section correspond to the simulations, in which inter-particle collisions, agglomeration and all breakup models are simultaneously taken into account. As mentioned before, in this second set of simulations the volume fraction of the disperse phase is set to a constant value of $\Phi_p = 10^{-5}$ in all cases by adjusting the number of the released agglomerates while fixing the number of primary particles in each agglomerate at 100. As argued in Section 9.2.2, owing to the relatively low volumetric fraction and to focus on the different powders, the two-way coupling is neglected.

Table 9.11 compares some of the most relevant results including the number of agglomeration events N_{ag}^{event} and the number of breakup events (by all mechanisms) N_{break}^{all} , both normalized by the number of released agglomerates. Besides, the contribution of each breakage mechanism (i.e., wall impact, turbulent stress, drag stress and rotary stress) are provided in percentage.

The results suggest that the number of breakage events $N_{break}^{all}/N_{ag}^{rel}$ increases overall with Re and levels off at the highest Re for powders **B** and **C**. An exception is detected for powder **A** between Re_1 and Re_2 . These observations are easily explained since at higher

Tab. 9.11. Summary of the most important results of the second set of simulations. The results are accumulated over a time interval of $\Delta T^* = 100$. The number of released agglomerates $N_{\text{ag}}^{\text{rel}}$ is 10^5 , 6400 and 730 agglomerates for powders **A**, **B** and **C**, respectively.

Powder	case	$N_{\text{ag}}^{\text{event}}/N_{\text{ag}}^{\text{rel}}$	$N_{\text{break}}^{\text{all}}/N_{\text{ag}}^{\text{rel}}$	wall impact [%]	turbulent [%]	drag [%]	rotary [%]
A	Re ₁	34.46	10.13	95.37	0.00	0.00	4.63
A	Re ₂	8.07	5.81	82.00	0.00	8.66	9.33
A	Re ₃	2.37	67.92	22.74	0.00	62.11	15.15
A	Re ₄	2.90	88.40	15.49	$2.2 \cdot 10^{-5}$	66.10	18.41
A	Re ₅	8.04	101.48	10.93	$4.7 \cdot 10^{-5}$	69.12	19.95
B	Re ₁	5.94	4.55	91.30	0.00	0.00	8.70
B	Re ₂	1.11	32.38	34.48	0.00	47.16	18.36
B	Re ₃	3.21	91.04	14.96	0.00	64.45	20.59
B	Re ₄	6.01	102.48	8.87	$1.4 \cdot 10^{-3}$	71.70	19.43
B	Re ₅	7.76	102.83	5.59	$1.9 \cdot 10^{-2}$	68.67	25.72
C	Re ₁	2.64	6.01	62.59	0.00	0.24	37.17
C	Re ₂	1.59	59.10	17.83	0.00	42.16	40.01
C	Re ₃	2.48	91.15	3.51	$1.7 \cdot 10^{-2}$	65.25	31.22
C	Re ₄	4.41	98.12	3.75	$5.0 \cdot 10^{-2}$	67.66	28.54
C	Re ₅	4.33	95.83	3.60	0.23	61.88	34.29

Re the following effects promoting breakup are augmented: The fluid stresses, the collision-induced rotation due to the enhanced mixing, and the intensity of the wall-impact events. However, as mentioned before the stresses compared to the strength of the agglomerates are relatively low for powder **A** at Re₁ resulting in more partial fragmentation, which means the generation of fragments that are able to break subsequently, increasing the breakage statistics for this case.

The effect of the strength of the agglomerate is also straightforward to interpret by comparing $N_{\text{break}}^{\text{all}}/N_{\text{ag}}^{\text{rel}}$ between the different powders at the same Re. As expected, an increase of the primary particle diameter leads to higher breakage counts owing to the reduced strength. This tendency is slightly disturbed at the highest Reynolds numbers due to the better mixing of particles inducing more re-agglomeration events for powders with smaller primary particle diameter as evident in $N_{\text{ag}}^{\text{event}}/N_{\text{ag}}^{\text{rel}}$ in Table 9.11. Hence, new agglomerates are formed, which are prone to breakage.

To discuss the role of the different breakage mechanisms, their contributions are compared in Table 9.11. Obviously, the contribution of the wall-impact breakage decreases with increasing Re since the role of the other breakup mechanisms (i.e., drag stress and rotary stress) becomes more significant leading to a disintegration of a larger number of agglomerates before they reach the wall. For instance, at Re₁ for all powders, the wall-impact breakage is the dominant mechanism and the rotary stress, promoted mostly

by rotation due to inter-particle collisions, takes the second place with a small contribution. The drag stress does not play a role at all at Re_1 except for powder **C** since the agglomerate strength in this case is relatively low. As Re increases, the contribution of the drag stress becomes larger surpassing first the effect of the rotary stress before it eventually dominates the breakage scenario overall. The turbulent stress mechanism has no effect at all in most cases. Nevertheless, it starts to contribute at higher Reynolds numbers although still in a negligible manner.

Next, the characteristics of the impact breakage are revisited to explore the influence of the other particle phenomena taken into account in this set of simulations. The PDFs of the total wall-impact velocity of the agglomerates are depicted in Fig. 9.14(a). Compared with the distributions in Fig. 9.12(a), the results in both cases are qualitatively similar. However, most peaks are now shifted towards smaller values of the impact velocities. This can be explained by the circumstance that smaller and thus less inertial agglomerates reach the wall due to the prior breakage by other mechanisms. In addition, agglomerates can be decelerated due to inter-particle collisions, which are taken into account here.

Moreover, the CDFs of the number of particles included in the agglomerates N_{pp}^{tot} which undergo wall-impact breakage are presented in Fig. 9.14(b). Obviously, increasing the Reynolds number and the diameter of the primary particles results in smaller fragments (i.e., comprising less particles) reaching the walls and breaking at the walls after other breakage events took place before.

In Fig. 9.14(c) the CDFs of the fragmentation ratios for the impact breakage are depicted. Again, the results are qualitatively very similar to those in Fig. 9.13(a). However, a noticeable difference here is that a broader distribution is obtained for powder **A** at Re_1 , meaning that more partial fragmentations are caused by the wall-impact breakage when the other breakup mechanisms and agglomeration are taken into account (i.e., the second set of simulations).

Lastly, the temporal evolution of the Sauter mean diameter is reported in Fig. 9.14(d). The predictions suggest that after a sufficiently long time ($\Delta T^* > 150$), agglomerates are nearly fully dispersed into primary particles ($R_{d_{32}} \sim 1$) except for powder **A** at Re_1 since the weak flow conditions and the high strength of the powder result in a certain steady-state fragment size distribution.

9.2.5 Part II: Comparison with the ANN-Based Wall-Impact Breakage Model

The ANN-based wall-impact breakage model is applied in the same turbulent duct flow simulations as before to describe the breakage behavior of agglomerates in a generic wall-bounded configuration. The main goal is to compare the predictions based on the new ANN-model with those reported in part I (i.e., Section 9.2.4) for the precursor model relying on classical regressions. For this purpose, the impact breakage behavior of agglomerates of varying strength levels is investigated under identical setups considering different flow conditions. The agglomerate strength is adjusted by the size of the primary particles. However, the investigation is restricted to agglomerates of powders **A** and **C** at three

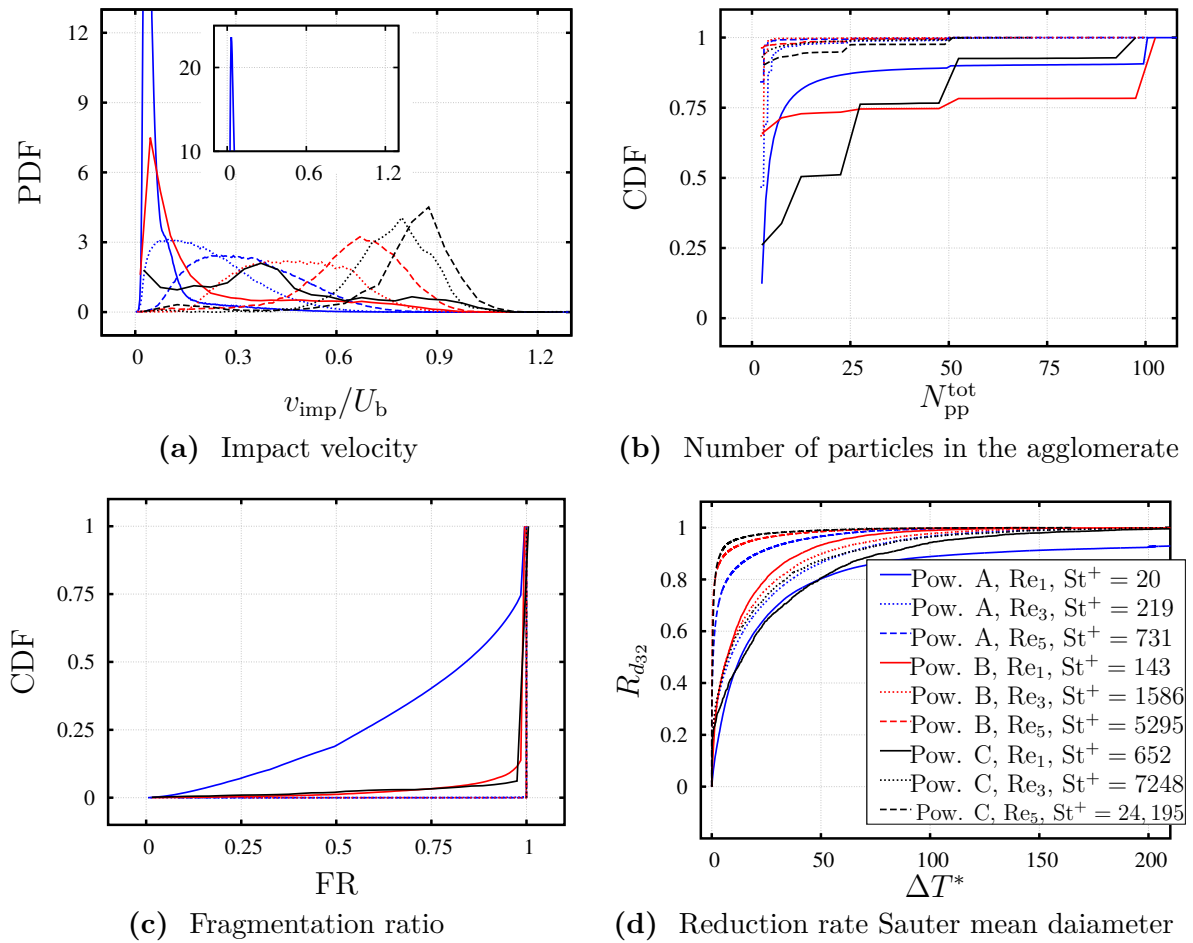


Fig. 9.14. Impact-breakage events in the second set of simulations accumulated over a time interval of $\Delta T^* = 100$: (a) Distribution functions for the dimensionless impact velocity, (b) Cumulative distribution functions of the number of particles included in the agglomerates undergoing wall-impact breakage, (c) Cumulative distribution functions of the fragmentation ratio, (d) Temporal evolution of the reduction rate of the Sauter mean diameter. The inset in subfigure (a) shows the peak of the distribution of the dimensionless impact velocity for powder A at Re_1 .

flow Reynolds numbers: $Re_1 = 8698$, $Re_2 = 17,397$, and $Re_3 = 34,794$. Powders **A** and **C** possess the highest and the lowest values of the strength, and the chosen Re cases allow to evaluate the ANN-based model based on reasonable statistics since they led in part **I** to higher contributions of the wall-impact breakage (see Table 9.11) compared to Re_4 and Re_5 .

The six simulations (two powders and three Re numbers) are conducted following the same procedure as in part **I** (see Section 9.2.2) to facilitate a proper comparison between the results. In short, the first set of simulations solely focuses on the wall-impact breakage phenomenon and ignores collisions, agglomerations and fluid-induced breakups. Since the two-way coupling and collisions are not taken into account, the predictions of the

disperse phase is independent of its volume fraction Φ_p . Therefore, an equal number of 10^5 agglomerates is injected for all powders.

The second set of simulations seeks to assess the significance of the wall-impact breakage under realistic conditions considering the effects of other relevant phenomena such as collisions, agglomerations and flow-induced breakups. In this set, the volume fraction of the disperse phase is again fixed to the same value, i.e., $\Phi_p = 10^{-5}$ for all powders. This value yields a sufficient number of agglomerates of about 10^5 and 730 agglomerates for powders **A** and **C**, respectively, enabling a meaningful analysis. In addition, the adopted volume fraction $\Phi_p = 10^{-5}$ is not much higher than the limit proposed by Elghobashi (1991) ($\Phi_p = 10^{-6}$), above which the effect of two-way coupling becomes important. Thus, the two-way coupling is neglected.

9.2.5.1 First Set of Simulations: Pure Wall-Impact Breakage

In this section, the effects of the Re number and the primary particle diameter on the wall-impact breakage behavior are discussed neglecting the contribution of other competing mechanisms such as inter-particle collisions, agglomeration, and breakup by fluid stress, i.e., the cases considered here refer to the first set of simulations (see Section 9.2.2). The focus is on the comparison of the results obtained by the ANN-based approach with the reported results of the regression-based breakage model. To ensure an accurate comparison, the simulations of the same case have exactly the same initial (flow and particle) conditions and are solely distinguished by the type of the breakage model.

Table 9.12 compares two measures of breakage between the different cases. The first is the number of breakage events per released agglomerate, $N_{\text{break}}^{\text{tot}}/N_{\text{ag}}^{\text{rel}}$, which is accumulated over a time interval of $\Delta T^* = 100$. The second quantity is the rate of reduction of the Sauter mean diameter, $R_{d_{32}} = (d_{32}^{\text{init}} - d_{32})/(d_{32}^{\text{init}} - d_{\text{pp}})$ determined at the end of the dimensionless time interval of $\Delta T^* = 100$. Comparing the results obtained by the ANN-based and the regression-based model, marginal deviations are found. Therefore, the trends present in Table 9.12 can be explained by the arguments used to discuss Table 9.10 in part I.

The predictions of the regression and the ANN-based breakage models do not only deliver similar temporally accumulated results but also lead to conforming instantaneous developments. For example, Figs. 9.15(a) and 9.15(b) depict nearly identical temporal evolutions of $R_{d_{32}}$ for powder **A** and **C** by both breakage models. The illustrated time histories confirm that agglomerates of powder **A** undergo deagglomeration at higher rates than for powder **C** despite the higher strength of the former, which is due to the more rapid transfer of agglomerates into the near-wall regions by the secondary flow as explained before.

Further insights are obtained by comparing the direct outputs of the breakage models, e.g., the fragmentation ratio of the successful breakage events for powder **A** and **C** in Figs. 9.15(c) and 9.15(d), respectively. Certain deviations are visible indicating that the ANN-based model leads to a wider range of FR, which means that more partial fragmentation events are taking place.

Tab. 9.12. Results obtained by the ANN-based model and the regression model in the first set of simulations. The number of released agglomerates $N_{\text{ag}}^{\text{rel}}$ is 10^5 for both powders. $N_{\text{break}}^{\text{tot}}$ is accumulated over a time interval of $\Delta T^* = 100$ and $R_{d_{32}}$ is given at the end of this time interval.

Powder	Case	St^+	$N_{\text{break}}^{\text{tot}}/N_{\text{ag}}^{\text{rel}}$		$R_{d_{32}}$	
			Reg.	ANN	Reg.	ANN
A	Re ₁	20	1.40	1.31	90.32%	89.98%
A	Re ₂	67	1.09	1.14	97.88%	97.70%
A	Re ₃	219	1.02	1.19	96.15%	96.12%
C	Re ₁	652	1.19	1.32	93.49%	94.13%
C	Re ₂	2214	0.37	0.39	47.61%	47.45%
C	Re ₃	7248	0.39	0.38	51.09%	51.05%

To elucidate the source of these deviations and to evaluate the performance of the ANN model for FR and ζ_i in general, Fig. 9.16 shows the fragmentation ratio FR (Fig. 9.16(a)) and the size ratio of the largest fragment ζ_1 (Fig. 9.16(b)) predicted by the ANN model as a function of the dimensionless number π_{imp} . The data points refer to the simulation of powder **A** at Re₁, which combines the weakest flow conditions and the powder with the strongest breakage resistance leading to about 1.4×10^4 breakage events covering the full spectrum of FR. Although the ANN model is independent on the functional relationship between the impact variables suggested by π_{imp} , the representation in Fig. 9.16 allows an easy comparison between the predictions of the ANN (see Section 7.5.2.2) and the corresponding regression model (7.32) based on π_{imp} appearing as a superimposed black curve. The predictions of both models agree well when the impact angle is larger than about 10° , i.e., for the *normal or oblique* impact case (non-green points compared to the black curve). For smaller impact angles typical for the *shear* impact case, the ANN model reproduces the trends learned from the training dataset (see green points in Fig. 7.20), whereas the regression model (i.e., the black curve) is limited to the predefined relationship (see Eq. (7.32a)) developed purely for the normal or oblique wall impact but not for the shear breakage case. More precisely, Fig. 9.16(a) suggests that compared to the regression model the ANN model results in lower FR values in the high π_{imp} range and higher FR values in the low π_{imp} range enabling partial breakage even in cases for which breakage is not detected at all according to the regression model. Similar results are found for ζ_1 as visible in Fig. 9.16(b) and the remaining size parameters ζ_2 and ζ_3 , which are not provided here for the sake of compactness.

To assess the performance of the second network (see Section 7.5.3.2) in the ANN model, which involves the prediction of the post-breakage kinetics of the fragments, the simulation of powder **A** at Re₁ is used again as an illustrative case. The predicted parameters λ and k of the Weibull PDFs for the reflection angle α , the spreading angle β , and the fragment

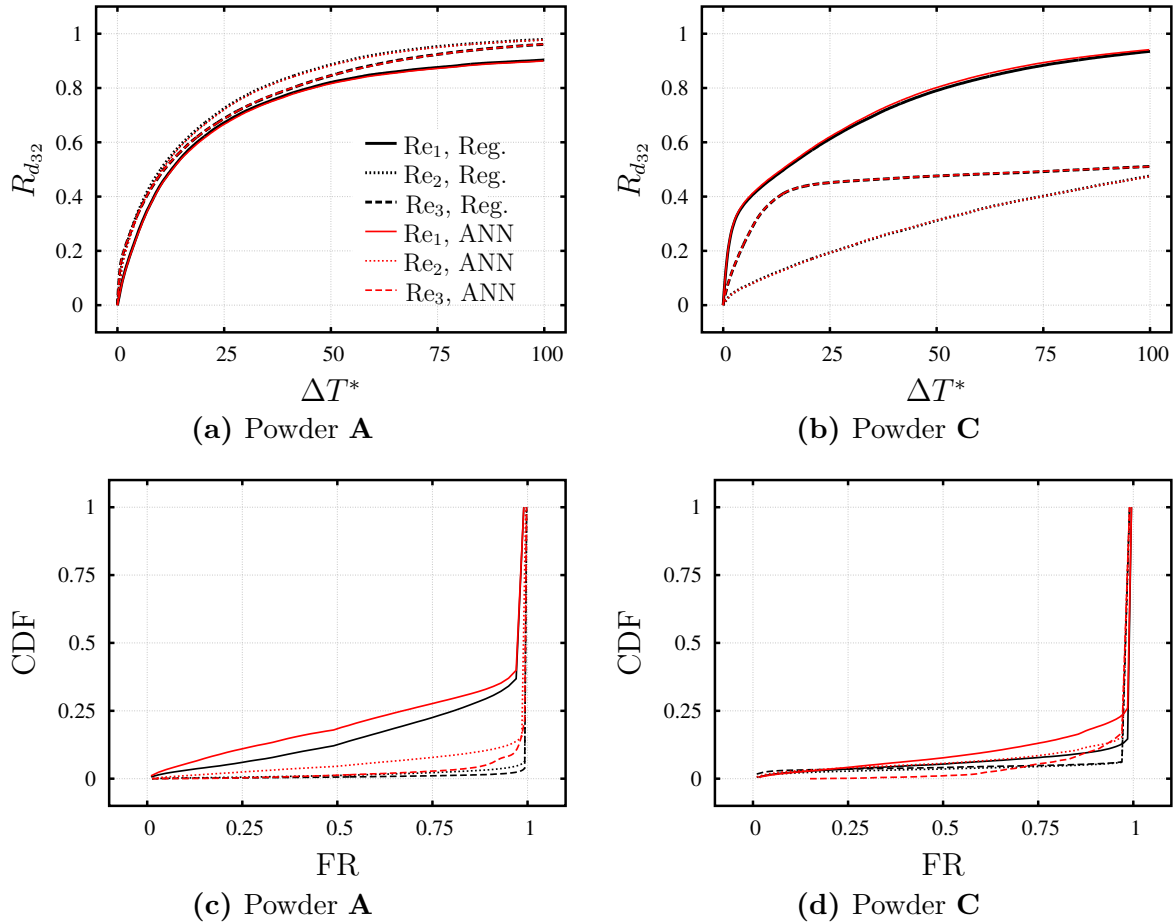


Fig. 9.15. Temporal evolution of the reduction rate of the Sauter mean diameter for powder (a) **A** and (b) **C**, respectively. Cumulative distribution functions of the fragmentation ratio in the first set of simulations (without collisions, agglomerations, and breakage by fluid stress) accumulated over a time interval of $\Delta T^* = 100$ for powder (c) **A** and (d) **C**, respectively.

velocity ratio v_{ratio} are plotted against the impact angle in Fig. 9.17. The depicted results closely follow the trends in the training dataset (see Fig. 7.24). Specifically, no remarkable outliers or odd trends appear despite the challenging inter- and extrapolations of the data caused by the sparsity and the small size of the training dataset of the second ANN.

Furthermore, in Fig. 9.18 the resulting reflection α and spreading β angles and the velocity ratio v_{ratio} which are assigned to the fragments after breakage are compared between the two models. The results show no significant differences between the predictions of the regression model and the ANN model. However, the latter model leads to slightly wider distributions of the reflection angle α (Fig. 9.18(a)) and the spreading angle β (Fig. 9.18(b)), and a narrower PDF of the fragment velocity ratio v_{ratio} (Fig. 9.18(c)).

Such discrepancies are expected since the DEM training dataset used to derive the ANN model is broader than the dataset used to devise the regression model. To explain this

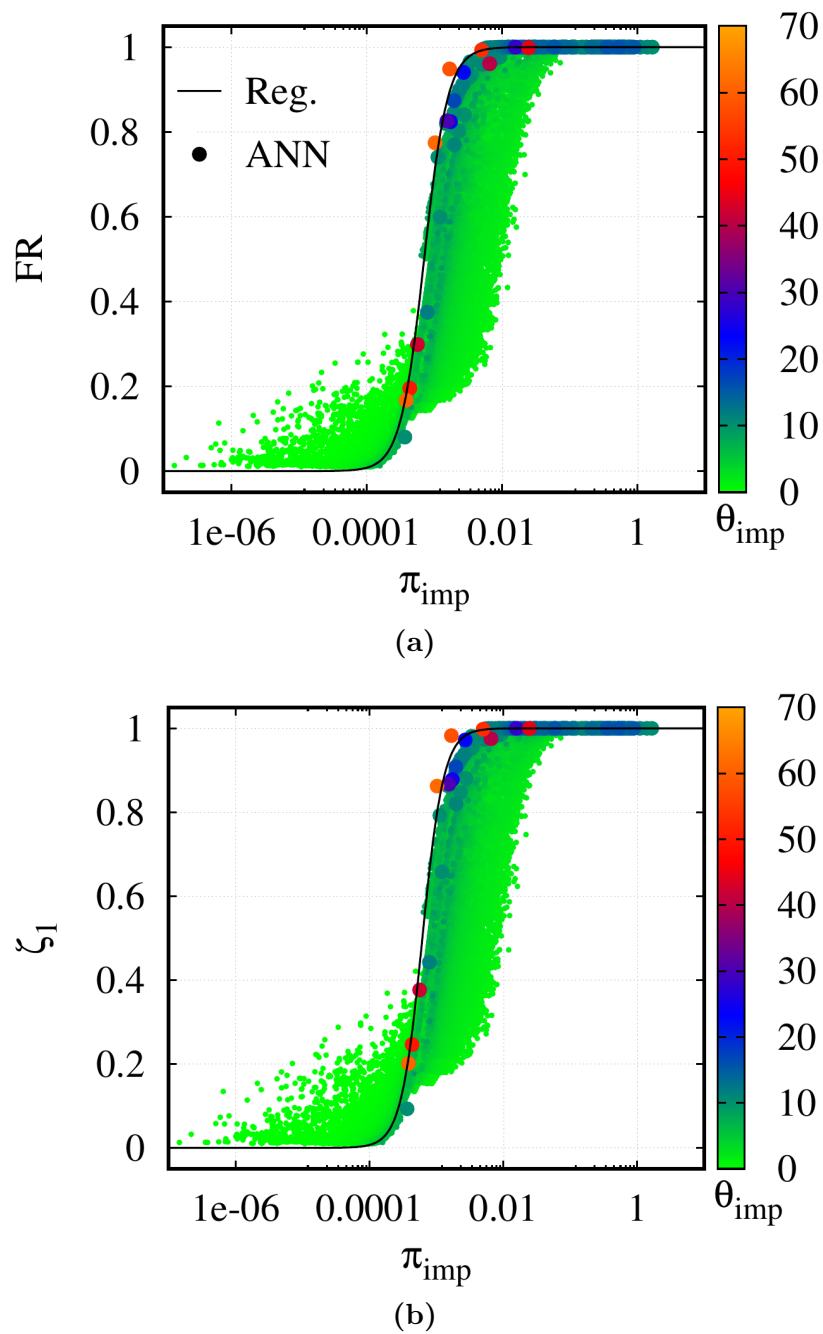


Fig. 9.16. Predictions of the ANN-based model (colored points) and the regression model (black curves) for the fragmentation ratio FR (a) and the fragment size parameters ζ_1 (b) as a function of the dimensionless number π_{imp} . The results refer to the breakage events obtained in the simulation of powder **A** at Re_1 accumulated over a time interval of $\Delta T^* = 100$. The points corresponding to impact angles below 10° are depicted in a reduced size in order to improve the visibility of the less frequent points representing larger impact angles.

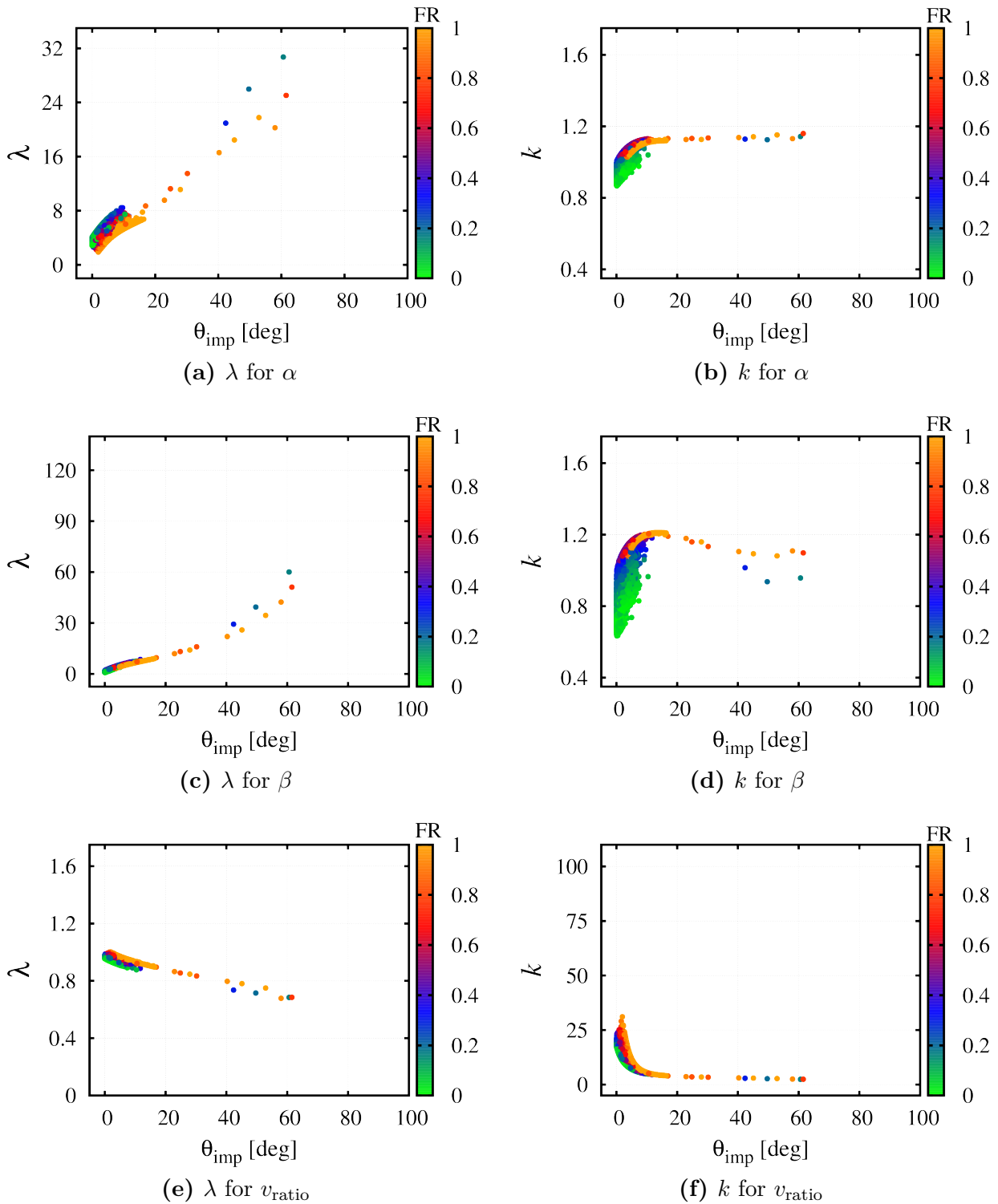


Fig. 9.17. Predictions of the ANN-based model of the Weibull PDF parameters λ and k of the reflection angle α , the spreading angle β , and the fragment velocity ratio v_{ratio} . The results refer to the breakage events obtained in the simulation of powder **A** at Re_1 accumulated over a time interval of $\Delta T^* = 100$.

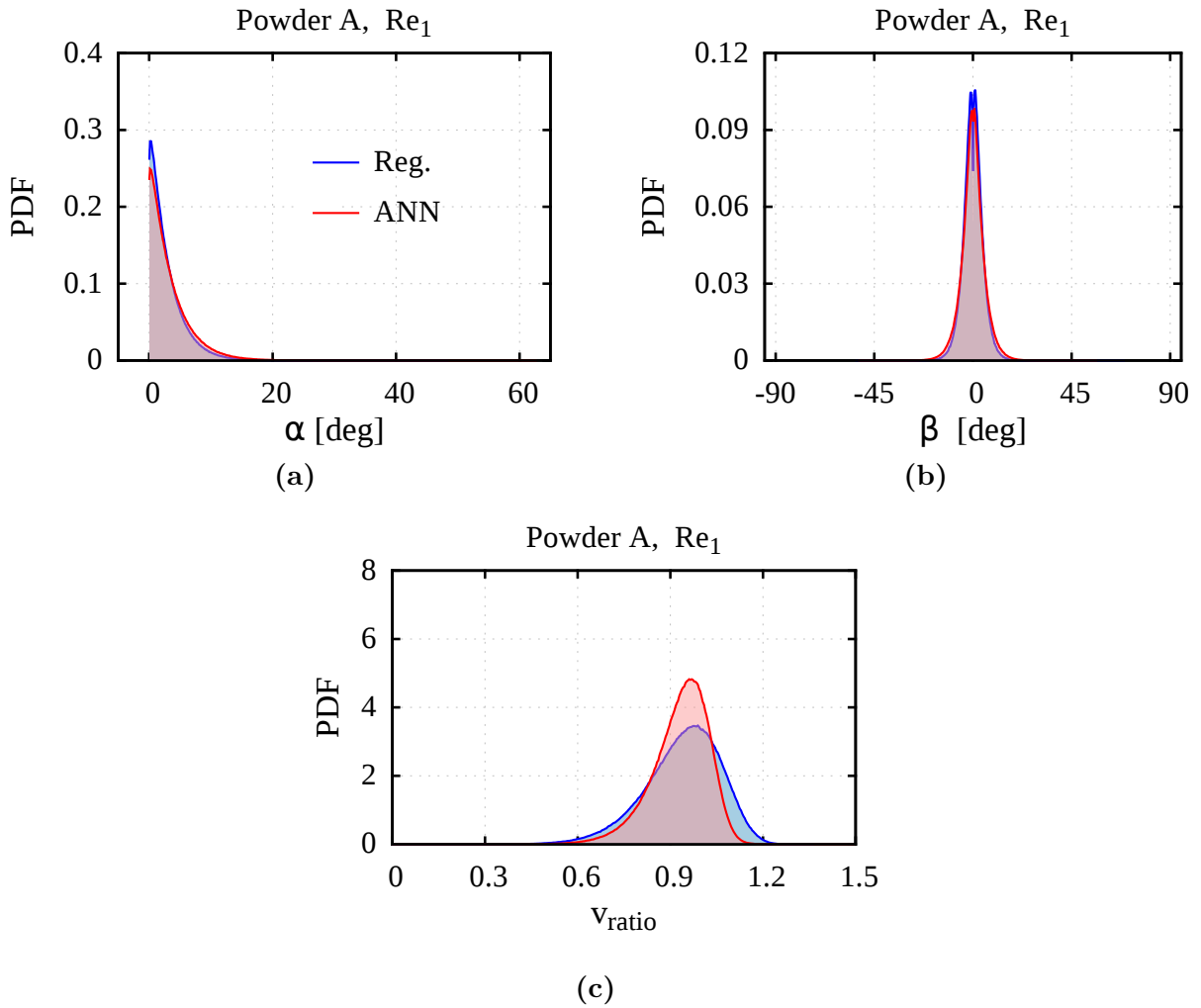


Fig. 9.18. Probability density functions of the predicted reflection angle α , spreading angle β , and fragment velocity ratio v_{ratio} based on the ANN model and the regression model. The results refer to the breakage events obtained in the simulation of powder **A** at Re_1 accumulated over a time interval of $\Delta T^* = 100$.

issue in more detail, the regression model relies on fourth-order polynomials to describe the dependence of the parameters λ and k of the Weibull PDFs solely as a function of the impact angle Θ_{imp} . Thus, for the sake of simplicity, the influence of other parameters such as the size of the agglomerate N_{pp}^{tot} and the fragmentation ratio FR is completely neglected (see Section 7.4.2.3). In addition, the small impact angles $\Theta_{imp} = 0.2^\circ$ and 3° , which are considered in the ANN model are not taken into account in the polynomial regression model. By extending the database to include this important range of small impact angles for the shear breakage case and adding further relevant parameters (i.e., N_{pp}^{tot} , and FR) as input quantities of the ANN, two weak points of the regression model are avoided. Thus, it can be stated that the ANN model predicts the real situation in a more general manner, since it additionally takes the shear breakage case into account.

9.2.5.2 Second Set of Simulations: Interaction with Other Phenomena

In this section, the results obtained in the second set of simulations allowing inter-particle collisions, agglomerations, and breakup events due to fluid stresses are discussed. Note that as stated before, the two-way coupling is also not considered in this set. Table 9.13 summarizes some of the most important statistics obtained at the end of a dimensionless time interval of $\Delta T^* = 100$. In general, when Re and d_{pp} (powder **A** to **C**) increase, the predictions of both breakage models (i.e., ANN and regression model) agree well concerning the number of agglomeration events per released agglomerates $N_{ag}^{event}/N_{ag}^{rel}$, the number of breakage events by all mechanisms (wall impact and fluid stresses) $N_{break}^{all}/N_{ag}^{rel}$, and the reduction rate $R_{d_{32}}$ of the Sauter mean diameter.

In fact, the only cases which show distinguishable deviations are powder **A** at Re_1 and Re_2 . As explained earlier, in comparison to the regression model the ANN model delivers slightly different results concerning the reflection and spreading angles of the fragments after breakage. In other words, according to the ANN model the fragments of different agglomerates undergoing breakage in the vicinity of each other at similar impact angles scatter over a broader spectrum. Consequently, the chance that these fragments collide with other fragments and form new agglomerates is not as high as in the simulation based on the regression breakage model, which explains the higher agglomeration rates by the latter model. Since the newly formed agglomerates are prone to further breakage, a larger number of breakage events is predicted by the regression model. However, the described scenario does not happen when Re is high or d_{pp} is large (i.e., powder **C**) due to the fact that agglomeration is more difficult under these conditions. This is conceivable since at high Re agglomerates generally impact the wall and reflect from the wall with high velocities while agglomeration requires weak inter-particle collisions. In addition, the increase of d_{pp} weakens the ability for agglomeration due to the higher ratio of the inertia

Tab. 9.13. Results obtained by the ANN-based model and the regression model in the second set of simulations. To ensure the same volume fraction, the number of released agglomerates N_{ag}^{rel} is 10^5 and 730 agglomerates for powders **A** and **C**, respectively. N_{ag}^{event} and N_{break}^{all} are accumulated over a time interval of $\Delta T^* = 100$ and $R_{d_{32}}$ is given at the end of this time interval.

Powder	Case	St ⁺	$N_{ag}^{event}/N_{ag}^{rel}$		$N_{break}^{all}/N_{ag}^{rel}$		$R_{d_{32}}$	
			Reg.	ANN	Reg.	ANN	Reg.	ANN
A	Re_1	20	34.46	27.64	10.13	7.26	88.81%	87.55%
A	Re_2	67	8.07	5.84	5.81	4.49	97.31%	96.59%
A	Re_3	219	2.37	2.37	67.92	67.65	96.66%	96.48%
C	Re_1	652	2.64	2.24	6.01	6.08	94.24%	95.03%
C	Re_2	2214	1.59	1.37	59.10	55.76	86.32%	85.25%
C	Re_3	7248	2.48	2.81	91.15	92.33	96.43%	96.84%

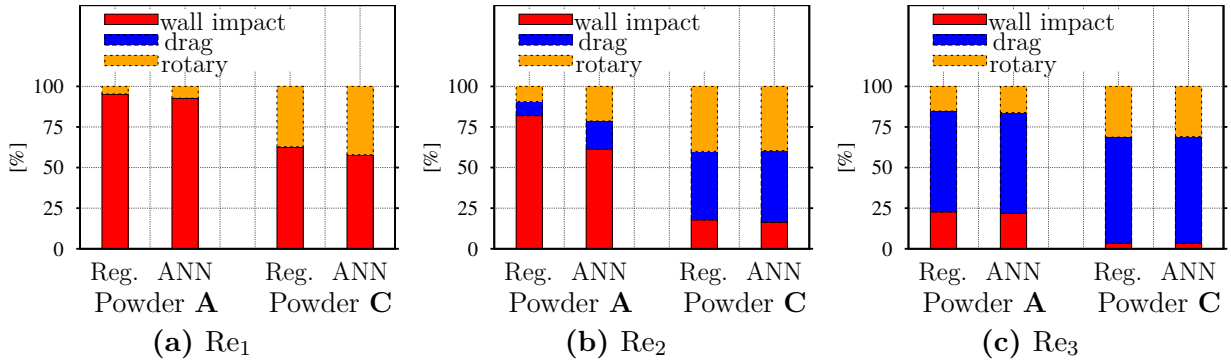


Fig. 9.19. Percentage contributions of different breakup mechanisms for (a) Re_1 , (b) Re_2 and (c) Re_3 accumulated over a time interval of $\Delta T^* = 100$. The contribution of the turbulent stress mechanism is omitted since it is negligibly small in all cases. The exact numbers are listed in Table 9.14.

force to the cohesive force.

The percentage contributions of the different mechanisms (wall-impact breakage and breakup due to turbulent, drag and rotary stresses) are graphically compared in Fig. 9.19 and the exact numbers are provided in Table 9.14. Again, the statistics are accumulated over a time interval of $\Delta T^* = 100$ by counting the number of specific breakup events and normalizing these values by the total number of breakage events. Note that the turbulent stress mechanism is not included, since its contribution is negligibly small.

As illustrated in Fig. 9.19(a), the mild flow conditions at Re_1 lead to an insignificant contribution of the drag stress for both powders, where agglomerates tend to break either due to the wall impact directly or due to the rotation induced by the wall impact or particle collisions. For increasing Re , agglomerates tend to break wherever they undergo a sufficiently high drag stress which frequently takes place in the strong shear layer before agglomerates reach the wall. Hence, the contribution of the drag stress increases and other mechanisms become less effective as depicted in Figs. 9.19(b) and 9.19(c). It is noticed that powder C is generally more affected by the drag stress than powder A at any Re , which is due to the lower strength of the former powder enabling more breakage by the relatively weak drag stress mechanism.

The contributions obtained by the two different breakage models (regression vs. ANN) show a good agreement except for powder A at Re_1 and Re_2 (see Figs. 9.19(a) and 9.19(b)). Again, the observed deviations are attributed to the improved modeling of the motion of the fragments after breakage by the ANN model, limiting fast re-agglomerations between the newly evolving fragments. Hence, the agglomeration rate in case of the regression model is higher as mentioned before. Since these agglomerates arise in the close vicinity of the wall, they very often impact the wall again leading to higher breakage rates for the regression model in general and a higher percentage contribution of wall-impact breakage to all breakup mechanisms in particular.

Tab. 9.14. Comparison between the percentage contributions of the different breakage mechanisms obtained by the ANN-based model and the regression model in the second set of simulations (including collisions, agglomerations, and breakage by fluid stresses and wall impacts).

Powder	Case	wall impact [%]		drag[%]		rotary [%]	
		Reg.	ANN	Reg.	ANN	Reg.	ANN
A	Re ₁	95.37	92.72	0.00	0.00	4.63	7.28
A	Re ₂	82.00	61.89	8.66	10.86	9.33	27.26
A	Re ₃	22.74	21.85	62.11	62.06	15.15	16.09
C	Re ₁	62.59	57.91	0.24	0.00	37.17	42.09
C	Re ₂	17.38	16.40	42.16	44.10	40.01	39.50
C	Re ₃	3.51	3.43	65.25	65.72	31.22	30.83

9.2.6 Summary and Conclusions

Two wall-impact breakage models derived by extensive DEM simulations are applied in order to gain insights into the wall-impact breakage behavior of agglomerates of different primary particle sizes in turbulent duct flows at five different Reynolds numbers.

In part I of this investigation, the wall-impact breakage model based on traditional regression techniques is applied. The main outcomes are:

- Considering the wall-impact breakage mechanism isolated from other particle related processes, the statistics of the wall-impact breakage depends on the complex interplay between the strength of the agglomerates, the severity of wall-impact events and the rate at which agglomerates are transported to the walls. For the considered turbulent duct flow, increasing Re or the diameter of the primary particle of the agglomerate means higher impact velocities and reduced agglomerate strength. However, due to the reduced responsiveness of the agglomerates to the secondary flow (higher St^+), agglomerates are not so effectively transported to the walls as otherwise leading to lower numbers of wall-impact breakage. However, in the limit of very large St^+ the role of other mechanisms such as the turbophoresis and the lift force are significantly larger improving the transport of agglomerates towards the walls again.
- Wall-impact breakage events occur at different (mostly flat) impact angles and over a wide range of impact velocities. Depending on the circumstances, full or partial fragmentation takes place. The latter commonly appears in the case of weak flow conditions and high agglomerate strength. Overall, these conditions demonstrate the necessity of taking a wide range of conditions into account during the development of wall-impact breakage models in order to achieve reliable predictions.
- The variations in the distributions of the breakage locations along the circumference of the duct can be explained depending on the Stokes number. The inertial agglom-

erates considered in the present study are known to preferentially accumulate in the duct corners. However, at the highest values of St^+ , agglomerates are additionally largely accumulated around the wall bisectors. Depending on the aforementioned accumulation trends and on the velocities of the agglomerates residing near the duct corner, the distributions of the locations of the breakage event might either favor the duct corner or are more uniform.

- Under physically relevant conditions, i.e., when particle-particle collisions, agglomeration and other agglomerate breakup mechanisms are taken into account, the general trends of the wall-impact breakage mechanism are not remarkably altered. By comparing the contributions of the different breakage mechanisms, it is found that at the smallest Re the wall-impact breakage is the dominant one with a small contribution for the rotary stress and negligible to zero contributions for the drag and turbulent stresses, respectively. The importance of the rotary and drag stress increases with Re . In the high Re range the drag stress is the most dominant, whereas the effect of the turbulent stress is overall negligible.

In part **II** of this investigation, the ANN-based wall-impact breakage model is applied. Three Re numbers and two powders are considered. A comparison with the regression model is carried out demonstrating the advantages of the new model. The most important conclusions are as follows:

- The results of the duct flow simulations reveal that in the absence of inter-particle collisions, agglomerations, and breakup events by fluid stresses, the ANN-based and the regression-based wall-impact breakage models yield very similar statistics regarding the reduction rate of the Sauter mean diameter and the total number of breakage events. However, the direct outputs of both breakage models are noticeably different due to the fact that the ANN-based model was trained based on a broader DEM database involving results for the shear breakage case relevant for particle-laden flow simulations.
- Noticeable deviations between the ANN and the regression model are found concerning the predictions of the reflection and the spreading angles of the fragments after breakage. For agglomerates undergoing breakage at similar impact angles, the ANN model derived for both the normal/oblique and the shear breakage case leads to a more realistic scattering behavior since the predicted reflection and spreading angles depend on further input parameters, i.e., FR and the size of the agglomerate. In contrast, the regression model purely derived for the normal/oblique impact case relates the post-breakage kinetics of the fragments solely to the impact angle leading to an overall similar scattering behavior of the agglomerates breaking in the vicinity of each other.
- Accordingly, when the inter-particle collisions and agglomerations are taken into account in the second set of simulations, less agglomeration events and subsequent breakage events take place in the simulations based on the ANN wall-impact breakage

model due to the improved description of the post-breakage kinetics of the fragments. This effect is mainly relevant for the lowest Re and the powder with the smallest primary particle size, since agglomeration is enhanced under these conditions.

- The percentage contributions of the breakage mechanisms show that the predictions based on the regression model (part **I**) and the ANN-based model (part **II**) are generally similar. Deviations are detected solely for the cases defined by powder **A** at Re_1 and Re_2 . These deviations are attributed to the improved modeling of the post-breakage behavior of the fragments in the ANN model.

9.3 Pipe Bend Flows

To further test the ANN-based wall impact breakage model developed in this thesis, a third investigation is carried out. The adopted setup is inspired by the experimental work of Adi et al. (2010) and the complementary numerical study by Tong et al. (2011). In these studies, the effect of the bend design on the deagglomeration performance of dry powder inhalers (DPI) is examined. The objective of DPIs is to provide an aerosol with a finely dispersed powder so that the active pharmaceutical ingredients can sufficiently penetrate the lower airways (Adi et al., 2013). To counter the enlargement of the particle size due to agglomeration, an effective breakage is required to achieve the desired particle sizes. In total, results for five different pipe bend designs at three volumetric flow rates are provided in the reference studies.

In this work, four cases defining two of the bend geometries and two flow Reynolds numbers are borrowed and investigated. As will be detailed below, a direct comparison between the present results and the data in the reference studies is not possible. The reason is that the DEM training data used for developing the ANN wall-impact breakage model are based on different material properties and size ranges of the agglomerates. However, the motivations for choosing this test case are as follows. First, besides wall impacts the provided bend geometries promote fluid stresses due to the shear layer and the abrupt acceleration occurring in the bends. That offers a plenty of data for the analysis in a reasonable time period. In addition, the relevance of the setups to the development of powder inhalers makes it a good example to demonstrate the advantage of efficient multiscale modeling strategies, allowing to simultaneously consider a large number of agglomerates.

9.3.1 Flow Configurations

The deflection of the flow in both pipe bends is 90 degrees and both pipes have a diameter of $D = 1.1 \cdot 10^{-2}$ m. In the first configuration the deflection is achieved by two straight intersecting pipes forming a sharp 90° bend at the outer and the inner corners (see Fig. 9.20(a)), whereas the second setup is composed of three straight intersecting pipes with an angle of 45° at the two junctures as depicted in Fig. 9.20(b). Similar to the previously described 90° pipe bend, the junctures are not rounded but sharp. The lengths of the pipe segments before the first and after the second bend are about $9D$, while the middle part has a length of approximately $2D$. For the 90° bend the pipe length upstream and downstream is $10D$. Both upstream and downstream lengths are not critical since on the one hand a fully developed flow field is provided at the inlet (see Section 9.3.2) and on the other hand the recirculation regions in the vicinity of the bend are far away from the outlet.

The considered fluid is air with a constant operating temperature of 295.15 K (Adi et al., 2010). The fluid properties are assumed to be constant with the following values: Density $\rho_f = 1.196$ kg/m³ and kinematic viscosity $\nu_f = 1.511 \cdot 10^{-5}$ m²/s. In order to investigate the effect of the Reynolds number on the breakage behavior of the agglomerates, two different volumetric flow rates of 60 and 120 l/min are considered. The corresponding

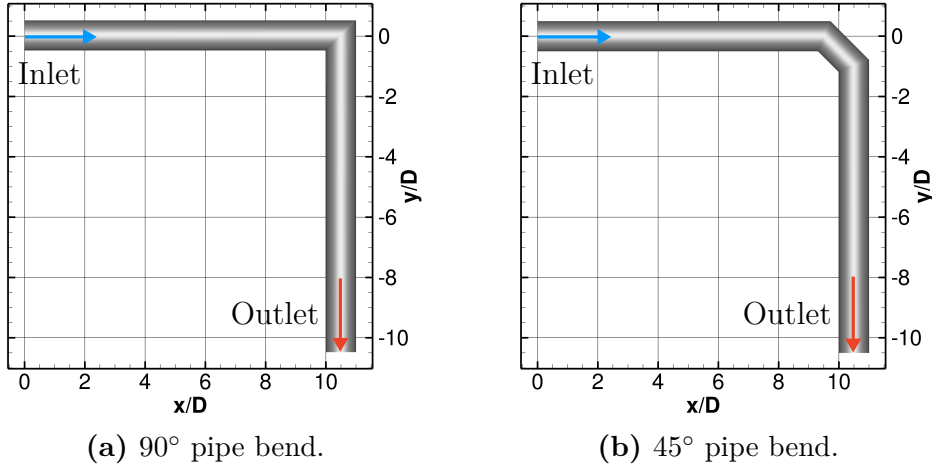


Fig. 9.20. Geometries of the investigated pipe bend configurations.

Reynolds numbers are $Re_L = 7660$ and $Re_H = 15,320$ defining a low and a high Reynolds number case, respectively. Thus, four different cases (two geometries times two Re numbers based on the bulk velocity and the pipe diameter) are investigated in total.

Spherical, dry and cohesive silica particles (Weiler, 2008) possessing the properties listed in Table 9.2 are studied. In fact, the primary particles here are identical to those considered in the two preceding investigations (see Sections 9.1 and 9.2). Particularly, the primary particles have a diameter of $0.97 \mu\text{m}$, which corresponds to powder **A**. As explained before, this powder is characterized by the smallest primary particle diameter leading to agglomerates of the largest strength compared to the other powders (Kendall, 1988; Rumpf, 1962). The restitution and friction coefficients in Table 9.2 are necessary to describe the hard-sphere particle-particle and particle-wall collisions as explained in Sections 4.3 and 4.4.

Note that in the original experimental study for the investigation of the agglomerate breakage behavior (Adi et al., 2010) mannitol agglomerates were studied. Thus, the properties used here deviate from those in Adi et al. (2010). The reason is that the data-driven wall-impact breakage model depends on results obtained by DEM simulations for silica agglomerates. Therefore, a CPU-time intensive data generation process based on thousands of new DEM simulations and a re-training of the ANNs would be required to ensure reliable predictions.

In the present study, the agglomerates are composed of $N_{pp}^{\text{tot}} = 1200$ primary silica particles. As explained in the model for the structural features in Chapter 5, the equivalent diameter of the agglomerates is determined based on a mass balance taking the reduced agglomerate density by the packing fraction into account. The resulting values are $d_{ag} \approx 19.17 \mu\text{m}$ and $\rho_{ag} \approx 311 \text{ kg/m}^3$. The packing fraction and coordination number are $f_{\text{pack}} = 0.156$ and $k_{ag} = 2$. Note that these values correspond to agglomerates consisting of 1000 primary particles since this is the largest size considered in the structural model. However, in the limit of large agglomerates both parameters (i.e., f_{pack} and k_{ag}) converge

to (nearly) constant values. Thus, the same values are applied for the slightly larger agglomerates used in the present simulations.

The Stokes number St defined by the convective characteristic time scale $\tau_f = D/(2U_b)$ of the released agglomerates is about 0.67 and 1.34 for the low and the high Reynolds number, respectively. If the viscous time scale $\tau_f^+ = \nu_f/u_\tau^2$ is used instead, the corresponding values of St^+ are 9.84 and 31.53. Note that in this case, u_τ refers to the friction velocity computed in the periodic pipe simulation at the corresponding Re number.

9.3.2 Computational Setup

The computational domains are already defined in Fig. 9.20. The boundary conditions are given as follows. At the walls, which are assumed to be ideally smooth, Stokes' no-slip condition and the impermeability condition are applied. That is possible since a wall-resolved simulation methodology is used as will be explained below. At the outlet a convective boundary condition is applied, where the convection velocity is set to the bulk velocity. At the inlet of the pipe the turbulent flow is assumed to be statistically fully developed mimicking the situation that the turbulent flow passes through a long entrance pipe before reaching the bends. In order to generate appropriate instantaneous inflow data, two supplementary simulations of pipe flows are carried out for the two Re numbers considered.

The straight pipe has a diameter D and a length of $2\pi D$. Assuming a statistically fully developed flow, periodic boundary conditions can be applied in these auxiliary simulations, since their sole task is to guarantee reliable inflow data for the main simulations. One arbitrary cross-section of the pipe is chosen and the time-resolved flow velocities are stored for a time series of $9 \cdot 10^5$ time steps which comprises a time interval of 900 and 630 dimensionless time units for the low and high Re number, respectively. The prerequisite for the direct usage of the stored data of the pipe flow as inflow conditions for the bends are that identical time-step sizes and identical grid point distributions in the cross-sections of both grids are chosen. A dimensionless time step of $\Delta t^* = 1.0 \cdot 10^{-3}$ is set for the Re_L case, whereas $\Delta t^* = 7.0 \cdot 10^{-4}$ is set for Re_H . That corresponds to CFL numbers of $4.6 \cdot 10^{-2}$ and $5.4 \cdot 10^{-2}$ for the Re_L and Re_H case, respectively.

The block-structured grids applied for the pipes and the bends have an O-type topology in the cross-section consisting of four equal outer blocks and one central block (see Fig. 9.21(c)). The maximal cell spacings of the grids in the streamwise direction (Δx_{\max}^+), the maximum circumferential spacing at the shell of the pipe ($\Delta(r\varphi)_{\max}^+$) and the distance of the cell center of the first cell to the wall (Δr_{1st}^+) are chosen according to the recommendations by Piomelli and Chasnov (1996). Note that the index "1st" denotes the center of the first cell near the wall. In addition, the superscript "+" refers to dimensionless quantities (e.g., $\Delta r_{1st}^+ = \Delta r_{1st} \cdot u_\tau / \nu_f$) normalized by the kinematic viscosity of the fluid ν_f and u_τ . The latter is predicted separately for each Reynolds number considered based on the friction factor proposed by Moody (1947) (see Eq. (9.3)), which is a standard design formula for turbulent pipe flows. The applied values in wall units are $\Delta x_{\max}^+ = 30$, $\Delta(r\varphi)_{\max}^+ = 15$, and $\Delta r_{1st}^+ = 0.5$ for the Re_L case. Furthermore, the grid is stretched in the radial direction towards the center of the pipe with a mild geometric stretching

Tab. 9.15. Number of grid points of the block-structured grids used for LES of the bend flows.

Geometry	Re	Streamwise	Cross-Section	Total
90°	7660	898	4725	4.2 million
	15,320	1498	7680	11.5 million
45°	7660	1077	4725	5.0 million
	15,320	1637	7680	12.6 million

factor of 1.05. Identical values are considered for the Re_H case except the circumferential spacing, which is chosen slightly larger, i.e., $\Delta(r\varphi)_{\max}^+ = 21$ instead of 15, in order to keep the total number of grid points affordable (see Table 9.15). Note that these settings are valid for both geometries (90° and 45° bends) investigated.

The number of grid points in the streamwise direction, in one cross-section and the finally resulting total number of points are listed in Table 9.15. For the generation of the grids, the commercial meshing software *Pointwise V18.2* is used, which allows to improve the grid quality by smoothening the grid lines based on an elliptic partial differential equation. Especially for the grids of the 90° pipe bends the improvement is significant, since the grid lines of the initial grids had a sharp 90° kink at the bend (see Fig. 9.21). Moreover, during the smoothening process the distance of the cell centers of the first cell to the wall is kept nearly equal to the initial values. Thus, an appropriate grid resolution in the wall-normal direction is ensured also after the smoothening process.

The quality of the generated grids can be demonstrated based on the equiangle skewness and the cell non-orthogonality index, which are provided directly by the meshing software *Pointwise V18.2*. The equiangle skewness is defined as the maximum ratio of the angle included in the cell to the angle of an equilateral element. The non-orthogonality index refers to the angle between a line connecting the centroids of the two cells and the normal of the shared face. The maximum value of this measure for all faces of a given cell represents the cell. The distributions of both measures for all four grids are depicted in Fig. 9.22. As expected, the quality of the grids for the 45° pipe bends is better since the deflection of the flow takes place in two steps.

For parallelization purposes based on domain decomposition and MPI, the geometric block structure is mapped to a parallel block structure consisting of 126 and 280 blocks for the Re_L and Re_H case, respectively.

9.3.3 Simulation Procedure

The pipe bend simulations are carried out applying the Euler–Lagrange methodology based on LES explained in Chapters 3 and 4. For mimicking the non-resolved scales the Smagorinsky model (Smagorinsky, 1963) extended by the van Driest damping function for the near-wall region is chosen. The classical Smagorinsky constant $C_S = 0.1$ is set. Considering the purpose of the present study and the given range of the Reynolds number, the Smagorinsky model is accepted. Furthermore, the present LES predictions are wall-

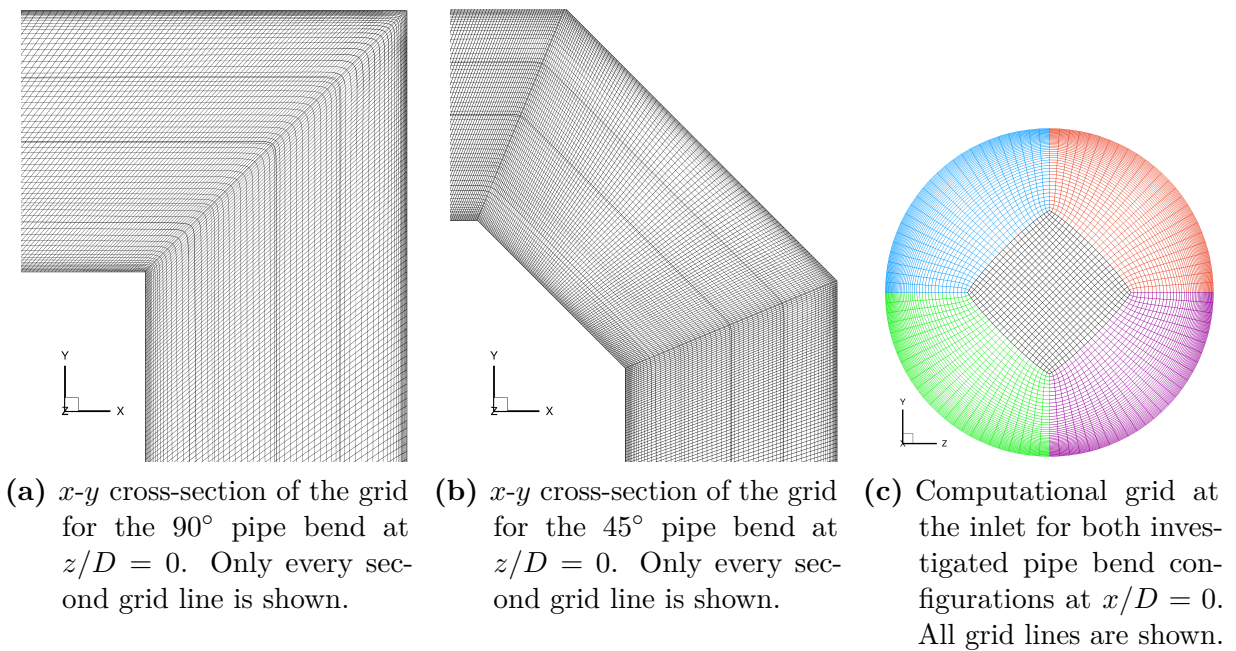


Fig. 9.21. Cross-section views of the computational grids of both bend configurations at Re_L . The grids for the high Reynolds number Re_H differ only in the number of grid points.

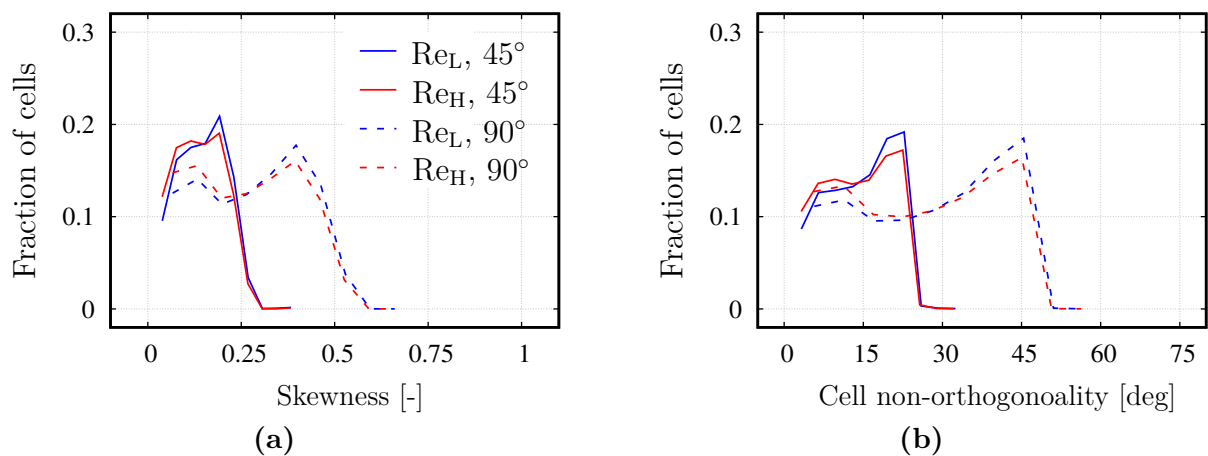


Fig. 9.22. Distribution of the (a) equiangle skewness and the (b) non-orthogonality index. Higher is worse applies for both measures.

resolved as explained above. That means that the near-wall grid resolution is sufficiently fine to apply Stokes' no-slip condition at solid walls which makes the use of other wall treatments superfluous.

Additionally, various particle-related models are accounted for. These are the stochastic Langevin particle subgrid-scale model (see Section 4.2.2), the inter-particle collisions and agglomeration (see Section 4.3), the fluid-induced breakup (see Chapter 6) and the wall-

impact breakage based on the ANN approach (see Section 7.5). However, the feedback effect of the disperse phase on the fluid flow is neglected, since in the present case the volume fraction of the particles is low as will be discussed next.

The simulations are initiated without releasing agglomerates into the flow to first establish a fully developed flow field. After reaching this state, the temporal averaging of the flow is carried out over dimensionless time intervals of 3300 and 2170 units for the Re_L and the Re_H case, respectively, to obtain the mean flow field and the turbulent statistics. Subsequently, the agglomerates are released into the flow at the inlet of the pipes assuming the same velocity as the flow. For the Re_L cases one agglomerate is released each 1000 time steps, while for the Re_H cases the interval is 1500 time steps since the time-step size is smaller. These frequencies ensure similar dimensionless time intervals separating the injection of two successive agglomerates for both Reynolds numbers.

The release position is varied within the whole cross-section of the inlet while keeping a certain distance to the walls of the pipe to avoid early breakage after the release. All simulations are run for the same dimensionless time interval which also means that nearly the same number of agglomerates are released in all cases, i.e., $N_{agg}^{rel} \approx 340$.

9.3.4 Validation of the Inflow Data

The aim of the simulations of the pipe flow with periodic boundary conditions is to provide fully developed inflow data for the simulations of the flow through the bends. In order to ensure suitable inflow conditions, the flow in the straight pipe is evaluated based on a comparison with experimental measurements. Durst et al. (1995) conducted experiments to measure the mean velocity and the velocity fluctuations of a turbulent fully developed pipe flow. The flow in a straight pipe was investigated using laser-Doppler anemometry. Different Reynolds numbers based on the pipe diameter and the bulk velocity were taken into account. Two cases ($Re = 7442$ and $13,500$) are comparable to those considered in the present study ($Re = 7660$ and $15,320$).

The periodic pipe simulations are carried out for a sufficiently long time interval while averaging the flow field in time and in the streamwise direction. The averaging time is about 405 and 160 flow-through times for the Re_L and Re_H cases, respectively. To facilitate the comparison with the experimental measurements, a transformation of the velocity field into a cylindrical coordinate system instead of the Cartesian coordinate system used in the predictions is performed. In addition, circumferential averaging is carried out.

Fig. 9.23 compares the LES results and the experimental measurements. Figs. 9.23(a) and 9.23(b) depict the profiles of the averaged streamwise velocity normalized by the bulk velocity $\langle u \rangle / U_b$ as a function of the normalized radius of the pipe r/D for both Re_L and Re_H , respectively. Although it is obvious that the profiles are symmetric, both halves are shown for the LES predictions, since this proves that the statistics are converged. As expected, the maximum streamwise velocity is found at the center of the pipe. The velocity profiles get flatter with increasing Re number leading to larger velocity gradients at the wall. Overall, a reasonable agreement between predictions and measurements is observed at both Re numbers.

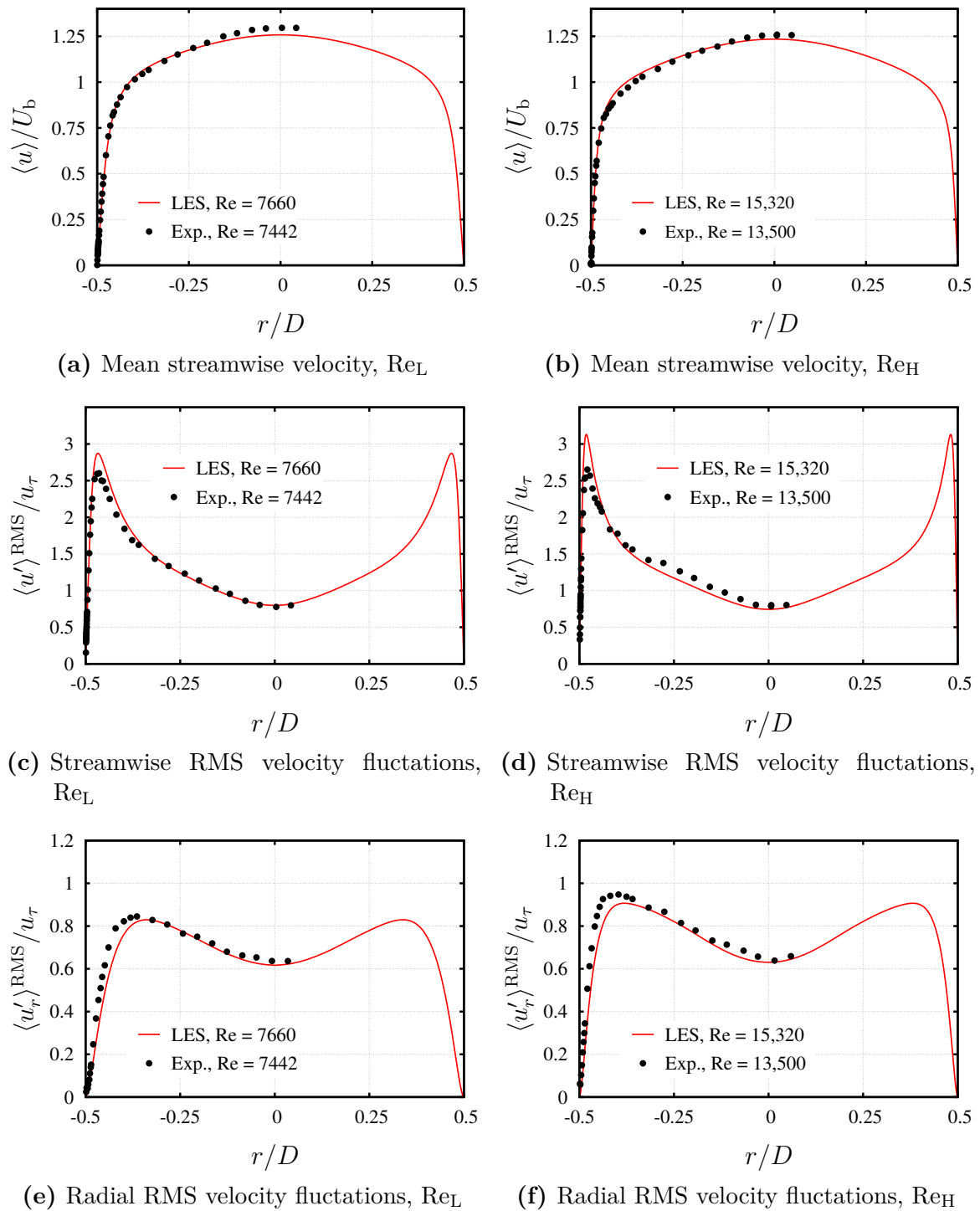


Fig. 9.23. Validation of the inflow data at both Re numbers. The experimental measurements are provided by Durst et al. (1995).

Furthermore, the root-mean-squared (RMS) velocity fluctuations $\langle u' \rangle^{\text{RMS}}$ in streamwise direction normalized by the friction velocity u_τ predicted in the simulation are shown in Figs. 9.23(c) and 9.23(d) for Re_L and Re_H , respectively. Here, it is worth mentioning that the experimentally measured shear velocity u_τ is solely provided for the Re_L case. For this reason, the shear velocity used for normalizing the experimental data for Re_H is computed based on the Darcy friction factor formula (9.3) by Moody (1947). The maximum fluctuations in Figs. 9.23(c) and 9.23(d) are found to possess a sharp peak in the region close to the wall. Towards the axis of the pipe, the fluctuations decrease and reach a minimum at the axis of the pipe. Some discrepancies between the measured and predicted peaks are found especially for the Re_H case. The peaks of the streamwise velocity fluctuations are slightly higher in the simulations than in the experiment.

The overall good agreement between the numerical and the experimental results is additionally demonstrated based on the root-mean-squared (RMS) velocity fluctuations in radial direction normalized by the friction velocity $\langle u'_r \rangle^{\text{RMS}}/u_\tau$, which are depicted in Figs. 9.23(e) and 9.23(f) for Re_L and Re_H , respectively. In general, the fluctuations in radial direction are less intense and their near-wall gradients are less steep compared to the fluctuations in streamwise direction.

It is worth mentioning that the fluctuations in the tangential directions are additionally compared (but not depicted here) and found to be in reasonable agreement. In summary, a satisfactory agreement between the measurements and the simulation results exists ensuring that the inflow data applied in the bend flow simulations are appropriate.

9.3.5 Continuous Flow in the Pipe Bends

The turbulent flow in sharp pipe bends is well known to exhibit separation zones at the inner and outer corners of the kink as well as secondary flow structures of the first kind (Prandtl, 1925) in the form of two counter-rotating helical vortices downstream of the bend (Tunstall and Harvey, 1968). These structures, which are known as Dean vortices (Dean, 1927), arise due to the counteracting centrifugal force and the radial pressure gradient inside the bend. The high-velocity fluid in the core region overcomes the effect of the adverse pressure gradient owing to the high centrifugal force and moves towards the outer wall of the bend. That does not apply for the slower moving fluid, which is driven towards the inner wall leading to the development of the secondary flow. It is worth mentioning that the secondary flow was found to be unsteady, since a single Dean vortex alternately dominates the other one at a low frequency (Tunstall and Harvey, 1968). The switching between the two stable states is well known as the swirl-switching phenomenon, which was found to occur in smooth as well as sharp bend flows (Hufnagel et al., 2018).

Next, the predicted flow fields of all cases considered are discussed focusing on the mean velocity field and the second-order statistics of the turbulent flow.

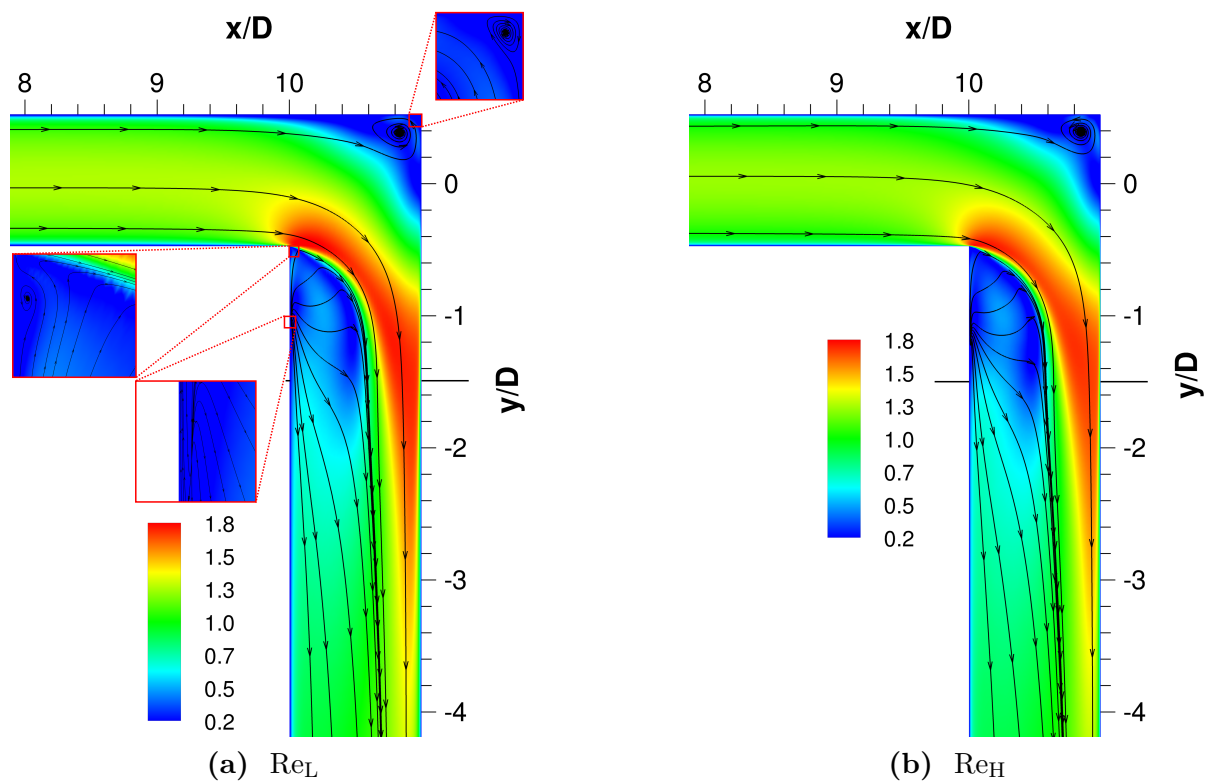


Fig. 9.24. Time-averaged dimensionless velocity magnitude and streamlines of the 90° case in the x - y plane at $z/D = 0$.

9.3.5.1 Flow in the 90° Pipe Bend

The time-averaged velocity magnitude normalized by the bulk velocity and the corresponding streamlines are depicted in Figs. 9.24(a) and 9.24(b) for the sharp 90° pipe bend at Re_L and Re_H , respectively. In both cases the fully-developed velocity profile upstream of the bend is consistent with the flow in a straight pipe. Further downstream an adverse pressure gradient in the streamwise direction develops towards the bends (not depicted here) leading to the growth of the boundary layer thickness at the outer side of the bend before the flow finally detaches. The separation of the flow gives rise to recirculation zones at the outer corners consisting of a series of asymmetric, counter-rotating vortices. In the present case two counter-rotating vortices could be resolved as depicted in the upper zoom in Fig. 9.24(a). Consequently, the flow cross-section is tapered, which causes the flow to be accelerated at the inner kink to globally conserve mass.

Inside the bend the deflected flow is driven to the outer side of the bend by the centrifugal forces. Therefore, the flow is accelerated in the axial direction leading to the reattachment of the boundary layer at the outer wall. At the inner side of the bend the flow detaches, since it can not follow the sharp bend. Consequently, a large separation zone is established on the inner wall directly after the bend. This zone is occupied by slowly moving fluid and possesses a reverse-flow region in its core. Obviously, a strong shear layer arises between the fast central region and the recirculation zone.

In Fig. 9.25 the contours of the downstream streamwise velocity $\langle v \rangle / U_b$ in a cross-section one pipe diameter downstream of the bend are shown. Additionally, the streamlines of the secondary flow are superimposed. As visible, the lowest streamwise velocity is located at the center of the separation zone. The Dean vortices, which are rotating around the two pressure minima, are nearly symmetric for the time-averaged flow field. That is a hint that the time-averaging period was sufficiently long.

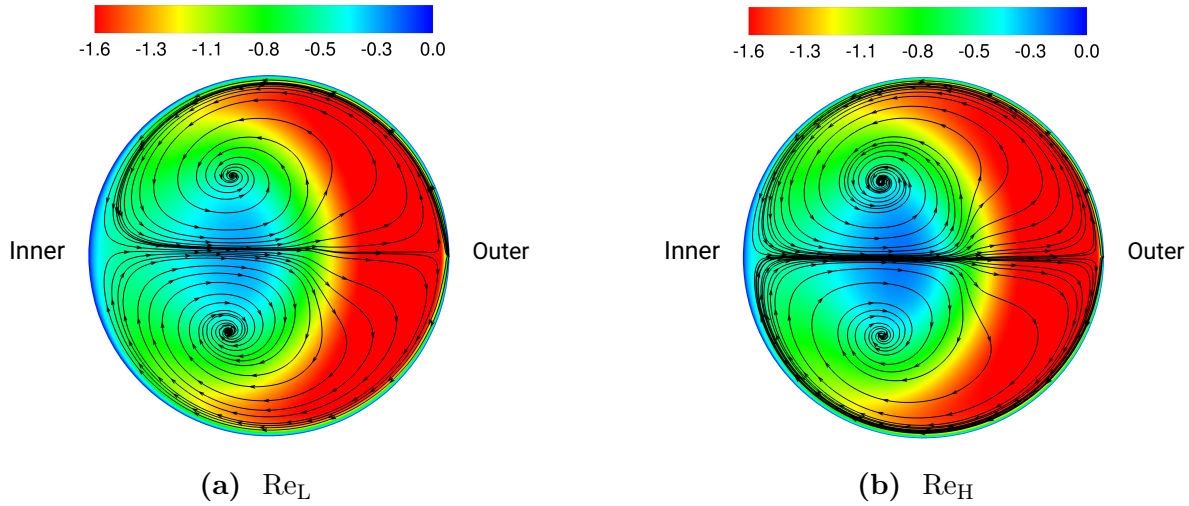


Fig. 9.25. Time-averaged dimensionless streamwise velocity $\langle v \rangle / U_b$ and streamlines of the 90° cases in the x - z plane at $y/D = -1.5$.

The resolved turbulent kinetic energy $\langle k \rangle = 1/2 (\langle u'u' \rangle + \langle v'v' \rangle + \langle w'w' \rangle)$ normalized by U_b^2 is shown in Figs. 9.26(a) and 9.26(b) for the Re_L and the Re_H cases, respectively. As expected, the strongest velocity fluctuations are found in the shear layer between the recirculation region and the core flow, and inside the recirculation region. Moreover, the resolved Reynolds shear stress $\langle u'v' \rangle / U_b^2$ is depicted in Figs. 9.26(c) and 9.26(d). The distributions can be attributed to the strong velocity gradients at the edge of the shear layer, where the fluid velocity increases strongly towards the outer wall. As visible in Fig. 9.24 showing the velocity magnitude in the symmetry plane as well as Fig. 9.25 depicting the streamwise velocity in a cross-section downstream on the bend, the velocity gradients also remain high a few diameters downstream of the bends. That explains why the Reynolds shear stress remains high far downstream of the bends.

In general, the results obtained at the two Reynolds numbers considered are qualitatively very similar. Moreover, the described flow patterns are in close agreement with the experimental observations (Bluestein et al., 2019; Tunstall and Harvey, 1968) and numerical results (Arun et al., 2020; Venters et al., 2021) reported in the literature concerning sharp 90° bend flows. However, a direct comparison can not be carried out, since on the one hand a different range of Re (up to $Re \approx 1.2 \cdot 10^5$) was investigated in these studies. On the other hand, a sharp duct bend with a square cross-section was taken into account in the studies employing comparable Re (Bluestein et al., 2019; Venters et al., 2021).

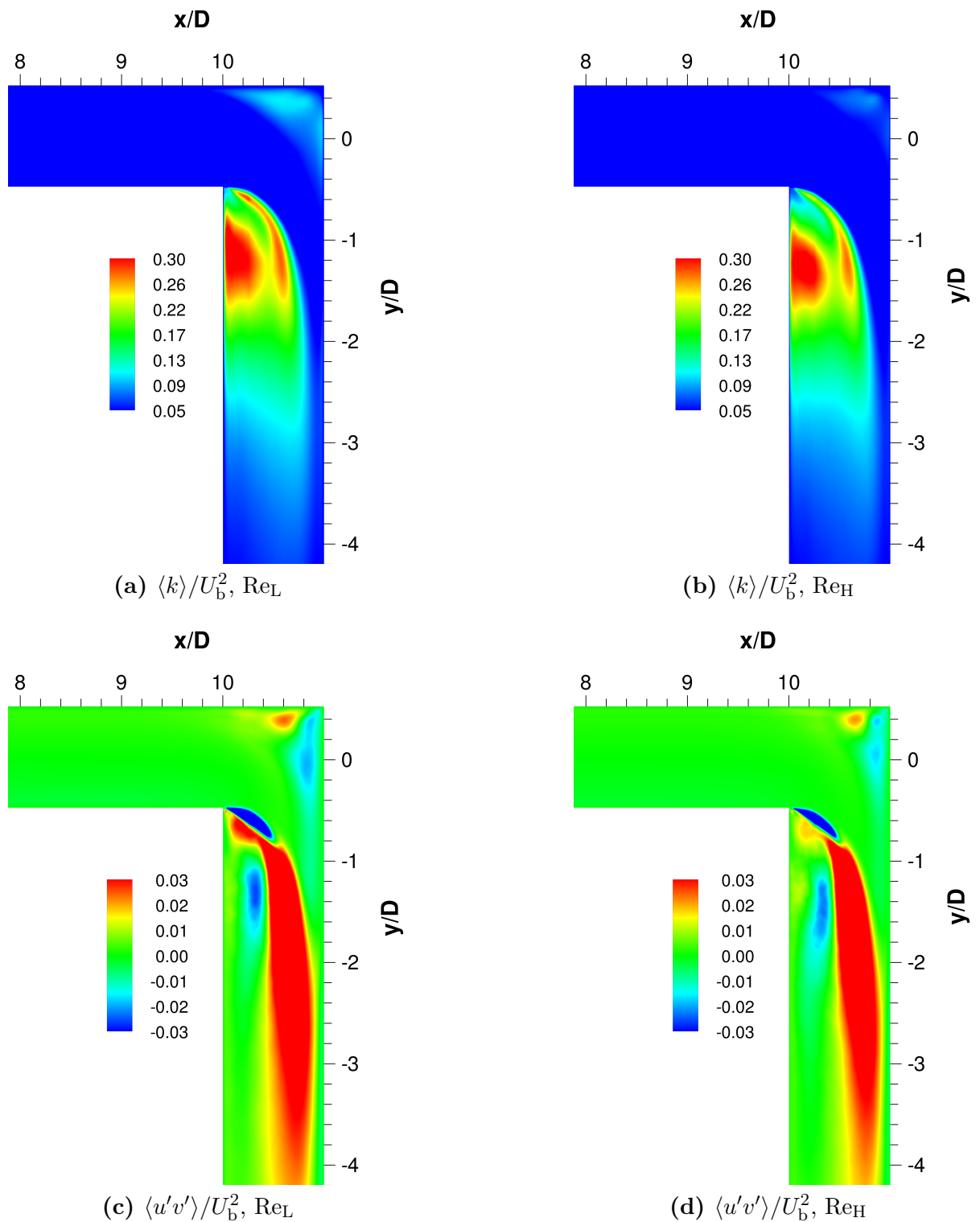


Fig. 9.26. Time-averaged dimensionless turbulent kinetic energy $\langle k \rangle / U_b^2$ ((a) and (b)) and Reynolds shear stress $\langle u'v' \rangle / U_b^2$ ((c) and (d)) of the 90° case in the x - y plane at $z/D = 0$.

9.3.5.2 Flow in the 45° Pipe Bend

In Fig. 9.27 the time-averaged velocity magnitude for the 45° pipe bends is shown for both Reynolds numbers. Due to the relatively sharp change of the flow direction an adverse pressure gradient develops in the upstream part. This leads to a recirculation region at the outer corner of the first bend which is found to be smaller than its corresponding 90° counterpart. The flow attaches again at the outer wall in the middle segment between the two bends owing to the centrifugal force. At the inner corner of the first bend the flow detaches giving rise to a separation zone over the inner side of the middle segment. Hence, the observed acceleration of the fluid at the first bend is attributed to the reduction of the cross-sectional area of the flow.

A similar scenario occurs at the second bend. An axial adverse pressure gradient leads to a vortical structure in the outer corner and the flow detaches again at the inner corner. Owing to the centrifugally induced pressure gradient, the high-velocity fluid is pushed to the outer side, whereas the low-velocity fluid is driven to the inner side downstream of the second bend. Hence, Dean vortices are formed as depicted by the streamlines of the secondary flow overlaying the contours of the downstream streamwise velocity $\langle v \rangle / U_b$ in Fig. 9.28. The centers of these Dean vortices are closer to the symmetry plane and closer to the inner bend radius compared with the flow in the 90° bend.

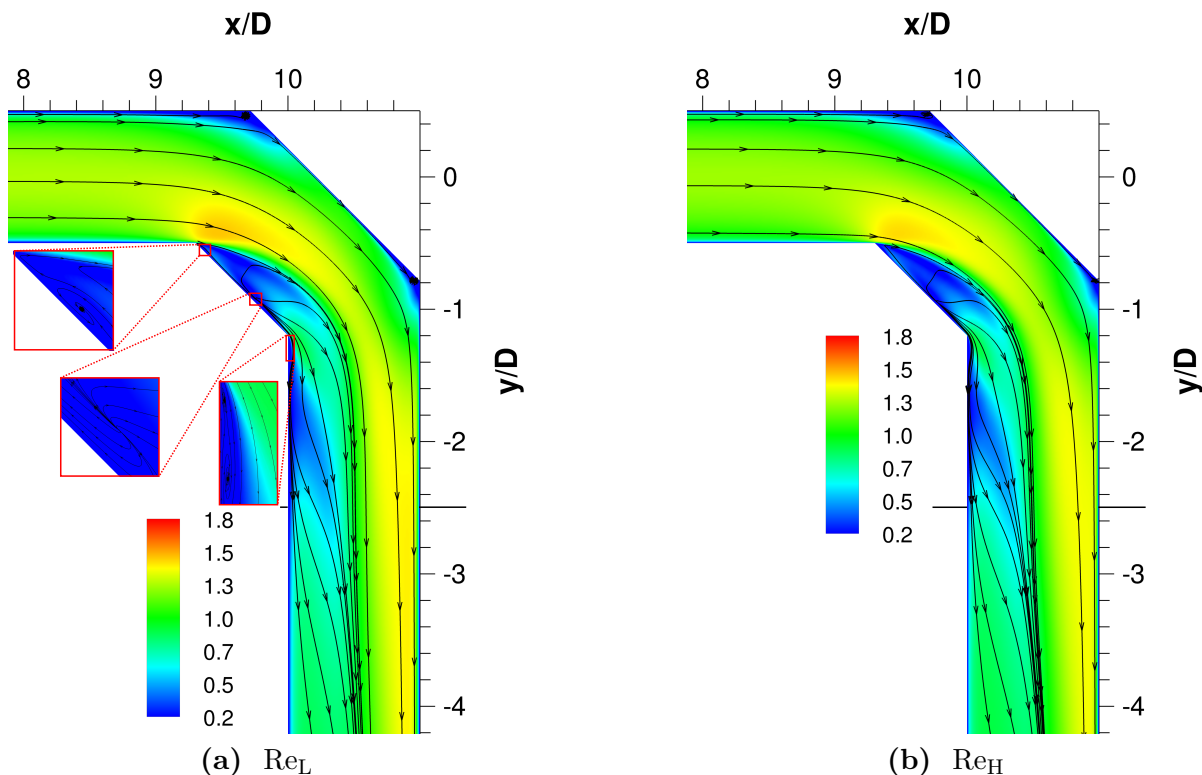


Fig. 9.27. Time-averaged dimensionless velocity magnitudes and streamlines of the 45° case in the x - y plane at $z/D = 0$.

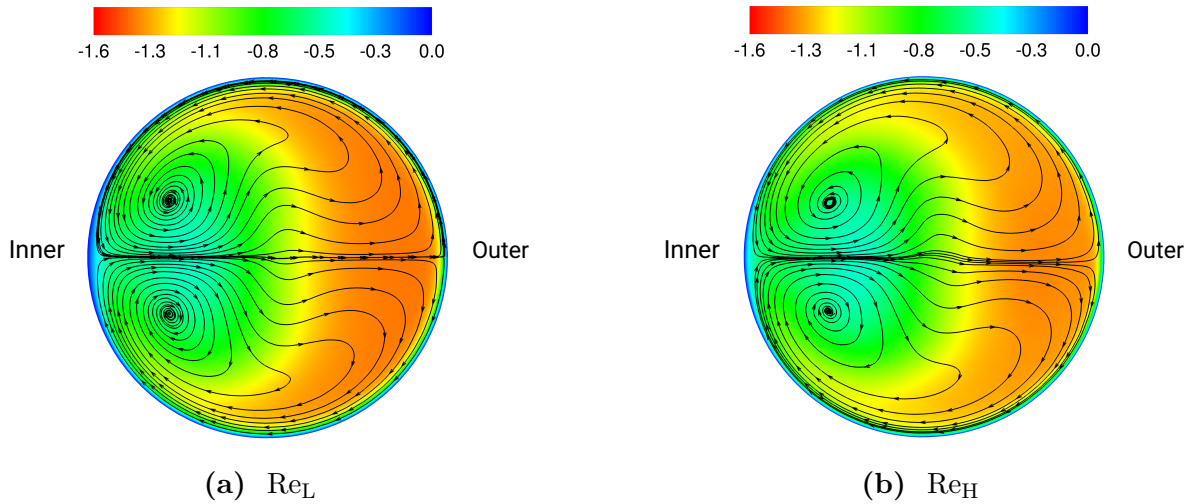


Fig. 9.28. Time-averaged dimensionless streamwise velocity $\langle v \rangle / U_b$ and streamlines of the 90° cases in the x - z plane at $y/D = -1.5$.

In Fig. 9.29 the time-averaged resolved turbulent kinetic energy $\langle k \rangle / U_b^2$ is depicted for both Reynolds numbers. The largest magnitudes are again found in the shear layers but in contrary to the 90° bend the turbulent kinetic energy is not very high in the recirculation regions itself. Furthermore, it has to be noted that the range of $\langle k \rangle / U_b^2$ depicted in Fig. 9.29 comprises only half of the range shown in Fig. 9.26. Obviously, redirecting the flow in two steps as done in the 45° bend leads to lower velocity magnitudes and thus a weaker shear layer. As a direct consequence the production of turbulent kinetic energy is reduced.

The same applies to the time-averaged Reynolds shear stress $\langle u'v' \rangle / U_b^2$ shown in Figs. 9.29(c) and 9.29(d). Again, the highest values are detected in the shear layers. Comparing the 45° bend with the 90° bend reveals that the deflection of the flow in two steps decreases the arising maxima of the Reynolds shear stress. In addition, in both geometries the size of the regions of high values of $\langle k \rangle / U_b^2$ and $\langle u'v' \rangle / U_b^2$ slightly decreases with increasing Reynolds number.

9.3.6 Breakage of Agglomerates

The breakage behavior of the agglomerates is evaluated based on analyzing the data obtained within a dimensionless time interval of $\Delta T^* = 350$, which starts at the release of the first agglomerate. Table 9.16 summarizes some of the most important results obtained for all considered cases. To begin with, the percentage contributions of the breakage mechanisms listed in the third and fourth column of Table 9.16 show that the breakage scenario is overwhelmingly predominated by wall impactions followed by a weak contribution of the rotary stress mechanism. Note that the contributions of the other two fluid-induced breakage mechanisms (i.e., drag and turbulence) are not included since they are found to be zero or negligibly small. The most obvious explanation for this

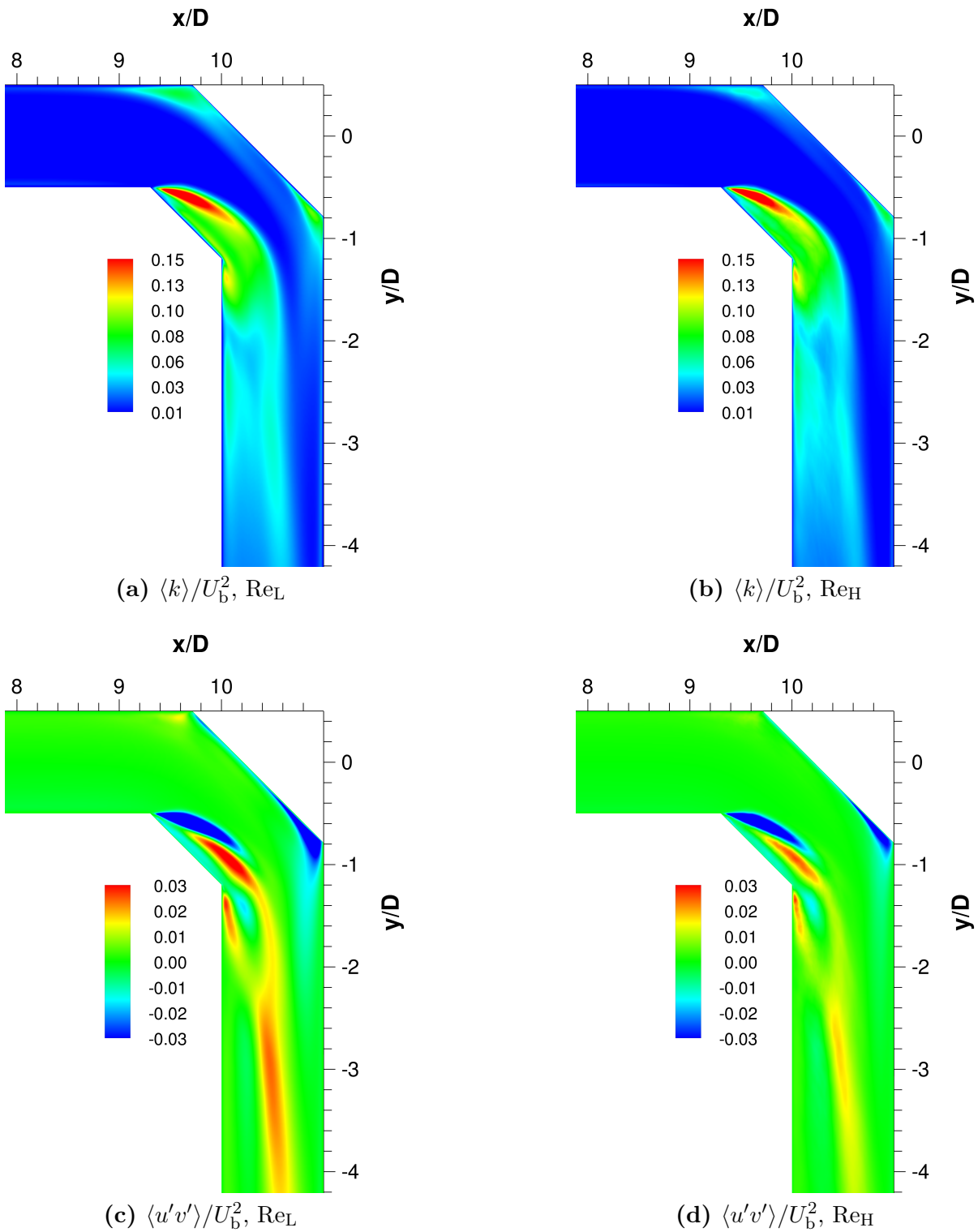


Fig. 9.29. Time-averaged dimensionless turbulent kinetic energy $\langle k \rangle / U_b^2$ ((a) and (b)) and Reynolds shear stress $\langle u'v' \rangle / U_b^2$ ((c) and (d)) of the 45° case in the x - y plane at $z/D = 0$.

observation is that the agglomerates collide with the wall before other physical effects such as strong shear or high turbulence intensities can have a significant effect on them. In other words, due to the geometrical setup most agglomerates simply do not reach the flow region which might lead to breakage by drag or turbulence. An exception is the rotary stress mechanism since agglomerates not breaking immediately at the first wall impact experience high rotation rates due to the collision with the wall which induces this breakage mechanism.

Tab. 9.16. Summary of the main breakage results obtained in the pipe bends. The evaluation time interval is $\Delta T^* = 350$ starting at the release of the first agglomerate.

Bend	Case	Wall Impact [%]	Rotation [%]	$N_{\text{break}}^{\text{tot}}/N_{\text{agg}}^{\text{rel}}$	$N_{\text{agg}}^{\text{event}}/N_{\text{agg}}^{\text{rel}}$	PPF [%]
90°	Re _L	97.0	3.0	52.8	289.1	84.7
90°	Re _H	98.9	1.1	54.1	357.2	93.5
45°	Re _L	98.6	1.4	69.2	320.1	75.0
45°	Re _H	98.3	1.7	74.5	516.0	88.9

The total number of breakage events per released agglomerate $N_{\text{break}}^{\text{tot}}/N_{\text{agg}}^{\text{rel}}$ listed in the fifth column of Table 9.16 suggests that breakage is enhanced with rising Re for both bend geometries. This can be clearly attributed to the higher impact velocities experienced by the agglomerates at Re_H compared to the case at Re_L. Furthermore, more breakage events take place in the 45° bend than in the corresponding 90° bend at the same Re. The analysis reveals that this trend is related to the higher number of agglomeration events $N_{\text{agg}}^{\text{event}}/N_{\text{agg}}^{\text{rel}}$ (see sixth column in Table 9.16) occurring in the 45° bends. In more detail, due to the introduction of a second bend the fragments of the agglomerates breaking in the middle segment tend to accumulate for a limited time in the regions near the corners of the second bend, where the fluid velocities are low. In these zones agglomeration is promoted due to the low-velocity interactions between the particles. The relatively smoother deflection of the flow in the 45° bends leads to impact events characterized by small impact angles Θ_{imp} as can be deduced by comparing the PDF distributions of Θ_{imp} between the 90° (Fig. 9.30(a)) and the 45° case (Fig. 9.30(b)). As a consequence, the resulting fragments bounce off from the outer wall of the middle segment with small angles and advance nearly parallel to the axis of the middle segment to reach the regions near the corners of the second bend. The newly formed agglomerates are very likely to break again since they are already in close vicinity of the walls leading to higher breakage statistics in the 45° bend compared to the 90° case.

To provide further insight into the effect of the shape of the bend on the breakage behavior, Fig. 9.31 depicts the positions of the breakage events along the axis of the pipes. Fig. 9.31(a) confirms that in the 90° pipe bend the majority of breakage events takes place near the kink at both Re. However, the distributions of the breakage events in the regions upstream and downstream of the bend are not similar at the two Re numbers. Obviously,

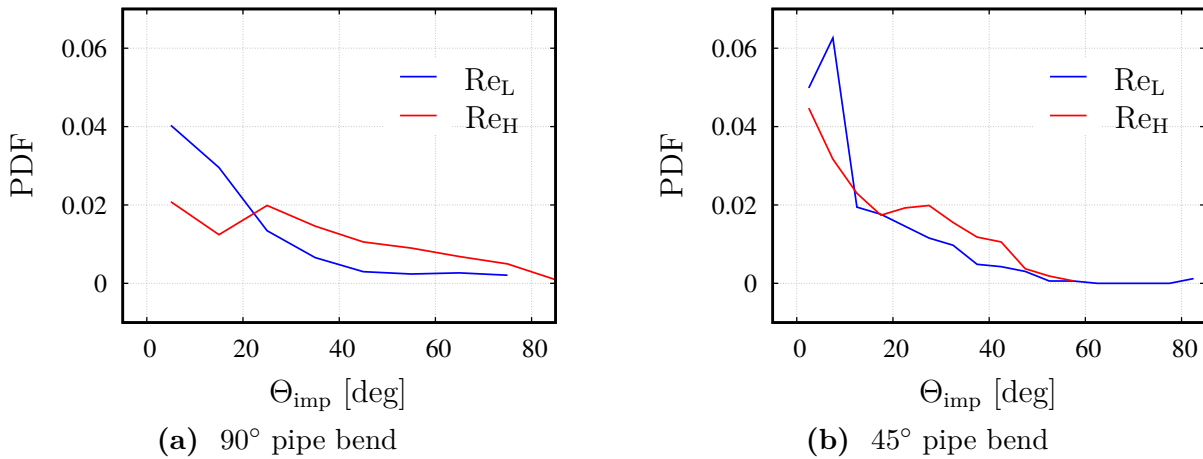


Fig. 9.30. PDF of the impact angles Θ_{imp} associated with the breakage events of the initial agglomerates comprising $N_{\text{pp}}^{\text{tot}} = 1200$ particles.

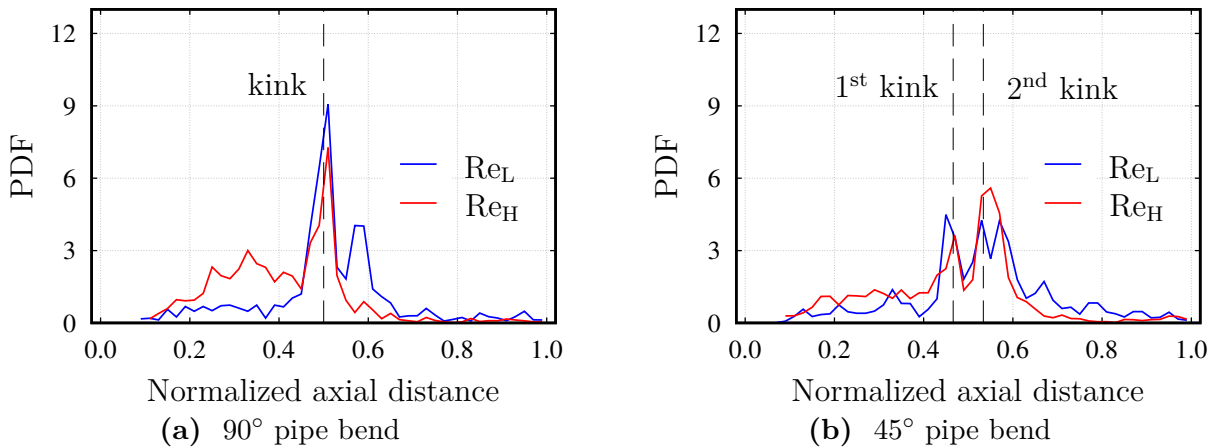


Fig. 9.31. Positions of the wall-impact breakage event along the axis of the pipe bend. The axial distance is normalized by the total length of the pipe.

more wall breakage events take place in the upstream region at Re_H , which is attributed to the higher flow velocity and hence the stronger wall-impact events encountered by the agglomerates even before reaching the bend. In contrast, the weaker flow conditions in the upstream region at Re_L shift the distribution of the breakage events towards the kink and the downstream section of the bend.

The trends are overall similar in the 45° pipe bend as illustrated in Fig. 9.31(b). In this bend configuration, the distributions show peaks near both kinks. Again, slightly higher numbers of breakage events are observed in the upstream region at Re_H , whereas in the Re_L case more agglomerates survive the critical regions around the kinks to break further downstream on their way towards the outlet.

An important aspect in the context of dry powder inhalers is the capability of the investigated pipe bends to deagglomerate powders. A common way to assess the deag-

glomeration performance is to analyze the fraction of particles arriving at the outlet with a certain size. For this purpose, the primary particle fraction (PPF) is evaluated. PPF is defined as the number of single primary particles reaching the outlet of the pipe divided by the total number of primary particles (i.e., including those forming agglomerates) reaching the outlet. The last column in Table 9.16 lists the PPF values obtained for the different configurations. As anticipated, the fraction of single primary particles reaching the outlet increases with the Reynolds number in both bends. In addition, for equal Re more single primary particles are detected at the outlet of the 90° than for the 45° bend. This consequence is owing to the enhanced agglomeration in the 45° bend as discussed above.

In the original numerical and experimental studies (Adi et al., 2010; Tong et al., 2011) in which the present geometrical configurations were introduced, the deagglomeration performance was characterized based on a quantity comparable to PPF. This quantity was denoted the fine particle fraction (FPF) and measures the mass fraction of the particles leaving the pipe with a diameter smaller than 5 μm . It was concluded that the 45° pipe bend offers a better deagglomeration performance (i.e., higher FPF) than the 90° pipe bend. This finding does not coincide with the present results. The discrepancy is obviously related to the difference in the material properties (mannitol vs. silica particle agglomerates) and the size of the initial agglomerates considered. Specifically, the cohesion between the particles in the mentioned studies is higher (i.e., higher Hamaker constant) and the initial agglomerates consist of a significantly larger number of primary particles (i.e., higher inertia). Hence, different motion and breakage patterns are expected making a direct comparison difficult. As mentioned before, reproducing the same agglomerates as applied in Adi et al. (2010) and Tong et al. (2011) would have required considerable efforts to generate completely new DEM training data (i.e., thousands of new DEM simulations) and to repeat the entire training procedure for the ANNs used in the breakage model. Thus, the present results specifically describe the breakage of relatively small silica particle agglomerates.

The primary particle fraction focuses on the primary particles and does not provide insight into the size distribution of the surviving agglomerates. In order to analyze this quantity, the agglomerate size achieved at the outlet of the pipes is evaluated by means of cumulative mass-weighted distributions Q_3 . The results are shown in Fig. 9.32. Similar trends are obtained for the 90° and the 45° pipe bends as visible in Figs. 9.32(a) and 9.32(b), respectively. Namely, small agglomerates comprising $N_{\text{pp}}^{\text{tot}} = 5$ particles or less constitute about 50% of the mass population at the outlet. In general, higher Re numbers lead to smaller agglomerates which is consistent with the higher number of breakage events recorded in Table 9.16. In addition, large agglomerates consisting of more than $N_{\text{pp}}^{\text{tot}} = 100$ particles are more present in the Re_L cases as can be inferred from the development of corresponding distributions. The small upsurge at the end of the cumulative distributions implies that in all cases some initial agglomerates (i.e., $N_{\text{pp}}^{\text{tot}} = 1200$ particles) manage to arrive intact at the outlet of the pipe in all four cases.

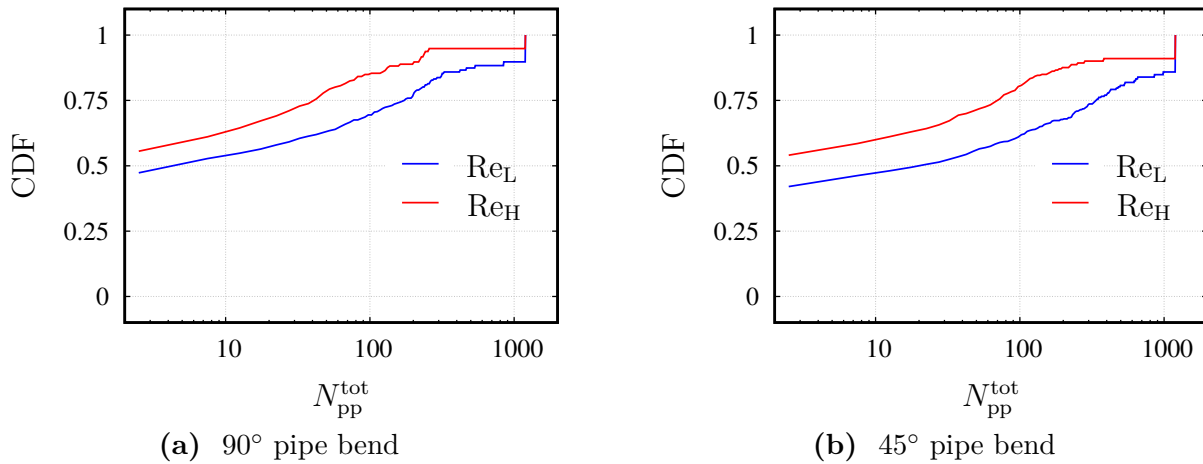


Fig. 9.32. Cumulative mass-weighted agglomerate size distribution Q_3 at the outlet of the pipe.

9.3.7 Summary and Conclusions

The scope of the study is to analyze the deagglomeration of silica agglomerates initially consisting of 1200 primary particles in four configurations defining two pipe bend geometries and two Reynolds numbers. In the adopted efficient methodology the structures of agglomerates are replaced by effective spheres, which allows to consider a large number of agglomerates in a single simulation in contrast to other detailed Euler–Lagrange approaches accounting for the full structure of agglomerates. The main outcomes are as follows:

- The flow in sharp pipe bends is mainly characterized by separation zones at the kinks of the bends and secondary flow structures known as Dean vortices. The presence of the separation regions accelerates the flow in the core of the bend. The abrupt deflection of the flow direction in the 90° bend leads to large separation regions, high velocities, and strong turbulent fluctuations. The two-step deflection of the flow in the 45° bend results in weaker flow conditions.
- In all four investigated configurations (two geometries and two Reynolds numbers) deagglomeration is mainly attributed to the wall-impact breakage followed by the breakage due to rotation. Other fluid-induced stress mechanisms such as drag and turbulence are found to be irrelevant under the considered, rather low Reynolds numbers. The same finding was reported by Tong et al. (2011) who studied the breakage of agglomerates employing the same pipe geometries and flow Reynolds numbers, albeit different particle properties. The geometry of the bend pipes also contributes to this circumstance, since breakage by wall impacts is promoted by the sharp kink before agglomerates reach the regions of high flow shear.
- In any of the two investigated bend geometries, increasing Re enhances breakage and leads to finer particle size distributions at the outlet of the pipe.

- Considering the same Re number, more breakage takes place in the 45° than in the 90° pipe bend. This is attributed to the favorable agglomeration conditions in the 45° case leading to more re-agglomerations and thus a higher breakage possibility. However, concentrating on the outlet of the pipe, a better deagglomeration performance is attained by the 90° bend. This is perceptible from the higher primary particle fractions in Table 9.16 and the finer agglomerate size distributions at the outlet of the 90° bends (see Fig. 9.32).

10 Conclusions and Outlook

Advancing the current understanding and the available methods for predicting the disintegration of particle agglomerates entrained in fluid flows is of a considerable interest for numerous applications, e.g., the widely spread medical powder inhalers. However, capturing the physics behind this phenomenon in full detail is arduous, since wide ranges of length and time scales covering several order of magnitudes are involved. For this reason, viable models delivering robust and affordable predictions are important.

In this thesis, a strategy for predicting the deagglomeration of cohesive particles in particle-laden flows applicable for the Euler–Lagrange framework has been developed and tested. Specifically, the present thesis contributes (1) a model providing improved descriptions for important structural features of agglomerates (i.e., the packing fraction and the coordination number), (2) a model for the disintegration of agglomerates by fluid-induced stresses, and (3) a model for the wall-impact breakage of agglomerates. The proposed models are especially useful for (but not limited to) efficient simulation methodologies relying on modeled fluid-particle interactions (point-particle approximation), modeled inter-particle and particle-wall collisions (hard-sphere treatment), and idealized structures of agglomerates (replacement by effective spheres).

10.1 Conclusions

The *model for the structural features of agglomerates* (see Chapter 5 and Breuer and Khalifa (2019a,b)) endows the spheres representing the agglomerates with properties (i.e., packing fraction and coordination number) characterizing the strength of the agglomerate by means of look-up tables. These tables are generated based on an analysis of artificially created agglomerates using a Monte-Carlo simulation and a scaling of the structural features of the agglomerates. Thus, the effect of the number comprising particles and the material properties on the structure are taken into account. Furthermore, owing to the fact that the model applies the convex-hull approach for computing the packing fraction, the obtained effective agglomerate diameters satisfy the recommendations by Dietzel et al. (2016) and Dietzel and Sommerfeld (2013) for an improved point-particle tracking of agglomerates represented by spheres. Hence, the proposed model provides a useful enhancement of the standard approaches applied for describing the effective sphere.

The *model for the fluid-induced breakup* (see Chapter 6 and Breuer and Khalifa (2019a,b)) follows a simple concept suggesting that if the stress acting on the agglomerate surpasses a certain threshold (strength of the agglomerate), breakup takes place. The strength of the agglomerate is computed based on the relation derived by Rumpf (1962) which relates the tensile strength to the cohesive van-der-Waals force, the diameter of

the primary particles and structural properties of the agglomerate, i.e., the coordination number and the packing fraction. Three disruptive mechanisms are considered: The turbulent, the drag and the rotary stress. Once breakup occurs, the agglomerate is replaced by a number of fragments moving away from each other in a deterministic manner.

The model builds on theories available in the literature and introduces various meaningful improvements to address important aspects of the breakage problem, which have not been satisfactorily undertaken before. Mainly, the model extends the commonly used drag stress formula (Tomi and Bagster, 1978) to predict the number of erodible particles. In addition, a new relation for determining the magnitude of the rotary stress is derived on the basis of the elasticity theory. Furthermore, descriptions for the post-breakage dynamics of the fragments are proposed taking the physics of the stress mechanism causing the breakup into account. A final important contribution is the introduction of a physically motivated time lag, which keeps the breakup time-scale independent of the simulation time-step size.

The *models for the wall-impact breakage* (see Chapter 7 and Khalifa and Breuer (2020, 2021), Khalifa et al. (2022) and Khalifa et al. (2021)) are derived based on knowledge acquired from a large number of DEM wall-impact simulations in an isolated environment taking the effect of various impact conditions (i.e., impact velocity, impact angle, number of primary particles, and size of primary particles) into account. The DEM results are thoroughly analyzed based on original parameters, which are derived to enable further modeling. Namely, the fragmentation ratio FR and the fragment size parameter ζ_i are used to represent the number of generated fragments and the fragment size distribution. In addition, the post-breakage velocities of the resulting fragments are modeled based on three quantities relating the motion of each fragment to the incident impact velocity of the original agglomerates. These quantities are the reflection angle α , the spreading angle β , and the velocity ratio v_{ratio} . Since a single breakage event results in a range of these fragment-specific quantities, a statistical description based on two-parameter Weibull PDFs is employed to describe α , β , and v_{ratio} . Consequently, the collective motion of the population resulting from a breakage event can be reproduced based on three sets of Weibull PDF parameters.

The concept behind the wall breakage model is to relate the parameters expressing the breakage outcomes, i.e., FR and ζ_i and the Weibull PDF parameters k and λ of α , β , and v_{ratio} to the impact conditions of the original agglomerate. For this purpose, two approaches are applied. The *first* relies on conventional regression techniques. Since multiple impact conditions are investigated, a unique dimensionless number π_{imp} is derived to reduce the number of attributes of the problem, which allows to express the fragmentation ratio FR and the fragment size parameters ζ_i as functions of a single variable, i.e., π_{imp} . In addition, it is found that the Weibull PDF parameters k , λ are strongly depending on the impact angle of the original agglomerates. This finding motivated expressing k and λ solely as 4th order polynomial functions of the impact angle while neglecting the effect of the other investigated conditions.

Based on additional DEM simulations for the shear impact case, which was not considered in the initial DEM investigations, it was found that the regression approach used to predict the normal and oblique impact cases is not best suited for the shear impact case. This conclusion motivated the introduction of the *second approach* based on artificial neural networks (ANNs). Two feed-forward ANNs are developed. The first approximates the relations between the impact conditions and FR and ζ_i , replacing the relations based on the dimensionless number π_{imp} . Similarly, the second ANN replaces the 4th order polynomials used to approximate the relation between the impact conditions and the Weibull PDF parameters k and λ of α , β , and v_{ratio} . Overall, it is concluded that the ANN approach leads to a better regression accuracy for all impact angles and agglomerate sizes.

The newly proposed models have been successfully incorporated into the in-house Euler–Lagrange CFD code based on LES, *LESOCC* (Breuer, 1998a,b, 2000, 2002). Prior to this work, the code *LESOCC* offered an advanced and efficient possibility for tracking a huge number of particles, droplets, and bubbles while taking a wide range of important physical phenomena into account. These include deterministically detected inter-particle collisions and wall impacts, particle agglomeration and wall deposition, and the effect of the LES subgrid-scale structures on the particles based on a Langevin-type SGS model.

The performance of the breakage models has been evaluated by applying the entire Euler–Lagrange methodology to study the deagglomeration of particles in various setups organized in three test cases. The first test case (see Section 9.1 and Breuer and Khalifa (2019a,b)) focuses on the fluid-induced breakup in a generic lab-scale powder disperser consisting of a main duct inter-crossed by a funnel (Weiler, 2008). Two flow Reynolds numbers and three powders distinguished by the size of the primary particles are investigated. The breakup models have been found reliable in reproducing the experimentally observed trends. Furthermore, for each combination of a powder and a Re number an important insight has been gained regarding the most critical regions for breakup and the most important breakup mechanism. Namely, it is concluded that the drag stress mechanism is the most effective one followed by the rotary stress, whereas the contribution of the turbulent stresses is negligible. Finally, the relative importance of agglomeration in the different cases has been elucidated.

In the second test case (see Section 9.2 and Khalifa and Breuer (2021) and Khalifa et al. (2022)), duct flow simulations are carried out taking in total five different Reynolds numbers and the same three powders into account. The main conclusion is that the frequency of the wall-impact breakage is governed by a complex interplay between the intensity of the wall impacts, the cohesion between particles, and the rate at which agglomerates are transported towards the walls. The latter is attributed to the responsiveness of the agglomerates to different flow phenomena known for duct flows such as the Dean vortices, turbophoresis, and the shear-induced lift force. Furthermore, under the investigated fluid and particle conditions it is deduced that breakage predominately occurs due to wall-impact and rotation-induced breakup comes in the second place. The drag and the turbulent stress mechanisms are insignificant. Furthermore, the regression wall-impact breakage model and the ANN counterpart achieved overall similar predictions despite

recognizable discrepancies for breakage events associated with flat impact angles. These deviations are comprehensible, since the ANN-based model is trained on a broader DEM database in which the shear impact case is accounted for.

The third test case (see Section 9.3 and Khalifa et al. (2021)) is inspired by the experimental work by Adi et al. (2010) and the numerical work by Tong et al. (2011) on the effect of the bend design on the deagglomeration performance of dry powder inhalers. Two bend geometries describing a single bend with 90° deflection and a double bend each with 45° deflection are investigated. In addition, two Reynolds numbers and a single powder are accounted for. The results demonstrated that the new modeling strategy can be beneficial in the decision-making processes regarding the development of technical applications such as dry powder inhalers. Specifically, the deagglomeration performance of each bend design was quantitatively characterized. In addition, important details on the most relevant breakage mechanisms, critical region for breakage, and the role of other related phenomena such as agglomeration have been analyzed.

Overall, the research carried out in the present thesis makes original useful contributions to the state-of-the-art cost-efficient modeling methods of particle-laden flows. The proposed models enable deterministic event-based predictions of the particle-size reduction due to deagglomeration in dense flow systems, while applying high-fidelity wall-resolved LES at manageable computational costs. The results of the simulations proved that the extended Euler–Lagrange methodology works well. Hence, despite the potential for improvement (see Section 10.2), serious advancements have been achieved.

10.2 Future Work

The knowledge and experience gained in the course of the present thesis gave rise to ideas which are worth exploring in the future. Therefore, building on the present work, further research is recommended. Firstly, while preserving the general concept behind the *model for the structural features of agglomerates* an alternative approach can be followed. In the present model the packing fraction and the coordination number of the agglomerates extracted from the Monte-Carlo packing are rescaled to account for the effect of the physical forces using DEM relations found in the literature (Yang et al., 2008). Since these scaling relationships were developed for agglomerates comprising 10^4 particles, their application to adjust the structural features of smaller agglomerates is associated with some error. Thus, an approach combining DEM and artificial neural networks is suggested. Large packings of particles can be generated in DEM accounting directly for the relevant physical forces (i.e., compression and cohesion). Each packing includes particles of unique material properties and particle diameter (monodisperse case). The agglomerates collected from these packings can be analyzed concerning their structural properties. The results may lead to a database, which can be used for training a neural network relating the structural features to the material properties and the number of particles. On a wider level, the practically more relevant case of polydisperse agglomerates

should also be investigated in the future.

The main limitation in the *model for the fluid-induced breakup* is that it expresses the fluid stresses assuming agglomerates as perfect, homogeneous spheres. In other words, the effect of the heterogeneous inter-particle network of contacts is not properly accounted for in the relationships used for computing the stresses (i.e., turbulent, drag, and rotary stresses). Therefore, it is suggested to calibrate these theory-based relationships based on detailed, fully-resolved simulations of single agglomerates.

Despite the huge number ($\mathcal{O}(10^4)$) of DEM simulations involved in the development of the present *model for the wall-impact breakage*, additional simulations (i.e., training data) would further widen the application area of the model. Specifically, it would be useful to extend the DEM cases towards: (1) agglomerates of larger number of primary particles, (2) agglomerates of distinctly different material properties, especially the cohesion-related parameters. Obviously, tackling polydisperse agglomerates would be a further advancement. However, it necessitates the introduction of new parameters specific for the polydisperse case leading to a new model formulation.

Moreover, the present work does not address the *breakage induced by collisions between agglomerates and other particles or agglomerates*. This is an important breakage mechanism which should be included by an appropriate model in the future. Definitely, the approach relying on ANNs trained by DEM results has a great potential. In addition, the knowledge achieved by the wall-impact breakage model provides a valuable foundation. However, the problem of the collision-induced breakage seems more challenging, since the effect of the size ratio of the two colliding entities needs to be additionally considered.

Lastly, the models introduced in this thesis must be further tested and validated against more detailed experimental data. In fact, experimental investigations focusing on the breakage in wall-bounded flows are scarce. The main challenge is that on the one hand it is indispensable to know all details of the experimental setup. That includes boundary and initial conditions, geometrical details and properties of the materials used. On the other hand, the experiments should provide as much as possible data which can be used for a detailed comparison. The experimental studies considered in the present work provide, to a large extent, sufficient details about the operating conditions. However, solely integral quantities (i.e., the dispersion ratio and the fine particle fraction) at the outlets of the setups (i.e., funnel-duct and pipe bends) are reported. Such quantities help to evaluate the overall simulation method but are too global to be used for validating the details of the deagglomeration models. Therefore, comprehensive experimental investigations on the breakup of dispersed agglomerates would be of great relevance in the future.

A Quantities Used in the Contact Models

For collision partners (particle-particle or particle-wall), the effective modulus of elasticity \hat{E} , the effective radius \hat{R} , the effective mass \hat{m} and the effective shear modulus \hat{G} are given by:

$$\frac{1}{\hat{E}} = \frac{1 - \nu_1^2}{E_1} + \frac{1 - \nu_2^2}{E_2}, \quad (\text{A.1})$$

$$\frac{1}{\hat{R}} = \frac{1}{R_1} + \frac{1}{R_2}, \quad (\text{A.2})$$

$$\frac{1}{\hat{m}} = \frac{1}{m_1} + \frac{1}{m_2}, \quad (\text{A.3})$$

$$\frac{1}{\hat{G}} = \frac{2(2 - \nu_1)(1 + \nu_1)}{G_1} + \frac{2(2 - \nu_2)(1 + \nu_2)}{G_2}. \quad (\text{A.4})$$

In the case of a particle-wall contact, $R_2 \gg R_1$ and $m_2 \gg m_1$ so that the effective radius and mass are approximated by $\hat{R} = R_1$ and $\hat{m} = m_1$.

The relationship between the Hamaker H constant in vacuum and the surface energy γ_s reads (Israelachvili, 2011):

$$H = \gamma_s 24 \pi \delta_0^2. \quad (\text{A.5})$$

B Verification of the Reflection and Spreading Model

Particle-laden flow simulations are carried out with $5 \cdot 10^4$ agglomerates each consisting of 100 primary particles. The setup corresponds to the duct flow case with the smallest Reynolds number $Re = 8698$ (see Section 9.2). All agglomerates are injected into the domain at a distance of $5 d_{pp}$ from the wall. The initial velocity vectors of the agglomerates are set in a manner to achieve an impact leading to a full fragmentation at an angle of $\Theta_{imp} = 45^\circ$. The results depicted in Fig. B.1 show that the derived model successfully reproduces the PDFs obtained in DEM.

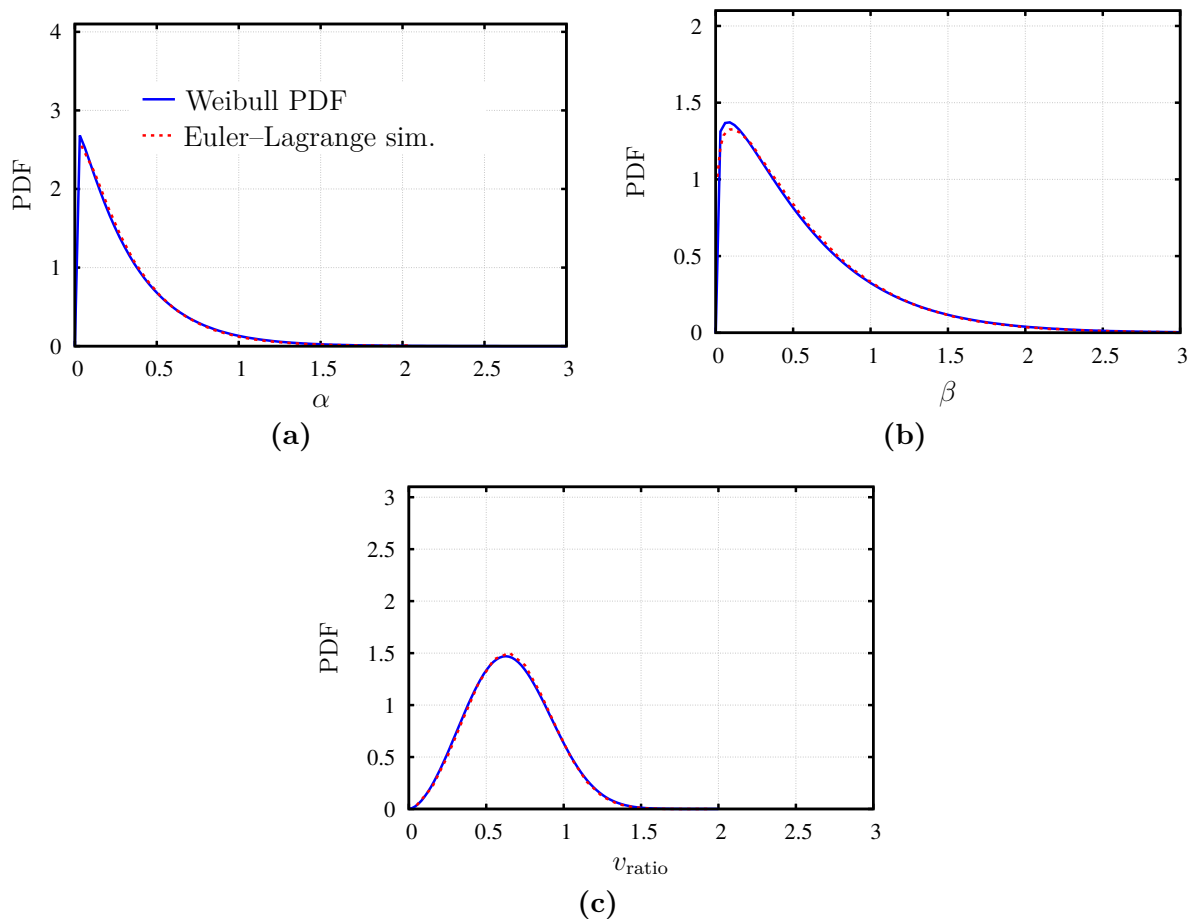


Fig. B.1. Verification of the model. The number of analyzed fragments in the Euler-Lagrange simulations is $5 \cdot 10^4 \times 100 = 5 \cdot 10^6$.

Bibliography

- Adi, S., H. Adi, H.-K. Chan, Z. Tong, R. Yang and A. Yu (2013). Effects of mechanical impaction on aerosol performance of particles with different surface roughness. *Powder Technology* 236. Special Issue: Pharmaceutical Powders, 164–170.
- Adi, S., Z. Tong, H.-K. Chan, R. Yang and A. Yu (2010). Impact angles as an alternative way to improve aerosolisation of powders for inhalation? *European Journal of Pharmaceutical Sciences* 41 (2), 320–327.
- Adler, P. M. and P. M. Mills (1979). Motion and rupture of a porous sphere in a linear flow field. *J. Rheology* 23 (1), 25–37.
- Ai, J., J.-F. Chen, J. M. Rotter and J. Y. Ooi (2011). Assessment of rolling resistance models in discrete element simulations. *Powder Technology* 206 (3), 269–282.
- Akiki, G. and S. Balachandar (2020). Shear-induced lift force on spheres in a viscous linear shear flow at finite volume fractions. *Phys. Fluids* 32 (11), 113306.
- Akiki, G., T. Jackson and S. Balachandar (2017a). Pairwise interaction extended point-particle model for a random array of monodisperse spheres. *J. Fluid Mech.* 813, 882–928.
- Akiki, G., W. Moore and S. Balachandar (2017b). Pairwise-interaction extended point-particle model for particle-laden flows. *J. Comp. Phys.* 351, 329–357.
- Alletto, M. (2014). Numerical investigation of the influence of particle-particle and particle-wall collisions in turbulent wall-bounded flows at high mass loadings. PhD thesis. Department of Fluid Mechanics, Helmut-Schmidt-University, Hamburg, Germany.
- Almohammed, N. (2018). Modeling and simulation of particle agglomeration, droplet coalescence and particle-wall adhesion in turbulent multiphase flows. PhD thesis. Department of Fluid Mechanics, Helmut-Schmidt-University, Hamburg, Germany.
- Almohammed, N. and M. Breuer (2016a). Modeling and simulation of agglomeration in turbulent particle-laden flows: A comparison between energy-based and momentum-based agglomeration models. *Powder Technology* 294, 373–402.
- Almohammed, N. and M. Breuer (2016b). Modeling and simulation of particle-wall adhesion of aerosol particles in particle-laden turbulent flows. *Int. J. Multiphase Flow* 85, 142–156.
- Ammar, Y., A. Dehbi and M. W. Reeks (2012). Break-up of aerosol agglomerates in highly turbulent gas flow. *Flow Turbulence Combustion* 89 (3), 465–489.

- Andersson, R. and B. Andersson (2006). On the breakup of fluid particles in turbulent flows. *AIChE J.* 52 (6), 2020–2030.
- Antia, H. (2002). *Numerical Methods for Scientists and Engineers*. Vol. 2. Birkhauser Verlag, Basel, Switzerland.
- Ariane, M., M. Sommerfeld and A. Alexiadis (2018). Wall collision and drug-carrier detachment in dry powder inhalers: Using DEM to devise a sub-scale model for CFD calculations. *Powder Technology* 334, 65–75.
- Arun, G., S. Kumaresh Babu, S. Natarajan and N. Kulasekharan (2020). Study of flow behaviour in sharp and mitred pipe bends. *Materials Today: Proceedings* 27, 2101–2108.
- Azomaterials.com (2018). *Silica – Silicon Dioxide (SiO₂)*. URL: <https://www.azom.com/properties.aspx?ArticleID=1114>. Accessed: Aug. 10, 2021.
- Bäbler, M. U., L. Biferale, L. Brandt, U. Feudel, K. Guseva, A. S. Lanotte, C. Marchioli, F. Picano, G. Sardina, A. Soldati and F. Toschi (2015). Numerical simulations of aggregate breakup in bounded and unbounded turbulent flows. *J. Fluid Mech.* 766, 104–128.
- Bäbler, M. U., L. Biferale and A. S. Lanotte (2012). Breakup of small aggregates driven by turbulent hydrodynamic stress. *Physical Review E* 85 (2), 025301.
- Bäbler, M. U., M. Morbidelli and J. Baldyga (2008). Modelling the breakup of solid in turbulent flows. *J. Fluid Mech.* 612, 261–289.
- Bagchi, P. and S. Balachandar (2002). Shear versus vortex-induced lift force on a rigid sphere at moderate Re. *J. Fluid Mech.* 473, 379–388.
- Bagster, D. F. and D. T. Tomi (1974). The stresses within a sphere in simple flow fields. *Chem. Eng. Sci.* 29 (8), 1773–1783.
- Balachandar, S. (2009). A scaling analysis for point-particle approaches to turbulent multiphase flows. *Int. J. Multiphase Flow* 35 (9), 801–810.
- Balachandar, S. and J. K. Eaton (2010). Turbulent dispersed multiphase flow. *Annu. Rev. Fluid Mech.* 42, 111–133.
- Balachandar, S., K. Liu and M. Lakhote (2019). Self-induced velocity correction for improved drag estimation in Euler-Lagrange point-particle simulations. *J. Comput. Phys.* 376, 160–185.
- Balachandar, S., W. Moore, G. Akiki and K. Liu (2020). Towards particle-resolved accuracy in Euler-Lagrange simulations of multiphase flow using machine learning and pairwise interaction extended point-particle (PIEP) approximation. *Theor. Comput. Fluid Dyn.* 34, 401–428.
- Bardina, J., J. H. Ferziger and W. C. Reynolds (1980). Improved subgrid-scale models for large-eddy simulations. *AIAA Paper*, 80-1357.

- Basset, A. B. (1888). III. On the motion of a sphere in a viscous liquid. *Philosophical Transactions of the Royal Society of London.(A.)* 179, 43–63.
- Beck, A., D. Flad and C.-D. Munz (2019). Deep neural networks for data-driven LES closure models. *J. Comput. Phys.* 398, 108910.
- Becker, V., E. Schlauch, M. Behr and H. Briesen (2009). Restructuring of colloidal aggregates in shear flows and limitations of the free-draining approximation. *J. Colloid and Interface Science* 339 (2), 362–372.
- Beetstra, R., M. A. van der Hoef and J. Kuipers (2007). Drag force of intermediate Reynolds number flow past mono- and bidisperse arrays of spheres. *AIChE J.* 53 (2), 489–501.
- Benocci, C. and A. Pinelli (1990). The role of the forcing term in the large-eddy simulation of equilibrium channel flow. In: *Engineering Turbulence Modelling and Experiments*. Ed. by W. Rodi and E. N. Ganić. Vol. 1. Elsevier Science Pub. Co. New York, 287–296.
- Binninger, B. (1989). Untersuchung von Modellströmungen in Zylindern von Kolbenmotoren. PhD thesis. Aerodynamisches Institut, RWTH Aachen, Aachen, Germany.
- Bird, G. A. (1976). *Molecular Gas Dynamics*. Clarendon Press: Oxford, UK.
- Bluestein, A. M., R. Venters, D. Bohl, B. T. Helenbrook and G. Ahmadi (2019). Turbulent flow through a ducted elbow and plugged tee geometry: An experimental and numerical study. *J. Fluids Engineering* 141 (8), 081101.
- Bogner, S., S. Mohanty and U. Råde (2015). Drag correlation for dilute and moderately dense fluid–particle systems using the lattice Boltzmann method. *Int. J. Multiphase Flow* 68, 71–79.
- Boussinesq, J. (1885). Sur la resistance qu’oppose un fluide indefini en repos, sans pesanteur, au mouvement varie d’une sphere solide qu’il mouille sur toute sa surface, quand les vitesses restent bien continues et assez faibles pour que leurs carres et produits soient negligiables. *CR Acad. Sc. Paris* 100, 935–937.
- Bradshaw, P. (1987). Turbulent secondary flows. *Annual Review of Fluid Mechanics* 19 (1), 53–74.
- Brennen, C. E. (1982). *A Review of Added Mass and Fluid Inertial Forces*. Tech. rep. Naval Civil Engineering Laboratory, Port Hueneme, CA, USA.
- Breuer, M. (1998a). Large–eddy simulation of the sub–critical flow past a circular cylinder: Numerical and modeling aspects. *Int. J. Numer. Meth. Fluids* 28 (9), 1281–1302.
- Breuer, M. (1998b). Numerical and modeling influences on large–eddy simulations for the flow past a circular cylinder. *Int. J. Heat Fluid Flow* 19 (5), 512–521.
- Breuer, M. (2000). A challenging test case for large–eddy simulation: High Reynolds number circular cylinder flow. *Int. J. Heat Fluid Flow* 21 (5), 648–654.

- Breuer, M. (2002). *Direkte Numerische Simulation und Large-Eddy Simulation turbulenter Strömungen auf Hochleistungsrechnern*. Habilitationsschrift, Universität Erlangen–Nürnberg, Berichte aus der Strömungstechnik. Shaker Verlag, Aachen.
- Breuer, M. and M. Alletto (2012). Efficient simulation of particle-laden turbulent flows with high mass loadings using LES. *Int. J. Heat Fluid Flow* 35, 2–12.
- Breuer, M. and N. Almohammed (2015). Modeling and simulation of particle agglomeration in turbulent flows using a hard-sphere model with deterministic collision detection and enhanced structure models. *Int. J. Multiphase Flow* 73, 171–206.
- Breuer, M., H. T. Baytekin and E. A. Matida (2006). Prediction of aerosol deposition in 90 degrees bends using LES and an efficient Lagrangian tracking method. *J. Aerosol Science* 37 (11), 1407–1428.
- Breuer, M. and F. Hoppe (2017). Influence of a cost-efficient Langevin subgrid-scale model on the dispersed phase of a large-eddy simulation of turbulent bubble-laden and particle-laden flows. *Int. J. Multiphase Flow* 89, 23–44.
- Breuer, M. and A. Khalifa (2019a). Revisiting and improving models for the breakup of compact dry powder agglomerates in turbulent flows within Eulerian–Lagrangian simulations. *Powder Technology* 348, 105–125.
- Breuer, M. and A. Khalifa (2019b). Refinement of breakup models for compact powder agglomerates exposed to turbulent flows considering relevant time scales. *Computers & Fluids* 194, 104315.
- Brooke, J. W., T. Hanratty and J. McLaughlin (1994). Free-flight mixing and deposition of aerosols. *Phys. Fluids* 6 (10), 3404–3415.
- Burton, T. M. and J. K. Eaton (2005). Fully resolved simulations of particle-turbulence interaction. *J. Fluid Mech.* 545, 67–111.
- Calvert, G., A. Hassanpour and M. Ghadiri (2011). Mechanistic analysis and computer simulation of the aerodynamic dispersion of loose aggregates. *Chemical Engineering Research and Design* 89 (5), 519–525.
- Capecelatro, J. (2021). Modeling high-speed gas-particle flows relevant to spacecraft landings: A review and perspectives. *arXiv preprint arXiv:2109.02523*.
- Capecelatro, J. S. (2014). A mesoscopic formalism for simulating particle-laden flows with applications in energy conversion processes. PhD thesis. Cornell University, New York, USA.
- Capecelatro, J. and O. Desjardins (2013). An Euler–Lagrange strategy for simulating particle-laden flows. *J. Comput. Phys.* 238, 1–31.
- Chen, M., K. Kontomaris and J. B. McLaughlin (1998). Direct numerical simulation of droplet collisions in a turbulent channel flow. Part I: Collision algorithm. *Int. J. Multiphase Flow* 24, 1079–1103.

- Chen, S. and S. Li (2020). Collision-induced breakage of agglomerates in homogeneous isotropic turbulence laden with adhesive particles. *J. Fluid Mech.* 902.
- Chree, C. (1895). The equilibrium of an isotropic elastic solid ellipsoid under the action of normal surface forces of the second degree, and bodily forces derived from a potential of the second degree. *Quarterly J. Pure and Applied Mathematics* 27, 338–353.
- Chun, J. and D. Koch (2005). Coagulation of monodisperse aerosol particles by isotropic turbulence. *Phys. Fluids* 17 (2), 027102.
- Cleary, P. W., G. Metcalfe and K. Liffman (1998). How well do discrete element granular flow models capture the essentials of mixing processes? *Applied Mathematical Modelling* 22 (12), 995–1008.
- Clifford, H. M., N. E. Spaulding, A. V. Kurbatov, A. More, E. V. Korotkikh, S. B. Sneed, M. Handley, K. A. Maasch, C. P. Loveluck, J. Chaplin et al. (2019). A 2000 year Saharan dust event proxy record from an ice core in the European Alps. *J. Geophysical Research: Atmospheres* 124 (23), 12882–12900.
- Crowe, C. T., M. P. Sharma and D. E. Stock (1977). The Particle-Source-In-Cell (PSI-CELL) model for gas-droplet flows. *Trans. ASME J. Fluids Eng.* 99, 325–332.
- Crowe, C. T., M. Sommerfeld and Y. Tsuji (1998). *Multiphase Flows with Droplets and Particles*. CRC Press.
- Crowe, C. T. (2005). *Multiphase Flow Handbook*. CRC Press.
- Crowe, C., J. Chung and T. Troutt (1988). Particle mixing in free shear flows. *Progress in Energy and Combustion Science* 14 (3), 171–194.
- Cui, Y. and M. Sommerfeld (2018). Application of lattice-Boltzmann method for analysing detachment of micron-sized particles from carrier particles in turbulent flows. *Flow Turbulence Combustion* 100 (1), 271–297.
- Cundall, P. A. and O. D. L. Strack (1979). A discrete numerical model for granular assemblies. *Geotechnique* 29, 47–65.
- Cundall, P. and O. Strack (1983). Modeling of microscopic mechanisms in granular material. In: *Studies in Applied Mechanics*. Vol. 7. Elsevier, 137–149.
- Dadkhah, M., M. Peglow and E. Tsotsas (2012). Characterization of the internal morphology of agglomerates produced in a spray fluidized bed by X-ray tomography. *Powder Technology* 228, 349–358.
- Darquenne, C. (2012). Aerosol deposition in health and disease. *J. Aerosol Medicine and Pulmonary Drug Delivery* 25 (3), 140–147.
- Davies, C., M. Aylward, D. Leacey et al. (1951). Impingement of dust from air jets. *Arch. Indust. Hyg. & Occupational Med.* 4 (4), 354–97.

- De Bona, J., A. S. Lanotte and M. Vanni (2014). Internal stresses and breakup of rigid isostatic aggregates in homogeneous and isotropic turbulence. *J. Fluid Mech.* 755, 365–396.
- De Motta, J. B., P. Costa, J. J. Derksen, C. Peng, L.-P. Wang, W.-P. Breugem, J.-L. Estivalezes, S. Vincent, E. Climent, P. Fede, P. Barbaresco and N. Renon (2019). Assessment of numerical methods for fully resolved simulations of particle-laden turbulent flows. *Computers & Fluids* 179, 1–14.
- Dean, W. (1927). XVI. Note on the motion of fluid in a curved pipe. *The London, Edinburgh, and Dublin Philosophical Magazine and Journal of Science* 4 (20), 208–223.
- Deng, X., Z. Huang, W. Wang and R. N. Davé (2016). Investigation of nanoparticle agglomerates properties using Monte Carlo simulations. *Advanced Powder Technology* 27 (5), 1971–1979.
- Dennis, S. C. R., S. N. Singh and D. B. Ingham (1980). The steady flow due to a rotating sphere at low and moderate Reynolds numbers. *J. Fluid Mech.* 101 (2), 257–279.
- Derjaguin, B. V., V. M. Muller and Y. P. Toporov (1975). Effect of contact deformations on the adhesion of particles. *J. Colloid and Interface Science* 53 (2), 314–326.
- Derksen, J. J. and D. Eskin (2010). Potential of microchannel flow for agglomerate breakage. *Industrial & Engineering Chemistry Research* 49 (21), 10633–10640.
- Devroye, L. (1986). *Non-Uniform Random Variate Generation*. Springer-Verlag. New York, USA.
- Di Felice, R. (1994). The voidage function for fluid-particle interaction systems. *Int. J. Multiphase Flow* 20 (1), 153–159.
- Di Renzo, A. and F. P. Di Maio (2005). An improved integral non-linear model for the contact of particles in distinct element simulations. *Chem. Eng. Sci.* 60 (5), 1303–1312.
- Dietzel, M., M. Ernst and M. Sommerfeld (2016). Application of the lattice-Boltzmann method for particle-laden flows: Point-particles and fully resolved particles. *Flow Turbulence Combustion* 97 (2), 539–570.
- Dietzel, M. and M. Sommerfeld (2013). Numerical calculation of flow resistance for agglomerates with different morphology by the lattice-Boltzmann method. *Powder Technology* 250, 122–137.
- Dizaji, F. F., J. S. Marshall and J. R. Grant (2019). Collision and breakup of fractal particle agglomerates in a shear flow. *J. Fluid Mech.* 862, 592–623.
- Dong, K. J., R. Y. Yang, R. P. Zou and A. B. Yu (2012). Settling of particles in liquids: Effects of material properties. *AIChE J.* 58 (5), 1409–1421.
- Dong, K., R. Yang, R. Zou and A. Yu (2006). Role of interparticle forces in the formation of random loose packing. *Phys. Rev. Letters* 96 (14), 145505.

- Duraisamy, K., G. Iaccarino and H. Xiao (2019). Turbulence modeling in the age of data. *Annu. Rev. Fluid Mech.* 51, 357–377.
- Durlofsky, L., J. F. Brady and G. Bossis (1987). Dynamic simulation of hydrodynamically interacting particles. *J. Fluid Mech.* 180, 21–49.
- Durst, F., J. Jovanović and J. Sender (1995). LDA measurements in the near-wall region of a turbulent pipe flow. *J. Fluid Mechanics* 295, 305–335.
- Eggersdorfer, M. L., D. Kadau, H. J. Herrmann and S. E. Pratsinis (2010). Fragmentation and restructuring of soft-agglomerates under shear. *J. Colloid and Interface Science* 342 (2), 261–268.
- Elghobashi, S. (1991). Particle-laden turbulent flows: Direct numerical simulation and closure models. *Applied Scientific Research* 48, 301–304.
- Elghobashi, S. (1994). On predicting particle-laden turbulent flows. *Applied Scientific Research* 52 (4), 309–329.
- Elghobashi, S. and T. Abou-Arab (1983). A two-equation turbulence model for two-phase flows. *Phys. Fluids* 26 (4), 931–938.
- Ernst, M., M. Dietzel and M. Sommerfeld (2013). A lattice Boltzmann method for simulating transport and agglomeration of resolved particles. *Acta Mech.* 224, 2425–2449.
- Esmaily, M., L. Villafane, A. Banko, G. Iaccarino, J. Eaton and A. Mani (2020). A benchmark for particle-laden turbulent duct flow: A joint computational and experimental study. *Int. J. Multiphase Flow* 132, 103410.
- Evrard, F., F. Denner and B. van Wachem (2020). Euler-Lagrange modelling of dilute particle-laden flows with arbitrary particle-size to mesh-spacing ratio. *J. of Computational Physics: X* 8, 100078.
- Fanelli, M., D. L. Feke and I. Manas-Zloczower (2006a). Prediction of the dispersion of particle clusters in the nano-scale—Part I: Steady shearing responses. *Chem. Eng. Sci.* 61 (2), 473–488.
- Fanelli, M., D. L. Feke and I. Manas-Zloczower (2006b). Prediction of the dispersion of particle clusters in the nano-scale—Part II, unsteady shearing responses. *Chem. Eng. Sci.* 61 (15), 4944–4956.
- Fayed, M. and L. Otten (2013). *Handbook of Powder Science & Technology*. Springer Science & Business Media.
- Fellay, L. S. and M. Vanni (2012). The effect of flow configuration on hydrodynamic stresses and dispersion of low density rigid aggregates. *J. Colloid and Interface Science* 388 (1), 47–55.
- Ferziger, J. H. and M. Perić (2002). *Computational Methods for Fluid Mechanics*. 3rd ed. Springer-Verlag, Berlin, Germany.

- Finney, J. L. (1970). Random packings and the structure of simple liquids. I. The geometry of random close packing. *Proc. R. Soc. Lond. A* 319 (1539), 479–493.
- Foerster, S. F., M. Y. Louge, H. Chang and K. Allia (1994). Measurements of the collision properties of small spheres. *Phys. Fluids* 6 (3), 1108–1115.
- Friedlander, S. K. (1977). *Smoke, Dust and Haze: Fundamentals of Aerosol Behavior*. Wiley, New York.
- Froeschke, S., S. Kohler, A. P. Weber and G. Kasper (2003). Impact fragmentation of nanoparticle agglomerates. *J. Aerosol Science* 34 (3), 275–287.
- Frungieri, G., G. Boccoardo, A. Buffo, D. Marchisio, H. A. Karimi-Varzaneh and M. Vanni (2020). A CFD-DEM approach to study the breakup of fractal agglomerates in an internal mixer. *The Canadian Journal of Chemical Engineering* 98 (9), 1880–1892.
- Frungieri, G. and M. Vanni (2021). Aggregation and breakup of colloidal particle aggregates in shear flow: A combined Monte Carlo-Stokesian dynamics approach. *Powder Technology* 388, 357–370.
- Gavrillakis, S. (1992). Numerical simulation of low-Reynolds number turbulent flow through a straight square duct. *J. Fluid Mech.* 244, 101–129.
- German, R. M. (1989). *Particle Packing Characteristics*. Metal Powder Industries Federation, Princeton, New Jersey.
- Germano, M., U. Piomelli, P. Moin and W. H. Cabot (1991). A dynamic subgrid-scale eddy viscosity model. *Phys. Fluids A* 3, 1760–1765.
- Ghadiri, M., R. Moreno-Atanasio, A. Hassanpour and S. J. Antony (2007). Analysis of agglomerate breakage. *Handbook of Powder Technology* 12, 837–872.
- Gray, W. A. (1968). *Packing of Solid Particles*. Chapman and Hall, London.
- Gregory, J. (1989). Fundamentals of flocculation. *Critical Reviews in Environmental Control* 19 (3), 185–230.
- Gröger, T., U. Tüzün and D. M. Heyes (2003). Modelling and measuring of cohesion in wet granular materials. *Powder Technology* 133 (1-3), 203–215.
- Hagan, M. T., H. B. Demuth, M. H. Beale and O. De Jesús (2014). *Neural Network Design*. Martin Hagan, Oklahoma State University, USA.
- Hamaker, H. C. (1937). The London–van der Waals attraction between spherical particles. *Physica* 4 (10), 1058–1072.
- Harada, S., R. Tanaka, H. Nogami and M. Sawada (2006). Dependence of fragmentation behavior of colloidal aggregates on their fractal structure. *J. Colloid and Interface Science* 301 (1), 123–129.
- Harshe, Y. M., L. Ehrl and M. Lattuada (2010). Hydrodynamic properties of rigid fractal aggregates of arbitrary morphology. *J. Colloid and Interface Science* 352 (1), 87–98.

- Hertz, H. (1882). Über die Berührung fester elastischer Körper. *J. für die reine und angewandte Mathematik* 92, 156–171.
- Higashitani, K., K. Iimura and H. Sanda (2001). Simulation of deformation and breakup of large aggregates in flows of viscous fluids. *Chem. Eng. Sci.* 56 (9), 2927–2938.
- Hiller, R. (1981). Der Einfluss von Partikelstoß und Partikel–Haftung auf die Abscheidung von Partikeln in Faserfiltern. PhD thesis. Universität Fridericiana Karlsruhe, Karlsruhe, Germany.
- Ho, C. A. and M. Sommerfeld (2002). Modelling of micro–particle agglomeration in turbulent flows. *Chem. Eng. Sci.* 57, 3073–3084.
- Hölzer, A. and M. Sommerfeld (2009). Lattice Boltzmann simulations to determine drag, lift and torque acting on non–spherical particles. *Computers & Fluids* 38 (3), 572–589.
- Hoppe, F. (2020). Euler–Lagrange simulations of turbulent bubble–laden flows including coalescence and breakup. PhD thesis. Department of Fluid Mechanics, Helmut-Schmidt-University, Hamburg, Germany.
- Hoppe, F. and M. Breuer (2020). A deterministic breakup model for Euler–Lagrange simulations of turbulent microbubble-laden flows. *Int. J. Multiphase Flow* 123, 103119.
- Hufnagel, L., J. Canton, R. Örlü, O. Marin, E. Merzari and P. Schlatter (2018). The three-dimensional structure of swirl-switching in bent pipe flow. *J. Fluid Mechanics* 835, 86–101.
- Israelachvili, J. N. (2011). *Intermolecular and Surface Forces*. Third. Academic Press.
- Jain, R., S. Tschisgale and J. Fröhlich (2021). Impact of shape: DNS of sediment transport with non–spherical particles. *J. Fluid Mech.* 916, A38.
- Jebakumar, A. S., K. N. Premnath, V. Magi and J. Abraham (2019). Fully–resolved direct numerical simulations of particle motion in a turbulent channel flow with the lattice–Boltzmann method. *Computers & Fluids* 179, 238–247.
- John, W. and V. Sethi (1993). Breakup of latex doublets by impaction. *Aerosol Science and Technology* 19 (1), 57–68.
- Jürgens, D. (2012). Modellierung und Simulation der Partikelagglomeration in turbulenten, dispersen Mehrphasenströmungen. Master thesis. Professur für Strömungsmechanik, Helmut-Schmidt-Universität, Hamburg, Germany.
- Kadish, J., J. R. Barber and P. D. Washabaugh (2005). Stresses in rotating spheres grown by accretion. *Int. J. Solids and Structures* 42 (20), 5322–5334.
- Kafui, D. and C. Thornton (1993). Computer simulated impact of agglomerates. In: *Powders and Grains 93, The Proceedings of the 2nd Int. Conf. on Micromechanics of Granular Media*. Balkema, Rotterdam, 401–406.

- Kempe, T. and J. Fröhlich (2012). Collision modelling for the interface-resolved simulation of spherical particles in viscous fluids. *J. Fluid Mech.* 709, 445–489.
- Kempe, T., B. Vowinckel and J. Fröhlich (2014). On the relevance of collision modeling for interface-resolving simulations of sediment transport in open channel flow. *Int. J. Multiphase Flow* 58, 214–235.
- Kendall, K. (1988). Agglomerate strength. *Powder Metallurgy* 31 (1), 28–31.
- Khalifa, A. and M. Breuer (2020). Data-driven model for the breakage of dry monodisperse agglomerates by wall impact applicable for multiphase flow simulations. *Powder Technology* 376, 241–253.
- Khalifa, A. and M. Breuer (2021). An efficient model for the breakage of agglomerates by wall impact applied to Euler-Lagrange LES predictions. *Int. J. Multiphase Flow* 142, 103625.
- Khalifa, A., M. Breuer and J. Gollwitzer (2022). Neural-network based approach for modeling wall-impact breakage of agglomerates in particle-laden flows applied in Euler-Lagrange LES. *Int. J. Heat Fluid Flow* 94, 108897.
- Khalifa, A., J. Gollwitzer and M. Breuer (2021). LES of particle-laden flow in sharp pipe bends with data-driven predictions of agglomerate breakage by wall impacts. *Fluids* 6 (12), 424.
- Kloss, C., C. Goniva, A. Hager, S. Amberger and S. Pirker (2012). Models, algorithms and validation for opensource DEM and CFD-DEM. *Progress in Computational Fluid Dynamics, An Int. J.* 12 (2-3), 140–152.
- Kosinski, P. and A. C. Hoffmann (2009). Extension of the hard-sphere particle-wall collision model to account for particle deposition. *Physical Review E* 79 (6), 061302.
- Kosinski, P. and A. C. Hoffmann (2010). An extension of the hard-sphere particle-particle collision model to study agglomeration. *Chem. Eng. Sci.* 65 (10), 3231–3239.
- Kosinski, P. and A. C. Hoffmann (2011). Extended hard-sphere model and collisions of cohesive particles. *Phys. Rev. E* 84 (3), 031303.
- Kousaka, Y., Y. Endo, T. Horiuchi and T. Niida (1992). Dispersion of aggregate particles by acceleration in air stream. *Kagaku Kogaku Ronbunshu* 18 (2), 233–239.
- Kousaka, Y., K. Okuyama, A. Shimizo and T. Yoshida (1979). Dispersion mechanism of aggregate particles in air. *J. Chemical Engineering of Japan* 12 (2), 152–159.
- Kousaka, Y., K. Okuyama and Yoshiyuki (1980). Re-entrainment of small aggregate particles from a plane surface by air stream. *J. Chemical Engineering of Japan* 13 (2), 143–147.
- Krupp, H. (1967). Particle adhesion theory and experiment. *Adv. Colloid Interf. Sci.* 1, 111–239.

- Kuerten, J. G. M. (2016). Point-particle DNS and LES of particle-laden turbulent flow – A state-of-the-art review. *Flow Turbulence Combustion* 97 (3), 689–713.
- Kunz, M. J. (2011). Effect of large dams in the Zambezi River basin: Changes in sediment, carbon and nutrient fluxes. PhD thesis. ETH Zürich, Zürich, Switzerland.
- Kurose, R. and S. Komori (1999). Drag and lift forces on a rotating sphere in a linear shear flow. *J. Fluid Mech.* 384, 183–206.
- Kusters, K. A. (1991). The influence of turbulence on aggregation of small particles in agitated vessels. PhD thesis. Technische Universiteit Eindhoven, Eindhoven, The Netherlands.
- Lavorini, F. (2019). Easyhaler®: An overview of an inhaler device for day-to-day use in patients with asthma and chronic obstructive pulmonary disease. *Drugs in Context* 8, 212596.
- Le Bouteiller, C. and M. Naaim (2011). Aggregate breakage under dynamic loading. *Granular Matter* 13 (4), 385–393.
- Li, S., J. S. Marshall, G. Liu and Q. Yao (2011). Adhesive particulate flow: The discrete-element method and its application in energy and environmental engineering. *Progress in Energy and Combustion Science* 37 (6), 633–668.
- Li, Y., Y. Xu and C. Thornton (2005). A comparison of discrete element simulations and experiments for 'sandpiles' composed of spherical particles. *Powder Technology* 160 (3), 219–228.
- Lilly, D. K. (1992). A proposed modification of the Germano subgrid-scale closure method. *Phys. Fluids A* 4, 633–635.
- Lilly, D. K. (1967). The representation of small-scale turbulence in numerical simulation experiments. *IBM Form*, 195–210.
- Liu, G., S. Li and Q. Yao (2010). On the applicability of different adhesion models in adhesive particulate flows. *Frontiers of Energy and Power Engineering in China* 4 (2), 280–286.
- Longest, P. W., Y.-J. Son, L. Holbrook and M. Hindle (2013). Aerodynamic factors responsible for the deaggregation of carrier-free drug powders to form micrometer and submicrometer aerosols. *Pharmaceutical Research* 30 (6), 1608–1627.
- Lu, S., Y. Ding and J. Guo (1998). Kinetics of fine particle aggregation in turbulence. *Advances in Colloid and Interface Science* 78 (3), 197–235.
- Ma, T., T. Ziegenhein, D. Lucas, E. Krepper and J. Fröhlich (2015). Euler–Euler large eddy simulations for dispersed turbulent bubbly flows. *Int. J. Heat and Fluid Flow* 56, 51–59.
- MacKay, D. J. C. (1992). Bayesian interpolation. *Neural Computation* 4 (3), 415–447.

- MacKay, D. J. C. (2003). *Information Theory, Inference and Learning Algorithms*. Cambridge University Press, Cambridge, UK.
- Mao, L. (2011). *Formulation considerations for inhaled products*. URL: <https://japan.catalent.com/content/download/1000/12639/file/Formulation%20Considerations%20of%20Inhaled%20Products.pdf>. Accessed: Aug. 10, 2021.
- Marchioli, C., V. Armenio and A. Soldati (2007). Simple and accurate scheme for fluid velocity interpolation for Eulerian–Lagrangian computation of dispersed flow in 3D curvilinear grids. *Computers & Fluids* 36, 1187–1198.
- Marchioli, C. and A. Soldati (2015). Turbulent breakage of ductile aggregates. *Physical Review E* 91 (5), 053003.
- Marchisio, D. L., J. T. Piktorna, R. O. Fox, R. D. Vigil and A. A. Barresi (2003). Quadrature method of moments for population–balance equations. *AIChE J.* 49 (5), 1266–1276.
- Marshall, J. S. (2009). Discrete–element modeling of particulate aerosol flows. *J. Computational Physics* 228 (5), 1541–1561.
- Masi, E., O. Simonin, E. Riber, P. Sierra and L. Y. Gicquel (2014). Development of an algebraic closure–based moment method for unsteady Eulerian simulations of particle–laden turbulent flows in very dilute regime. *Int. J. Multiphase Flow* 58, 257–278.
- Maxey, M. R. and J. J. Riley (1983). Equation of motion for a small rigid sphere in a non–uniform flow. *Phys. Fluids* 26, 883–889.
- Mei, R. (1992). An approximate expression for the shear lift force on a spherical particle at finite Reynolds number. *Int. J. Multiphase Flow* 18 (1), 145–147.
- Mindlin, R. D. (1949). Compliance of elastic bodies in contact. *J. Appl. Mech., ASME* 16, 259–268.
- Mindlin, R. D. and H. Deresiewicz (1953). Elastic spheres in contact under varying oblique forces. *Transactions of ASME, Series E. J. Applied Mech.* 20, 327–344.
- Mishra, B. K. and C. Thornton (2001). Impact breakage of particle agglomerates. *Int. J. of Mineral Processing* 61 (4), 225–239.
- Montáns, F. J., F. Chinesta, R. Gómez-Bombarelli and J. N. Kutz (2019). Data-driven modeling and learning in science and engineering. *Comptes Rendus Mécanique* 347 (11), 845–855.
- Moody, L. F. (1947). An approximate formula for pipe friction factors. *Trans. ASME* 69 (12), 1005–1011.
- Moreau, M., O. Simonin and B. Bédat (2010). Development of gas–particle Euler–Euler LES approach: A–priori analysis of particle sub–grid models in homogeneous isotropic turbulence. *Flow Turbulence Combustion* 84 (2), 295.

- Moreno, R., M. Ghadiri and S. Antony (2003). Effect of the impact angle on the breakage of agglomerates: A numerical study using DEM. *Powder Technology* 130 (1-3), 132–137.
- Moreno, R. (2003). Numerical simulation of impact breakage behaviors of spherical agglomerates using distinct element method. PhD thesis. University of Surrey, Guildford, UK.
- Moreno-Atanasio, R. and M. Ghadiri (2006). Mechanistic analysis and computer simulation of impact breakage of agglomerates: Effect of surface energy. *Chem. Eng. Sci.* 61 (8), 2476–2481.
- Moreno-Atanasio, R. (2012). Energy dissipation in agglomerates during normal impact. *Powder Technology* 223, 12–18.
- Mühle, K. (1993). Floc Stability in Laminar and Turbulent Floc. In: *Coagulation and Flocculation*. Ed. by B. Dobia. Decker, New York, 355–390.
- Neeße, T., K. Mühle and A. Ivanauskas (1987). Zur physikalisch begründeten Modellierung des Flockungsprozesses Teil V: Flockenaufbruch und Flockenerosion in turbulenter Strömung. *Chem.-Ing.-Techn.* 39, 292–295.
- Nguyen, D. and B. Widrow (1990). Improving the learning speed of 2-layer neural networks by choosing initial values of the adaptive weights. In: *1990 IJCNN Int. Joint Conf. on Neural Networks, San Diego, CA, USA, 17-21 June 1990*. IEEE, 21–26.
- Niedballa, S. and K. Husemann (2000). Modeling of the dispersion force and experimental study of influence of dispersion stress. *Chemical Engineering and Technology* 23 (9), 795–801.
- Ning, Z., R. Boerefijn, M. Ghadiri and C. Thornton (1997). Distinct element simulation of impact breakage of lactose agglomerates. *Advanced Powder Technology* 8 (1), 15–37.
- Njobuenwu, D. O. and M. Fairweather (2018). Large eddy simulation of particle agglomeration with shear breakup in turbulent channel flow. *Phys. Fluids* 30 (6), 063303.
- Nolan, G. T. and P. E. Kavanagh (1992). Computer simulation of random packing of hard spheres. *Powder Technology* 72 (2), 149–155.
- Noorani, A., R. Vinuesa, L. Brandt and P. Schlatter (2016). Aspect ratio effect on particle transport in turbulent duct flows. *Phys. Fluids* 28 (11), 115103.
- Oesterlé, B. and T. Bui Dinh (1998). Experiments on the lift of a spinning sphere in a range of intermediate Reynolds numbers. *Exp. Fluids* 19, 16–22.
- O'Rourke, P. J. and A. A. Amsden (1987). The TAB method for numerical calculation of spray droplet breakup. *SAE technical paper 872089*.
- Oseen, C. W. (1927). *Neuere Methoden und Ergebnisse in der Hydrodynamik*. Leipzig: Akademische Verlagsgesellschaft mbH.

- Packomania (2013). *Packings of equal spheres in fixed-sized containers with maximum packing density*. URL: <http://www.packomania.com>. Accessed: Nov. 24, 2021.
- Parteli, E. J. R., J. Schmidt, C. Blümel, K.-E. Wirth, W. Peukert and T. Pöschel (2014). Attractive particle interaction forces and packing density of fine glass powders. *Scientific Reports* 4, 6227.
- Phares, D. J. and G. Sharma (2006). A DNS study of aerosol deposition in a turbulent square duct flow. *Aerosol Science and Technology* 40 (11), 1016–1024.
- Picano, F., W.-P. Breugem and L. Brandt (2015). Turbulent channel flow of dense suspensions of neutrally buoyant spheres. *J. Fluid Mech.* 764, 463–487.
- Piomelli, U. and J. R. Chasnov (1996). Large-eddy simulations: Theory and applications. In: *Turbulence and Transition Modeling*. Ed. by M. Hallböck, D. S. Henningson, A. V. Johansson and P. H. Alfredson. Kluwer Academic Publishers, 269–331.
- Pope, S. B. (2000). *Turbulent Flows*. Cambridge University Press, Cambridge.
- Portela, L. M. and R. V. Oliemans (2003). Eulerian–Lagrangian DNS/LES of particle–turbulence interactions in wall-bounded flows. *Int. J. Numer. Meth. Fluids* 43 (9), 1045–1065.
- Poustis, J.-F., J.-M. Senoner, D. Zuzio and P. Villedieu (2019). Regularization of the Lagrangian point force approximation for deterministic discrete particle simulations. *Int. J. Multiphase Flow* 117, 138–152.
- Pozorski, J. and S. V. Apte (2009). Filtered particle tracking in isotropic turbulence and stochastic modeling of subgrid-scale dispersion. *Int. J. Multiphase Flow* 35, 118–128.
- Prandtl, L. (1925). Über die ausgebildete Turbulenz. *Zeitschrift für Angewandte Mathematik und Mechanik (ZAMM)* 5, 136–139.
- Prandtl, L. (1927). Über die ausgebildete Turbulenz. In: *Verhandlungen des II. Internationalen Kongresses für Angewandte Mechanik*. Ed. by Füßli. Springer. Zürich, 62–75.
- Press, W. H., S. A. Teukolsky, W. T. Vetterling and B. P. Flannery (2007). *Numerical Recipes: The Art of Scientific Computing*. 3rd. Cambridge University Press. New York, NY, USA.
- Ramkrishna, D. (2000). *Population Balances: Theory and Applications to Particulate Systems in Engineering*. Elsevier.
- Rhie, C. M. and W. L. Chow (1983). A numerical study of the turbulent flow past an isolated airfoil with trailing edge separation. *AIAA J.* 21, 1525–1532.
- Robinson, S. K. (1991). Coherent motions in the turbulent boundary layer. *Annual Review of Fluid Mechanics* 23 (1), 601–639.

- Rubinow, S. I. and J. B. Keller (1961). The transverse force on a spinning sphere moving in a viscous fluid. *J. Fluid Mech.* 11, 447–459.
- Rumelhart, D. E., G. E. Hinton and R. J. Williams (1986). Learning representations by back-propagating errors. *Nature* 323, 533–536.
- Rumpf, H. (1958). Grundlagen und Methoden des Granulierens. *Chem.-Ing.-Techn.* 30 (3), 144–158.
- Rumpf, H. (1962). The strength of granules and agglomerates. *Agglomeration – Proc. of the First Int. Symp. on Agglomeration, (ed. W.A. Knepper), Interscience, New York*, 379–418.
- Rumpf, H. and J. Raasch (1962). Desagglomeration in Strömungen. In: *1. Europ. Symp. Zerkleinern 10.-13.4.1962*. Verlag Chemie, Weinheim und VDI-Verlag, Düsseldorf, 151–159.
- Saha, D. (2013). Experimental analysis of aggregate breakup in flows observed by three-dimensional particle tracking velocimetry. PhD thesis. ETH Zürich, Zürich, Switzerland.
- Saha, D., M. U. Bäbler, M. Holzner, M. Soos, B. Lüthi, A. Liberzon and W. Kinzelbach (2015). Breakup of finite-size colloidal aggregates in turbulent flow investigated by three-dimensional (3D) particle tracking velocimetry. *Langmuir* 32 (1), 55–65.
- Samimi, A., R. Moreno and M. Ghadiri (2004). Analysis of impact damage of agglomerates: Effect of impact angle. *Powder Technology* 143, 97–109.
- Sauter, J. (1926). Die Größenbestimmung der im Gemischnebel von Verbrennungskraftmaschinen vorhandenen Brennstoffteilchen. In: *Forschungsarbeiten auf dem Gebiete des Ingenieurwesens, Heft 279, 1–34*. VDI-Verlag, Berlin SW 19.
- Sawatzki, O. (1970). Das Strömungsfeld um eine rotierende Kugel. *Acta Mechanica* 9 (3), 159–214.
- Scales, L. E. (1985). *Introduction to Non-linear Optimization*. Springer-Verlag New York.
- Schäfer, F. and M. Breuer (2002). Comparison of c-space and p-space particle tracing schemes on high-performance computers: accuracy and performance. *Int. J. Numerical Methods Fluids* 39 (4), 277–299.
- Scherer, P. O. (2013). Equations of motion. In: *Computational Physics*. Springer, 207–235.
- Schiller, L. and A. Naumann (1933). A drag coefficient correlation. *VDI Zeitschrift* 77, 318–320.
- Schubert, H. (2003). *Handbuch der mechanischen Verfahrenstechnik*. Wiley-VCH Verlag GmbH & Co. KGaA, Weinheim.
- Schutte, K. C. J., L. M. Portela, A. Twerda and R. A. W. M. Henkes (2018). Formation and break-up of rigid agglomerates in turbulent channel and pipe flows. *J. Fluid Mech.* 857, 539–561.

- Schutte, K. C. J., L. M. Portela, A. Twerda and R. A. W. M. Henkes (2015). Hydrodynamic perspective on asphaltene agglomeration and deposition. *Energy & Fuels* 29 (5), 2754–2767.
- Scott, G. D. (1962). Radial distribution of the random close packing of equal spheres. *Nature* 194, 956–957.
- Serra, T., J. Colomer and X. Casamitjana (1997). Aggregation and breakup of particles in a shear flow. *J. Colloid and Interface Science* 187 (2), 466–473.
- Serway, R. A. and C. Vuille (2007). *Essentials of College Physics*. Thomson.
- Seto, R., R. Botet and H. Briesen (2011). Hydrodynamic stress on small colloidal aggregates in shear flow using Stokesian dynamics. *Physical Review E* 84 (4), 041405.
- Smagorinsky, J. (1963). General circulation experiments with the primitive equations, I, The basic experiment. *Monthly Weather Review* 91, 99–165.
- Sommerfeld, M. (2001). Validation of a stochastic Lagrangian modelling approach for inter-particle collisions in homogeneous isotropic turbulence. *Int. J. Multiphase Flow* 27, 1829–1858.
- Sommerfeld, M. (2003). Analysis of collision effects for turbulent gas-particle flow in a horizontal channel: Part I. Particle transport. *Int. J. Multiphase Flow* 29, 675–699.
- Sommerfeld, M., Y. Cui and S. Schmalfuß (2019). Potential and constraints for the application of CFD combined with Lagrangian particle tracking to dry powder inhalers. *European Journal of Pharmaceutical Sciences* 128, 299–324.
- Sommerfeld, M. and S. Stübing (2017). A novel Lagrangian agglomerate structure model. *Powder Technology* 319, 34–52.
- Sommerfeld, M., B. van Wachem and R. Oliemans (2008). Best Practice Guidelines for Computational Fluid Dynamics of Dispersed Multiphase Flows. In: *SIAMUF, Swedish Industrial Association for Multiphase Flows, ERCOFTAC*.
- Sonntag, R. C. and W. B. Russel (1986). Structure and breakup of flocs subjected to fluid stresses: I. Shear experiments. *J. Colloid and Interface Science* 113 (2), 399–413.
- Sonntag, R. C. and W. B. Russel (1987). Structure and breakup of flocs subjected to fluid stresses: II. Theory. *J. Colloid and Interface Science* 115 (2), 378–389.
- Soos, M., A. S. Moussa, L. Ehrl, J. Sefcik, H. Wu and M. Morbidelli (2008). Effect of shear rate on aggregate size and morphology investigated under turbulent conditions in stirred tank. *J. Colloid and Interface Science* 319 (2), 577–589.
- Stone, H. L. (1968). Iterative solution of implicit approximations of multidimensional partial differential equations. *SIAM J. Num. Anal.* 5, 530–558.
- Subero, J., Z. Ning, M. Ghadiri and C. Thornton (1999). Effect of interface energy on the impact strength of agglomerates. *Powder Technology* 105 (1-3), 66–73.

- Suzuki, M. and T. Oshima (1989). Relationship between average coordination number and void fraction in randomly packed systems of uniform-sized spheres developed by four kinds of computer simulation [translated]. *KONA Powder and Particle J.* 7, 22–28.
- Swope, W. C., H. C. Andersen, P. H. Berens and K. R. Wilson (1982). A computer simulation method for the calculation of equilibrium constants for the formation of physical clusters of molecules: Application to small water clusters. *The Journal of Chemical Physics* 76 (1), 637–649.
- Tanaka, T. and Y. Tsuji (1991). Numerical simulation of gas–solid two–phase flow in a vertical pipe: On the effect of inter–particle collision. In: *4th Int. Symp. on Gas–Solid Flows, In: Gas–Solid Flows*. Vol. 121. ASME, 123–128.
- Thomas, D. G. (1963). Transport characteristics of suspensions VII. Relation of hindered–settling floc characteristics to rheological parameters. *AIChE J.* 9 (3), 310–316.
- Thomas, D. G. (1964). Turbulent disruption of flocs in small particle size suspensions. *AIChE J.* 10 (4), 517–523.
- Thornton, C., K. K. Yin and M. J. Adams (1996). Numerical simulation of the impact fracture and fragmentation of agglomerates. *J. Physics D: Applied Physics* 29 (2), 424–435.
- Timoshenko, S. P. and J. N. Goodier (1970). *Theory of Elasticity*. Mc-Graw-Hill Book Company, New York.
- Tomi, D. T. and D. F. Bagster (1978). The behavior of aggregates in stirred vessels. *Transactions of the Institution of Chemical Engineers* 56 (1), 9–18.
- Tong, Z. B., S. Adi, R. Y. Yang, H.-K. Chan and A. B. Yu (2011). Numerical investigation of the de-agglomeration mechanisms of fine powders on mechanical impaction. *J. Aerosol Science* 42 (11), 811–819.
- Tong, Z. B., R. Y. Yang, A. B. Yu, S. Adi and H. K. Chan (2009). Numerical modelling of the breakage of loose agglomerates of fine particles. *Powder Technology* 196 (2), 213–221.
- Tong, Z., B. Zheng, R. Yang, A. Yu and H.-K. Chan (2013). CFD–DEM investigation of the dispersion mechanisms in commercial dry powder inhalers. *Powder Technology* 240, 19–24.
- Tsubaki, J. and G. Jimbo (1984). Theoretical analysis of the tensile strength of a powder bed. *Powder Technology* 37 (1), 219–227.
- Tsuji, Y., T. Kawaguchi and T. Tanaka (1992). Lagrangian numerical simulation of plug flow of cohesionless particles in a horizontal pipe. *Powder Technology* 71, 239–250.
- Tunstall, M. J. and J. K. Harvey (1968). On the effect of a sharp bend in a fully developed turbulent pipe-flow. *J. Fluid Mechanics* 34 (3), 595–608.

- Uhlmann, M. (2005). An immersed boundary method with direct forcing for the simulation of particulate flows. *J. Comput. Phys.* 209 (2), 448–476.
- Uhlmann, M. (2008). Interface-resolved direct numerical simulation of vertical particulate channel flow in the turbulent regime. *Phys. Fluids* 20 (5), 053305.
- Uhlmann, M. and A. Chouippe (2017). Clustering and preferential concentration of finite-size particles in forced homogeneous-isotropic turbulence. *J. Fluid Mech.* 812, 991–1023.
- Van Driest, E. R. (1956). On turbulent flow near a wall. *J. Aero. Sci.* 23.
- Van Wachem, B. and A. Almstedt (2003). Methods for multiphase computational fluid dynamics. *Chem. Eng. J.* 96 (1-3), 81–98.
- Van Wachem, B., J. Schouten, C. van den Bleek, R. Krishna and J. Sinclair (2001). Comparative analysis of CFD models of dense gas-solid systems. *AIChE J.* 47 (5), 1035–1051.
- Van Wachem, B., K. Thalberg, D. Nguyen, L. M. de Juan, J. Remmelgas and I. Niklasson-Bjorn (2020). Analysis, modelling and simulation of the fragmentation of agglomerates. *Chem. Eng. Sci.* 227, 115944.
- Van Wachem, B., K. Thalberg, J. Remmelgas and I. Niklasson-Björn (2017). Simulation of dry powder inhalers: Combining micro-scale, meso-scale and macro-scale modeling. *AIChE J.* 63 (2), 501–516.
- Vanni, M. and A. Gastaldi (2011). Hydrodynamic forces and critical stresses in low-density aggregates under shear flow. *Langmuir* 27 (21), 12822–12833.
- Venters, R., B. T. Helenbrook, G. Ahmadi, D. Bohl and A. Bluestein (2021). Flow through an elbow: A direct numerical simulation investigating turbulent flow quantities. *Int. J. Heat Fluid Flow* 90, 108835.
- Vowinckel, B., J. Withers, P. Luzzatto-Fegiz and E. Meiburg (2019a). Settling of cohesive sediment: Particle-resolved simulations. *J. Fluid Mech.* 858, 5–44.
- Vowinckel, B., E. Biegert, P. Luzzatto-Fegiz and E. Meiburg (2019b). Consolidation of freshly deposited cohesive and noncohesive sediment: Particle-resolved simulations. *Phys. Rev. Fluids* 4 (7), 074305.
- Vowinckel, B., T. Kempe and J. Fröhlich (2014). Fluid-particle interaction in turbulent open channel flow with fully-resolved mobile beds. *Adv. Water Resour.* 72, 32–44.
- Vreman, A. (2016). Particle-resolved direct numerical simulation of homogeneous isotropic turbulence modified by small fixed spheres. *J. Fluid Mech.* 796, 40–85.
- Wang, Y., Y. Zhao and J. Yao (2019). Particle dispersion in turbulent, square open duct flows of high Reynolds number. *Powder Technology* 354, 92–107.

- Weiler, C. (2008). Generierung leicht dispergierbarer Inhalationspulver mittels Sprühtrocknung. PhD thesis. Johannes Gutenberg-Universität Mainz, Mainz, Germany.
- Weiler, C., M. Wolkenhauer, M. Trunk and P. Langguth (2010). New model describing the total dispersion of dry powder agglomerates. *Powder Technology* 203 (2), 248–253.
- Wengeler, R. and H. Nirschl (2007). Turbulent hydrodynamic stress induced dispersion and fragmentation of nanoscale agglomerates. *J. Colloid and Interface Science* 306 (2), 262–273.
- Yali Tang, Y., E. Frank Peters, J. Hans Kuipers, S. Sebastian Kriebitzsch and M. Martin van der Hoef (2015). A new drag correlation from fully resolved simulations of flow past monodisperse static arrays of spheres. *AIChE J.* 61 (2), 688–698.
- Yang, J., C.-Y. Wu and M. Adams (2015). Numerical modelling of agglomeration and deagglomeration in dry powder inhalers: A review. *Current Pharmaceutical Design* 21 (40), 5915–5922.
- Yang, R. Y., A. B. Yu, S. K. Choi, M. S. Coates and H. K. Chan (2008). Agglomeration of fine particles subjected to centripetal compaction. *Powder Technology* 184 (1), 122–129.
- Yao, J. and M. Fairweather (2012). Particle deposition in turbulent duct flows. *Chem. Eng. Sci.* 84, 781–800.
- Yao, J., M. Fairweather and Y. Zhao (2014). Numerical simulation of particle deposition in turbulent duct flows. *Industrial & Engineering Chemistry Research* 53 (8), 3329–3341.
- Yao, J., Y. Zhao and M. Fairweather (2015). Numerical simulation of turbulent flow through a straight square duct. *Applied Thermal Engineering* 91, 800–811.
- Yao, Y. and J. Capecelatro (2021). Deagglomeration of cohesive particles by turbulence. *J. Fluid Mech.* 911.
- Yeung, A., A. Gibbs and R. Pelton (1997). Effect of shear on the strength of polymer-induced flocs. *J. Colloid and Interface Science* 196 (1), 113–115.
- Yu, A. B., C. L. Feng, R. P. Zou and R. Y. Yang (2003). On the relationship between porosity and interparticle forces. *Powder Technology* 130 (1-3), 70–76.
- Zaccone, A., M. Soos, M. Lattuada, H. Wu, M. U. Bäbler and M. Morbidelli (2009). Breakup of dense colloidal aggregates under hydrodynamic stresses. *Physical Review E* 79 (6), 061401.
- Zeiser, T. (2008). Simulation und Analyse von durchströmten Kugelschüttungen in engen Röhren unter Verwendung von Hochleistungsrechnern. PhD thesis. Universität Erlangen–Nürnberg, Nürnberg, Germany.
- Zhang, D. and A. Prosperetti (1997). Momentum and energy equations for disperse two-phase flows and their closure for dilute suspensions. *Int. J. Multiphase Flow* 23 (3), 425–453.

- Zhang, H., F. X. Trias, A. Gorobets, Y. Tan and A. Oliva (2015). Direct numerical simulation of a fully developed turbulent square duct flow up to $Re_\tau = 1200$. *Int. J. Heat Fluid Flow* 54, 258–267.
- Zhao, K., F. Pomes, B. Vowinkel, T.-J. Hsu, B. Bai and E. Meiburg (2021). Flocculation of suspended cohesive particles in homogeneous isotropic turbulence. *J. Fluid Mech.* 921, A17.
- Zheng, Z., S. S. Y. Leung and R. Gupta (2021). Flow and particle modelling of dry powder inhalers: Methodologies, recent development and emerging applications. *Pharmaceutics* 13 (2), 189.
- Zhou, L. (2010). Advances in studies on two-phase turbulence in dispersed multiphase flows. *Int. J. Multiphase Flow* 36 (2), 100–108.
- Zhou, Y. C., B. D. Wright, R. Y. Yang, B. H. Xu and A.-B. Yu (1999). Rolling friction in the dynamic simulation of sandpile formation. *Physica A: Statistical Mechanics and its Applications* 269 (2-4), 536–553.

Publications

Articles in Peer-Reviewed International Journals

1. Khalifa, A., M. Breuer and J. Gollwitzer (2022). Neural-network based approach for modeling wall-impact breakage of agglomerates in particle-laden flows applied in Euler-Lagrange LES. *Int. J. Heat Fluid Flow* 94, 108897.
2. Khalifa, A., J. Gollwitzer and M. Breuer (2021). LES of particle-laden flow in sharp pipe bends with data-driven predictions of agglomerate breakage by wall impacts. *Fluids* 6 (12), 424.
3. Khalifa, A., Breuer, M., 2021. An efficient model for the breakage of agglomerates by wall impact applied to Euler-Lagrange LES predictions. *Int. J. Multiphase Flow* 142, 103625.
4. Khalifa, A., Breuer, M., 2020. Data-driven model for the breakage of dry monodisperse agglomerates by wall impact applicable for multiphase flow simulations. *Powder Technology* 376, 241–253.
5. Breuer, M., Khalifa, A., 2019. Refinement of breakup models for compact powder agglomerates exposed to turbulent flows considering relevant time scales. *Computers & Fluids* 194, 104315.
6. Breuer, M., Khalifa, A., 2019. Revisiting and improving models for the breakup of compact dry powder agglomerates in turbulent flows within Eulerian-Lagrangian simulations. *Powder Technology* 348, 105–125.

Conference Proceedings with Peer Review

1. Breuer, M., and A. Khalifa, 2019. Breakup of agglomerates in turbulent flows: An Euler-Lagrange LES study. Twelfth Int. ERCOFTAC Workshop on DNS and LES: DLES-12, Madrid, Spain, June 5–7, 2019, ERCOFTAC Series, vol. 27, pp. 127–133, *Direct and Large-Eddy Simulation XII*, eds. M. García-Villalba et al., ISBN 978-3-030-42821-1, Springer Nature Switzerland AG, (2020).